

APPLIED
COMPUTATIONAL
ELECTROMAGNETICS
SOCIETY
JOURNAL

November 1996
Vol. 11 No. 3

ISSN 1054-4887

DTIC QUALITY INSPECTED 8

DISTRIBUTION STATEMENT A

Approved for public release;
Distribution Unlimited

GENERAL PURPOSE AND SCOPE. The Applied Computational Electromagnetics Society Journal hereinafter known as the **ACES Journal** is devoted to the exchange of information in computational electromagnetics, to the advancement of the state-of-the-art, and to the promotion of related technical activities. A primary objective of the information exchange is the elimination of the need to "re-invent the wheel" to solve a previously-solved computational problem in electrical engineering, physics, or related fields of study. The technical activities promoted by this publication include code validation, performance analysis, and input/output standardization; code or technique optimization and error minimization; innovations in solution technique or in data input/output; identification of new applications for electromagnetics modeling codes and techniques; integration of computational electromagnetics techniques with new computer architectures; and correlation of computational parameters with physical mechanisms.

SUBMISSIONS CONTENT. The **ACES Journal** welcomes original, previously unpublished papers, relating to **applied computational electromagnetics**.

Typical papers will represent the computational electromagnetics aspects of research in electrical engineering, physics, or related disciplines. However, papers which represent research in **applied computational electromagnetics** itself are equally acceptable.

For additional details, see "Information for Authors" on the back cover.

SUBSCRIPTIONS. All members of the Applied Computational Electromagnetics Society (**ACES**) who have paid their subscription fees are entitled to receive the **ACES Journal** with a minimum of three issues per calendar year. See page 103 for ACES membership and Newsletter and Journal Subscription form.

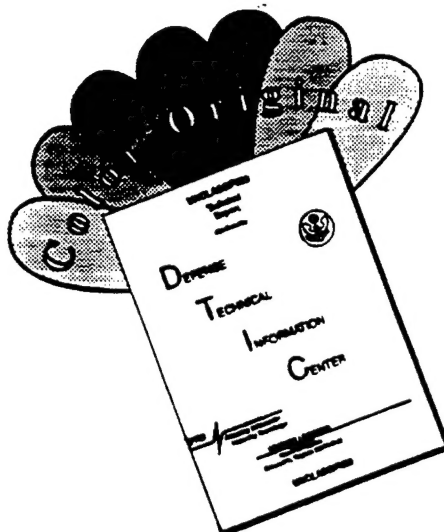
Back issues, when available, are \$15.00 each. Subscriptions to **ACES**, orders for back issues of the **ACES Journal** and changes of addresses should be sent to:

Dr. Richard Adler
ACES Executive Officer
ECE Department, Code ECAB
Naval Postgraduate School
833 Dyer Road, Room 437
Monterey, CA 93943-5121 USA

Allow four week's advance notice for change of address. Claims for missing issues will not be honored because of insufficient notice or address change or loss in mail unless the secretary is notified within 60 days for USA and Canadian subscribers or 90 days for subscribers in other countries, from the last day of the month of publication. For information regarding reprints of individual papers or other materials, see "Information for Authors".

LIABILITY. Neither ACES or the **ACES Journal** editors are responsible for any consequence of misinformation or claims, express or implied, in any published material in an **ACES Journal** issue. This also applies to advertising, for which only camera-ready copies are accepted. Authors are responsible for information contained in their papers. If any material submitted for publication includes material which has already been published elsewhere, it is the author's responsibility to obtain written permission to reproduce such material.

DISCLAIMER NOTICE



THIS DOCUMENT IS BEST QUALITY AVAILABLE. THE COPY FURNISHED TO DTIC CONTAINED A SIGNIFICANT NUMBER OF COLOR PAGES WHICH DO NOT REPRODUCE LEGIBLY ON BLACK AND WHITE MICROFICHE.

APPLIED
COMPUTATIONAL
ELECTROMAGNETICS
SOCIETY
Journal

November 1996
Vol. 11 No. 3

ISSN 1054-4887

The ACES Journal is abstracted in INSPEC, in Engineering Index, and in DTIC.

The second, third, fourth, and fifth illustrations on the front cover have been obtained from Lawrence Livermore National laboratory.

The first illustration on the front cover has been obtained from FLUX2D software, CEDRAT S.S. France, MAGSOFT Corporation, New York.

THE APPLIED COMPUTATIONAL ELECTROMAGNETICS SOCIETY

JOURNAL EDITORS

EDITOR-IN-CHIEF/ACES

W. Perry Wheless, Jr.
University of Alabama, EE Dept.
PO Box 870286
Tuscaloosa, AL 35487-0286 USA

ASSOC. EDITOR-IN-CHIEF/JOURNAL

Adalbert Konrad
University of Toronto
Toronto, ON. CANADA M5S 1A4

Brian A. Austin
University of Liverpool
Liverpool, UK

Fulvio Bessi
Ingegneria dei Sistemi S.p.A.
Pisa, ITALY

Robert Bevensee
Box 812
Alamo, CA, USA

John R. Bowler
University of Surrey
Surrey, UK

Robert T. Brown
Lockheed Aeronautical Sys. Co.
Valencia, CA, USA

Chalmers M. Butler
Clemson University
Clemson, SC, USA

Edgar Coffey
Advanced Electromagnetics
Albuquerque, NM, USA

Tony Fleming
Telecom Australia.
Clayton, Victoria, AUSTRALIA

Pat Foster
Microwave & Antenna Systems
Gt. Malvern, Worc. UK

Gregory R. Haack
DSTO
Salisbury, SA, AUSTRALIA

Christian Hafner
Swiss Federal Inst. of Technology
Zurich, SWITZERLAND

Roger Harrington
Syracuse University
Syracuse, NY, USA

Donald F. Herrick
ERIM
Ann Arbor, MI, USA

Kueichien C. Hill
Wright Laboratory
Wright-Patterson AFB, OH, USA

EDITOR-IN-CHIEF/JOURNAL

Duncan C. Baker
EE Dept. University of Pretoria
0002 Pretoria, SOUTH AFRICA

EDITOR-IN-CHIEF, EMERITUS

Robert M. Bevensee
Box 812
Alamo, CA, 94507-0516 USA

Todd H. Hubing
University of Missouri-Rolla
Rolla, MO, USA

Nathan Ida
The University of Akron
Akron, OH, USA

Magdy F. Iskander
University of Utah
Salt Lake City, UT, USA

Kiyohiko Itoh
Hokkaido University
Sappora, JAPAN

Randy J. Jost
SRI International
Arlington, VA, USA

Linda P.B. Katehi
University of Michigan
Ann Arbor, MI, USA

Peter Krylstedt
National Defence Research Est.
Sundbyberg, SWEDEN

Stanley Kubina
Concordia University
Montreal, Quebec, CANADA

Karl J. Langenberg
Universitat Kasse
Kassel, GERMANY

Ronald Marhefka
Ohio State University
Columbus, OH, USA

Gerald Meunier
NPG/ENSIEG
St. Martin-d'Heres Cedex, FRANCE

Edmund K. Miller
LASL
Santa Fe, NM, USA

Giorgio Molinari
University of Genova
Genova, ITALY

Kenzo Miya
University of Tokyo
Tokyo, JAPAN

MANAGING EDITOR

Richard W. Adler
833 Dyer Rd. Room 437
Naval Postgraduate School Code EC/AB
Monterey, CA 93943-5121 USA

EDITOR-IN-CHIEF, EMERITUS

David E. Stein
USAF Scientific Advisory Board
Washington, DC 20330 USA

Osama A. Mohammed
Florida International Univ.
Miami, FL, USA

Frederic A. Molinet
Societe Mothesim
Plessis-Robinson, FRANCE

Gerrit Mur
Technische Universiteit Delft
Delft, NETHERLANDS

Takayoshi Nakata
Okayama University
Okayama, JAPAN

Andrew F. Peterson
Georgia Institute of Technology
Atlanta, GA, USA

Harold A. Sabbagh
Sabbagh Associates
Bloomington, IN, USA

Chris Smith
Delfin Systems
Santa Clara, CA, USA

David E. Stein
USAF Scientific Advisory Board
Washington, DC, USA

C.W. "Bill" Trowbridge
Vector Fields Limited
Oxford, UK

Jean-Claude Verite
Electricite de France
Clamart, Cedex, FRANCE

John W. Williams
SAIC
Germantown, MD, USA

Frank Walker
Boeing Defence & Space Group
Houston, TX, USA

Keith W. Whites
University of Kentucky
Lexington, KY, USA

Manfred Wurm
FB Technik
Kiel, GERMANY

THE APPLIED COMPUTATIONAL ELECTROMAGNETICS SOCIETY

JOURNAL

TABLE OF CONTENTS

Vol. 11 No. 3

November 1996

"Solution of LaPlace's Equation Using Multiple Paths Method (MPM)" by J. Rashed-Mohassel and M. Fasih	4
"A New Design Method for Low Sidelobe Level Log-Periodic Dipole Antennas" by J.K. Breakall and R.A. Rodriquez Solis	9
"Numerical Evaluation of Singular Integrands in the Application of the Charge Simulation Method with Distributed Charge Density" by E. Cardelli and L. Faina	16
"Measured RCS Polar Contour Maps for Code Validation" by C.L. Larose, S.R. Mishra, and C.W. Trueman	25
"An Efficient Method of Analysis of Co-Planar Dipole Array Antennas" by A.I. Imoro, N. Inagaki, and N. Kikuma	44
"An Algorithm for Solution of the Inverse Electromagnetic Liquid Metal Confinement Problem" by G.J. Bendzsak	55
"Comparison of Magnetically Induced ELF Fields in Humans Computed by FDTD and Scalar Potential FD Codes" by T.W. Dawson, J. De Moerloose, and M.A. Stuchly	63
"Analytic Validation of a Three-Dimensional Scalar-Potential Finite-Difference Code for Low-Frequency Magnetic Induction" by T.W. Dawson and M.A. Stuchly	72
"The Gradient Associated Conjugate Direction Method" by M. Zhang	82
Institutional Membership	99
Announcements:	
Copyright Form	101
Application for ACES Membership and Newsletter and Journal Subscription	103
Advertising Rates	104
Copy Information - Deadline for Submission of Articles	104

© 1996, The Applied Computational Electromagnetics Society

SOLUTION OF LAPLACE'S EQUATION USING MULTIPLE PATHS METHOD (MPM)

J. Rashed-Mohassel
Dept. of Electrical and Computer Engineering
Faculty of Engineering, Tehran University
Tehran, IRAN

M. Fasih
Dept. of Mathematics
University of Sistan and Baluchestan
Zahedan, IRAN

ABSTRACT

A probabilistic method called the multiple paths method (MPM) is presented to solve the potential equation. Unlike other probabilistic techniques there is no need for the generation of a grid resulting in less computation time and simplicity. The method is based on the calculation of the probability of absorption of a particle at a point on the boundary. The random walk is along a "path" which is a line passing through the starting point, where the potential is to be determined. The results show good agreement with other probabilistic methods and numerical techniques.

Keywords: Probabilistic potential theory, probabilistic methods, Multiple paths method, Laplace's equation, Electrostatics

1 INTRODUCTION

Numerical methods are frequently employed in solving electromagnetic problems [1-4]. Other techniques include probabilistic methods such as Monte Carlo (MCM) [5,6,7] and the exodus method [8]. In this work a new method called the multiple paths method (MPM) based on stochastic processes is presented to solve the potential equation in a two dimensional region. Unlike other probabilistic techniques the generation of a grid is not needed resulting in a less computation time and greater simplicity, particularly in the case of irregular regions. Consider Laplace's equation:

$$\nabla^2 V = 0 \text{ with } V = V_b \text{ on the boundary} \quad (1)$$

In probabilistic methods the evaluation of the potential, $V(x_0, y_0)$ at a point (x_0, y_0) in the region is based on the following equation:

$$V(x_0, y_0) = \sum_{k=1}^m p_k V_p(k) \quad (2)$$

where p_k is the probability of absorption of a random walking particle at point K on the boundary, $V_p(k)$ is the prescribed potential at that point and m is the number of trial points. The accuracy of the potential increases with an increasing m . In this equation $V_p(k)$ is known and only p_k is to be determined. In the present method different lines called "paths" are drawn passing through the point (x_0, y_0) whose potential $V(x_0, y_0)$ is to be determined and the random walk is considered along these paths. The complexities arising from the irregularities of the boundary are not present in this method. The method is applied to regions of uniform permittivity as well as different dielectric constants. Since there is no need to generate a grid for a random walk, the evaluation of the potential requires much less computation time.

2 MULTIPLE PATHS METHOD (MPM)

Consider Laplace's equation, (1) with Dirichlet boundary conditions in which the potential, $V(x_0, y_0)$ at (x_0, y_0) is to be determined. In order to determine p_k in (2) an arbitrary point in the region is chosen randomly. The line passing through (x_0, y_0) and this point intersects the boundary at points K and K' with the prescribed potential $V_p(k)$ and $V_p(k')$ respectively and KK' which includes the point (x_0, y_0) is called a path. We divide the path into n segments with equally spaced stations one of which is

located at (x_0, y_0) . Figure 1 shows such a segmentation. The length of KK' is denoted by A while B is the distance of K' to the point (x_0, y_0) . If B is divided into m stations, we have $m = B/d$ and therefore;

$$n = \left(\frac{A}{B}\right) \times m \quad (3)$$

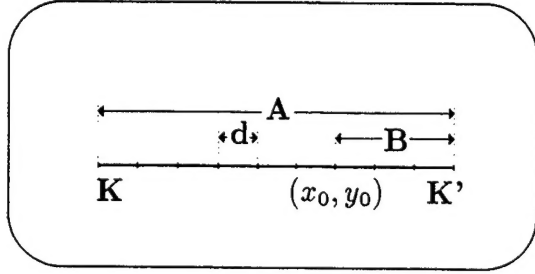


Fig. 1: A Segmented path with a separation 'd' between two neighboring stations.

We consider two cases; (I): n is an integer which is the ideal case and (II): n is not an integer, in which case we can either change m and continue the process until case (I) is reached or we can round off n to an integer. In the latter case we will introduce an error which is not significant for small segments corresponding to a large n . We will show, however, that for homogeneous regions the process is independent of choosing m and such a consideration for m and n is irrelevant. Now consider a particle at (x_0, y_0) for this path and let the probabilities of absorption of the particle at K and K' be p_k and $p_{k'}$ respectively. The problem is now one of a random walk on the specified path (Fig. 2). The probability of absorption to state c when we start from state i (transition state) is denoted by $\Pi_i(c)$ and the probability of absorption to state c starting from state i , after n walks, is denoted by $\Pi_i^n(c)$. Hence,

$$\Pi_i(c) = \sum_{n=1}^{\infty} \Pi_i^n(c) \quad (4)$$

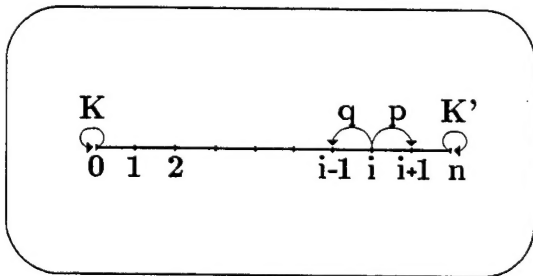


Fig. 2: A path KK' showing the motion of a particle from one state to the next state.

For the probability of absorption after n walks, employing mathematical induction, it can be easily shown that

$$\Pi_i^n(c) = \sum_{j \in T} p_{ij} \Pi_j^{n-1}(c) ; \forall n > 1, i \in T \quad (5)$$

where T is the state space. From system of equations (5), we deduce that

$$\Pi_i(c) = \Pi_i^1(c) + \sum_{j \in T} p_{ij} \Pi_j(c) ; \forall n > 1, i \in T \quad (6)$$

Since Π is a probability function; $\Pi_j \geq 0$ and $\Pi_i(c)$ is the unique, bounded, solution of system of equations (6). P_{ij} 's are the elements of the state transition matrix [9]. In view of the system of equations (6) and Fig. 2, we have, $T = 1, 2, \dots, n-1$ and the transition matrix, P , is given by:

$$P = \begin{bmatrix} 1 & 0 & 0 & \dots & \dots & 0 \\ q & 0 & p & \dots & \dots & 0 \\ 0 & q & 0 & p & \dots & \dots \\ \dots & \dots & \dots & \ddots & \dots & \dots \\ 0 & 0 & 0 & \dots & \dots & 1 \end{bmatrix} \quad (7)$$

in which, $p + q = 1$.

Consider Fig. 2 and suppose that u_i is the probability of starting from state i and ending at state zero (point K) and similarly v_i is the probability of starting at state i and ending at state n (point K'). Hence $u_i = \Pi_i(0)$, and $v_i = \Pi_i(n)$. From the system of equations (6) we will have:

$$\begin{aligned} u_1 &= q + pu_2 \\ u_2 &= qu_1 + pu_3 \\ &\vdots \\ u_j &= qu_{j-1} + pu_{j+1} \\ &\vdots \\ u_{n-1} &= qu_{n-2} \end{aligned}$$

and we will finally deduce, for the probability u_r , [9]:

$$u_r = \frac{\left(\frac{q}{p}\right)^n - \left(\frac{q}{p}\right)^r}{\left(\frac{q}{p}\right)^n - 1} ; p \neq q \quad (8)$$

and

$$u_r = \frac{n-r}{n} ; p = q = 1/2 \quad (9)$$

By a similar procedure v_r can be determined which finally yields:

$$v_r = 1 - u_r \quad (10)$$

Therefore the probability of absorption at each boundary point of the region can be determined from (8), (9) and (10) accordingly. In view of these equations, the computation time reduces by a factor of two since determination of u_k provides v_k simply by (10) and no further computation is needed. The potential $V_1(x_0, y_0)$, based on the first path is therefore given by:

$$V_1(x_0, y_0) = u_i(0)V_p(K) + v_i(n)V_p(K')$$

or equivalently,

$$V_1(x_0, y_0) = [V_p(K) - V_p(K')]u_i + V_p(K') \quad (11)$$

where $V_1(x_0, y_0)$ is the potential at (x_0, y_0) obtained from path (1) and $V_p(K)$ and $V_p(K')$ are the potentials at K and K' on the boundary respectively.

Equation (11) can repeatedly be used to find the potential at (x_0, y_0) for different paths (Fig. 3). If m paths are selected and $V_s(x_0, y_0)$ is the potential obtained at (x_0, y_0) for path s , then for the potential, $V(x_0, y_0)$, at (x_0, y_0) , [5]:

$$V(x_0, y_0) = \frac{\sum_{s=1}^m V_s(x_0, y_0)}{m} \quad (12)$$

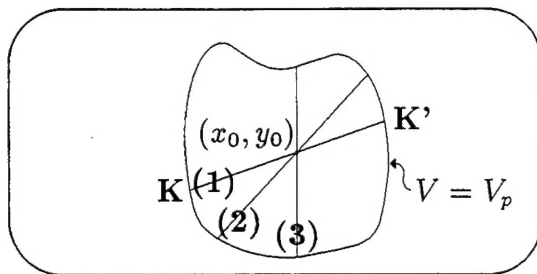


Fig. 3: Some paths used for calculating the potential at the point of interest, (x_0, y_0) .

Consider Fig. 1 where the length of KK' is A and $m = B/d$ with each segment having a length ' d '. Then for the total number of segments in the path, n , equation (3) yields: $n = A/d$ and since for homogeneous regions, $p = q = 1/2$, from (9) and (10) we obtain

$$u_r = \frac{B}{A} \text{ and } v_r = 1 - \frac{B}{A} \quad (13)$$

In this case a solution will clearly be reached quickly and accurately since u_r and v_r depend on A and B and not the segmentation of the path. As was indicated, the generation of a grid in the region is not needed in this method. This is particularly useful for regions with irregular boundaries.

3 RESULTS

In probabilistic methods such as the Monte Carlo method with either fixed or random walk, or the exodus method, the region is subdivided into a grid with square cells and the probability of absorption of a random walking particle to a boundary point, u_r , is considered. For each trial particle, the calculation of this probability needs considerable time since we have a two dimensional grid with the random walking particle along the sides of the square cells in the grid which results in an increasingly higher computation time for the calculation of the probability. In the MPM however, each single path yields two probabilities associated with the end points of the path simply by equation (13) without further computation. This feature of the method along with the elimination of the grid considerably reduces the computation time.

For a better understanding of the method, consider Laplace's equation within a normalized 1 by 1 square with zero potentials on each side except on the upper boundary which it is assumed to be 100 volts. The results are tabulated in Table (I) for three points and different numbers of paths, N . Close agreement is observed with the exact solution with an error less than 5 percent. The potential is also plotted for different numbers of paths, N , when N is varied in steps of 10 (Fig. 4). The smooth variations of potential vs. N shows the convergence of the solution.

Table(I): Comparison of the MPM with the Exact Solution in a 1 by 1 Square

(x,y)	N	MPM	N	MCM	Exact
(0.25,0.75)	50	44.1	500	41.8	43.2
	60	44.25	1000	41.10	
	70	42.75	1500	42.48	
	80	43.73	2000	43.35	
(0.5,0.5)	50	24.00	500	23.6	25.00
	60	25.00	1000	25.8	
	70	25.71	1500	25.27	
	80	25.00	2000	25.1	
(0.75,0.25)	30	5.83	500	6.6	6.80
	40	6.25	1000	7.5	
	50	6.00	1500	7.6	
	60	7.08	2000	7.3	

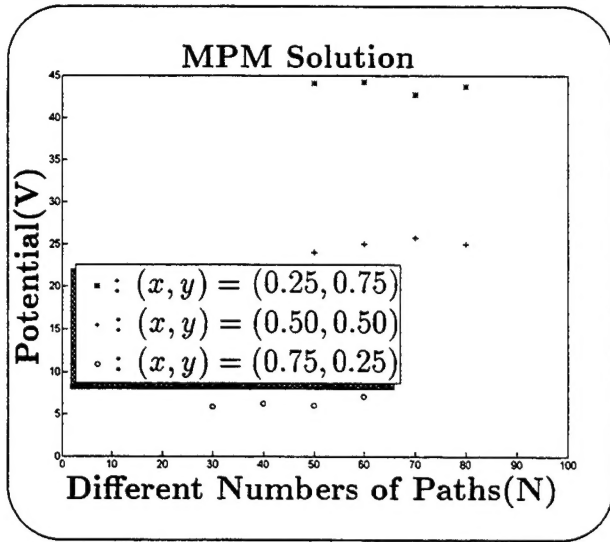


Fig. 4: Potential, V , at three points for different numbers of paths, N .

The Monte Carlo solution with fixed random walk from previous data [7] is also included in Table (I) along with the corresponding N , numbers of walks, for each point. It is observed that for the numbers of paths ranging from 50 to 80, multiple paths method yields comparable results to MCM with 500 to 2000 walks. This justifies the considerable reduction in computation time for MPM.

4 COMPARISON WITH OTHER METHODS

Consider Laplace's equation in a triangular region (Fig. 5). The MPM results are given in Table (II) and compared to the known solutions using finite element (FE), finite difference (FD) and the Monte Carlo methods [2,7] for several points in the region. It is observed that the MPM results agree with other methods. In the case of nonhomogeneous regions a modification of the random walk probabilities at the interface of the dielectrics is needed [9]. In this case (8) is used for u_r at the interface and the random walk probabilities should be evaluated using the appropriate boundary conditions. For instance in Fig. 6 the random walk probabilities in a direction normal to the interface are given by [8,9]:

$$\begin{aligned} P_{n+} &= \frac{\epsilon_1}{2(\epsilon_1 + \epsilon_2)} \\ P_{n-} &= \frac{\epsilon_2}{2(\epsilon_1 + \epsilon_2)} \end{aligned} \quad (14)$$

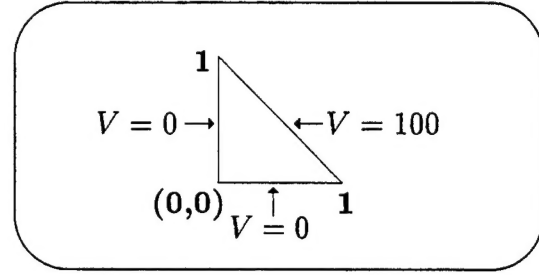


Fig. 5: The triangular region under consideration.

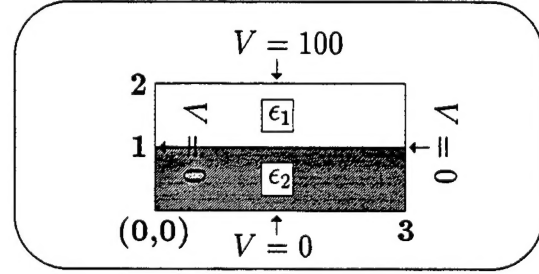


Fig. 6: A 3 by 2 region with two dielectrics.

Table (II): Comparison of the (MPM) Solutions to the Results of Finite Element (FE), Finite Difference (FD) and the Monte Carlo Method (MCM)

(X,Y)	MPM	FEM	FDM	MCM
(0.2,0.4)	36.35	36.36	34.88	36.34
(0.2,0.6)	58.31	59.09	58.72	55.46
(0.4,0.2)	36.20	36.36	26.74	36.93
(0.4,0.4)	68.63	65.15	65.41	69.60
(0.6,0.2)	53.07	59.09	56.69	53.76

While for the tangential probabilities:

$$P_{t+} = P_{t-} = 1/4 \quad (15)$$

The multiple paths method is employed to obtain the solution in a 3 by 2 rectangular region of Fig. 6 with $\epsilon_1 = \epsilon_0$ and $\epsilon_2 = 2.25\epsilon_0$. The results are compared to the previously given data [8]. For simplicity, the values of normal random walk probabilities are used as an average which simplifies the calculations. Since the potential at the interface does not change significantly, particularly for smaller steps an average value is justifiable [10] in return for much less computation time. The solutions show good agreement with the data obtained by previous techniques. These results are given in Table (III) and compared with the exodus method, Monte Carlo method and finite differences [8]. The exact value is also given as a reference.

To have an estimate of computation time and convergence, the MPM results of Table (III) are compared with the MCM, FD, and the exact solution in Table (IV). For the multiple paths method (MPM), the corresponding

numbers of paths, N , is also presented ranging from 50 to 100. The MCM results are for $N = 2000$ walks and the FD results are reported for 1000 iterations [8]. The fast convergence makes the method suitable for real time computation.

Table (III): Comparison of the MPM with Other Methods, Exodus, Monte Carlo and Finite Differences. The Exact Value is Also Given as a Reference

(x,y)	Exodus	MCM	FD	MPM	Exact
(0.5,1.0)	13.41	13.40±1.113	13.16	13.18	13.41
(1.0,1.0)	21.13	20.85±1.162	20.74	21.69	21.13
(1.5,1.0)	23.43	23.58±1.213	22.99	23.29	23.43
(1.5,0.5)	10.52	10.13±0.879	10.21	11.62	10.51
(1.5,1.5)	59.36	58.89±2.138	59.06	59.41	59.34

Table (IV): Comparison of Convergence of Multiple Paths Method (MPM) with MCM and FD

(x,y)	N	MPM	N	MCM	N	FD
(0.5,1.0)	60	13.18	2000	13.40±1.113	1000	13.16
(1.0,1.0)	50	21.69	2000	20.85±1.162	1000	20.74
(1.5,1.0)	60	23.29	2000	23.58±1.213	1000	22.99
(1.5,0.5)	200	11.62	2000	10.13±0.879	1000	10.21
(1.5,1.5)	100	59.41	2000	58.89±2.138	1000	59.06

5 CONCLUSIONS AND DISCUSSION

A probabilistic method called the multiple paths method (MPM) was introduced in this work. The method is based on the calculation of the probability of absorption of a particle on the boundary. The random walk is chosen along an arbitrary path passing through the point whose potential is to be determined. A random number generator is used to select a random path. Unlike other probabilistic methods in which a grid is generated a simple path is used for the random walk. The simple result given by (9) and (10) provides less computation time and faster convergence. In rectangular grids, however, each random walk ends up at one point on the boundary and a large array storage is needed. The MPM results are comparable to other probabilistic techniques and numerical methods as well. There are two factors affecting the error and computation time in probabilistic methods: The finite number of trials and the finite number of steps in a grid. In the new method the probabilities p and q are independent of the number of steps for a homogeneous region and therefore the method is fast and accurate for a uniform medium.

Although MPM introduces less computation time and is simple to apply it still needs improvements. For concave regions and near the boundary, there may arise situations where a "shadow region" is not accessible by any

path and hence part of the boundary may not incorporate in the calculation which can be a source of error. If part of the boundary is occluded by another and the concave region can be divided in two convex regions the shrinking boundary method can be used. The value of the potential on the border line of the two regions can be incorporated as new boundary points into the calculation. A combination of the MPM and a floating random walk, shrinking boundary method or an exodus method routine can be effective in these special cases.

REFERENCES

1. Iskandar, M. F., Morrison, M. D., Datwyler, W. C. and Hamilton, M. S., "A New Course on Computational Methods in Electromagnetics", *IEEE Trans. Educ.*, Vol.31 No.2, pp.101-115, May 1988.
2. Sadiku, M. N. O., "A Simple Introduction to Finite Element Analysis of Electromagnetic Problems", *IEEE Trans. Educ.*, Vol.32 No. 2, pp. 85-93, May 1989.
3. Sadiku, M. N. O., Makki, A. Z. and Lawrence, C. A., "A Further Introduction to Finite Element Analysis of Electromagnetic Problems", *IEEE Trans. Educ.*, Vol.34, No. 4 pp. 322-329, Nov. 1991
4. Hagler, M., "Spreadsheet Solution of Partial Differential Equations", *IEEE Trans. Educ.*, Vol E-30 No., pp. 130-134, Aug. 1987.
5. Royer, G. M., "A Monte Carlo Procedure for Potential Theory Problems", *IEEE Trans. Microwave Theory Tech.*, Vol. MTT-19, No. 10, pp. 813-818, Oct. 1971.
6. Bevensee, R. M., "Probabilistic Potential Theory Applied to Electrical Engineering Problems", *Proc. IEEE*, Vol. 61, No.4, pp. 423-437, Apr. 1973.
7. Sadiku, M. N. O., "Monte Carlo Methods in an Introductory Electromagnetic Course", *IEEE Trans. Educ.*, Vol. 33, No. 1, pp. 73-80, Feb. 1990.
8. Sadiku, M. N. O. and Hunt, D. T., "Solution of Dirichlet Problems by the Exodus Method", *IEEE Trans. Microwave Theory Tech.*, Vol. 40, No. 1, pp. 89-95, Jan. 1992.
9. Karlin, S. and Taylor, H. M., "A First Course in Stochastic Processes", *Academic Press*, 2nd Ed., New York, 1975.
10. Dworsky, L. N., "Modern Transmission Line Theory and Application", *John-Wiley & Sons*, Chap. 9 New York, 1979.

A NEW DESIGN METHOD FOR LOW SIDELOBE LEVEL LOG-PERIODIC DIPOLE ANTENNAS

James K. Breakall and Rafael A. Rodríguez Solís, Department of Electrical Engineering
The Pennsylvania State University

Abstract- A new design procedure for log-periodic dipole arrays is presented in this paper. In this method, either the scale factor or the number of dipole elements is selected, after the boom length, and the operating frequency region are specified. The procedure is applied iteratively, in conjunction to the Numerical Electromagnetic Code, to produce a design with low sidelobe levels. With this new procedure, the antenna designer has more control over the boom length; in older techniques, the boom length and the element spacing were dependent on previous calculations, which frequently resulted on unreasonable values.

Results for several designs are presented, showing the peak gain to peak-sidelobe level ratio, and the antenna gain as a function of frequency, for different scale factors and boom lengths, for a frequency range of 13 to 30 MHz.

I. INTRODUCTION

Log-periodic dipole array (LPDA) antennas are truly broadband structures which can be fabricated to operate over almost any frequency band [1]. These structures commonly present excellent VSWR characteristics over the design bandwidth. However, the radiation characteristics have not been exceptional for most designs; this is particularly true when the designed antenna is placed over ground. The peak gain to peak sidelobe level ratio for these antennas varies from poor to average (10-15 dB).

The design procedure for the LPDA relies mostly on the use of design curves and a series of calculations to obtain the scale factors, τ , σ and α , the dipole element lengths, the spacing between elements, and the boom length. Since the boom length is a result of the design process, an unreasonably large value can be obtained for the boom length, and the procedure must be repeated until a reasonable boom length is obtained. Sometimes, after the procedure is completed, and the antenna dimensions are specified, it is found that the antenna radiation pattern is unacceptable.

For the purpose of improving the design procedure of log-periodic antennas, a new method is presented in this paper. The new design procedure requires as inputs the frequency band of operation, the boom length, L , and either the scale factor, τ , or the number of dipole elements, N . The resulting design is simulated numerically to verify the gain, and peak gain to peak sidelobe level ratio.

This paper presents a comparative study of the peak gain to peak sidelobe level ratio and antenna gain for different scale factors, and boom lengths. Computer simulations were performed using NEC [2].

The results reported show that this new procedure can yield very good designs. Peak gain to peak sidelobe level

ratios in the order of 25-30 dB are possible, while maintaining good VSWR characteristics, and reasonable antenna dimensions.

Two design examples are presented, one following the standard handbook procedure, and one following the new procedure developed here. The resulting array sizes are then compared with each other.

II. BACKGROUND

A. Basic Theory

Log-periodic antennas were introduced by DuHamel and Isbell in 1955 [3,4], as a modification to the equiangular log-spiral antenna characterized by Rumsey [3,4]. Isbell then introduced the LPDA, the most widely used log-periodic structure [4]. The LPDA consists of a sequence of parallel dipoles, with successively increasing lengths outward from the feed point at the apex [5], as shown in Fig. 1 [6]. The feed lines cross over between adjacent elements to provide a 180° phase shift between elements. This phase reversal is necessary to produce a beam pointing in the direction of the smallest elements. In this way, interference from the longer elements is avoided, and the smaller elements act as director elements as in the Yagi-Uda array.

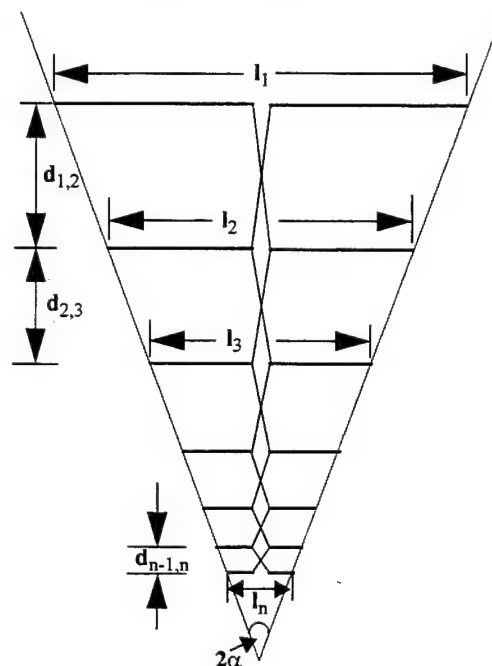


Fig. 1. Log-periodic dipole array geometry

Note from Fig. 1 that the dipole lengths increase along the structure so that the angle α is constant. The geometry of the log-periodic antenna is chosen so that the electrical properties repeat periodically with the logarithm of the frequency [4]. The length and radius of the dipole elements, and the inter-element spacing are scaled so that [7]

$$\tau = \frac{l_{i+1}}{l_i} = \frac{d_{i,i+1}}{d_{i-1,i}} \quad (1)$$

where l_i is the length of dipole i , and $d_{i,i+1}$ is the distance between the centers of dipoles i and $i+1$. Since in practice it is difficult to find wires or tubing with different exact radii, then either only one radius, or a few different radii can be used in the antenna manufacturing without significantly degrading the antenna performance [8].

This self scaling property stated in (1), implies that the array has the same radiating characteristics at frequencies related by a factor τ , e.g., at frequencies $f_1, f_2=\tau f_1, f_3=\tau^2 f_1$, etc.

Not all the elements in the array are active at a given frequency. The elements slightly smaller than a half wavelength constitute the active region, since they support much more current than the rest of the elements.

The frequency band of operation is roughly determined by the frequencies at which the longest and shortest dipoles are half-wavelength resonant, i.e. [5]

$$l_1 = \frac{\lambda_1}{2} \quad \text{and} \quad l_N = \frac{\lambda_N}{2} \quad (2)$$

where l_1 , and l_N are the longest and shortest dipoles, respectively, and λ_1 and λ_N are the wavelengths corresponding to the lower and upper frequency limits, respectively.

The other two parameters that characterize the LPDAs are the spacing factor, σ , and the angle, α . The angle α forms an imaginary wedge that bounds the dipole elements, as shown in Fig. 1. The scaling factor τ , the spacing factor σ , and the angle α are interrelated and are given by [4]

$$\sigma = \frac{d_{i,i+1}}{2l_i} = \frac{1-\tau}{4 \tan \alpha} \quad (3)$$

$$\alpha = \tan^{-1} \left(\frac{1-\tau}{4\sigma} \right) \quad (4)$$

B. Present Handbook Design Procedure

The design procedure is well known, and details on the procedure are available in the literature [8-12]. A short summary of this method is presented in the following paragraphs.

The antenna gain, radiation pattern, and input impedance, depend upon the spacing factor, σ , and the scale factor,

τ . The constant gain contours are given by [4], and are plotted as function of σ and τ in Fig. 2. Note that these contours are reduced by 1.5 dB from the original contours presented by Carrel in [13]. This reduction is an average correction for the error made by Carrel in the calculation of the E-plane pattern [3].

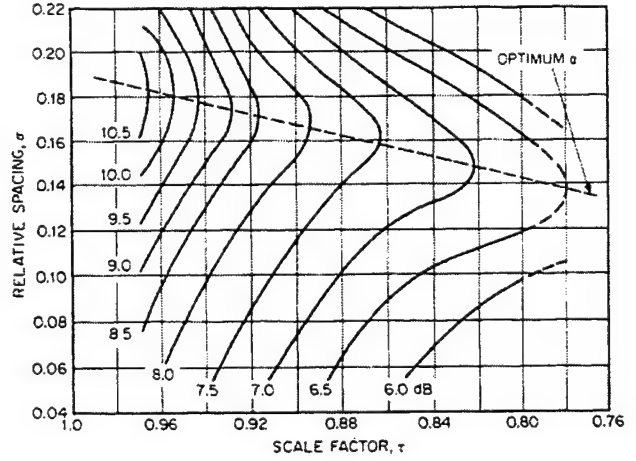


Fig. 2. Gain contours for a log-periodic dipole array (from [4], after Reference [14])

For this procedure, first the antenna bandwidth is selected. Then, the values for σ and τ are found using Fig. 2 and the desired antenna gain; the value of α is found from (4). The lengths of the longest and shortest elements are calculated using (2), and the rest of the element lengths are found from (1). The inter-element spacings can be found from (3), and, finally, the boom length is found by adding all the inter-element spacings.

C. Example

It is desired to design a LPDA that operates between 13 and 30 MHz, with a gain of at least 10.5 dBi, and peak gain to peak sidelobe level ratio of at least 15 dB.

Using Fig. 2, $\sigma=0.179$, and $\tau=0.964$, and from (4), $2\alpha=5.75^\circ$. After applying (2), and (1), the dipole element lengths were calculated. The LPDA antenna designed required 24 elements. The spacings were then calculated from (3), and the boom length turned out to be 65.364 m. Selected values of the dipole lengths and the inter-element spacings are shown in Table I.

Note the excessively long boom length that resulted from this design procedure. A new design technique is developed in order to produce LPDAs with excellent electrical characteristics, while having a reasonable size and fewer elements than those obtained in this case.

III. LPDA ANTENNA DESIGN

A. New Design Procedure

The new design methodology is simplified from that of the standard procedure, by taking advantage of the log-periodic properties of the antenna structure. In the new proce-

ture, the boom length is specified beforehand, to ensure a physically realizable design is obtained. The classical design methodology has the boom length as an output parameter, and therefore, there is the possibility of obtaining a design that is not physically realizable.

TABLE I: SELECTED LENGTHS AND SPACINGS FOR LPDA ANTENNA

i	Dipole Length, l_i (m)	$i-1, i$	Spacing, $d_{i-1, i}$ (m)
1	11.12	1,2	4.13
2	10.72	2,3	3.98
23	5.15	22,23	1.91
24	4.97	23,24	1.84

The new design procedure takes the boom length, L , the frequency range of operation, $f_L < f < f_H$, and either the scale factor, τ , or the number of dipole elements, N , as input parameters. The dipole lengths, l_i , the inter-element spacings, $d_{i-1, i}$, and either N or τ , are then calculated.

The resulting design is then simulated numerically to verify that the gain, and the peak gain to peak sidelobe level ratio comply with the specifications. The procedure is explained in detail in the following paragraphs.

1. Specify the boom length, L , the lowest operating frequency, f_L , and the highest operating frequency, f_H .
2. Set $f_1 = f_L$, and $f_N = 1.5f_H$, to ensure smooth high frequency characteristics.

Recall that the dipole lengths are given by

$$\begin{aligned}
 l_1 &= \frac{\lambda_1}{2} = \frac{c}{2f_1} \\
 l_2 &= \tau l_1 = \tau \frac{c}{2f_1} = \frac{c}{2f_2} \\
 l_i &= \tau^{i-1} l_1 = \tau^{i-1} \frac{c}{2f_1} = \frac{c}{2f_i} \\
 l_N &= \tau^{N-1} l_1 = \tau^{N-1} \frac{c}{2f_1} = \frac{c}{2f_N}
 \end{aligned} \tag{5}$$

and that the spacing between dipole elements is given by

$$\begin{aligned}
 d_{2,3} &= \tau d_{1,2} \\
 d_{3,4} &= \tau d_{2,3} = \tau^2 d_{1,2} \\
 d_{i-1,i} &= \tau^{i-2} d_{1,2} \\
 d_{N-1,N} &= \tau^{N-2} d_{1,2}
 \end{aligned} \tag{6}$$

where l_i is the wavelength at frequency f_i , l_1 is the longest dipole element, l_N is the shortest dipole element, $d_{i-1, i}$ is the spacing between elements $i-1$ and i , and c is the speed of light in a vacuum.

Therefore, rearranging (5),

$$\frac{l_N}{l_1} = \frac{f_1}{f_N} = \tau^{N-1} \tag{7}$$

3. Specify either τ or N .

If τ is specified, taking the logarithm of (7)

$$(N-1) \log \tau = \log \left(\frac{f_1}{f_N} \right) \tag{8}$$

$$N = \frac{\log \left(\frac{f_1}{f_N} \right)}{\log \tau} + 1 \tag{9}$$

If N is specified, then, rearranging (8),

$$\log \tau = \frac{\log \left(\frac{f_1}{f_N} \right)}{(N-1)} \tag{10}$$

$$\tau = 10^{\frac{\log \left(\frac{f_1}{f_N} \right)}{(N-1)}} \tag{11}$$

4. Find the spacing between the two largest elements, $d_{1,2}$.

Recall that L is the sum of all inter-element spacings,

$$L = d_{1,2} + d_{2,3} + \dots + d_{N-1,N} = \sum_{i=2}^N d_{i-1,i} \tag{12}$$

Using (6), (12) becomes

$$L = d_{1,2} + \tau d_{1,2} + \dots + \tau^{N-2} d_{1,2} \quad (13)$$

$$= d_{1,2} \sum_{i=0}^{N-2} \tau^i$$

Equation (13) can be simplified as

$$L = d_{1,2} \left[\frac{\tau^{N-1} - 1}{\tau - 1} \right] \quad (14)$$

Therefore,

$$d_{1,2} = L \left[\frac{\tau - 1}{\tau^{N-1} - 1} \right] \quad (15)$$

5. Find the dipole lengths using (5), and the spacing between elements from (6).
6. Simulate the resulting antenna design, and examine the peak gain to peak sidelobe level ratio, and the antenna gain.
7. Repeat the procedure by changing L , τ or N , until the design meets the specifications.

In the next section, a LPDA antenna is designed following the aforementioned procedure.

B. Example

Design a LPDA as specified in Section II-B, but with a minimum peak gain of 12 dBi over average ground, and a peak gain to peak sidelobe level ratio greater than 20 dB.

1. $f_L=13$ MHz, $f_H=30$ MHz, $L=7.3, 9.14, 11, 12.8, 14.6$ m.
2. $f_1=13$ MHz, $f_N=1.5(30)=45$ MHz.
3. $\tau=0.85, 0.87, 0.89, 0.91, 0.93, 0.95$; $N=9, 10, 12, 14, 18, 25$.

The scale factor, τ , (or the number of elements) is varied for each boom length case. The resulting antenna design for each case is modeled using NEC 3. In the simulation, the antenna is placed 16.8 m above ground with relative permittivity $\epsilon_r=13.0$, and conductivity $\sigma=5.0$ mS/m. The boom is modeled as a transmission line, of characteristic impedance $Z_0=200 \Omega$, connecting the dipole elements. The peak gain to peak sidelobe level ratio is recorded for elevation angles of 0° to 40° , and its largest value is plotted against frequency. The antenna gain is also plotted against frequency.

Results are shown for the case of $L=14.6$ m. Figures 3 and 4 show the peak gain to peak sidelobe level ratio, and the

antenna gain, respectively, for $\tau=0.85, 0.87, 0.89$. Figures 5 and 6 show the peak gain to peak sidelobe level ratio, and the antenna gain, respectively, for $\tau=0.91, 0.93, 0.95$.

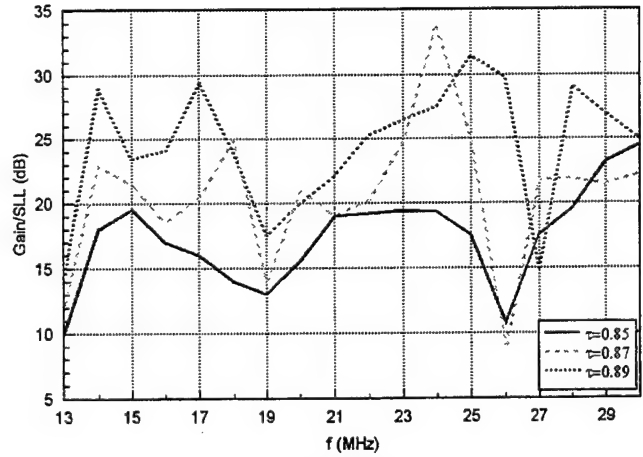


Fig. 3. Peak gain to peak sidelobe level ratio for $L=14.6$ m and $h=16.8$ m.

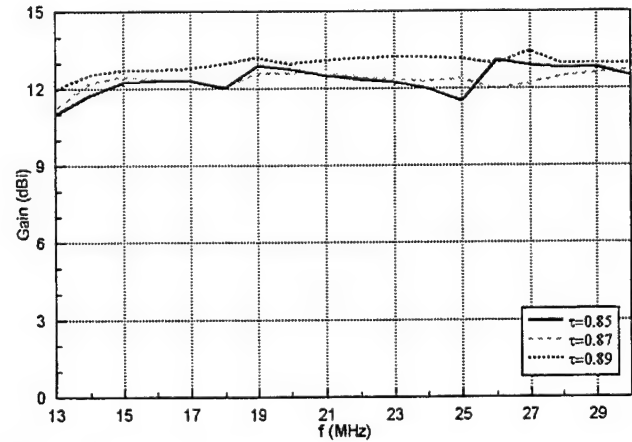


Fig. 4. Gain for $L=14.6$ m and $h=16.8$ m.

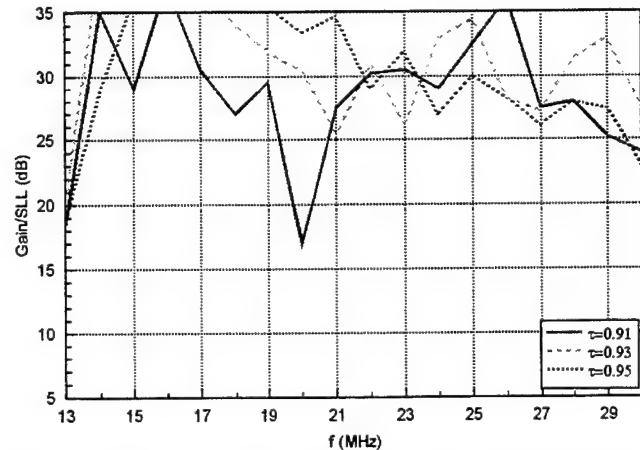


Fig. 5. Peak gain to peak sidelobe level ratio for $L=9.14$ m and $h=16.8$ m.

Note that as τ increases, so does the peak gain to peak sidelobe level ratio. The condition of having a peak gain to peak sidelobe level ratio greater than 20 dB is met only for

$\tau=0.93$, and $\tau=0.95$. However, increasing τ from 0.93 to 0.95, increases the number of elements by seven.

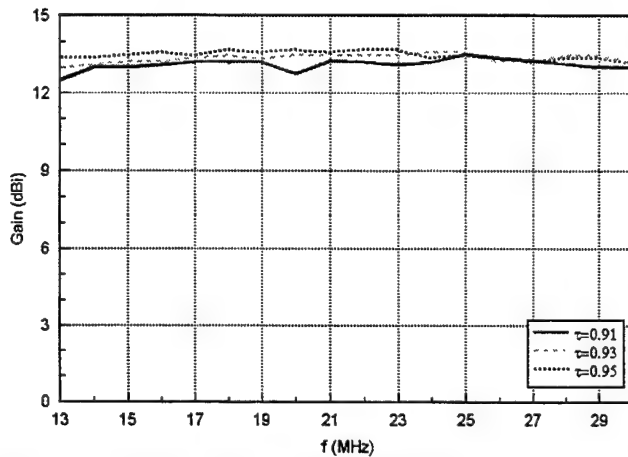


Fig. 6. Gain for $L=9.14$ m and $h=16.8$ m.

For smaller boom lengths, the peak gain to peak side-lobe level ratio criterion was met for other values of τ , and numbers of elements.

The antenna gain is very flat over the entire frequency band, having a value of about 13 dBi. As the boom length is shortened, the gain slightly decreases. Therefore, a scale factor, $\tau=0.93$, is selected, yielding an 18 element LPDA. Selected values for the dipole lengths and inter-element spacings are presented in Table II. All dipole elements have a radius of 12.7 mm.

TABLE II: SELECTED LENGTHS AND SPACINGS FOR LPDA ANTENNA

i	Dipole Length, l_i (m)	$i-1, i$	Spacing, $d_{i-1, i}$ (m)
1	11.54	1,2	1.44
2	10.73	2,3	1.34
17	3.61	16,17	0.48
18	3.33	17,18	0.45

Figures 7-12 show representative azimuth and elevation patterns calculated with NEC for the selected design, at 14.2, 21.2, and 28.5 MHz. Fig. 13 shows that a VSWR of less than 1.4 was obtained for the entire frequency band.

Note that the gain of this antenna is higher than the one expected for the antenna designed with the traditional method. This improvement over the standard handbook method was achieved with a smaller number of elements, and a shorter boom length. If the LPDA antenna with minimum gain of 12 dBi was to be designed with the traditional method, the number of elements would increase to 43, and the boom length would be almost twice the original value computed for the antenna with 10.5 dBi gain.

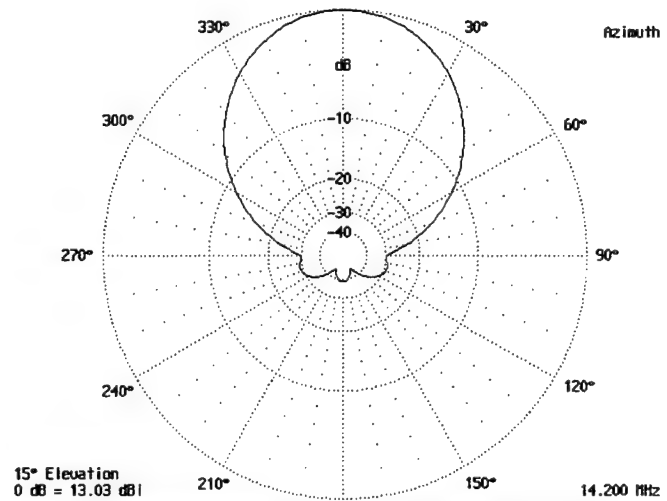


Fig. 7. Azimuth pattern for $f=14.2$ MHz and $h=16.8$ m.

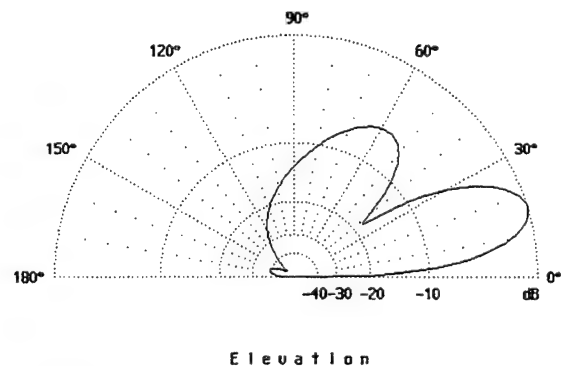


Fig. 8. Elevation pattern for $f=14.2$ MHz and $h=16.8$ m.

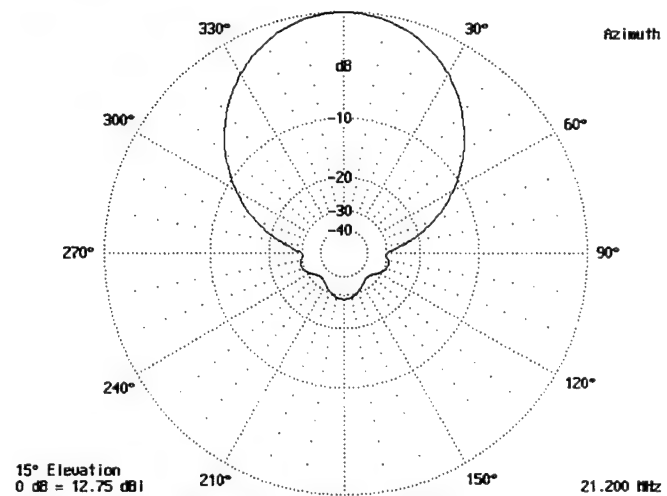
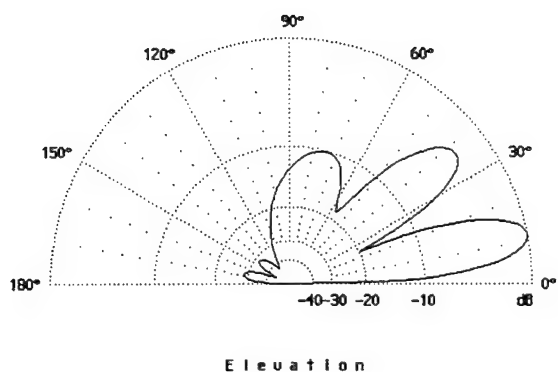
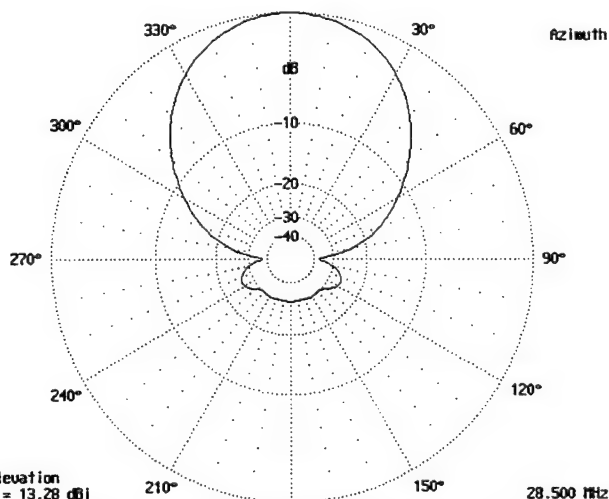


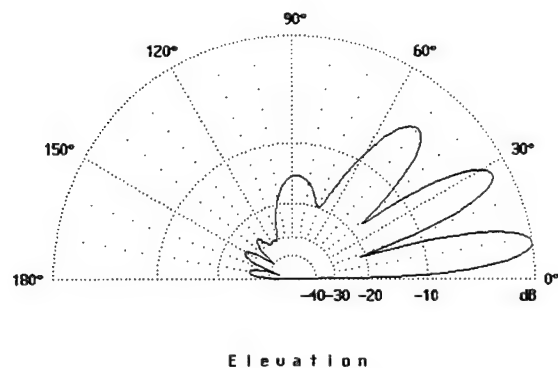
Fig. 9. Azimuth pattern for $f=21.2$ MHz and $h=16.8$ m.



0 dB = 13.56 dBi
Fig. 10. Elevation pattern for $f=21.2$ MHz and $h=16.8$ m.



8° Elevation
0 dB = 13.28 dBi
Fig. 11. Azimuth pattern for $f=28.5$ MHz and $h=16.8$ m



0 dB = 13.35 dBi
Fig. 12. Elevation pattern for $f=28.5$ MHz and $h=16.8$ m.

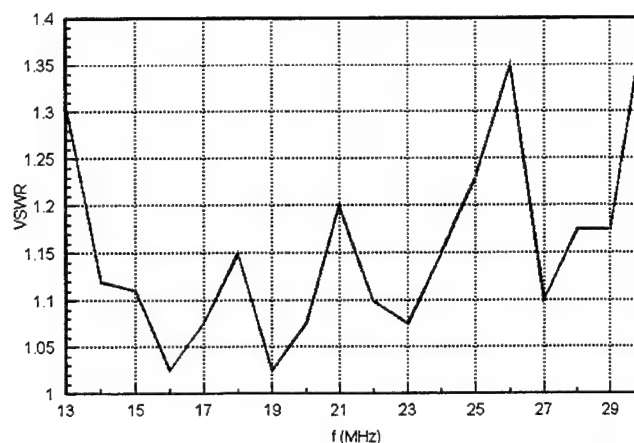


Fig. 13. VSWR for final design, $\tau=0.93$, $L=14.6$ m, and $h=16.8$ m.

IV. CONCLUSIONS

A new procedure for the design of log-periodic dipole array antennas has been developed. In this new procedure, the boom length is selected beforehand. Specifying the boom length as the first step in the design procedure, ensures that impractical values for the boom length do not arise.

An antenna was designed following both the old and the new procedures. It was shown that the new design technique produced a smaller antenna size, and a fewer number of elements than the old procedure, while maintaining excellent radiation and VSWR characteristics.

It was also shown that the peak gain to peak sidelobe level ratio increases as the τ factor is increased, for a given boom length. The antenna gain was very flat over the frequency band of interest, and it increased slightly for larger values of τ , and L .

ACKNOWLEDGMENTS

The authors would like to thank José G. Colom, and Athena McDowell, for their help and input in the review of the paper.

REFERENCES

- [1] Collin, R. E., *Antennas and Radiowave Propagation*, New York, NY: McGraw Hill, 1985, Chapter 3.
- [2] Burke, G. J., and A. J. Poggio, "Numerical Electromagnetics Code (NEC)-Method of Moments", Lawrence-Livermore National Laboratory UCID-18834, January, 1981.
- [3] Mittra, R., "Log-Periodic Antennas", in *Antenna Theory, Part 2*, Collin and Zucker, eds., New York, NY: McGraw Hill, 1969, Chapter 22.
- [4] DuHamel, R. H., and G. G. Chadwick, "Frequency-Independent Antennas", in *Antenna Engineering Handbook, Second Edition*, Johnson and Jasik, eds., New

York, NY: McGraw Hill, 1984, Chapter 14.

- [5] Stutzman, W. L., and G. A. Thiele, *Antenna Theory and Design*, New York, NY: John Wiley & Sons, 1981, pp 294-303.
- [6] Isbell, D.E., "Log-Periodic Arrays", *IRE Transactions Antennas and Propagation*, vol. AP-8, pp. 260-267, 1960.
- [7] Kraus, J. D., *Antennas*, New York, NY: McGraw Hill, 1988, pp 703-708.
- [8] Balanis C. A., *Antenna Theory, Analysis and Design*, New York, NY: Harper & Row, 1982, pp 427-439.
- [9] DeVito, G., and G.B. Stracca, "Comments on the Design of Log-Periodic Antennas", *IEEE Transactions Antennas and Propagation*, vol. AP-21, pp 303-308, 1973.
- [10] Smith, C. E., *Log Periodic Antenna Design Handbook*, Cleveland, Ohio: Smith Electronics, 1966.
- [11] DeVito, G., and G.B. Stracca, "Further Comments on the Design of Log-Periodic Antennas", *IEEE Transactions Antennas and Propagation*, vol. AP-22, pp 714-718, 1974.
- [12] Butson, P. C. and G. T. Thomson, "A Note on the Calculation of the Gain of Log -Periodic Dipole Antennas" *IEEE Transactions of Antennas and Propagation*, vol. AP-14, pp 105-106, 1976.
- [13] Ma, M. T. *Theory and Applications of Antenna Arrays*, New York, NY: Wiley, 1974.
- [14] Carrel, R. "The design of log-periodic dipole antennas", *IRE International Convention, Part 1*, pp 61-75, 1961.

Numerical Evaluation of Singular Integrands in the Application of the Charge Simulation Method with Distributed Charge Density

Ermanno Cardelli
Istituto di Energetica, Univ. di Perugia
Str. S. Lucia Canetola, 06125 Perugia (Italy)
Tel. +39 75 5852731, Fax# +39 75 5852703
e-mail: ermanno@turbo.isten.unipg.it

Loris Faina
Dip. di Matematica, Univ. di Perugia
Via L. Vanvitelli 1, 06100 Perugia (Italy)
Fax# +39 75 5855024
e-mail: faina@unipg.it

Abstract: As it is well known the Charge Simulation Method is a numerical method for the computation of the electric field in three-dimensional problems, based on the concept of the substitution of the electrostatic geometry with a series of elementary charge suitably arranged. In this paper we will show a possible, useful way to overpass the difficulties arising in the numerical computations on the integral expression of the electric potential in the contour points where the boundary conditions are imposed, when distributed surface charges are used in the simulation. The numerical approach presented here allows us to evaluate with accuracy the potential coefficients on the metallic surfaces, avoiding the presence of oscillatory numerical solutions in the computation of the electric potential and of the electric field strength around the electrodes, that generally occurs when discrete charges are used in the simulation.

1 Introduction

As it is well-known, the calculation of electrostatic fields requires the solution of Laplace's and Poisson's equations with the imposition of suitable boundary conditions.

Generally the geometrical complexity of the systems involved in engineering applications such as high voltage plants, power transmission lines, makes impossible to find analytical solutions for the distribution of the electric field and its gradient strength. Therefore, numerical methods are commonly used. Among these methods, integral approaches to the solution of Laplace's and Poisson's equations, like the Charge Simulation Method ([7],[8],[3],[2],[1]), are widely used, especially in ultra high voltage systems design, for its good applicability to full three dimensional problems. This method is based on the concept of the substitution of the electrodes geometry with a series of unknown discrete charges. The value of these charges are determined by imposing that their global effect satisfies the boundary conditions in a selected number of points, located in the boundary regions. As electric fields distribution so obtained due to these arrangements of charges satisfies the Laplace's or Poisson's equation inside the domain under analysis, the numerical solution found is unique inside the domain. The discrete nature of this approach requires the selection and the placement of a large number of fictitious charges to reach the required numerical accuracy, especially in problems with more than two different dielectric materials and/or in presence of thin dielectric or conductors layers. Moreover, the use of discrete charges in shape of point, segment or annular sector involves their placement at a certain distance outside the boundary, to avoid singularity problems, and this fact leads to significantly loss in accuracy of the numerical computation near the interface between electrodes and dielectrics, especially in presence of sharp edges and of thin layers of materials.

A possible way to maintain the number of the simulation charges to a practically treatable one and, at the same time, to overpass this problem, seems to be the use of distributed charge densities in the discretization.

In this paper a possible application of the Charge Simulation Method with the use of distributed charge densities, placed in the surface of the electrodes, is described, solving the problem of the numerical treatment of the singularities contained in the integral expression used for the evaluation of the electric potential and the field strength.

2 Numerical Formulation

In the Charge Simulation Method, for the calculation of the magnitude of the electric charges used in the discretization, n points on the surface of the conductors, called contour points, are chosen and at any of these points the electric potential resulting from the superposition of the effects of the charges is posed equal to the known boundary values:

$$V_k = \sum_{i=1}^n p_{i,k} q_i \quad (2.1)$$

where $p_{i,k}$ are the electric potential coefficients, q_i the distributed charges, and V_k the values of the voltage.

In general, the integral expression of the coefficients $p_{i,j}$ can be written as follows:

$$p_{i,k} = \frac{1}{4\pi\epsilon |\Omega_i|} \iint_{\Omega_i} \frac{d\Omega_i}{r_{i,k}} \quad (2.2)$$

where Ω_i is the portion of the surface of the electrodes where the surface charge q_i is distributed, and contain a discontinuity in the integrand functions when the i -th point coincides with the k -th one.

The numerical treatment of these discontinuity has been avoided up to now by replacing the distributed surface charges by discrete, fictitious charges, for instance in shape of point, segment, and ring. Unfortunately, numerical experiments performing this technique of arrangement have generally shown a reduction in the numerical accuracy of the results and the presence of oscillatory numerical solutions in the zones near the electrodes, where on the other hand the accurate evaluation of the electric potential and of the electric field strength are often required for the design of the devices.

In the following, a possible technique used to solve numerically the treatment of these discontinuities is described, and it is applied to the main surface portions that can be used in the numerical simulation of the behaviour of high voltage devices and systems.

2.1 Case (a). The cylindrical surface sector

Let us parametrize the cylindrical surface in cylindrical coordinates and consider the following discretization (see fig. 1):

$$h_0 = 0 < \dots < h_i < \dots < h_n = L \quad \text{and} \quad \theta_0 = 0 < \dots < \theta_j < \dots < \theta_m = 2\pi, \quad (2.3)$$

where $h_i = \frac{Li}{n}$; $i = 0, \dots, n$ and $\theta_j = \frac{2\pi j}{m}$; $j = 0, \dots, m$.

We will denote by $P = (R_P \cos \theta_P, R_P \sin \theta_P, h_P)$ a generic point in \mathbf{R}^3 , and by

$$P_{i,j} = \left(r \cos \frac{\theta_{j+1} + \theta_j}{2}, r \sin \frac{\theta_{j+1} + \theta_j}{2}, \frac{h_{i+1} + h_i}{2} \right) = (r \cos \theta^j, r \sin \theta^j, h^i)$$

the generic point on the cylinder's surface. The general expression for the potential coefficient $p_{(i,j),P}$ on a point P generated by the surface element $\Omega_{i,j} = \{(h, \theta) : h_i \leq h < h_{i+1}, \theta_j \leq \theta < \theta_{j+1}\}$ of the cylinder is:

$$p_{(i,j),P} = \frac{r}{4\pi\epsilon |\Omega_{i,j}|} \int_{\theta_j}^{\theta_{j+1}} \int_{h_i}^{h_{i+1}} \frac{d\theta dh}{\sqrt{R_P^2 + r^2 - 2R_P r \cos(\theta - \theta_P) + (h - h_P)^2}}. \quad (2.4)$$

The integration with respect to the variable h can be performed in an analytical way:

setting,

$$A^2 = R_P^2 + r^2 - 2R_P r \cos(\theta - \theta_P) \quad , \quad h - h_P = H$$

we get,

$$\int \frac{dh}{\sqrt{R_P^2 + r^2 - 2R_P r \cos(\theta - \theta_P) + (h - h_P)^2}} = \int \frac{dH}{\sqrt{A^2 + H^2}}. \quad (2.5)$$

Setting,

$$\sqrt{A^2 + H^2} = H + t \quad , \quad H = \frac{A^2 - t^2}{2t} \quad , \quad dH = -\frac{A^2 + t^2}{2t^2} dt$$

we have,

$$\int \frac{dH}{\sqrt{A^2 + H^2}} = -\ln t = -\ln(\sqrt{A^2 + H^2} - H). \quad (2.6)$$

By imposing the inverse substitution, we get

$$\begin{aligned} F_j^P(\theta) &= \int_{h_i}^{h_{i+1}} \frac{dh}{\sqrt{R_P^2 + r^2 - 2R_P r \cos(\theta - \theta_P) + (h - h_P)^2}} \\ &= \ln \left(\frac{\sqrt{R_P^2 + r^2 - 2R_P r \cos(\theta - \theta_P) + (h_i - h_P)^2} - (h_i - h_P)}{\sqrt{R_P^2 + r^2 - 2R_P r \cos(\theta - \theta_P) + (h_{i+1} - h_P)^2} - (h_{i+1} - h_P)} \right) \\ &= \ln \left(\frac{\sqrt{R_P^2 + r^2 - 2R_P r \cos(\theta - \theta_P) + (h_i - h_P)^2} - (h_i - h_P)}{R_P^2 + r^2 - 2R_P r \cos(\theta - \theta_P)} \right) \\ &\quad + \ln \left(\sqrt{R_P^2 + r^2 - 2R_P r \cos(\theta - \theta_P) + (h_{i+1} - h_P)^2} + (h_{i+1} - h_P) \right) \end{aligned} \quad (2.7)$$

with a simple rationalization.

Now, if the point P is different from $P_{i,j}$, then the integration of (2.7) with respect to θ can be performed with a simple Gaussian quadrature. For the case $P = P_{i,j}$, let us study the only singular term

$$\ln(2r^2(1 - \cos(\theta - \theta^j))). \quad (2.8)$$

The next step is to find the order of singularity of (2.8). To this end, let us consider

$$\lim_{\theta \rightarrow \theta^j} \frac{\ln(2r^2(1 - \cos(\theta - \theta^j)))}{\left(\frac{1}{\theta - \theta^j}\right)^\beta} = \lim_{\theta \rightarrow \theta^j} \frac{\sin(\theta - \theta^j)}{1 - \cos(\theta - \theta^j)} \frac{(\theta - \theta^j)^{\beta+1}}{-\beta} = 0$$

for every $\beta > 0$. This means that (2.8) has a singularity of logarithmic type. Thus, we can consider the following technique as a suitable way for reducing the singularity of $F_j^{P_{i,j}}(\theta)$:

$$\begin{aligned} \int_{\theta_j}^{\theta_{j+1}} F_j^{P_{i,j}} d\theta &= \int_{\theta_j}^{\theta^j} F_j^{P_{i,j}} d\theta + \int_{\theta^j}^{\theta_{j+1}} F_j^{P_{i,j}} d\theta \\ &= \frac{1}{1-\gamma} \left[\int_0^{(\theta^j - \theta_j)^{1-\gamma}} t^{\frac{\gamma}{1-\gamma}} F_j^{P_{i,j}}(\theta^j - t^{\frac{1}{1-\gamma}}) dt \right. \\ &\quad \left. + \int_0^{(\theta_{j+1} - \theta^j)^{1-\gamma}} t^{\frac{\gamma}{1-\gamma}} F_j^{P_{i,j}}(\theta^j + t^{\frac{1}{1-\gamma}}) dt \right] \end{aligned} \quad (2.9)$$

for any γ , with $0 < \gamma < 1$, making the change of variables $t = (\theta - \theta_j)^{1-\gamma}$ in the first integral and $t = (\theta - \theta^j)^{1-\gamma}$ in the second integral. The evaluation of these integrals is again performed by means of a Gaussian quadrature method. From our tests, it results that any γ between 0 and 1 is suitable for improving the numerical results. For the numerical simulation, we choose the value $\gamma = \frac{1}{2}$, because it is the most convenient value from a computational point of view. In fact, with $\gamma = \frac{1}{2}$, we have only to do square roots and raising to the power of two, while with $\gamma \neq \frac{1}{2}$ we have to use several routines for the raising to the power of a fractional value that are much more time consuming.

2.2 Case (b). The flat disk sector

Let us parametrize the flat disk in polar coordinates and consider the following discretization (see fig. 2):

$$\rho_0 = 0 < \dots < \rho_i < \dots < \rho_n = r \quad \text{and} \quad \theta_0 = 0 < \dots < \theta_j < \dots < \theta_m = 2\pi, \quad (2.10)$$

where $\rho_i = \frac{ri}{n}$; $i = 0, \dots, n$ and $\theta_j = \frac{2\pi j}{m}$; $j = 0, \dots, m$.

We will denote by $P = (R_P \cos \theta_P, R_P \sin \theta_P, h_P)$ a generical point in \mathbf{R}^3 , and by

$$P_{i,j} = \left(\frac{\rho_{i+1} + \rho_i}{2} \cos \frac{\theta_{j+1} + \theta_j}{2}, \frac{\rho_{i+1} + \rho_i}{2} \sin \frac{\theta_{j+1} + \theta_j}{2}, 0 \right) = (\rho^i \cos \theta^j, \rho^i \sin \theta^j, 0)$$

the generic point on the flat disk. The general expression for the potential coefficient $p_{(i,j),P}$ on a point P generated by the surface element $\Omega_{i,j} = \{(\rho, \theta) : \rho_i \leq \rho < \rho_{i+1}, \theta_j \leq \theta < \theta_{j+1}\}$ of the flat disk is:

$$p_{(i,j),P} = \frac{1}{4\pi\epsilon |\Omega_{i,j}|} \int_{\theta_j}^{\theta_{j+1}} \int_{\rho_i}^{\rho_{i+1}} \frac{\rho d\theta d\rho}{\sqrt{R_P^2 + \rho^2 - 2R_P\rho \cos(\theta - \theta_P) + h_P^2}}. \quad (2.11)$$

The integration with respect to the variable ρ can be performed in an analytical way:

setting,

$$\begin{aligned} A^2 &= 2R_P \cos(\theta - \theta_P), \quad B^2 = R_P^2 + h_P^2 \\ \sqrt{\rho^2 - A^2\rho + B^2} &= \rho + t, \quad \rho = \frac{B^2 - t^2}{A^2 + 2t} \\ d\rho &= \frac{-2(t^2 + A^2t + B^2)}{(A^2 + 2t)^2} dt \end{aligned}$$

we get,

$$\int \frac{d\rho}{\sqrt{\rho^2 - A^2\rho + B^2}} = -\ln(A^2 + 2t).$$

Therefore,

$$\begin{aligned} F_j^P(\theta) &= \int_{\rho_i}^{\rho_{i+1}} \frac{\rho d\rho}{\sqrt{\rho^2 + R_P^2 + h_P^2 - 2\rho R_P \cos(\theta - \theta_P)}} \\ &= \frac{1}{2} \left[\int_{\rho_i}^{\rho_{i+1}} \frac{(2\rho - 2R_P \cos(\theta - \theta_P)) d\rho}{\sqrt{\rho^2 + R_P^2 + h_P^2 - 2\rho R_P \cos(\theta - \theta_P)}} \right. \\ &\quad \left. - A^2 \ln \left(2\sqrt{\rho^2 - A^2\rho + B^2} - (2\rho - 2R_P \cos(\theta - \theta_P)) \right) \right]_{\rho_i}^{\rho_{i+1}} \\ &= \frac{1}{2} \left[\sqrt{\rho_{i+1}^2 + B^2 - 2\rho_{i+1}R_P \cos(\theta - \theta_P)} - \sqrt{\rho_i^2 + B^2 - 2\rho_iR_P \cos(\theta - \theta_P)} \right. \\ &\quad \left. + A^2 \ln \left(\frac{2\sqrt{\rho_1^2 - 2R_P\rho_1 \cos(\theta - \theta_P)} + R_P^2 + h_P^2 - (2\rho_1 - 2R_P \cos(\theta - \theta_P))}{4R_P^2 \sin^2(\theta - \theta_P) + 4h_P^2} \right) \right. \\ &\quad \left. + A^2 \ln \left(2\sqrt{\rho_2^2 - 2R_P\rho_2 \cos(\theta - \theta_P)} + R_P^2 + h_P^2 + (2\rho_2 - 2R_P \cos(\theta - \theta_P)) \right) \right] \end{aligned} \quad (2.12)$$

with a simple rationalization.

Now, if the point P is different from $P_{i,j}$, then the integration of (2.12) in θ can be performed with a simple Gaussian quadrature. For the case $P = P_{i,j}$, proceeding in analogy to the case (a), we discover that (2.12) has a singularity of logarithmic type, and a change of variables of type (2.9) with $\gamma = \frac{1}{2}$ will solve all the numerical problems due to the singularity of (2.12).

2.3 Case (c). The spherical surface sector

Let us parametrize the spherical surface in spherical coordinates and consider the following discretization (see fig. 3):

$$\phi_0 = 0 < \dots < \phi_i < \dots < \phi_n = 2\pi, \quad \text{and} \quad \theta_0 = 0 < \dots < \theta_j < \dots < \theta_m = \pi, \quad (2.13)$$

where $\phi_i = \frac{2\pi i}{n}$; $i = 0, \dots, n$ and $\theta_j = \frac{\pi j}{m}$; $j = 0, \dots, m$.

We will denote by

$$P = (R_P \sin \theta_P \cos \phi_P, R_P \sin \theta_P \sin \phi_P, R_P \cos \theta_P)$$

a generic point in \mathbf{R}^3 , and by

$$\begin{aligned} P_{i,j} &= \left(r \sin \frac{\theta_{j+1} + \theta_j}{2} \cos \frac{\phi_{i+1} + \phi_i}{2}, r \sin \frac{\theta_{j+1} + \theta_j}{2} \sin \frac{\phi_{i+1} + \phi_i}{2}, r \cos \frac{\theta_{j+1} + \theta_j}{2} \right) \\ &= (r \sin \theta^j \cos \phi^i, r \sin \theta^j \sin \phi^i, r \cos \theta^j) \end{aligned}$$

the generical point on the spherical surface. The general expression for the potential coefficient $p_{(i,j),P}$ on a point P generated by the surface element $\Omega_{i,j} = \{(\phi, \theta) : \phi_i \leq \phi < \phi_{i+1}, \theta_j \leq \theta < \theta_{j+1}\}$ is:

$$p_{(i,j),P} = \frac{r^2}{4\pi\epsilon |\Omega_{i,j}|} \int_{\theta_j}^{\theta_{j+1}} \int_{\phi_i}^{\phi_{i+1}} \frac{\sin \theta d\theta d\phi}{\sqrt{R_P^2 + r^2 - 2R_P r [\cos \theta_P \cos \theta + \cos(\phi - \phi_P) \sin \theta \sin \theta_P]}}. \quad (2.14)$$

Now, if the point P is outside the finite element $\Omega_{i,j}$, then this double integral can be efficiently calculated with two nested Gaussian quadrature routines. But, if the point $P = P_{i,j}$, then the formula (2.14) becomes

$$p_{(i,j),P} = \frac{r^2}{4\sqrt{2}\pi\epsilon |\Omega_{i,j}|} \int_{\theta_j}^{\theta_{j+1}} \int_{\phi_i}^{\phi_{i+1}} \frac{\sin \theta d\theta d\phi}{\sqrt{1 - [\cos \theta_P \cos \theta + \cos(\phi - \phi_P) \sin \theta \sin \theta_P]}} \quad (2.15)$$

and the integrand

$$f_{i,j}^{P_{i,j}}(\theta, \phi) = \frac{\sin \theta}{\sqrt{1 - [\cos \theta_P \cos \theta + \cos(\phi - \phi_P) \sin \theta \sin \theta_P]}} \quad (2.16)$$

has a singularity in (θ^j, ϕ^i) .

For determining the order of singularity of the integration of $f_{i,j}^{P_{i,j}}$ with respect to ϕ let us proceed as follows: setting,

$$A^2 = 1 - \cos \theta_P \cos \theta, \quad B^2 = \sin \theta_P \sin \theta$$

(note that $A^2 - B^2 \geq 0$) we consider the change of variables

$$t = \tan \frac{\phi - \phi_P}{2},$$

$$\cos(\phi - \phi_P) = \frac{1 - t^2}{1 + t^2}, \quad dt = \frac{1}{2}(1 + t^2) d\phi;$$

Then, we have

$$\int \frac{d\phi}{\sqrt{A^2 - B^2 \cos(\phi - \phi_P)}} = \int \frac{2 dt}{(1 + t^2) \sqrt{(A^2 + B^2)t^2 + (A^2 - B^2)}}.$$

Again, with the change of variables

$$(A^2 - B^2) + (A^2 + B^2)t^2 = Z^2, \quad dt = \frac{Z dZ}{\sqrt{A^2 + B^2} \sqrt{Z^2 - (A^2 - B^2)}}$$

we get

$$\int_{\phi_j}^{\phi_{j+1}} \frac{d\phi}{\sqrt{A^2 - B^2 \cos(\phi - \phi_P)}} = \int_{\sqrt{A^2 - B^2}}^{\sqrt{A^2 - B^2 + (A^2 + B^2) \tan^2 \frac{\phi_{j+1} - \phi_j}{2}}} \frac{2\sqrt{A^2 + B^2} dZ}{(Z^2 + 2B^2) \sqrt{Z - \sqrt{A^2 - B^2}} \sqrt{Z + \sqrt{A^2 - B^2}}}$$

and this integral has a singularity of order $\frac{1}{2}$. The integration of $f_{i,j}^{P_{i,j}}$ between ϕ_j and ϕ^j is treated in the same way. Now, in order to determine the degree of singularity of the outer integration of (2.15), let us consider the approximation $f_{i,j}^1$ of $f_{i,j}^{P_{i,j}}$ given by:

$$f_{i,j}^1(\theta, \phi) = \frac{\sin \theta}{\sqrt{1 - \cos \theta^j \cos \theta - \sin \theta \sin \theta^j + \sin \theta \sin \theta^j \frac{(\phi - \phi^i)^2}{2}}} \quad (2.17)$$

Now, we know how to integrate analytically $f_{i,j}^1$ with respect to ϕ :

setting,

$$A^2 = 1 - \cos \theta \cos \theta^j - \sin \theta \sin \theta^j, \quad B^2 = \frac{\sin \theta \sin \theta^j}{2}, \quad Z = \phi - \phi^i$$

we consider the change of variables

$$\begin{aligned} \sqrt{A^2 + B^2 Z^2} &= BZ + t, \\ Z &= \frac{A^2 - t^2}{2Bt}, \quad dZ = -\frac{1}{2B} \frac{A^2 + t^2}{t^2} dt; \end{aligned} \quad (2.18)$$

Then, we have

$$\int \frac{dZ}{\sqrt{A^2 + B^2 Z^2}} = -\frac{1}{B} \ln(\sqrt{A^2 + B^2 Z^2} - BZ).$$

Therefore,

$$\begin{aligned} F_{i,j}^1 &= \int_{\phi_i}^{\phi_{i+1}} f_{i,j}^1(\theta, \phi) d\phi \\ &= \frac{\sin \theta}{\sqrt{\frac{\sin \theta \sin \theta^j}{2}}} \left[\ln \left(\frac{\sqrt{1 - \cos \theta \cos \theta^j - \sin \theta \sin \theta^j + \sin \theta \sin \theta^j \frac{(\phi_i - \phi^i)^2}{2}} - B(\phi_i - \phi^i)}{[1 - \cos(\theta - \theta^j)]} \right) \right. \\ &\quad \left. + \ln \left(\sqrt{1 - \cos \theta \cos \theta^j - \sin \theta \sin \theta^j + \sin \theta \sin \theta^j \frac{(\phi_{i+1} - \phi^i)^2}{2}} + B(\phi_{i+1} - \phi^i) \right) \right] \end{aligned}$$

Following the same analytical procedures described in the case (a), we can prove that this function has a singularity of logarithmic type in $\theta = \theta^j$. These results allow us to consider the following change of variables as a possible and suitable way for reducing the singularity of the double integral in (2.15):

$$\begin{aligned} F_{i,j}^{P,i,j}(\theta) &= \int_{\phi_i}^{\phi_{i+1}} f_{i,j}^{P,i,j}(\theta, \phi) d\phi \\ &= \int_0^{\sqrt{\frac{\phi_i - \phi_i}{2}}} 2t f_{i,j}^{P,i,j}(\theta, \phi^i - t^2) dt + \int_0^{\sqrt{\frac{\phi_{i+1} - \phi_i}{2}}} 2t f_{i,j}^{P,i,j}(\theta, \phi^i + t^2) dt; \end{aligned} \quad (2.19)$$

$$\int_{\theta_j}^{\theta_{j+1}} F_{i,j}^{P,i,j}(\theta) d\theta = \int_0^{\sqrt{\frac{\theta_j - \theta_j}{2}}} 2t F_{i,j}^{P,i,j}(\theta^j - t^2) dt + \int_0^{\sqrt{\frac{\theta_{j+1} - \theta_j}{2}}} 2t F_{i,j}^{P,i,j}(\theta^j + t^2) dt. \quad (2.20)$$

2.4 Case (d). The annular surface sector

Let us parametrize the annular surface in the following way:

$$\begin{aligned} x &= (R - r \cos \theta) \cos \phi \\ y &= (R - r \cos \theta) \sin \phi \\ z &= r \sin \theta \end{aligned} \quad (2.21)$$

and consider the following discretization (see fig. 4):

$$\phi_0 = 0 < \dots < \phi_i < \dots < \phi_n = 2\pi \quad \text{and} \quad \theta_0 = 0 < \dots < \theta_j < \dots < \theta_m = 2\pi, \quad (2.22)$$

where $\phi_i = \frac{2\pi i}{n}$; $i = 0, \dots, n$ and $\theta_j = \frac{2\pi j}{m}$; $j = 0, \dots, m$.

We indicate as $P = ((R_P - r_P \cos \theta_P) \cos \phi_P, (R_P - r_P \cos \theta_P) \sin \phi_P, r_P \sin \theta_P)$ a generical point in \mathbf{R}^3 , and by

$$\begin{aligned} P_{i,j} &= ((R - r \cos \frac{\theta_{j+1} + \theta_j}{2}) \cos \frac{\phi_{i+1} + \phi_i}{2}, (R - r \cos \frac{\theta_{j+1} + \theta_j}{2}) \sin \frac{\phi_{i+1} + \phi_i}{2}, r \sin \frac{\theta_{j+1} + \theta_j}{2}) \\ &= ((R - r \cos \theta^j) \cos \phi^i, (R - r \cos \theta^j) \sin \phi^i, r \sin \theta^j) \end{aligned}$$

the generical point on the annular surface. The general expression for the potential coefficient $p_{(i,j),P}$ on a point P generated by the surface element $\Omega_{i,j} = \{(\phi, \theta) : \phi_i \leq \phi < \phi_{i+1}, \theta_j \leq \theta < \theta_{j+1}\}$ of the torus is:

$$p_{(i,j),P} = \frac{r}{4\pi\epsilon |\Omega_{i,j}|} \int_{\theta_j}^{\theta_{j+1}} \int_{\phi_i}^{\phi_{i+1}} \frac{(R - r \cos \theta) d\theta d\phi}{\|P_{i,j} - P\|} \quad (2.23)$$

Now, if the point P is outside the finite element $\Omega_{i,j}$, this double integral can be efficiently calculated with two iterated Gaussian quadrature.

But, if the point $P = P_{i,j}$, then the formula (2.23) becomes

$$p_{(i,j),P} = \frac{r}{4\pi\epsilon |\Omega_{i,j}|} \int_{\theta_j}^{\theta_{j+1}} \int_{\phi_i}^{\phi_{i+1}} \frac{(R - r \cos \theta) d\theta d\phi}{\sqrt{2(R - r \cos \theta)^2 [1 - \cos(\phi - \phi^i)] + r^2 (\sin \theta - \sin \theta^j)^2}} \quad (2.24)$$

and the integrand

$$f_{i,j}^{P_{i,j}}(\theta, \phi) = \frac{(R - r \cos \theta)}{\sqrt{2(R - r \cos \theta)^2 [1 - \cos(\phi - \phi^i)] + r^2 (\sin \theta - \sin \theta^j)^2}} \quad (2.25)$$

has a singularity in (θ^j, ϕ^i) .

As we did in the case (c), in order to determine the degree of singularity of the outer integration of (2.24), let us consider the approximation $f_{i,j}^1$ of $f_{i,j}^{P_{i,j}}$ given by:

$$f_{i,j}^1(\theta, \phi) = \frac{(R - r \cos \theta)}{\sqrt{(R - r \cos \theta)^2 (\phi - \phi^i)^2 + r^2 (\sin \theta - \sin \theta^j)^2}} \quad (2.26)$$

Now, by operating in analogy with the case (c), we find that the iterated integrations in (2.24) have the same order of singularity as in the spherical case, and therefore we can reduce the singularity of the double integral in (2.24) with two changes of variables as we did in (2.19) and (2.20).

3 Numerical Tests

Taking into account the shape of the integrand functions, we used the Gauss-Legendre quadrature method for the numerical computation of the potential coefficients.

As it is well known, the choice of the number of weights and points used in the quadrature routines is a critical point. To this purpose, we have to distinguish the evaluation of the potential coefficients containing a singularity from those having no singularity. In absence of singularity, that is when $i \neq k$ in (2.1), few points are sufficient for a good numerical approximation; we found that 8 points for each step of integration are more than sufficient for an accuracy of 6 or more digits. In presence of a singularity, it is expected a sensible growth of the number of points needed for an accurate numerical integration, although the change of variables of the type (2.19) and (2.20) remove the singularity from an analytical point of view. In fact, the quadrature routine must evaluate the product of two critical terms: one very small and the other very large. Even if this product has a finite value, the evaluation is not very stable from a numerical point of view.

The table 1 shows how the quadrature routines (we use a routine in [4] for the generation of the weights and points) behave in the four cases (a)-(d). The quadrature routines works in double precision. The execution time is referred to a Pentium 90 MHz processor. We estimated the degree of precision by comparison with the analytical solution when it exists (i.e. the case of the insulated whole spherical surface), elsewhere by taking into account the number of digits that remain unchanged when a large number of weights and points in the Gauss-Legendre quadrature routines is used.

the execution time is quite short, bearing in mind the plain hardware computer board used. The first accuracy and execution time results are related to the routines implementing the change of variables, the second without the change of variables. It is straightforward to derive that by using our method the accuracy in the calculations is significantly better and the time needed reasonably contained.

It should be underlined that it is convenient to use a limited number of points in the Gauss-Legendre quadrature routines, as shown in table 1. This fact occurs for two reasons: first, the increasing of the number of points does not affect significantly the accuracy, but it increases the computational time; secondly, if we take a large number of points there is the risk that the numerical results of some operations in the calculation may have overflow and underflow problems. For example, referring to table 1, we found that numerical problems occurred when we used more than 130 points.

Table 1: Numerical tests.

Sector Type	N. of points for outer integration	N. of points for inner integration	Accuracy Digits		Execution time in ms.	
			with	without	with	without
Cylinder and Flat Disk	—	8	4	1	< 10	< 10
	—	16	5	1	< 10	< 10
	—	32	6	2	< 10	< 10
	—	64	8	3	< 10	< 10
	—	128	8	3	< 10	< 10
Sphere and Annulus	8	16	3	1	< 50	< 50
	16	16	4	1	< 50	< 50
	16	32	5	2	< 50	< 50
	16	64	5	2	< 50	< 50
	32	32	5	2	< 50	< 50
	32	64	6	2	50	< 50
	64	64	6	2	220	110
	64	128	6	2	320	170
	100	128	7	2	550	305

4 Conclusions

In this paper a possible, useful numerical approach to the accurate evaluation of the potential coefficients in integral methods, such as the Charge Simulation Method taking into account surface distributed charges is shown.

The approach consists in a complete mathematical study of the integral singularity resulting in a suitable change of variables, whose effects is to reduce the singularity from an analytical point of view. Following this approach, degrees of precision of six or more digits can be easily obtained and the numerical accuracy of the electrostatic analysis may be conveniently improved especially in critical zones, such as near the electrodes, in presence of sharp edges or of thin dielectric layers. Of course, further developments and more detailed numerical tests dealing with practical engineering problems are opportune and necessary.

References

- [1] A. Blaszczyk. Computation of quasi-static electric fields with region-oriented charge simulation. *IEEE Trans. on Magnetism*, **32**(3):828-831, (1996).
- [2] A. Blaszczyk and H. Steinbigler. Region-oriented charge simulation. *IEEE Trans. on Magnetism*, **30**(5):2924-2927, (1994).
- [3] E. Cardelli, R. Del Zoppo, and G. Venturini. Electric fields emission propulsion studies. *Proc. of the 7th European Conference on Electrotechnics- Advanced Technologies and Processes in Communication and Power Systems, Paris*, pages 416-420, April 1986.
- [4] B. P. Flannery, W. H. Press, S. A. Teukolsky, and W. T. Vetterling. *Numerical Recipes in C*. Cambridge Univ. Press, Cambridge, (1992).
- [5] M. Kobayashi and H. Iijima. Surface magnetic charge distributions of cylindrical tubes. *IEEE Transaction on Magnetism*, **32**(1):270-273, (1996).
- [6] M. Kobayashi and Y. Ishikawa. Surface magnetic charge distributions and demagnetizing factors of circular cylinders. *IEEE Trans. on Magnetism*, **28**(3):1810-1814, (1992).
- [7] H. Singer, H. Steinbigler, and P. Weiss. A charge simulation method for the calculation of high voltage fields. *IEEE Trans. on PAS*, pages 1660-1668, 1974.
- [8] D. Utmischi. Charge substitution method for three-dimensional high voltage fields. *Proc. Third International Symposium on High Voltage Engineering*, sec. 11.01:1-4, 1979.

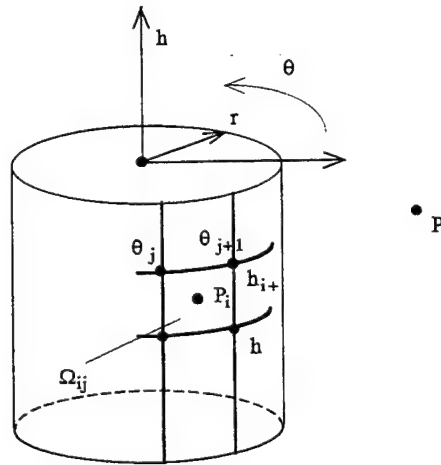


Fig. 1 - The cylindrical surface sector.

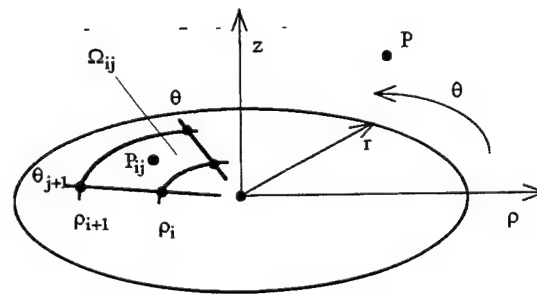


Fig. 2 - The flat disk sector.

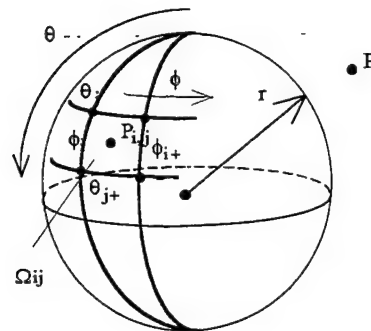


Fig. 3 - The spherical surface sector.

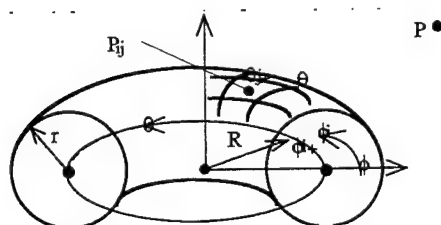


Fig. 4 - The annular surface sector.

MEASURED RCS POLAR CONTOUR MAPS FOR CODE VALIDATION

C.L. Larose
S.R. Mishra
David Florida Laboratory
Canadian Space Agency
Ottawa, Canada

C.W. Trueman
EMC Laboratory
Concordia University
Montreal, Canada

ABSTRACT. *Measured radar cross-section(RCS) data as a function of the angle of incidence and of the frequency over a wide range provide an excellent basis for code validation. This paper examines the RCS of six targets measured as a function of the angle of incidence of the plane wave, and of the frequency, through and beyond the resonance range of target size. The RCS is presented as a function of frequency and incidence angle using a color contour map in a polar format, with the radius proportional to the frequency. Such polar contour maps exhibit striking patterns. This paper relates such patterns to the underlying scattering mechanisms and target geometry. The RCS as a function of incidence angle and frequency is available from the authors for an extensive collection of targets.*

1. INTRODUCTION

Developers of new computer codes in computational electromagnetics carry out "code validation", in which computations are compared with reference data, both to demonstrate how accurately the code can solve a given problem, and to identify requirements of the code, such as the minimum number of elements per wavelength distance. In the literature, scattering codes are often validated by comparing monostatic or bistatic scatter patterns with measurements at a single frequency. A thorough evaluation of a computer code includes comparisons over a wide frequency range, to try to establish the limits of the validity of the code[1].

The open literature makes available the RCS as a function of frequency for only a few targets, such as a square plate from 0.25λ to 1.1λ in size[2], a metallic strip 0.53λ tall and from 0.5λ to 1.3λ in length[3], a metallic cube from 0.1λ to 3.7λ in size[4], each for only one angle of incidence. Our initial RCS measurements extended this set of "canonical" targets to include metallic strips and rods, over a 9 to 1 frequency range, for one or two individual angles of incidence such as broadside or end-on[5], for the validation of computations by wire-grid modeling and by the finite-difference time-domain method[6]. We then

undertook to build a data base of measured radar cross-sections for over a hundred shapes, including discs, right-circular cones, cone-spheres, ellipsoids, pyramids, and simplified aircraft and ships[7]. For each target the RCS has been measured over a 9 to 1 frequency range, at one degree angle steps over 360 degrees when there is no axis of symmetry, or 180 degrees when there is one symmetry axis, and so forth. The measured RCS as a function of both frequency and incidence angle permits both the comparison of the measured RCS with the computed RCS as a function of frequency at a given incidence angle, and the traditional comparison as a function of incidence angle at a given frequency, and so provides a comprehensive set of reference data for code validation for that target for plane wave incidence in one plane.

This paper presents the RCS of six of the targets in our data base. By graphing the RCS vs. frequency and angle as a color contour map in a polar format[8], intriguing patterns of maxima and minima are seen. This paper lends insight into these patterns by relating them to the scattering mechanisms of the target. Our measured RCS data may present a challenge to others to demonstrate that their computer codes can accurately predict the scattering mechanisms suggested by our simple analysis.

1.1 Measured RCS

The scattered field is measured at the David Florida Laboratory in a 6 by 6 by 6 m anechoic chamber, using the setup shown in Fig. 1. The target is mounted on a styrofoam column on a rotator which can turn the target for $0 \leq \theta \leq 360$ degrees. The target is illuminated by a transmit horn and the scattered field measured by a receive horn. Hence the bistatic scattered field at a fixed range distance is measured. This section defines the bistatic, finite-range "radar cross-section" as graphed in this paper, and discusses its relationship to the true, monostatic RCS.

The transmit horn in Fig. 1 illuminates the target with a spherical wave of amplitude E_i evaluated at the centre of

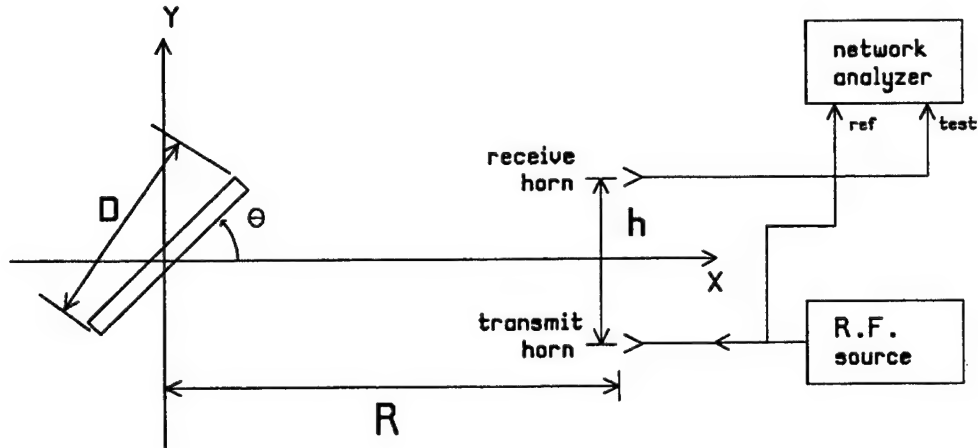


Fig. 1 The geometry of the measurement setup.

rotation. The target scatters field back to the receive horn, which measures field strength E_t , where the "t" subscript stands for or "target". The bistatic, finite range RCS, which we will also call the "measured RCS", is defined by

$$RCS(R, h, \theta, f) = 10 \log \left(\frac{4 \pi R^2 |E_t|^2}{|E_i|^2} \right) \quad \dots(1)$$

in dB, and depends on the horn separation h , the measurement range R , the angle of incidence, and the frequency. The calibration procedure for the measurement setup extracts E_t from three voltages measured by the network analyzer: V_1 with the target on the support column; V_2 with a reference sphere on the support column, namely an 50.8 mm, highly-polished steel ball-bearing; and V_3 with nothing on the support column, representing the scattered field of the support column plus the residual scattered field of the anechoic chamber. Assuming that the target does not interact with the support column, the column-plus-room contribution can simply be subtracted. The "target response" is the difference at each frequency between the response with the target on the column, and that with nothing on the column, $V_t = V_1 - V_3$. Similarly, the "sphere response" is the difference between the response with the sphere on the column, and that with nothing on the column, $V_s = V_2 - V_3$. The scattered field at the location of the receive horn is proportional to the received voltage, hence for the target, $E_t = CV_t$, and for the sphere, $E_s = CV_s$, where C is a complex-valued, frequency-dependent constant accounting for the gains of the horns, the losses and phase shifts in the cables, and so forth. To find the value of C we evaluate the scattered field of the sphere $E_s = E_{Mie}$ using the Mie[9] series for plane wave scattering from a perfectly-conducting sphere, with

the appropriate bistatic angle. Then $C = E_{Mie} / V_s$ and the scattered field of the target is

$$E_t = \left(\frac{E_{Mie}}{V_s} \right) V_t \quad \dots(2)$$

In using the Mie series for plane wave scattering from a sphere we are assuming that the measurement setup satisfies "far field" conditions, and we may be introducing a systematic error. Also we assume that the sphere is perfectly-conducting, which may not be appropriate for a steel sphere. Equations (1) and (2) define the "measured RCS" as graphed in this paper.

1.2 Geometric Error

The relationship between the "measured RCS" of Eqn. (1), based on the bistatic scattered field at finite range, and the true monostatic RCS is a complex one. Part of the difference between our measured RCS and the monostatic RCS is due to the bistatic, finite-range geometry, and we will call this the "geometric error", and part due to other sources of error[10]. True RCS measurement requires an incident plane wave, for which the field amplitude does not change with distance traveled, and for which the phase is constant in planes perpendicular to the direction of travel. In the measurement setup, the incident wave is spherical and so the illuminating field strength varies as inverse distance. Hence the part of the target nearest the horns is more strongly illuminated than that farthest from the horns. Also, the phase of the illuminating field is not uniform in planes perpendicular to the direction of propagation. And, the distances from various parts of the target to the receive horn differ from those associated with backscattered field, which alters the phase relationship of the scattered fields at

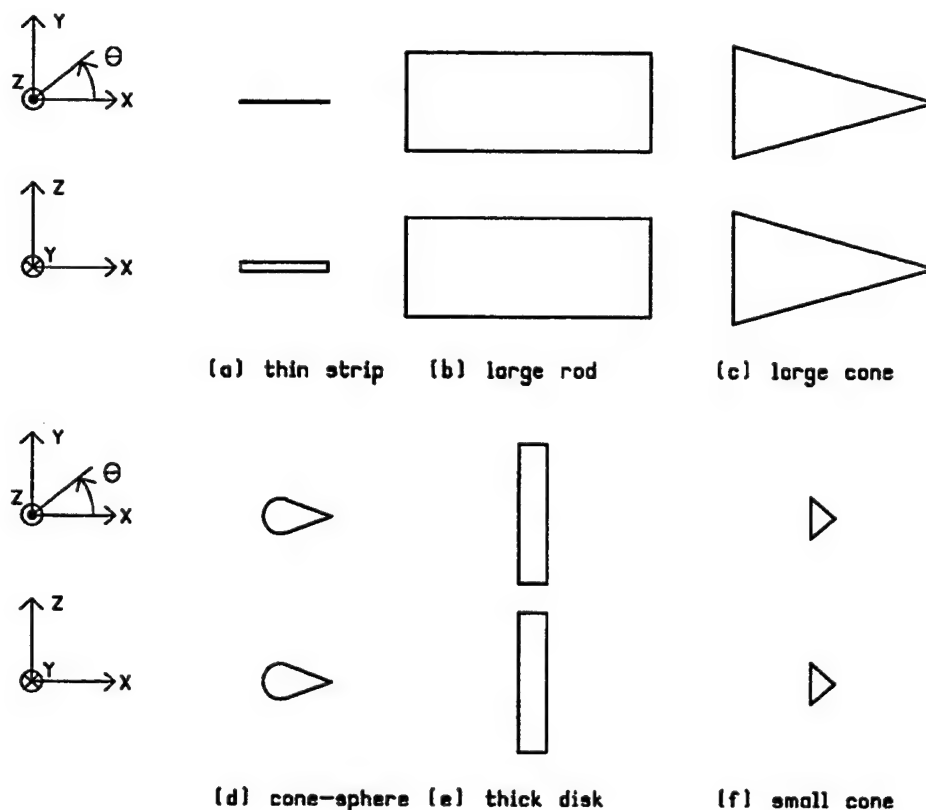


Fig. 2 The relative sizes of the six targets, and their orientations in the coordinate system.

Table 1
The dimensions of each target, and the range distance and bistatic angle of the measurement.

Target	Dimensions mm	Polarization	Bistatic angle degrees	Range m	D mm	f_{\max} GHz
thin strip	63.6x6.36x0.32	vertical	8.3	1.2	63.9	44.1
large rod	177.8x71.1x71.1	horizontal	3.0	3.35	204.3	12.0
large cone	80.5 mm base diameter 147.6 mm length	horizontal	7.7	1.295	153.0	8.3
cone-sphere	25.3 mm sphere diameter 50.1 mm overall length	horizontal	8.2	1.217	50.1	72.7
thick disk	100.9 mm diameter 20.4 mm thickness	horizontal and vertical	7.7	1.295	102.9	18.3
small cone	29.8 mm base diameter 17.85 mm length	vertical	8.3	1.2	23.3	202.7

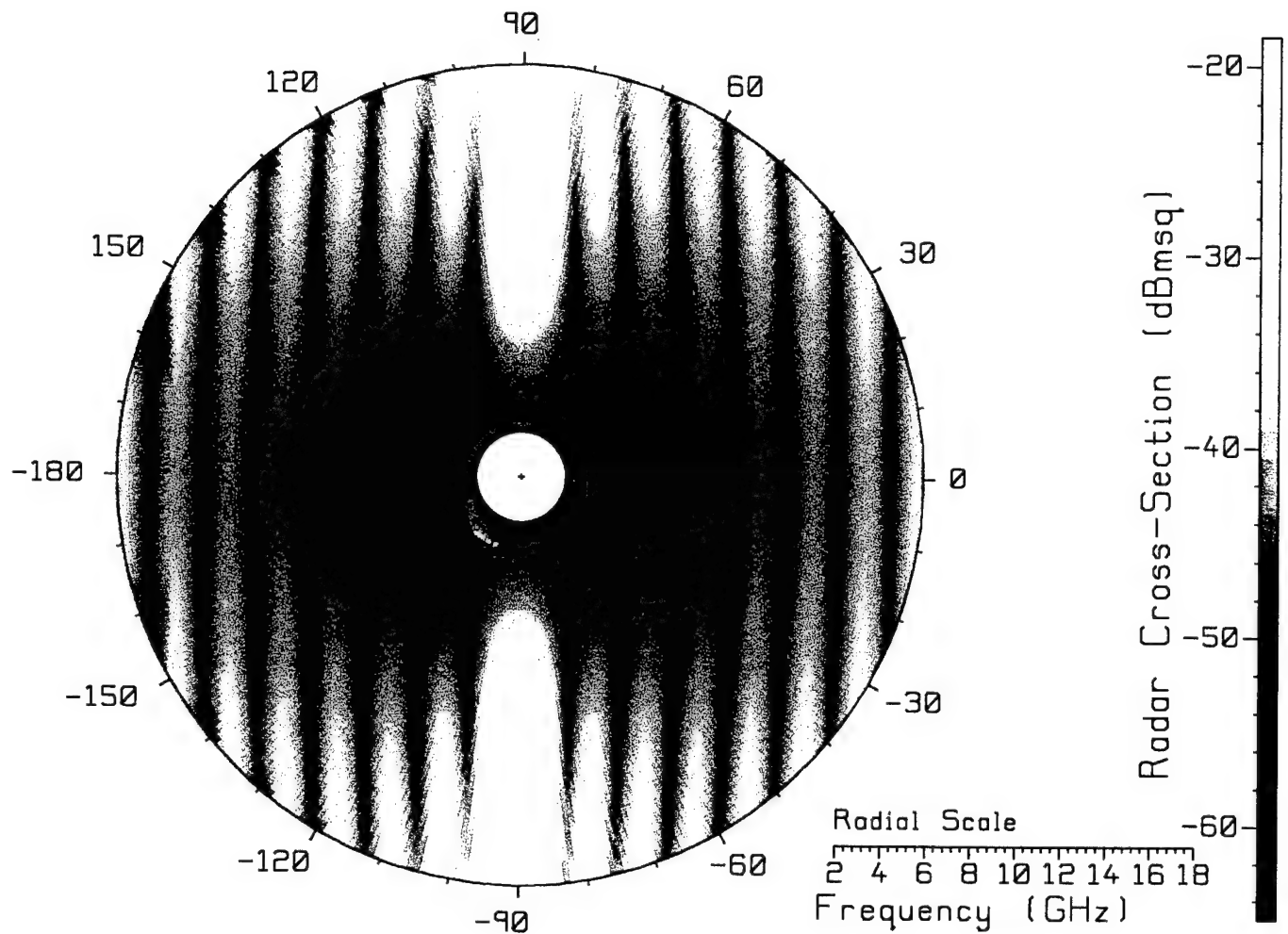


Fig. 3 The RCS of the thin strip of Fig. 2(a) for vertical polarization, with the incident electric field vector parallel to the z axis. The RCS is shown with color contours as a function of the angle of incidence θ in the xy plane, and of the frequency, with the radial axis proportional to the frequency, from 2 GHz at the inner circle to 18 GHz at the outer circle.

the location of the receiver. All these differences contribute to the geometric error.

If D is the maximum diagonal dimension of the target, then if $R \gg D$ and $R \gg h$, the measurement setup approaches the conditions for monostatic RCS measurement, and we expect that the geometric error will be "small". The commonly-accepted "rule-of-thumb" for choosing a sufficiently large range R to control the geometric error is [10]

$$R_{\min} = \frac{2D^2}{\lambda} \quad \dots(3)$$

where λ is the wavelength. More elaborate minimum-range conditions are reviewed in [11]. Hence for a given

target size D and range R , the maximum frequency at which the rule-of-thumb is satisfied is

$$f_{\max} = \frac{Rc}{2D^2} \quad \dots(4)$$

where c is the free-space speed of light. But the rule-of-thumb of Eqn. (3) does not provide an estimate of the geometric error in the RCS at that range.

Ref. [12] discusses the geometric error as follows. At a frequency and angle of incidence where the RCS has a maximum, small differences in the strength of the illumination and in the phase of the illumination of various scattering centers on the target, and small path differences back from the scattering centers to the receive horn, can be

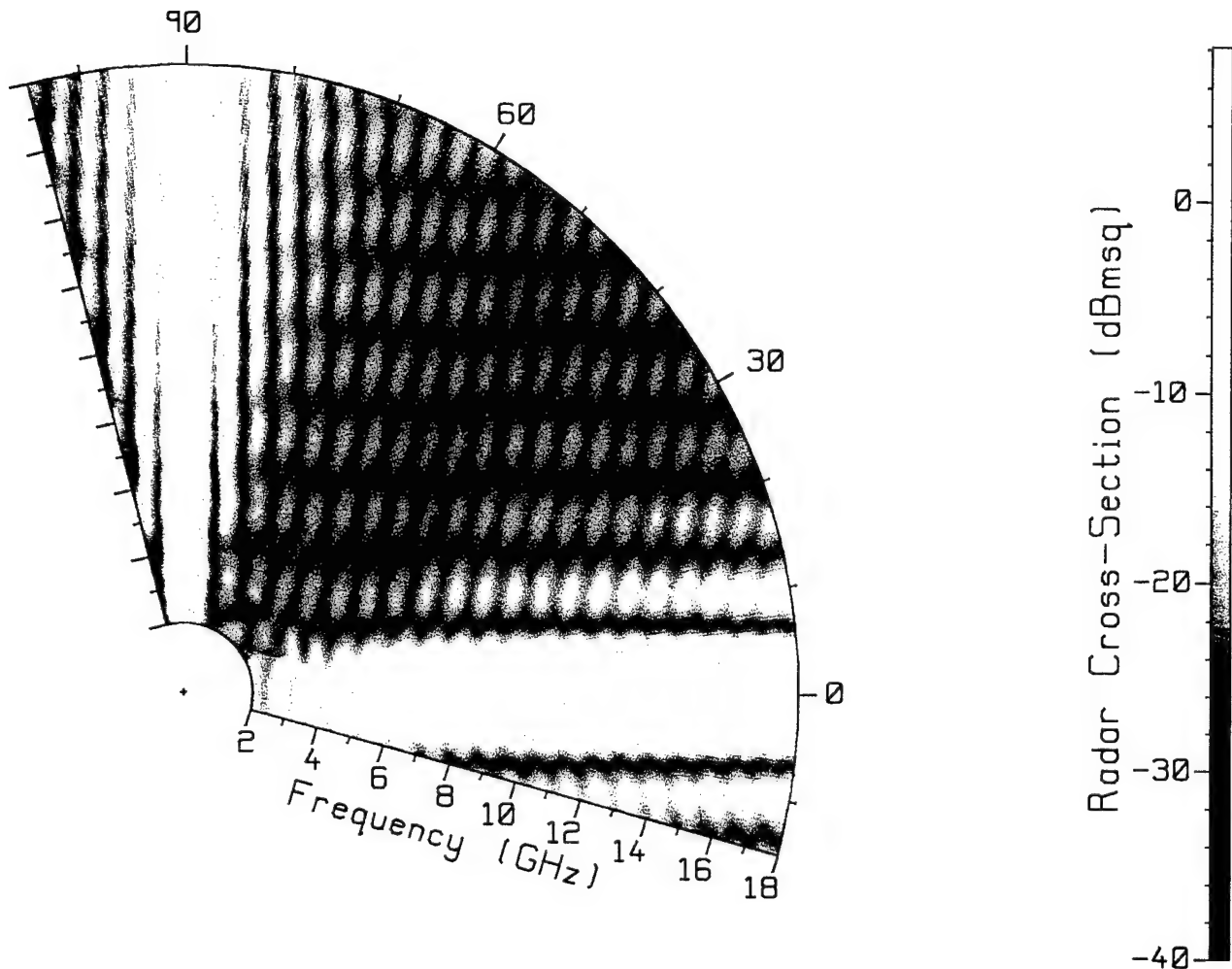


Fig. 4 The RCS of the large rod of Fig. 2(b) over one quadrant of the xy plane, for horizontal polarization, with the electric field vector parallel to the xy plane.

unimportant, and the error in the measured RCS compared to the monostatic RCS can be small. However minima in the RCS arise due to cancellation of the scattered field from various parts of the target, and then small differences in the strength and phase of the illumination, and in the path lengths back to the receive horn, can lead to very large errors in the RCS. Hence the geometric error in the RCS maxima can be small but that in the RCS minima large. Ref. [12] provides a tool for choosing the measurement range R and horn separation h to limit the geometric error to a preset maximum over a chosen range of RCS values below the maximum RCS.

The measured RCS contains other errors as well, associated with the signal-to-noise ratio, with the time-gating measurement method[10], with target alignment, and so forth[10,12]. We do not have a quantitative estimate of these errors in our measurements at this time. Dybdal[10] estimates the maximum achievable absolute accuracy in RCS measurement under carefully-controlled conditions as 0.5 dB.

For code validation purposes, comparisons of computations of the monostatic RCS against our measured RCS are approximate. Such comparisons will lead to good agreement in the RCS maxima, and differences in the minima. This is illustrated in Ref. [5], which compares the measured RCS of Eqn. (3) for the strip target of Fig. 2(a) with the computed monostatic RCS, from 2 to 18 GHz. The range and angle are given for the strip in Table 1. Excellent agreement is seen in Ref. [5] in the RCS maxima. However, the sharp, deep minima differ between the measurement and computation.

To make the best use of our measured bistatic, finite-range RCS data for code validation, the measurement setup of Fig. 1 should be simulated in the computation. This is easily done by locating a point source at the position of the feed horn, and computing the scattered field at the location of the receive horn. Then the measured and computed scattered fields correspond to the same geometry, greatly increasing the value of the comparison.

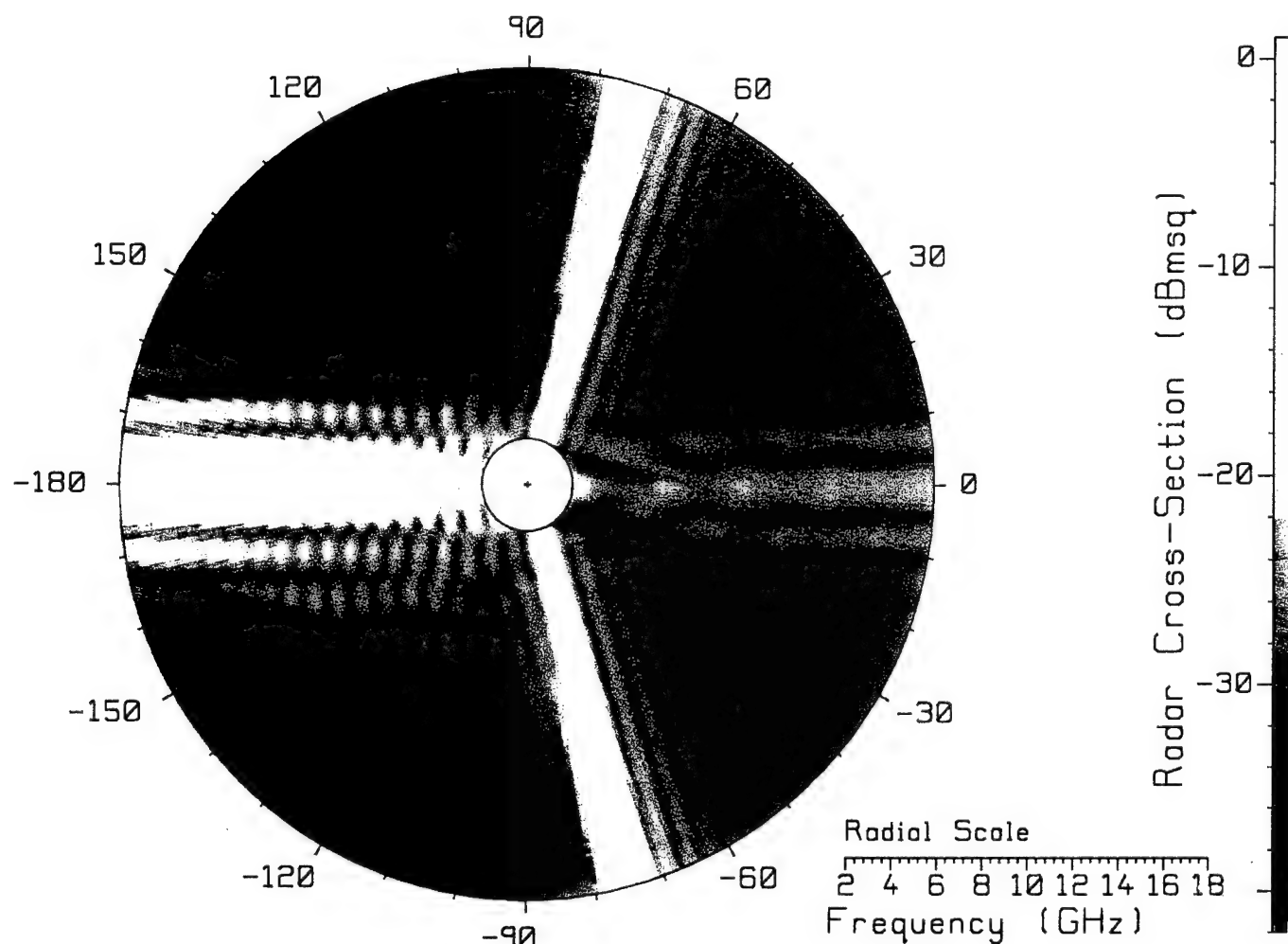


Fig. 5 The RCS of the large cone of Fig. 2(c) for horizontal polarization. outer circle.

1.3 Six Targets

Fig. 2 shows the set of six targets which will be discussed in this paper. Table 1 lists the range R and bistatic angle α used in the measurement of the scattered field for each target. In all cases the horn separation is 17.46 cm, and the bistatic angle is $\alpha = 2 \tan^{-1}(h/(2R))$. The measured data in this paper was taken from 2 to 18 GHz. Table 1 lists the maximum frequency from Eqn. (4) at which the "rule-of-thumb" of Eqn. (3) is satisfied. The measured data for the strip, the cone-sphere, the thick disk and the small cone targets satisfy Eqn. (3) to beyond 18 GHz, but for the large rod and the large cone the range is too short.

Fig. 2 shows the shapes and relative sizes of the targets which will be studied in this paper. The figure shows two views of each target, in an xy plane at the top, and in an xz plane at the bottom. All six targets in Fig. 2 are metallic. The targets are: (a) a thin strip, of length 10 times its

height; (b) a large rod of square cross-section; (c) a large right-circular cone; (d) a small cone-sphere; (e) a thick disk; and (f) a small cone. Table 1 gives the dimensions of each target. Fig. 2 shows the orientation of each target relative to the xyz coordinate system corresponding to the measurement setup in Fig. 1. In Table 1, "vertical polarization" has the electric field vector parallel to the z axis, and "horizontal polarization" has the electric field in a plane parallel to the xy plane.

1.4 Polar Color Maps

Figs. 3 to 8 show "polar color maps" of the RCS of each target in dB relative to the square metre. The angle axis corresponds to the angle of incidence θ on the target, with the x direction oriented toward the right and the y direction pointing upward. Radial distance from the center of the graph is proportional to the frequency f . To preserve the geometric relationships discussed later in this paper, the center of the polar axes must correspond to zero frequency.

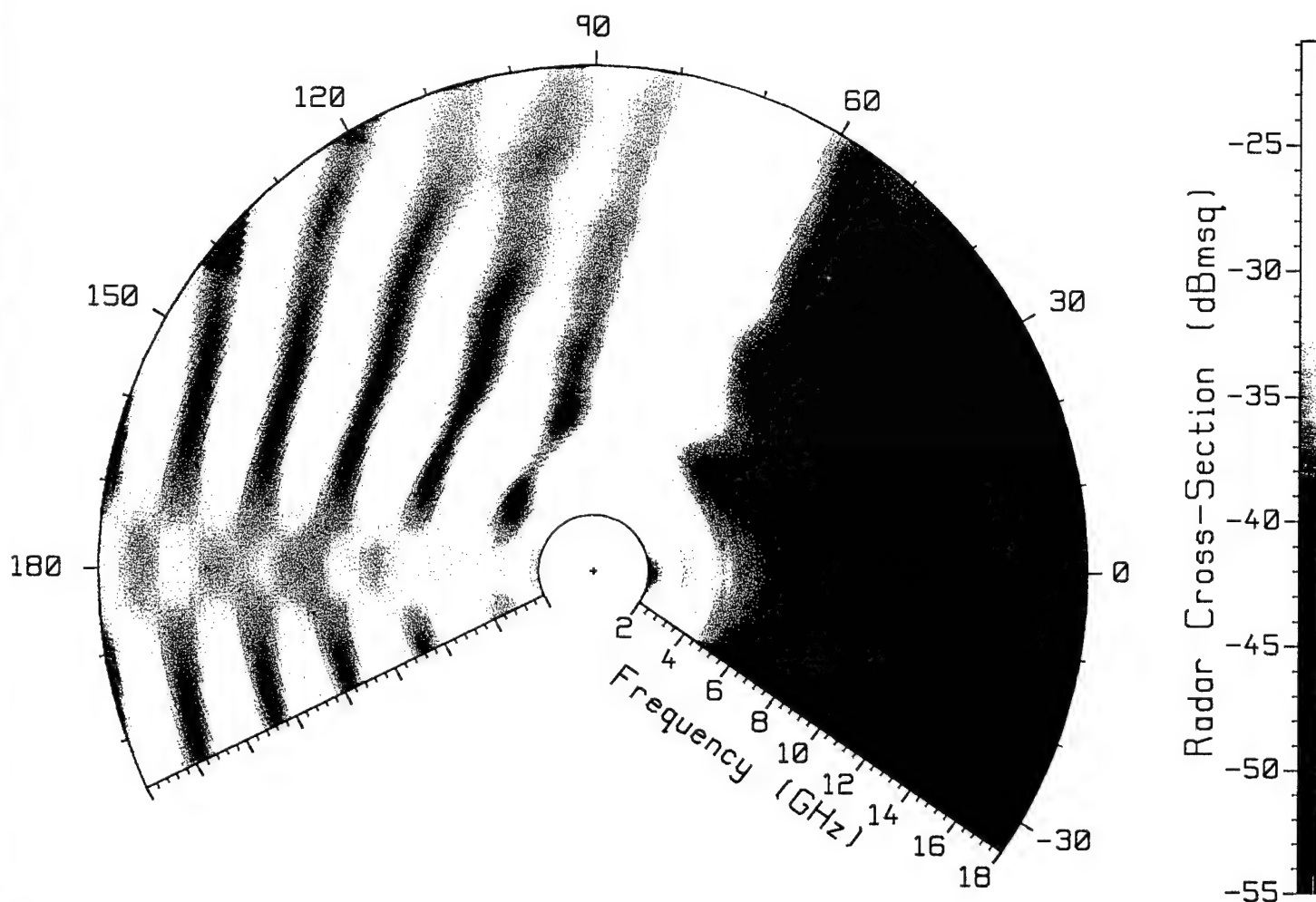


Fig. 6 The RCS of the cone-sphere of Fig. 2(d) for horizontal polarization.

In the polar axes in Figs. 3 to 8, the inner circle corresponds to 2 GHz, and the frequency increases linearly with radius to 18 GHz on the outer circle. Each point (f, θ) between the inner and outer circle represents a unique frequency and incidence angle. The rectangular coordinates of point (f, θ) will be denoted using (u, v) , where $u = f \cos \theta$ and $v = f \sin \theta$ have the units of frequency.

The RCS could be graphed as a conventional contour map using solid lines to show RCS contours at specified levels, say 3 dB apart. Contour lines can be drawn in color, with colors corresponding systematically to levels of RCS contours, making the regions of high and of low RCS easier to distinguish. By filling the regions between contours with color, we obtain a "color contour map", which reveals patterns in the RCS more boldly than do simple contour lines. Such a map is constructed by assigning a color to each range of RCS σ ; thus color $\#k$ is used to plot RCS values in a range $\sigma_{k-1} \leq \sigma < \sigma_k$. Various color scales were

discussed in Ref. [8]. The RCS at each pixel location is interpolated from the measured data near that frequency and incidence angle, then each pixel is assigned a color according to the RCS value. If only 16 colors are used, then the changes in color are clearly seen as curves of constant RCS at levels σ_k . When the number of colors is increased to about 200, the color appears to vary continuously, as shown in Figs. 3 to 8. These figures were made using program POLPLOT, which was written to display RCS and other data in the polar color map format. POLPLOT for Microsoft Windows is available from the authors at no charge.

Figures 3 to 8 show some remarkable geometric patterns. Figs. 3, 4, and 7 show distinct straight bands of maximum and minimum RCS. Figs. 4 and 5 show sets of dark bands, delineating a pattern of bright dots. Fig. 6 shows hyperbolas. Figs. 7(b) and 8 show parts of ellipses. In the following we will identify simple scattering mechanisms that give rise to these features. To understand the patterns

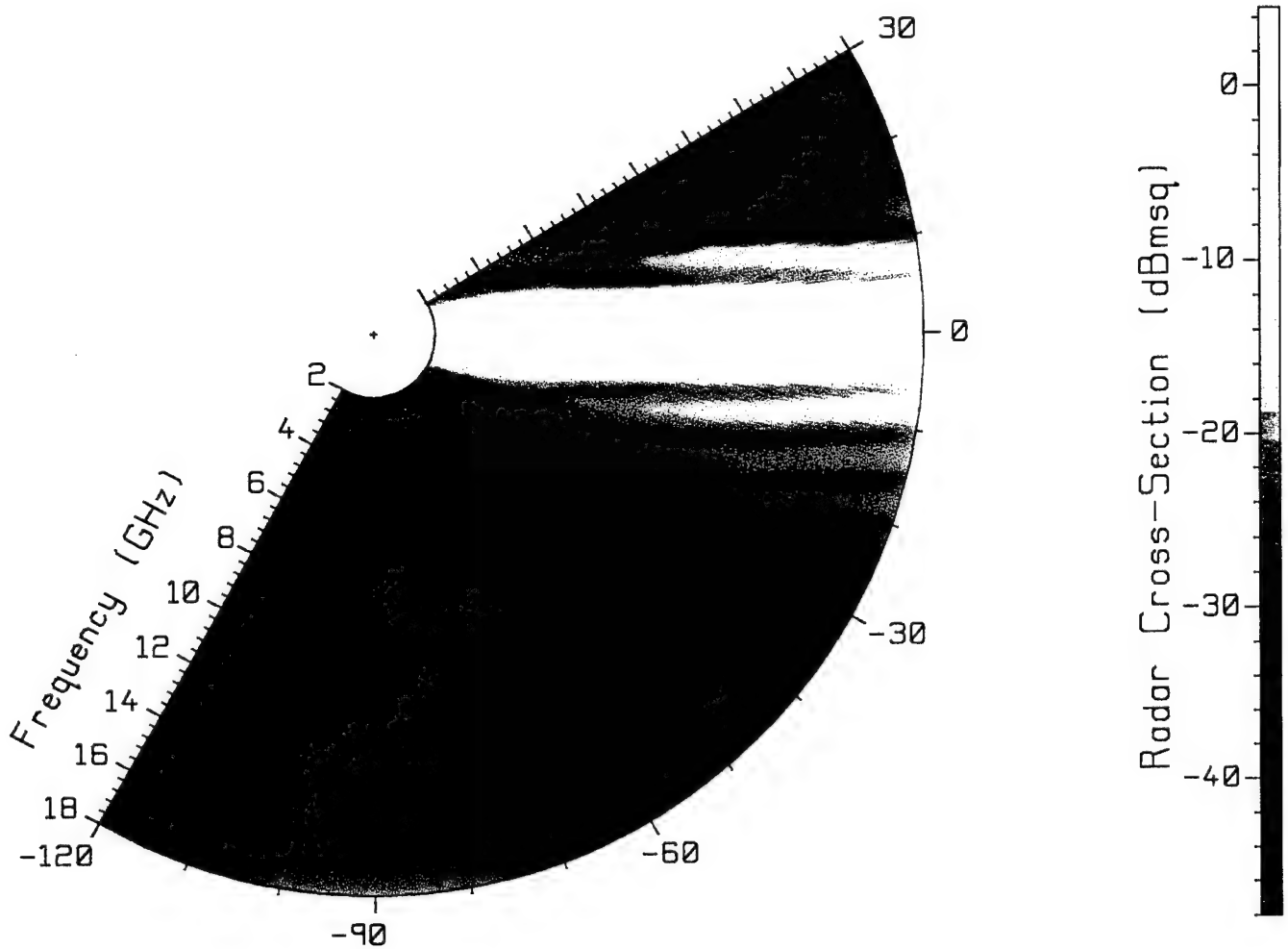


Fig. 7(a) The RCS of the thick disk of Fig. 2(e) for horizontal polarization.

seen in the figures, and associate them with target scattering mechanisms, it will be sufficient to assess the backscattered field due to an incident plane wave, rather than analyze the more complex measurement geometry of Fig. 1.

2. INTERFERENCE OF POINT SOURCES

Many of the targets of Fig. 2 scatter by diffraction from points on edges or from tips. This section shows that interference of the scattered fields from two point sources leads to a set of parallel lines of maximum and minimum RCS on a contour map in polar format.

Fig. 9 shows a plane wave traveling parallel to the xy plane in direction θ to the x axis. The plane wave scatters from two diffraction points, such as points on edges. In Fig. 9, the diffraction points are located on the x axis, separated by distance d . The observer is at a distant point in the xy plane in the backscatter direction. The round trip path

length from the observer to point #1 and back to the observer is L_1 , and that to and from point #2 is L_2 . The difference between the path lengths is

$$L_2 - L_1 = 2d \cos \theta \quad \dots(5)$$

Let α_1 and α_2 be the phase changes associated with the diffraction process at source #1 and source #2, respectively. Then if the plane wave has zero phase at the observer, the phase of the diffracted field due to source #1 is $\alpha_1 - kL_1$, and to source #2, $\alpha_2 - kL_2$, where $k = 2\pi f / c$ is the wave number and c is the speed of light. There will be an RCS maximum when the phase difference between the diffracted fields at the observer is $-2\pi n$, where n is an integer, positive, zero, or negative. Thus there will be an RCS maximum when

$$-k(L_2 - L_1) + (\alpha_2 - \alpha_1) = -2\pi n \quad \dots(6)$$

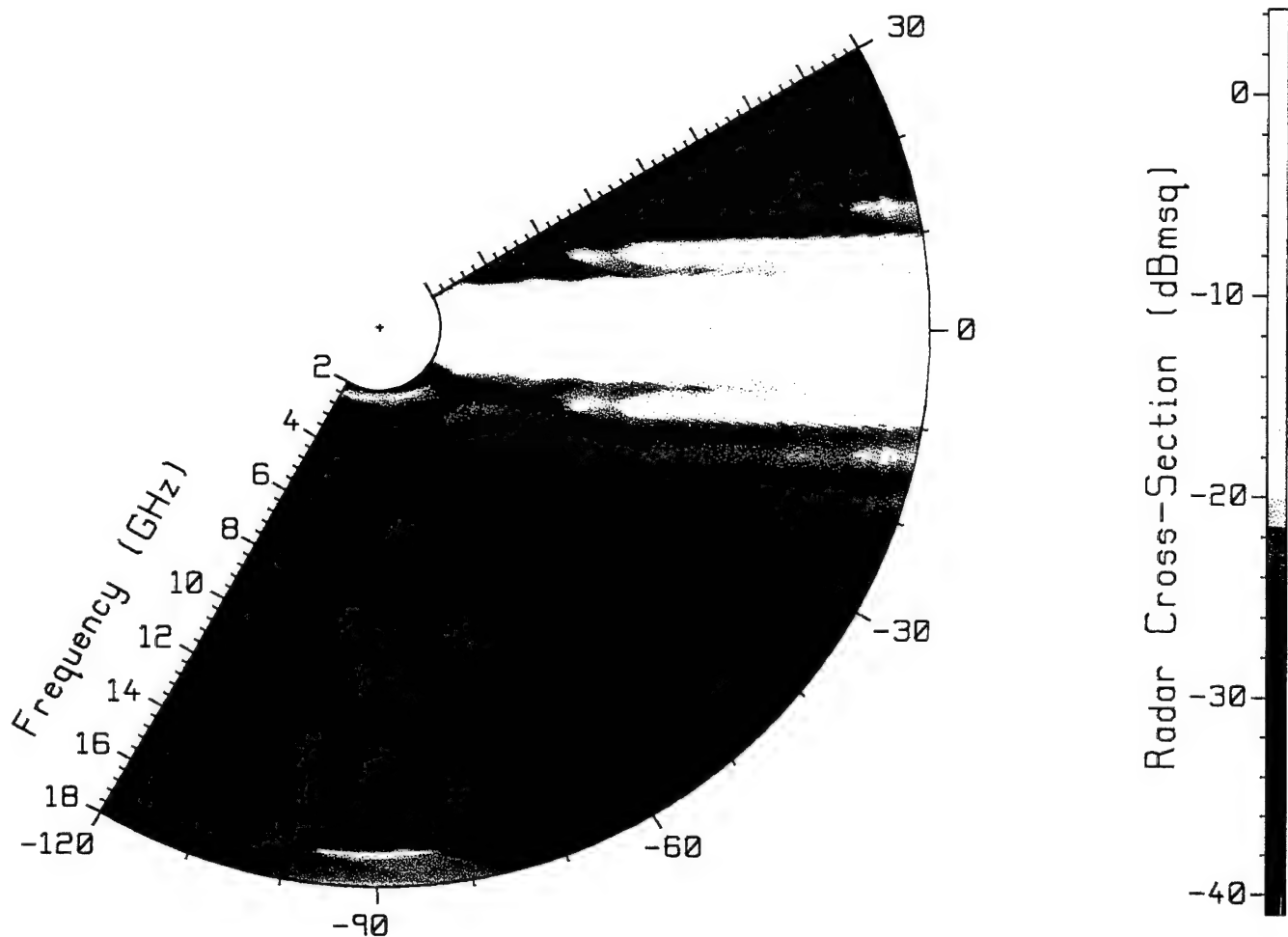


Fig. 7(b) The RCS of the thick disk of Fig. 2(e) for vertical polarization.

Equations. (5) and (6) can be rearranged to show that contours of maximum RCS satisfy

$$f \cos \theta = \frac{c}{2d} \left(n + \frac{\alpha_2 - \alpha_1}{2\pi} \right) \quad \dots(7)$$

The results presented in the following indicate that the phase changes associated with the diffraction process, α_1 and α_2 , are reasonably constant with frequency and incidence angle. If (u, v) gives the location of a point on a polar contour map, then $u = f \cos \theta$, and Eqn. (7) states that the curves of maximum RCS have constant u , that is, are straight lines parallel to the v axis. The lines of maximum RCS are at positions

$$u_n = \frac{c}{2d} \left(n + \frac{\alpha_2 - \alpha_1}{2\pi} \right) \quad \dots(8)$$

The spacing of these lines is given by

$$\Delta u = u_{n+1} - u_n = \frac{c}{2d} \quad \dots(9)$$

Note that curves of minimum RCS satisfy Eqn. (6) with the right-hand side replaced by $-2\pi n - \pi$, hence lead to vertical straight lines with the same spacing as the lines of maximum RCS. The spacing of these lines of minimum or maximum RCS provides a convenient comparison with the measured data because it is independent of α_1 and α_2 . The following demonstrates lines of maximum and minimum RCS for the strip, the large rod, and the right circular cone.

2.1 The Thin Strip

The thin metallic strip of Fig. 2(a) has length 63.6 mm, width 6.36 mm, and thickness 0.32 mm. The strip lies in the xz plane with the long dimension parallel to the x axis. The RCS was measured with the incident electric field

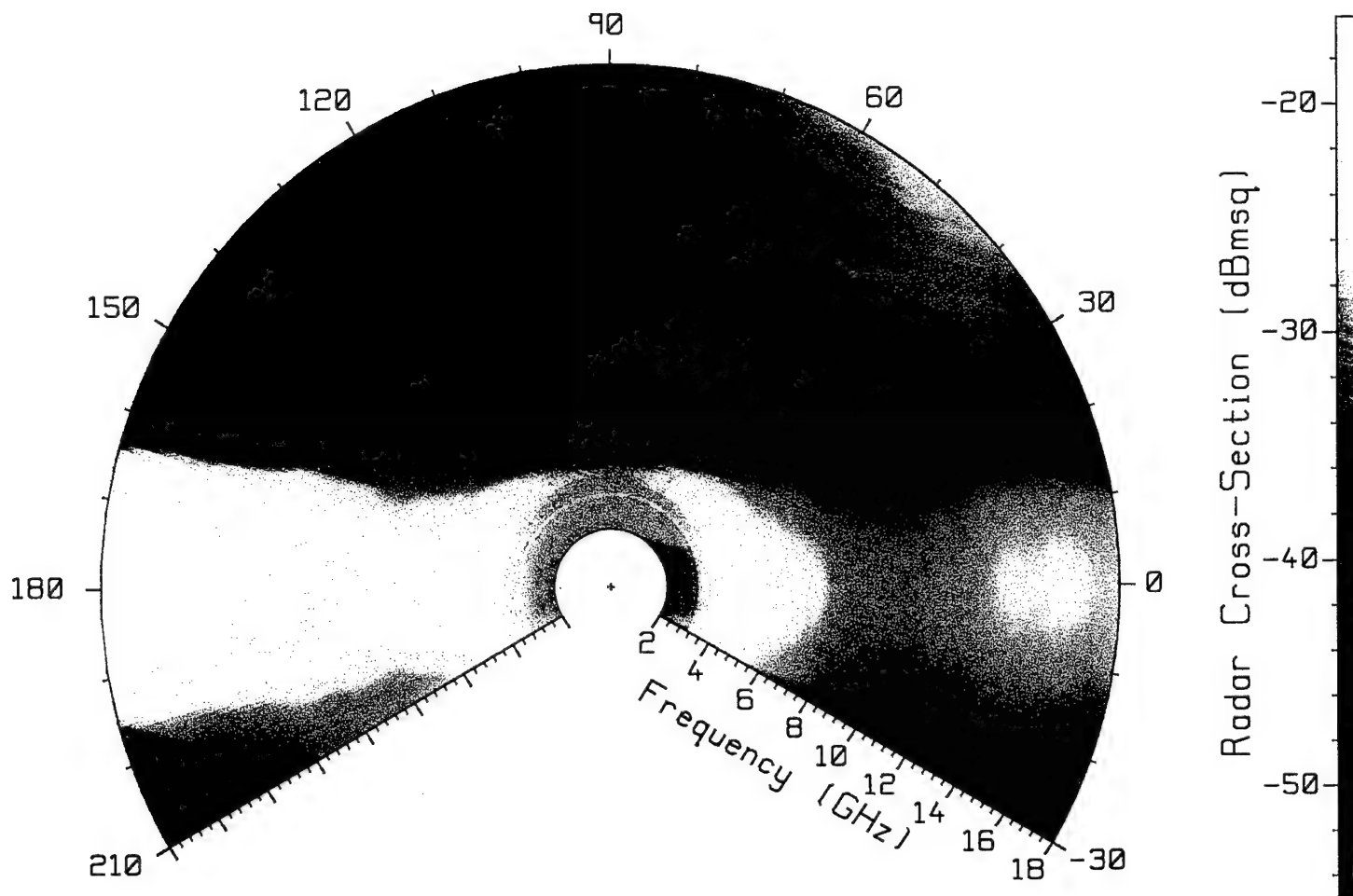


Fig. 8 The RCS of the small cone of Fig. 2(f) for vertical polarization.

parallel to the z axis, that is, with “vertical polarization”. The RCS was measured from 2 to 18 GHz, for angles of incidence from $\theta=0$ or “end-on” through $\theta=90$ or “broadside”, all the way around back to $\theta=0$, to obtain the polar color map of Fig. 3. The maxima in the RCS show a striking pattern of bright vertical bands, separated by dark bands of minimum RCS. For end-on incidence, the frequencies at which the maxima fall in Fig. 3 can be read from their intersections with the horizontal axis, to obtain 3.4, 5.8, 8.2, 10.6, 13.0 and 15.4 GHz, spaced 2.4 GHz apart. The largest maximum in Fig. 3 falls on the vertical axis, for $\theta=90$ degrees or “broadside” incidence, and is due to specular reflection from the face of the strip.

The bands in Fig. 3 are readily explained by ignoring the thickness of the strip, and considering interference between the fields diffracted from the two ends of the strip. For a plane wave incident in the xy plane and an observer located at any finite distance in the backscatter direction, there is only one point on the leading edge of the strip and only one point on the trailing edge that satisfy the law of

diffraction[9]. The scattering geometry is that of Fig. 9 with $d=63.6$ mm, so we expect the maxima in the RCS to fall along vertical lines spaced according to Eqn. (9) by $c/(2d)=2.36$ GHz, close to the 2.4 GHz spacing seen in Fig. 3.

We can estimate the phase change associated with diffraction at the leading end and trailing end of the strip using the wedge diffraction coefficients given in Ref. [9]. Thus considering the ends of the strip to be wedges of angle zero degrees, we can evaluate the phase of the soft diffraction coefficient D_s , for backscatter with the angle of incidence equal to the angle of diffraction. For the leading end we obtain $\alpha_1=3\pi/4$ and for the trailing end $\alpha_2=-\pi/4$, and so $\alpha_2-\alpha_1=-\pi$. Evaluating Eqn. (8) with $d=63.6$ mm obtains maxima at 1.2, 3.5, 5.9, 8.3, 10.6, 13.0, 15.3 and 17.7 GHz, quite close to the values of 3.4, 5.8, 8.2, 10.6, 13.0 and 15.4 GHz, read from Fig. 3.

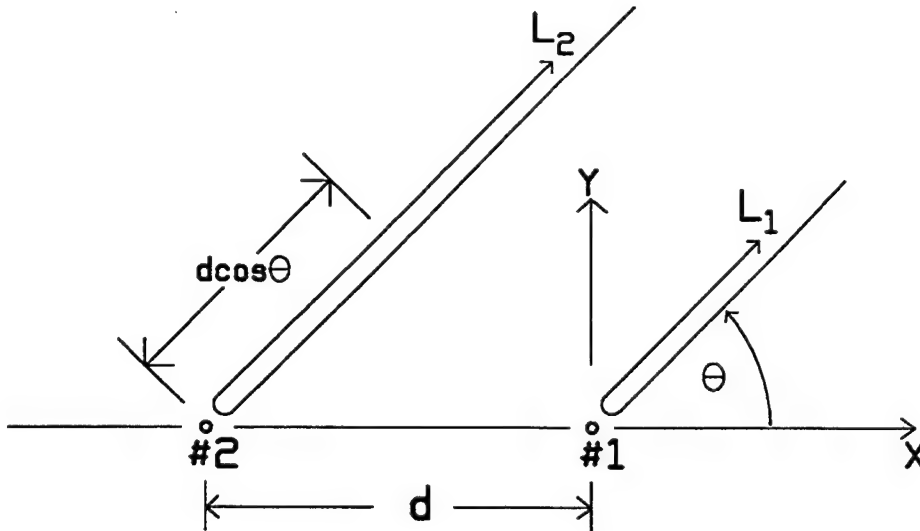


Fig. 9 Two scattering points separated by distance d , showing the path lengths L_1 and L_2 .

If there were no specular reflection, we would expect to see bands of maximum RCS in Fig. 3 intersecting the horizontal axis at $u = \pm 1.2$ GHz, separated by a minimum at $u=0$ on the vertical axis. Specular reflection merges these two bands into a single wide band centered on the vertical axis. It is interesting to note in Fig. 3 that this bright band of specular reflection has a constant width as distance from the center of the graph increases, that is, as the frequency f increases. This is consistent with the fact that the angular width $\Delta\theta$ of a lobe due to specular reflection is inversely proportional to the frequency[9], $\Delta\theta \propto 1/f$. The arc width of the reflection on the polar map, $\Delta s = f\Delta\theta$, becomes constant when $\Delta\theta$ is proportional to $1/f$, and this is clearly seen in Fig. 3.

2.2 The Large Rod

Fig. 2(b) shows a metallic rod of length 177.8 mm and square cross-section of size 71.1 mm. The rod is oriented with its edges parallel to the coordinate axes, and the long axis parallel to the x direction. The RCS was measured with the incident electric field horizontally polarized, that is, with the electric field vector parallel to the xy plane in Fig. 2. Fig. 4 shows the polar color map of the RCS of the rod in the first quadrant. We see a pattern of vertical dark bands of minimum RCS intersecting a pattern of horizontal dark bands, with the vertical bands more closely spaced than the horizontal. There is a third set of parallel dark bands oriented obliquely. The three sets of dark bands define a pattern of bright dots of maximum RCS. The spacing of the bands can be read directly from the color map with the aid of a ruler, dividers, and a calculator. The vertical bands are spaced by 0.842 GHz, the horizontal bands by 2.00 GHz, and the oblique bands by 0.776 GHz.

We can understand the scattered field of the rod as arising from diffraction from the three z -directed edges exposed to the plane wave for any direction of incidence. The diffraction points on two adjacent edges spaced by the length of the rod lead to a set of equally-spaced dark vertical bands of minimum RCS on the polar color map, with the expected spacing given by $c/2d = 300/(2 \times 177.8) = 0.844$ GHz, close to the value of 0.842 GHz read from Fig. 4. The two adjacent edges spaced by the width of the rod give rise to a set of dark bands of RCS parallel to the horizontal axis, spaced by $c/2d = 300/(2 \times 71.1) = 2.11$ GHz. The third pair of edges are diagonally opposite one another, and are spaced by 191.5 mm. These produce the oblique set of bands, spaced by $c/2d = 300/(2 \times 191.5) = 0.783$ GHz, close to the value of 0.776 GHz seen in Fig. 4. The tilt of this set of bands is expected to be at an angle of $\tan^{-1}(177.8/71.1) = 68$ degrees to the horizontal, and agrees quite well with the color map. The bright dots in the pattern have the same relative proportions as the target.

2.3 The Cone for Horizontal Polarization

The cone of Fig. 2(c) has a half angle of 15.26 degrees and the diameter of the base is 80.5 mm. The long axis of the cone lies along the x axis, with the tip pointing in the $+x$ direction. The cone length from the tip to the center of the base is 147.6 mm, and the "side length" from the tip to the edge of the base is 153.0 mm. The RCS was measured with horizontal polarization from 2 to 18 GHz over a full 360 degrees and is plotted as a polar color map in Fig. 5. The figure shows a maximum return for $\theta = 180$ degrees, due to specular reflection when the plane wave is normally incident on the flat base of the cone. The RCS is also large

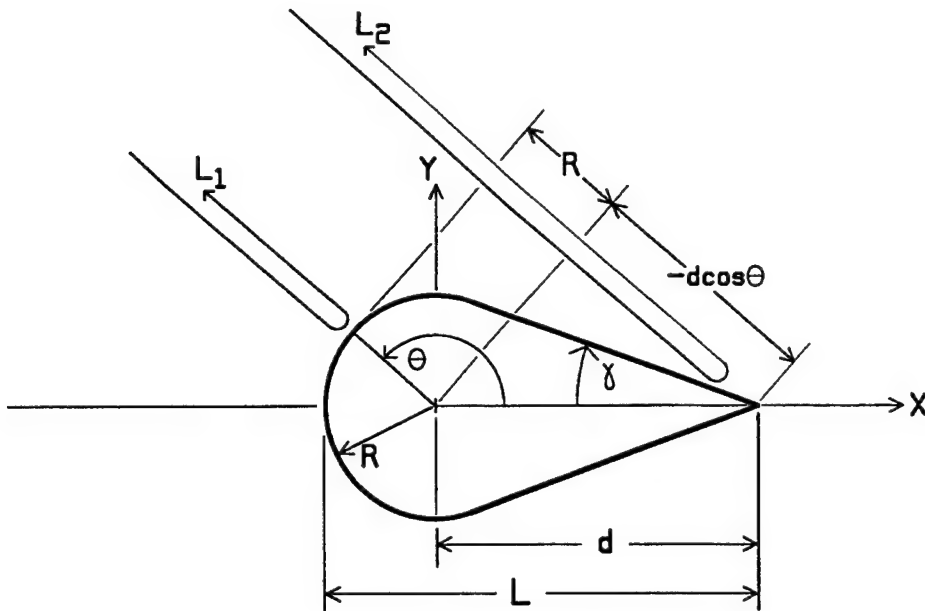


Fig. 10 The cone-sphere, showing the path lengths L_1 and L_2 for an incidence angle in the second quadrant.

along the bands oriented at ± 75 degrees to the positive x axis, looking perpendicular to the surface of the cone.

For incidence angles near zero degrees, the color map of Fig. 5 shows a pattern of horizontal bands of maximum and minimum RCS. This arises from the interference of the edge-diffracted fields from two diametrically-opposite points on the edge of the base. The two diffraction points lie in the xy plane in the coordinates of Fig. 2, and are separated by 80.5 mm, hence we expect the maxima or the minima to be spaced by $c/2d = 300/(2 \times 80.5) = 1.86$ GHz. The spacing of the minima near 0 degrees in Fig. 5 can be read from the color map as roughly 1.7 GHz, reasonably consistent with the expected value. For incidence angles greater than 15 degrees, the incident plane wave no longer "sees" the point on the cone base in the $-y$ half-space, and the set of bands fades away.

At 75 degrees incidence, the direction of travel of the plane wave is normal to the surface of the cone and there is a strong specular return. For angles between about 50 and 90 degrees, Fig. 5 shows a set of parallel bands of maximum RCS, parallel to the strong return at 75 degrees. From these incidence angles there is interference in the backscatter direction between the diffracted field from the nearest point on the edge of the base and the diffracted field from the tip. These points are separated by the cone's side length of 153 mm and so we expect the minima to be spaced by $c/2d = 300/(2 \times 153) = 0.98$ GHz. A ruler and dividers can be used to estimate the spacing of these minima in Fig. 5 as about 1.03 GHz, consistent with our expectations.

For incidence angles between 90 and 165 degrees, the incident plane wave sees the tip plus the two diffraction points on the edge of the base. These three scattering points lead to three sets of intersecting dark bands of minimum RCS. Diffraction from the two points on the edge gives rise to a continuation of the set of horizontal bands spaced by 1.86 GHz that is seen between 0 and 15 degrees incidence. There are two pairs consisting of the tip plus one of the two diffraction points on the edge. Diffraction from the tip plus the scattering point on the edge in the $+y$ half-space gives rise to a set of parallel bands tilted at an angle of about 15 degrees from the vertical direction toward the positive horizontal axis in the color map. This set of dark bands is parallel to the direction of the large return at about 75 degrees and is clearly seen in the 90 to 165 degree angular sector. The tip plus the diffraction point on the base in the $-y$ half-space produces a set of parallel bands inclined at 15 degrees from the vertical direction toward the negative horizontal axis, and is also clearly seen in the color map. The spacing of the oblique bands can be read from Fig. 5 as about 1 GHz, close to the expected value of 0.98 GHz. The three sets of intersecting dark bands in Fig. 5 define a pattern of bright dots of maximum RCS similar to that of the rod in Fig. 4. For incidence angles between 165 and 195 degrees, the tip is not seen, as it lies in the shadow of the base. The dot pattern is replaced by the pattern of horizontal bands associated with scattering from the two diffraction points on the edge.

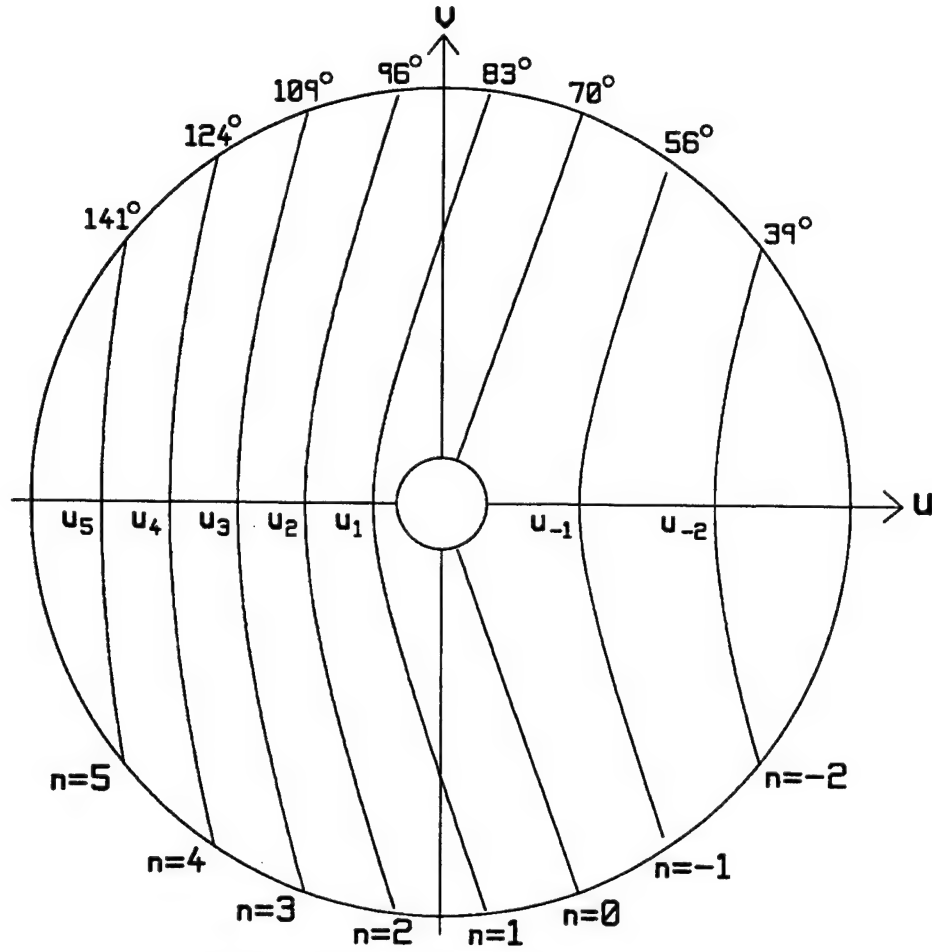


Fig. 11 Hyperbolas of minimum RCS for the cone-sphere.

3. INTERFERENCE OF A SPHERE REFLECTION AND A TIP DIFFRACTION

The cone-sphere of Fig. 10 illustrates interference between reflection from the spherical endcap and diffraction from the tip. The cone-sphere is oriented with its axis along the x -axis. There is no edge at the junction of the cone and the spherical endcap, that is, the unit-normal to the surface is continuous in passing from the surface of the cone to the surface of the sphere. In Fig. 10, a plane wave incident on the cone-sphere in the angular range $(90 - \gamma) < \theta < (180 - \gamma)$ sees both the surface of the sphere and the tip of the cone. The difference between the round-trip distance L_1 from the observer to the sphere back to the observer, and L_2 from the observer to the tip and back, is

$$L_2 - L_1 = 2(R - d \cos \theta) \quad \dots(10)$$

The curves of minimum RCS satisfy

$$-k(L_2 - L_1) + (\alpha_2 - \alpha_1) = -\pi - 2\pi n \quad \dots(11)$$

hence the RCS is a minimum when

$$f = \frac{c}{2(R - d \cos \theta)} \left(n + \frac{\pi + \alpha_2 - \alpha_1}{2\pi} \right) \quad \dots(12)$$

where α_1 is the phase change associated with the reflection from the surface of the sphere, and α_2 with the diffraction process at the tip of the cone. Eqn. (12) defines a set of hyperbolas[13] having their major axes aligned with the horizontal axis, such as those shown in Fig. 11. It may be shown that the crossing points of the hyperbolas with the negative horizontal axis are given by

$$u_n = -\frac{c}{2(d + R)} \left(n + \frac{\pi + \alpha_2 - \alpha_1}{2\pi} \right) \quad \dots(13)$$

Hence the crossings of the negative u axis are evenly spaced with the spacing given by

$$\Delta u = \frac{c}{2(d+R)} \quad \dots(14)$$

The spacing of the crossing points provides a convenient comparison with the measured RCS.

3.1 The Cone-Sphere

The metallic cone-sphere of Fig. 2(d) has a half-angle of $\gamma = 19.7$ degrees, and an overall length of $L = 50.1$ mm. The diameter of the sphere is 25.3 mm. The distance from the center of the sphere to the tip of the cone is $d = 37.45$ mm. The RCS was measured with horizontal polarization from 2 to 18 GHz over an angular range from -30 to 210 degrees as shown in Fig. 6. The map shows a strong reflection at an incidence angle of 70 degrees, looking normal to the cone surface. Also there is strong reflection from about 160 to 200 degrees, looking normal to the surface of the sphere, over the angular range where the tip of the cone is not visible. In the left-hand plane in Fig. 6 there is a set of five sharp bands of minimum RCS, separated by broad regions of large RCS.

Fig. 11 shows the set of hyperbolas of minimum RCS specified by Eqn. (12) for the cone-sphere dimensions of $R = 12.65$ mm and $d = 37.45$ mm. In Fig. 11 the radial axis corresponds to Fig. 6, with zero frequency at the center, 2 GHz at the inner circle, and 18 GHz at the outer. We expect the reflection from the sphere surface to have a phase change of $\alpha_1 = \pi$. The phase change associated with the tip diffraction is more difficult to estimate, and was simply made equal to zero, $\alpha_2 = 0$. Comparing Figs. 6 and 11 we see that the dark bands of minimum RCS in Fig. 6 have the same shape as the hyperbolas of Fig. 11. There are five hyperbolas in Fig. 6, and five in Fig. 11, in the negative- u half-space. In Fig. 6, only segments of the hyperbolas are seen. For $\theta < 70$ degrees the surface of the cone hides the surface of the sphere, and so there is no reflection and the hyperbolas are not formed. From $\theta = 160$ to 200 degrees, the tip of the cone is not visible and so the segments of the hyperbolas that cross the horizontal axis are not seen. By smoothly joining the portions of the hyperbolas in the negative half-space with those in the positive, we can estimate the spacing of the zero crossings as about 2.9 GHz, in reasonable agreement with the spacing of 3.0 GHz predicted by Eqn. (14).

Another comparison of the position of the hyperbolas in Figs. 6 and 11 can be made by reading the angles at which they cross the 18 GHz circle. Thus in Fig. 6, the minima in

the RCS at 18 GHz occur at about 82, 93, 106, 120 and 138 degrees. In Fig. 11, these crossings fall at 83, 96, 109, 124 and 141 degrees. The alignment of the hyperbolas predicted by our simple interference theory with those in the measured RCS is quite good, especially considering that the phase change α_2 associated with diffraction at the tip of the cone was simply set to zero. If we use $\alpha_2 = -45$ degrees, then the minima at 18 GHz fall at 82, 95, 108, 122 and 138 degrees, in better agreement with the measurement, and so the phase change associated with tip diffraction must be closer to -45 degrees than to 0 degrees.

4. INTERFERENCE OF AN EDGE WAVE AND AN EDGE DIFFRACTION

To analyze the polar color maps of scattering from the thick disk and the small cone of Fig. 2 parts (e) and (f), it is useful to consider a wave which travels around the edge of the target, called an "edge wave"[14]. Fig. 12 shows a thin disk in the yz plane, with a plane wave incident nearly edge-on to the disk. The wave diffracts from the nearest point on the disk edge, with path length L_1 . The wave also diffracts from the disk edge at a point diametrically opposite, but the path is not shown in Fig. 12. In addition, the wave couples to the edge of the disk and becomes an "edge wave", which travels around the edge, shedding energy tangentially as it goes. After traveling a distance of πR around the edge, the edge wave launches some of its energy in the backscatter direction. We will show that interference between the two scattered fields shown in Fig. 12 creates a pattern of ellipses.

4.1 Interference Analysis

Fig. 12 compares the path lengths L_1 traveled by the wave diffracted from the edge of the disk, and L_2 traveled by the wave that couples to the edge and follows it around a semicircle. For $0 \leq \theta \leq 180$ degrees, the difference in path length is

$$L_2 - L_1 = \pi R + 2R \sin \theta \quad \dots(15)$$

Assuming the wave travels around the edge with the same phase constant as in free space, these waves will be 180 degrees out of phase in the backscatter direction when Eqn. (15) is satisfied, leading to curves of minimum RCS which satisfy

$$f = \frac{c}{(\pi + 2 \sin \theta) R} \left(n + \frac{\pi + \alpha_2 - \alpha_1}{2\pi} \right) \quad \dots(16)$$

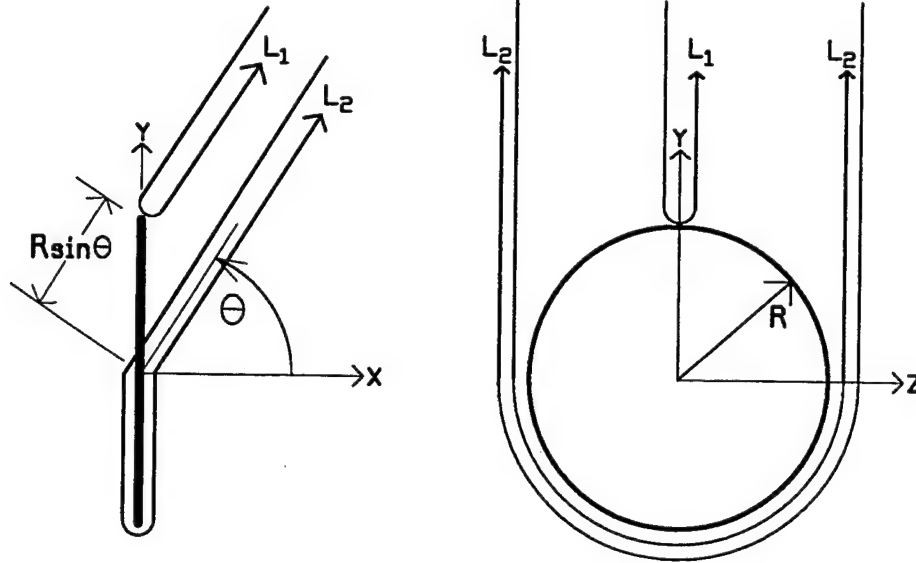


Fig. 12 A thin disk, showing diffraction from the edge with path length L_1 , and scattering by an edge wave which travels around the edge of the disk, with path length L_2 .

where $n=0, +1, +2, \dots$. Angles α_1 and α_2 are phase changes associated with the scattering process for the edge-diffracted wave and for the wave that travels around the edge. For $180 < \theta < 360$ degrees, we must use the diffraction point diametrically opposite on the edge, hence $L_2 - L_1 = \pi R - 2R \sin \theta$, and the curves of minimum RCS satisfy

$$f = \frac{c}{(\pi - 2 \sin \theta) R} \left(n + \frac{\pi + \alpha_2 - \alpha_1}{2\pi} \right) \quad \dots(17)$$

Equations (16) and (17) can generate both positive and negative frequencies, depending on the values of n , α_1 and α_2 , but only the positive frequencies are physically meaningful.

Each of Equations (16) and (17) represents a family of ellipses, with the major axis aligned along the vertical axis and one focus at the origin[13]. To illustrate interference ellipses that arise due to the edge wave, these equations were graphed using the radius of the base of the small cone of Fig. 2(f), $R=29.8/2=14.9$ mm, and using $\alpha_1=135$ degrees, and $\alpha_2=-136$ degrees as explained below. The set of ellipses so obtained is shown in Fig. 13. Eqn. (16) leads to positive and negative frequencies depending on n and on $\alpha_2 - \alpha_1$; only those ellipses having positive frequencies are graphed in Fig. 13. The ellipses of Eqn. (16) were drawn using solid curves in the upper half-space where Eqn. (15) holds; dashed curves were used in the lower half-space to show the orientation of the major axis.

Eqn. (17) leads to the set of ellipses shown with solid curves in the lower half-space in Fig. 13.

In Fig. 13, the points at which the ellipses cross the vertical axis have been labeled v_1, v_2 , and so forth. Eqn. (16) is easily evaluated with $\theta=90$ degrees to show that if α_1 and α_2 are independent of the frequency, then the spacing of the crossing points is uniform and is given by

$$\Delta v = v_{n+1} - v_n = \frac{c}{(\pi + 2)R} \quad \dots(18)$$

The thick disk of Fig. 2(e) and the cone of Fig. 2(f), with its circular-disk base, will be used to illustrate ellipses in RCS polar color maps.

4.2 The Thick Disk

The disk of Fig. 2(e) demonstrates the edge wave for vertical polarization, and its absence for horizontal polarization. The disk is metallic, of radius $R=50.45$ mm and thickness 20.4 mm. The disk was oriented so that its flat faces lie parallel to the yz plane. The RCS was measured for both horizontal polarization, Fig. 7(a), and vertical polarization, Fig. 7(b), from 2 to 18 GHz. There are strong similarities between the two cases. In both cases specular reflection from the face of the disk obtains a very strong RCS at $\theta=0$ degrees. In both parts of Fig. 7 there is a set of bands of maximum and of minimum RCS parallel to the horizontal axis near $\theta=0$ degrees. But near $\theta=-90$ degrees, which is edge-on incidence to the

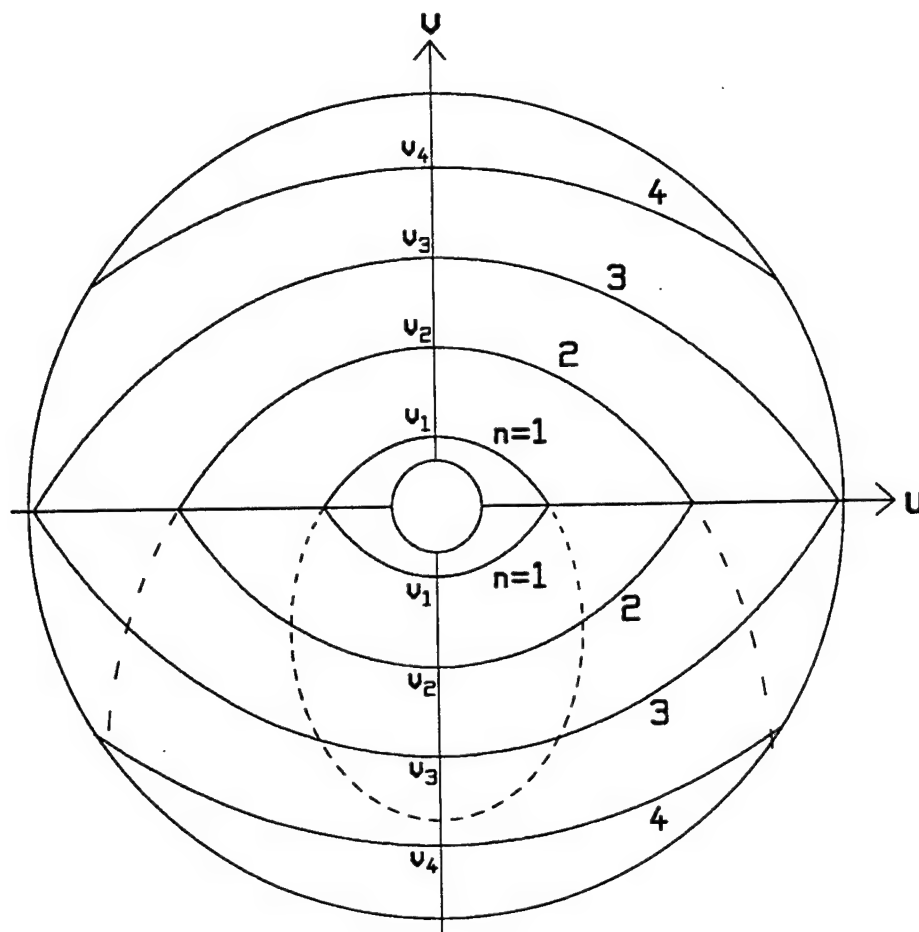


Fig. 13 Ellipses of minimum RCS for the small cone.

disk, the two cases are significantly different. For horizontal polarization the pattern of parallel straight bands continues from $\theta = 0$ to $\theta = -90$ degrees. However, for vertical polarization, part (b), the set of maxima and minima near $\theta = -90$ degrees have substantial curvature. These appear to be segments of ellipses.

The set of horizontal bands near $\theta = 0$ degrees for both polarizations arise due to diffraction from two diametrically-opposite points on the edge of the disk, where the disk intersects the xy plane. These points are spaced by the disk diameter of $d=2R=100.9$ mm, and Eqn. (9) predicts the band spacing to be $c/(2d)=300/(2 \times 100.9)=1.49$ GHz. For horizontal polarization in Fig. 7(a), the spacing can be read from the figure as 1.46 GHz, close to the expected value. For horizontal polarization, this pattern of horizontal bands continues with the same spacing throughout the whole color map. The pattern is clearly seen along the $\theta = -90$ degrees direction from 2 to about 9 GHz, but the RCS tends to become flat for $\theta = -90$ above 9 GHz. Note that there are two vertically-oriented

dark bands, at 7.5 and 15 GHz. These arise due to the thickness of the disk. In addition to the two diffraction points on the front edge of the disk, there is a third diffraction point on the back edge. For the pair of points separated by the disk thickness, we expect an interference pattern of vertical bands spaced by $c/2d=300/(2 \times 20.4)=7.35$ GHz, corresponding to the vertical dark bands seen at about 7.5 and 15 GHz in Fig. 7(a).

For vertical polarization in Fig. 7(b), we see the parallel horizontal bands expected near $\theta = 0$. Near $\theta = -90$ degrees, the edge wave mechanism dominates, and we see a family of ellipses. We can read the spacing of the ellipses from Fig. 7(b) to be about 1.14 GHz, closer than the 1.46 GHz spacing of the pattern of horizontal bands in part (a) of the figure. The edge wave model predicts ellipses that cross the vertical axis with a spacing given by Eqn. (18) of $c/((\pi+2)R)=300/((\pi+2) \times 50.45)=1.16$ GHz, about equal to the value read from Fig. 7(b).

The pattern of ellipses is of greater angular extent at the low end of the frequency band, being visible from $\theta = -90$ degrees to angles of -30 or even -20 degrees. As the frequency increases, the angular extent of the pattern diminishes, so that near 18 GHz the pattern is clearly seen only for $-105 \leq \theta \leq -75$ degrees, 15 degrees away from edge-on incidence. The pattern of ellipses has an almost constant arc-length, and is reminiscent of the constant width of the bright band associated with specular reflection, discussed above in conjunction with scattering from the strip.

The pattern of ellipses is sharp along $\theta = -90$ degrees from 2 to about 6 GHz, but becomes increasingly blurred as the frequency approaches 18 GHz. The edge wave mechanism is quite frequency dependent, with the wave shedding more of its energy as it travels around the edge at higher frequencies. Hence at higher frequencies the wave has less energy to scatter back in the direction of the incident wave, and the interference pattern is less distinct.

4.3 The Cone for Vertical Polarization

The small metallic cone in Fig. 2(f) has half-angle 39.85 degrees, base diameter 29.8 mm, and length 17.85 mm. The cone was positioned with its main axis on the x axis. In this orientation the base of the cone lies in a yz plane. The RCS was measured with the incident wave vertically polarized, from 2 to 18 GHz, and is shown in Fig. 8. There is a strong specular reflection around $\theta = 180$ degrees, when the wave is normally incident on the cone's base. There is also a weaker specular reflection from the curved surface of the cone, near $\theta = 50$ degrees. The pattern of light and dark bands between $\theta = 70$ degrees and $\theta = 130$ degrees have the elliptical shape characteristic of edge wave scattering.

We might expect to see a pattern of horizontal bands near $\theta = 180$ degrees, due to interference of the fields diffracted from two diametrically opposite points on the cone's edge. The expected spacing would be $c/(2d) = 300 / (2 \times 29.8) = 5.0$ GHz. There is a hint of dark horizontal bands of minimum RCS intersecting the 18 GHz outer circle at about 140 degrees and at about 160 degrees and 200 degrees, but the target is too small to produce a clear pattern. The spacing is about 5 GHz as expected.

To compare the location of the measured ellipses of minimum RCS in Fig. 8 with those predicted by our simple interference theory and Eqn. (18), Fig. 13 was drawn using the small cone's base radius of 14.9 mm. The phase change associated with diffraction from the edge was estimated using the "soft" diffraction coefficient[9], D_s , for a straight edge with a wedge of angle 50 degrees, and incidence at

$\theta = 90$ degrees, to obtain $\alpha_1 = 135$ degrees. The phase change associated with the edge wave was estimated using the thin disk expression given by Eqn. (14) in Ref. [14]. This equation includes the phase change of $-k\pi R$ associated with the distance traveled by the edge wave. In addition to some phase terms that are constant with frequency, there is a phase change associated with $-\alpha_i\pi R$, where[14]

$$\alpha = \alpha_r + j\alpha_i = 0.5k(kR)^{-2/3}e^{-j\pi/6} \quad \dots(19)$$

Thus the phase change associated with the edge wave, α_2 , is not constant with frequency, but instead includes a term proportional to $f^{1/3}$. Eqn. (14) in Ref. [14] was evaluated for the cone's base radius of 14.9 mm. It was found that α_2 varies from -154 degrees at 2 GHz to -112 degrees at 18 GHz; a representative value of -136 degrees was chosen to plot Fig. 13.

Fig. 13 shows the curves of minimum RCS expected for the small cone, plotted from 2 GHz at the inner circle to 18 GHz at the outer. The curves in Fig. 13 are quite similar to the dark bands of minimum RCS seen in Fig. 8, from about 70 to about 130 degrees. The expected curves in Fig. 13 cross the vertical axis at 2.9, 6.9, 10.8 and 14.7 GHz. This corresponds quite well to the frequencies where the dark bands cross the vertical axis in Fig. 8, of about 6.3, 10.5 and 14.4 GHz. The curve expected at 2.9 GHz is not seen in Fig. 8.

Another example of edge wave scattering can be seen in Fig. 5(a) of Ref. [8]. The figure shows a polar color map for the RCS with vertical polarization of a large right-circular cone of base diameter 83.6 mm, length 50.0 mm, and half angle 40 degrees. The base diameter is much larger than that of the 29.8 mm cone used for Fig. 8, and comparable in size to the thick disk discussed above. The polar color map in Ref. [8] Fig. 5(a) shows a striking pattern of ellipses between $\theta = 60$ degrees and 140 degrees. There are 11 maxima along the vertical axis, spaced about 1.45 GHz apart. This agrees reasonably well with Eqn. (18), which predicts a spacing of 1.40 GHz.

5. CONCLUSION

This paper presented the measured RCS of six simple targets as a color map in polar coordinates. Such "polar color maps" show striking patterns of bright and dark bands. In each angular range, these patterns arise due to interference between two or three scattered waves: two or three edge diffractions; two edge diffractions plus a tip

diffraction; a reflection plus a tip diffraction; or an edge diffraction plus an edge wave. The identification of primary scattering mechanisms by recognizing patterns on polar color maps provides the RCS specialist with an effective diagnostic and educational tool.

Not discussed in this paper is the effect of target resonance[15] in a polar color map. The resonant frequencies of a structure are independent of the angle of incidence of the plane wave, hence give rise to RCS maxima and minima at constant radius on a polar color map. However, the degree to which the resonance is excited does depend on the angle of incidence. Hence, resonance on a polar color map leads to circles whose intensity varies with incidence angle. Fig. 8 in Ref. [8] shows the RCS of a rod with an attached wire; the wire is resonant when its length is approximately equal to odd multiples of the quarter-wavelength. The color map clearly shows resonance circles.

RCS data as a function of frequency and of incidence angle are often used with two-dimensional signal processing techniques to draw a rectangular-format color contour map of the intensity of the return as a function of distance, down-range and cross-range[16]. Such maps show strong returns from localized scattering sources such as the wing-tips of an aircraft, and the resulting images bear a shadowy resemblance to the target. The techniques presented here may be complementary in that specific scattering mechanisms not associated with point-source scattering are readily identified.

Methods and computer codes in computational electromagnetics become established as useful analysis tools by "code validation": the building of an "experience base" of problems solved and compared with reference data. The conclusions drawn from code validation should be stated as "modeling guidelines"[17] which provide rules-of-thumb for constructing a model for solution by that computational method, and specify geometrical restrictions on the input geometry which respect the limitations on the validity of the CEM code. The usefulness of a CEM code for solving a new problem, perhaps by an inexperienced user, is closely related to the quality and explicitness of the associated modeling guidelines.

Modeling guidelines are best developed by comparing computations with measurements as a function of frequency over a wide range, as well as by examining individual radiation or scattering patterns at single frequencies. Although calculating the RCS as a function of both frequency and incidence angle is a massive computation, comparing measured and computed polar color maps of the RCS provides a comprehensive evaluation of the performance of a computer code for a given problem, and

may be useful for formulating modeling guidelines. This paper has related features on a polar color map, such as lines, hyperbolas, and ellipses, to the scattering mechanisms of the target, and may provide insight into the cause of features seen or missing from computed RCS maps compared to the measured RCS.

Our own code validation studies have compared computations of the monostatic RCS with our measurements[5,6,15,18]. It was noted above that the differences in the computed and measured RCS are largest in the sharp, deep minima, and that this is expected due to the measurement geometry. Because our scattered field measurements are bistatic, and are made at a finite range from the horns, our data is most valuable for code validation when the scattered field due to a point source is computed at the location of the receive horn in Fig. 1. Simulating the measurement setup explicitly in the computation, rather than computing backscattered field due to plane wave incidence, removes the geometry error as a source of difference in comparing the measurement and the computation.

Our data base contains the measured RCS and the phase of the scattered field for a wide variety of metallic and dielectric targets[7]. Some targets are small enough to be studied by moment methods, by the multiple multipole method, or by the finite-difference time-domain method. Others are so large that ray-tracing would be the natural approach. This extensive data presents a challenge to the computational electromagnetics community for code validation. Our measured data, and the associated plotting software, POLPLOT and other programs, are freely available to the community and can be fetched by ftp from "lucas.incen.doc.ca", or by referring to our world-wide-web page "http://lucas.incen.doc.ca/rsc.html".

REFERENCES

1. S.J. Kubina and C.W. Trueman, "The Validation of EM Modelling Codes - A User Viewpoint", *The Applied Computational Electromagnetics Society Journal*, Special Issue on Electromagnetics Computer Code Validation, 1989.
2. R.G. Kouyoumjian, *The Calculation of the Echo Area of Perfectly Conducting Objects by the Variational Method*, Ph.D. dissertation, The Ohio State University, Columbus, Ohio, November, 1953.
3. E.F. Knott, V.V. Liepa and T.B.A. Senior, "Plates and Edges", *IEEE Trans. on Antennas and Propagation*, vol. AP-19, no. 6, pp. 788-789, November, 1971.
4. A.D. Yaghjian and R.V. McGahan, "Broadside Radar Cross-Section of the Perfectly-Conducting Cube",

- IEEE Trans. on Antennas and Propagation*, vol. AP-33, no. 3, March, 1985.
5. C.W. Trueman, S.J. Kubina, S.R. Mishra and C. Larose, "RCS of Four Fuselage-Like Scatterers at HF Frequencies", *IEEE Trans. on Antennas and Propagation*, vol. AP-40, no. 2, pp. 236-240, February 1992.
6. S.R. Mishra, C.L. Larose and C.W. Trueman, "Precision Radar Cross-Section Measurements for Computer Code Validation", *IEEE Trans. on Instrumentation and Measurement*, vol. 42, no. 2, pp. 179-185, April 1993.
7. S.R. Mishra, C.L. Larose, M. Flynn and C.W. Trueman, "A Database of Measured Data for RCS Code Validation", *Conference Proceedings of the 10th Annual Review of Progress of the Applied Computational Electromagnetics Society*, Monterey, California, March 21-26, 1994.
8. C.L. Larose, S.R. Mishra and C.W. Trueman, "Graphics for Visualizing RCS as a Function of Frequency and Angle", *IEEE Antennas and Propagation Magazine*, vol. 36, pp. 7-13, June 1994.
9. A. Balanis, *Advanced Engineering Electromagnetics*, Wiley, 1989.
10. R.B. Dybdal, "Radar Cross-Section Measurements", *Proc. IEEE*, vol. 75, pp. 498-516, April, 1987.
11. R.G. Kouyoumjian and L. Peters, "Range Requirements in Radar Cross-Section Measurements", *Proc. IEEE*, vol. 53, pp. 920-928, August, 1965.
12. S.R. Mishra and C.W. Trueman, "Accuracy of RCS Measurements", *Proceedings of the 18th Annual Meeting and Symposium of the Antenna Measurement Techniques Association(AMTA)*, Seattle, Washington, Sept. 30-Oct. 4, 1996..
13. M.R. Spiegel, *Mathematical Handbook of Formulas and Tables*, Schaum's Outline Series, McGraw-Hill, 1968.
14. A.K. Dominek, "Transient Scattering Analysis for a Circular Disk", *IEEE Trans. on Antennas and Propagation*, vol. 39, no. 6, pp. 815-819, June 1991.
15. C.W. Trueman, S.J. Kubina, S.R. Mishra and C. Larose, "RCS of Scatterers with Attached Wires", *IEEE Trans. on Antennas and Propagation*, Vol. 41, No. 3, pp. 351-355, March 1993.
16. E.K. Walton, I.J. Gupta, M.W. Tu and A. Moghaddar, "Super Resolution Radar Target Imaging of Realistic Targets", *Proceedings of the 14th Annual Meeting and Symposium of the Antenna Measurement Techniques Association(AMTA)*, pp. 6-28 to 6-32, Oct. 19-23, 1992.
17. C.W. Trueman and S.J. Kubina, "Verifying Wire-Grid Model Integrity with Program CHECK", *Applied Computational Electromagnetics Society Journal*, vol. 5, no. 2, Winter, 1990, pp. 17-42.
18. C.W. Trueman, S.J. Kubina, S.R. Mishra and C. Larose, "RCS of a Generic Aircraft at HF Frequencies", *Canadian Journal of Electrical and Computer Engineering*, Vol. 18, No. 2, pp. 59-64, April 1993.

An Efficient Method of Analysis of Co-Planar Dipole Array Antennas

A. I. Imoro, N. Inagaki, N. Kikuma

Department of Electrical and Computer Engineering
Nagoya Institute of Technology
Gokiso-cho, Showa-ku, Nagoya 466, Japan

Abstract - Generalized impedance formulas for non-uniform array configurations based on the *Improved Circuit Theory* (ICT) are presented for the first time in an English text. To further enhance the ICT as an accurate and fast method for evaluations, a new and more compact closed-form formula is derived to replace a function requiring time intensive numerical integration during the implementation of the ICT algorithm in co-planar dipole array antenna evaluations. The resulting ICT computational scheme reduces the required CPU time by a factor of two and has the same order of accuracy as the conventional MoM. The new ICT implementation would be of considerable use as a *Computer Aided Design* (CAD) tool of co-planar dipole array antennas.

I. Introduction

The *Improved Circuit Theory* (ICT), which was first published in 1969 [1], is still an attractive analytical method for multielement dipole antenna evaluations. It was originally developed from the understanding that the classical EMF method, which had been used for decades, included several inconsistencies. Classical EMF theory assumes the current distribution is independent of the combinations of the driving voltages, that the self-impedances are not affected by the presence of other elements, and that the mutual impedances of elements are determined by the related two elements only [2]. The expression of the input impedance obtained by the EMF method coincides with that of the method of variations, which is the reason why the results are satisfactory for situations [3] where the antenna length is about a half wavelength for which the current distribution is well expressed as a simple sinusoidal function. The idea of the ICT was to introduce a second function for

the current distribution in the variational method to improve the EMF method. The ICT method executed this by employing King's [4] two term current expression. But, it is surprising that only one additional current function in the EMF method made the ICT method an accurate analytical method compared to MoM. This later turned out to correspond to the Galerkin's method applied in the implementation of the MoM.

An important feature of the ICT method is that it excludes all the above inconsistencies of the EMF method, and achieves an accurate evaluation scheme for the impedance and other important antenna parameters like the gain and far-field radiation patterns.

The ICT method has considerable advantages over other conventional methods of evaluating antennas such as the MoM. It has been empirically known that the required CPU time is less than that in a standard MoM by a factor of more than ten. For certain applications, run time is important. Our task in this paper is to achieve this optimization using an improved ICT method in co-planar dipole array analysis.

The presentation of the rest of the paper follows. Section II discusses the essentials of the ICT method which includes the presentation of the generalized input impedance formulas for any arbitrary array configuration based on the ICT theory for the first time in English text. The main advantages of the ICT method compared to other conventional methods like the classical EMF and MoM methods are also discussed in this section. Section III discusses the application of the ICT method and points out the importance of an optimum running time in an antenna CAD tool. Section IV considers the optimization of the CPU time by replacing a function requiring time intensive numerical integration with an approximate but accurate closed-form equivalent. Section V demonstrates the accuracy and the reduction in the CPU time with case studies of array systems us-

ing the ICT method with the numerical integration and closed-formed schemes compared with the conventional MoM method. Section VI states the conclusion followed by an appendix in Section VII where details of the main formulas are given.

II. Essentials of ICT Method

Figure 1 shows a general antenna system which can be analyzed by the ICT. This include arrays with elements of different lengths, spacing and radii which

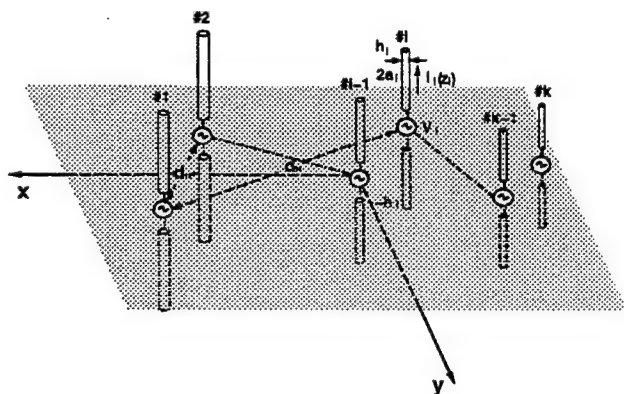


Figure 1: Dipole Antenna Array of Non-uniform Geometry.

are symmetrical with respect to the x-y plane with feeds on a common plane such as in Yagi-Uda and log-periodic dipole arrays.

Before the advent of modern computers and the possibility of versatile numerical methods like MoM, a common conventional method of analyzing such arrays for various antenna parameters was by the EMF method. The EMF method makes assumptions which lead to inaccuracies especially for non-resonant dipole antenna lengths [2]. However, the variational characteristics of the impedance of the EMF allows us to treat such a system as a variational problem. This is because the impedance expression in terms of current distribution by EMF coincides with the variational expression except for the definition of the inner product. The inner product takes the complex conjugate form in EMF while it takes the direct symmetric product form in the variational method [10].

For resonant dipoles the current functions are approximated by real functions, and the two forms coincide with each other. Thus, if the N element system in Fig. 1 is regarded as a variational problem, the expression of the current function $I_i(z_i)$ adopted from

the Ritz method is [1]

$$I_i(z_i) = \sum_{l=1}^M I_i^l f_i^l(z_i), \quad f_i^l(0) = 1, \quad (i = 1, 2, \dots, N). \quad (1)$$

The ICT uses the two-term current function represented as $M = 2$ given as

$$\begin{aligned} f_i^1(z_i) &= \sin k(h_i - |z_i|) \\ f_i^2(z_i) &= 1 - \cos k(h_i - |z_i|). \end{aligned} \quad (2)$$

Based on this current function, the ICT circuit equation for the system in Fig. 1 is given as [1]

$$\sum_{m=1}^2 [Z^{lm}] [I^m] = [V], \quad (l = 1, 2), \quad (3)$$

where the $N \times 1$ matrices $[V]$ and $[I^m]$ are the input voltage and current respectively and $[Z^{lm}]$ is the generalized impedance matrix of order $N \times N$ whose details are given in Section VII.A of the appendix. The ICT circuit equation as defined in Eq. (3) is a considerable improvement over the EMF method for the evaluation of multielement antennas.

It is important to note that in the ICT method, the use of the current functions in Eq. (2) makes it possible to express the far-field radiation patterns in closed-form as [8]

$$F(\theta, \phi) = \sum_{i=1}^N \sum_{m=1}^2 I_i^m g_i^m(\theta, \phi) \quad (4)$$

where

$$\begin{aligned} g_i^1(\theta, \phi) &= \frac{\cos(kh_i \cos \theta) - \cos kh_i}{\sin \theta} \\ g_i^2(\theta, \phi) &= \frac{\sin(kh_i \cos \theta) \sin \theta}{\cos \theta} \\ &\quad - \frac{\sin kh_i - \sin(kh_i \cos \theta) \cos \theta}{\sin \theta}. \end{aligned} \quad (5)$$

This yields a considerable saving in time compared with the conventional MoM. In the latter, more than two current expansion terms per element are required to accurately evaluate the same quantities.

III. Applications of the ICT method

The ICT method has been popular among antenna designers in Japan. For instance, Inagaki et al. [5]

carried out design of dipole arrays with specified radiation patterns in the magnetic plane. The configuration of the elements in the array are non-uniform and the integral of the current distribution is expressed applying the Improved Circuit Theory. This was the first antenna synthesis theory which considered the change of current distributions to be dependent on the combination of the driving voltages. Oyama et al. applied the ICT method in finding an expression for the characteristics of Yagi-Uda antennas with a vector diagram. They also applied it in the optimum design of Yagi-Uda antennas with a minimum gain specified [6-7]. Kawakami et al. applied ICT in the analysis of log-periodic dipole antennas [8].

The ICT scheme has been installed in an expert system for linear antennas developed by ATR, Japan. Originally designed as a prototype *Computer Aided Engineering* (CAE) tool of wire antennas on PCs, this system now runs on an *Engineering Work Station* (EWS) and can be used to display graphics of analyzed results of different antenna geometries simultaneously [9]. An ICT algorithm has been found useful in this system because of the relatively quicker response required by such interactive and real time system.

IV. Faster ICT Implementation Scheme

For the antenna designer, the importance of having a fast method of evaluating an antenna system cannot be overemphasized. A faster method is especially desirable in an expert system discussed in the previous section.

In furtherance of the objective of achieving a faster antenna evaluating method, a recent study [11-12] shows the usefulness of replacing time consuming functions within the ICT algorithm. To achieve this in the *Faster Improved Circuit Theory* (FICT) [11-12], closed-form approximate formulas are derived to replace the most time consuming function in the algorithm. Part of resulting formula in FICT is bulky because it is based on polynomial functions derived from data banks using least square curve fitting techniques.

In this section, the same function [11-12] is analyzed again and a new and more compact closed-form formula is proposed which avoids time intensive numerical integration in the implementation of the ICT method. The new formula is shown to be capable of reproducing the results of the numerical integration scheme and reduces more than half the time required in implementing the conventional ICT method. It is

applicable to the practical range of most co-planar dipole arrays of arbitrary configurations.

A. Closed-Form Formula

The current method of evaluating Eq. (27) of Section VII.A of the appendix which is restated here as

$$E_y(x) = 2 \int_0^x \frac{\exp(-j\sqrt{t^2 + y^2})}{\sqrt{t^2 + y^2}} dt. \quad (6)$$

is by numerical integration, which is considerably time intensive. In Eq. (6) each variable ($x = kh, y = kd$), has been multiplied by k (the wavenumber) to achieve non-dimensionality. This function has been shown [11-12] to require more than fifty percent of the total CPU time during a typical analysis of a multielement system of linear arrays and has therefore been identified as the most time consuming function in the ICT algorithm. The objective here is to find a closed-form formula which avoids numerical integration. Two partial formulas are derived for large and small element spacing respectively, and then combined to replace the original equation (Eq. 6).

1) *Partial Formula for Large Inter-Element Spacing:* For the general case of large inter-element spacing between elements of a linear array of antennas the following formula can be derived to replace Eq. 6. For such situations, we make the substitution $t = y \sinh w$ in Eq. (6) and simplify to get

$$E_y(x) = 2 \int_0^{\sinh^{-1} \frac{x}{y}} e^{-jy \cosh w} dw. \quad (7)$$

Using Mathematica [13] the integrand of Eq. (7) is expanded in a power series with respect to w and then integrated over the limits given. The resulting approximate function is given as the two-variable function

$$E_y(x) \approx 2f(x, y)e^{-jy}. \quad (8)$$

Details of $f(x, y)$ are given in Section VII.B of the appendix.

2) *Partial Formula for Small Inter-Element Spacing:* It will later be shown that Eq. (8) is accurate only for large values of y . For this reason we would seek for another closed-form solution of Eq. (6) which is valid for smaller values of y . This applies to evaluation of the self-term where the spacing is equivalent to the element radius and also for situations of electrically small spacing. For this case Eq. (6) is first expressed as

$$E_y(x) = E_y(y) + F_y(x) \quad (9)$$

where $E_y(y)$ is as defined in Eq. (8) and

$$F_y(x) = 2 \int_y^x \frac{\exp(-j\sqrt{t^2 + y^2})}{\sqrt{t^2 + y^2}} dt. \quad (10)$$

To find an approximate function for Eq. (10) we make the substitution $w = t + \sqrt{t^2 + y^2}$ to get

$$F_y(x) = 2 \int_{(\sqrt{2}+1)y}^{x+\sqrt{x^2+y^2}} \frac{e^{-j\left(\frac{w}{2} + \frac{y^2}{2w}\right)}}{w} dw. \quad (11)$$

The following component of the function in the integrand of Eq. (11) which is difficult to treat analytically is expanded into a power series with respect to w

$$f(y) = e^{-j\frac{y^2}{2w}}. \quad (12)$$

Using Mathematica [13] it can be shown that in the interval $2 \leq y \leq 10$, the difference between a five term power series expansion of $f(y)$ of Eq. (12) and the original function is less than 10^{-4} .

Therefore using this five term series expansion of Eq. (12) we can express Eq. (11) approximately as

$$F_y(x) \approx 2 \int_{(\sqrt{2}+1)y}^{x+\sqrt{x^2+y^2}} \left(1 - \frac{y^4}{8w^2} - j\frac{y^2}{2w}\right) \frac{e^{-j/2w}}{w} dw. \quad (13)$$

Equation (13) is then easily integrated using Mathematica [13] to give

$$F_y(x) = 2g(x, y) \quad (14)$$

where details of $g(x, y)$ is given in the Section VII.C of the appendix. *It should be noted that Eq. 9 is valid when Eq. 8 is also valid, but the converse is not necessarily so.*

3) Valid Regions of Partial Formulas: In this section we shall establish the valid regions of Eqs. 8 and 9. To achieve this we examine an array configuration of two elements of length $(2h/\lambda)$ in the interval $0.1 \leq 2h/\lambda \leq 2$ and inter-element spacing in the interval $10^{-4} \leq d/\lambda \leq 10$. This is then used to validate Eqs. (8) and (9). Most practical arrays of interest would normally fall within this region. The lower values of d/λ represent the radius of an element in

the array. Relative error in amplitude for Eqs. (8) and (9) on one hand, and Eq. (6) on the other (all dimensionless complex quantities) are computed and compared. The one with least error would be best in representing Eq. (6) for any particular array configuration. Our aim is to have a function which gives minimum error at optimum time in order to reduce the time required to carry out the analysis of wire antennas using the ICT method.

As shown in Eq. (29) of Section VII.B of the appendix, Eqs. (8) and (9) are functions of the power expansions of b defined as

$$b = \ln \frac{x + \sqrt{x^2 + y^2}}{y}. \quad (15)$$

Eq. (15) is such that, for certain combinations of x and y , higher order terms of it are vanishingly small and so some terms of Eq. (29) which are series expansion of this equation can be truncated, thereby optimizing the CPU time.

To determine the valid regions of the two equations we have computed and plotted various contour graphs of the percent relative amplitude errors between them and Eq. (6). A first heuristic choice is to fix a maximum permissible relative amplitude error of 1%. Fig. 2 (a) shows the 1% relative amplitude error contours for Eqs. (8) and (9). From Fig. 2(a) we can deduce that except for very small portions (shaded), at least one of the Eqs. (8) or (9) can be used in the computation of Eq. (6) for any particular array configuration. Increasing the maximum permissible error to 1.26% gives the contour plot in Fig. 2(b) which shows that at least one of the equations can be used to compute Eq. (6) with maximum error of 1.26% for the entire region.

4) Combined Formula: For this condition we have fitted a linear relationship between x and y as:

$$s(x, y) = x - 0.216831y - 0.0533064, \quad (16)$$

where Eqs. (8) and (9) are evaluated based on the conditions

$$E_y(x) \approx \begin{cases} 2f(x, y) & s(x, y) \geq 0 \text{ Eq. 8} \\ 2f(x, y) + 2g(x, y) & s(x, y) < 0 \text{ Eq. 9.} \end{cases} \quad (17)$$

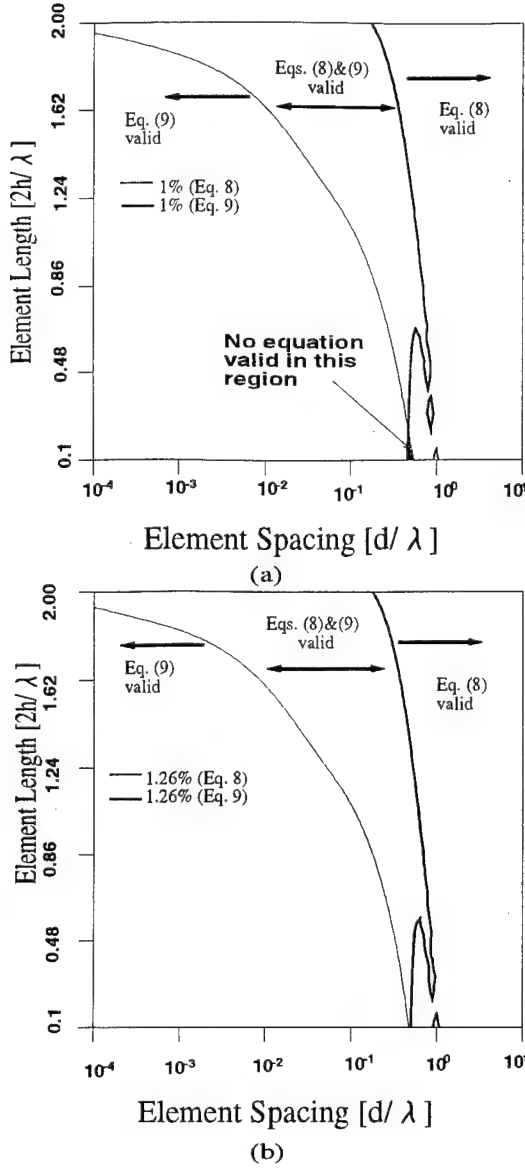


Figure 2: Contour plots of relative error in amplitude (a) 1%, (b) 1.26%, with valid formulas for each region indicated.

Further more detailed analysis shows that the following relations can be used to truncate unnecessary terms (Eq. 15) of Eq. (29) in the evaluation of Eq. (17):

$$\begin{aligned}
 s_1(x, y) &= 4.4612y - x - 0.2458 \\
 s_2(x, y) &= 0.57312y - x + 0.811 \\
 s_3(x, y) &= 0.11y - x + 0.33 \\
 s_4(x, y) &= 32.475y - x - 3.4895.
 \end{aligned} \quad (18)$$

Table 1: Conditions for detail evaluation of Eq. (17).

Solution of Eq. (6) with	Terms of Eq. (29) Required	Relation Between x and y
Eq. (8)	21	$s_1(x, y) < 0$
Eq. (8)	15	$s_1(x, y) \geq 0,$ $s_2(x, y) < 0$
Eq. (8)	9	$s_3(x, y) < 0$
Eq. (8)	5	$s_3(x, y) \geq 0$
Eq. (9)	9	$s_4(x, y) \leq 0$
Eq. (9)	5	$s_4(x, y) > 0$

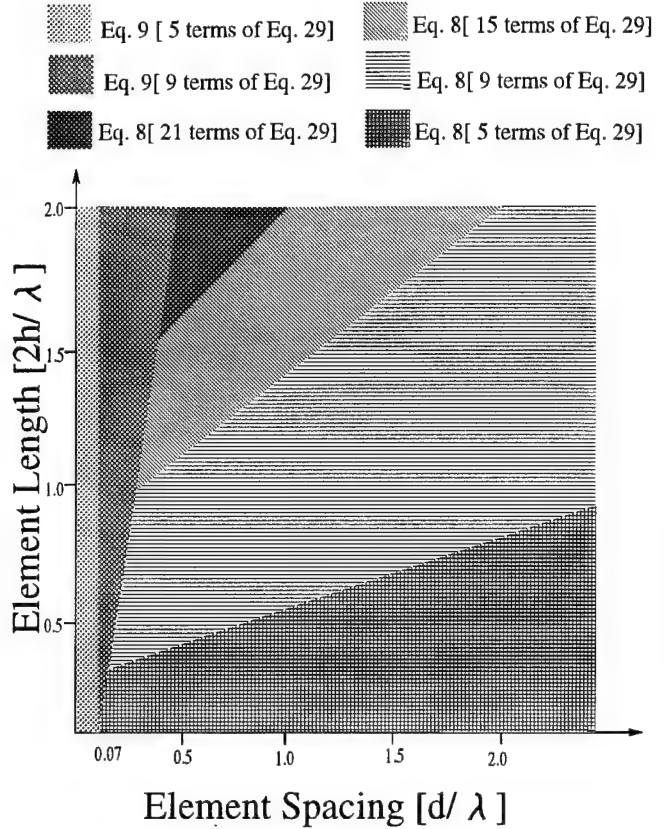


Figure 3: Demarcated regions.

Using the relations defined in Eq. (18) the following conditions in Table 1 are used for detailed evaluation of the closed-formed function defined in Eq. (17).

By way of explaining the rationale behind Table 1, the accurate evaluation of Eqs. 8 and 9 depends on the number of terms (defined by Eq. 15) of Eq. 29 used. Now for certain array configurations, some terms of Eq. 29 can be ignored since they are negligibly small but their very inclusion could only serve

to increase the CPU time without improving on the numerical accuracy. The truncation of such terms using the relations in the term column of the Table 1 has been shown to improve considerably the computational efficiency of the algorithm.

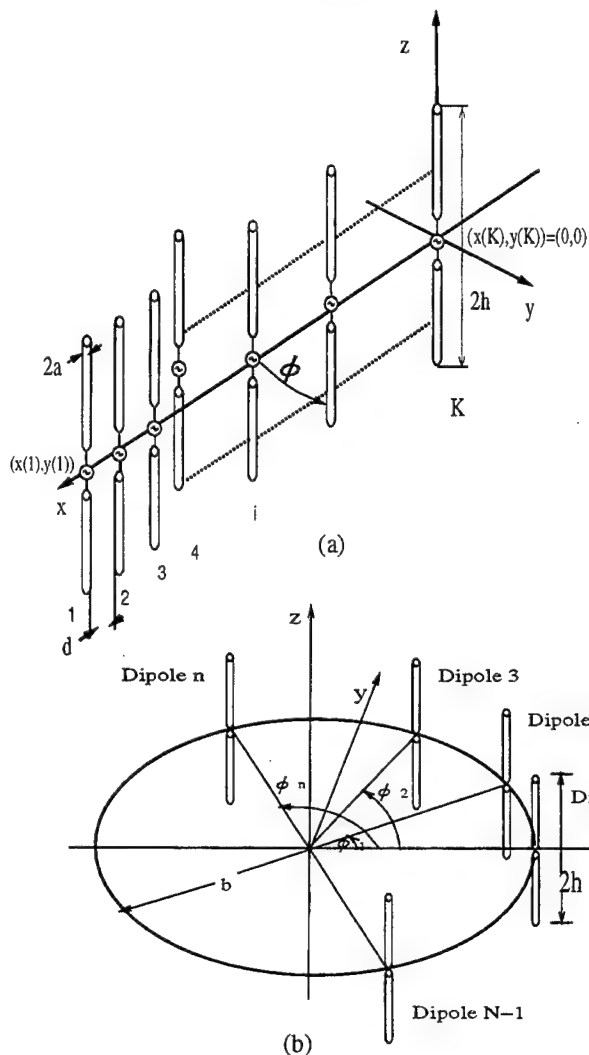


Figure 4: (a) Linear and (b) circular array systems.

The relations in Table 1 have been used to draw an approximate and more graphic demarcation for each function as shown in Fig. 3. These relations are then easily used as a closed-form replacement of Eq. 6. The valid region of Eq. 17 falls within the practical range of linear array systems.

V. Case Study Using Modified Algorithm

In this section we validate the new ICT algorithm by considering the analysis of various co-planar dipole

arrays including tightly-coupled systems like Yagi-Uda array antennas. The results are compared with those of the conventional ICT method and MoM.

The computational times and storage required by these methods are also compared to demonstrate the efficiency of the new ICT implementation. The ICT algorithm using the closed-form formula (Eq. 17) is designated as MICT.

A. Linear and Circular Arrays of Equal Lengths and Spacing

Analysis of typical linear and circular array systems of the form shown in Fig. 4 have been carried using ICT and MICT. The results are compared with analysis of a similar system by Thiele et al. [14]. The MoM procedure in this paper is based on seven current expansions a piecewise sinusoidal *Garlekin method*. These number of expansion functions have been found adequate in accuracy compared to the two ICT methods.

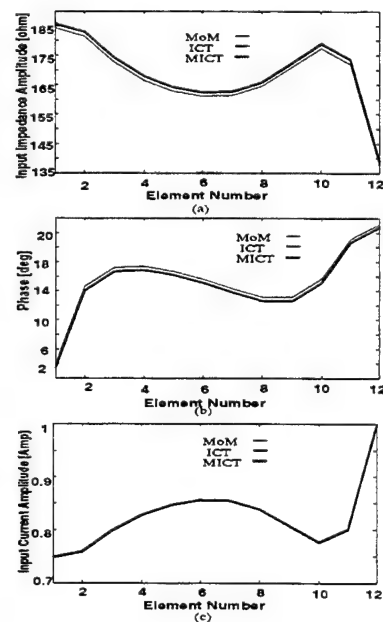


Figure 5: Twelve Element Linear Array (a) Impedance, (b) phase of impedance, and (c) current.

Following [14], we consider a typical linear array made of 12 elements each of equal length, radius and inter-element spacing of $\lambda/2$, 0.0001λ and $\lambda/2$ respectively. Each element in the array is considered to be supplied from co-phasal sources of uniform amplitude and with a series resistance of 72Ω . For this end-fire linear array, the main beam maximum is pointed at $\phi = 45^\circ$ as shown in Fig. 4(a) [14]. Fig. 5 shows the results of an analysis with the different methods.

The circular array we consider is similar to the linear system described above except that the main beam direction is now pointed at $\phi = 0^\circ$ shown in Fig. 4(b). The results of the three methods are given in Fig. 6. Fig. 7 shows the far-field patterns of linear and circular arrays described above. It is clear from these results that the three methods are very much in agreement, especially in the computation of the far-field radiation patterns.

In particular the results of the two ICT methods are so close that we can not easily distinguish between them, thus validating the accuracy of the closed-form formula.

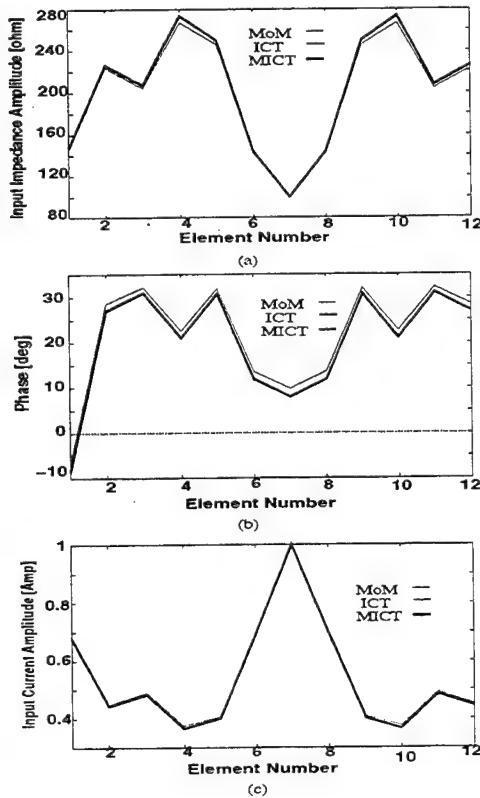


Figure 6: Twelve Element Circular Array (a) Impedance, (b) phase of impedance, and (c) current.

B. Analysis of Yagi-Uda Arrays

Using the generalized impedance formulas defined in Eqs. 19-20 and the new closed-form formula (Eq. 17), we have analyzed various Yagi-Uda Arrays of a typical form shown in Fig. 8.

The characteristic of a particular case of a six element Yagi-Uda Array ($L_R = 0.482\lambda$, $L = 0.456\lambda$, $L_D = 0.437\lambda$) of equal inter-element spacing of (0.2λ) and equal radii of 0.0025λ are shown in Table 2 for the different methods. Here L_R , L and L_D are the

lengths of reflector, driver and directors respectively. The results of a similar structure in [14] also based on MoM are shown. The MoM used in this paper is based on [15] with 126 pulse expansion functions used to achieve the input impedance formulas as the other methods. All results are in reasonable agreement.

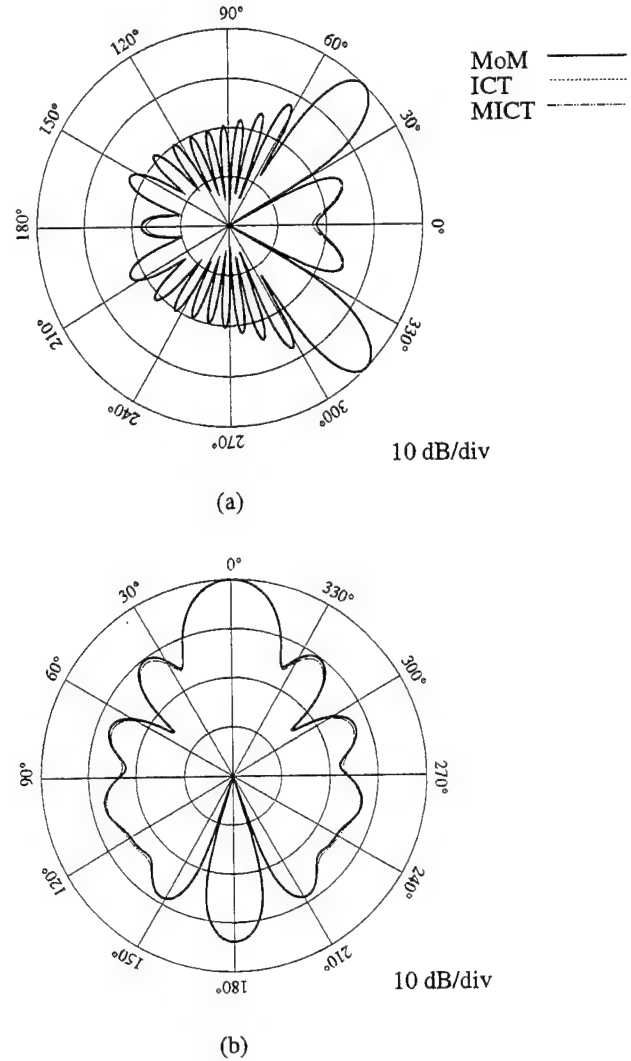


Figure 7: Patterns of 12 Element (a) linear with main beam direction steered to $\phi = 45^\circ$, (b) circular array.

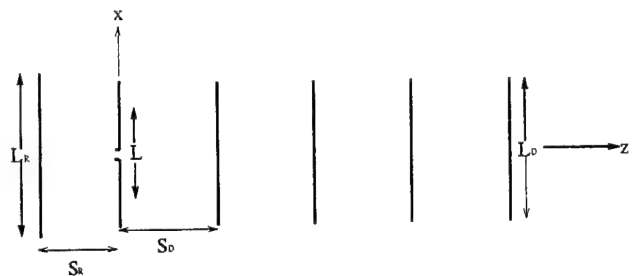


Figure 8: Configuration of a general Yagi-Uda Array.

Table 2: Characteristics of Equally Space Yagi-Uda Array.

Method	Gain [dB]	Input
		Impedance [Ω]
MoM [14]	11.2	$51.3 - j1.9$
MoM[15]	11.23	$50.6 - j4.03$
ICT	11.25	$50.3 - j2.48$
MICT	11.25	$50.3 - j2.54$

Table 3: Characteristics of a Yagi-Uda Array for TV Channel 15 operation.

Method	Gain [dB]	Input
		Impedance [Ω]
MoM [14]	11.50	$59.50 + j47.50$
MoM[15]	11.54	$59.45 + j44.61$
ICT	11.53	$59.26 + j43.70$
MICT	11.52	$59.17 + j43.50$

The characteristics and H-plane radiation pattern of a six element Yagi-Uda with the following geometry: $L_R = 0.5\lambda$, $L = 0.47\lambda$, $L_D = 0.43\lambda$, $S_R = 0.25\lambda$, $S_D = 0.30\lambda$ are shown in Table 3 and Fig. 9 respectively. Each element is of radius 0.0026λ . This configurations is a typical Yagi-Uda antenna for operation of midband frequency for Channel 15 [14]. Again, all the methods are in close agreement.

C. CPU Time and Computer Storage

Since the conventional workstation is time sharing by nature with variable loading not easily controllable by a particular user, it is quite difficult to establish similar conditions in order to accurately determine the CPU time requirements of each method described in the previous section. It has therefore be found more convenient to use an NEC PC-9801VX personal computer to carry out the CPU time statistics analysis.

1) *CPU Time of Numerical and Closed-form Formulas:* The CPU time required in the evaluation using the closed-form and numerical integration is first carried out. To ensure that we cover each sub-region of the closed-form formula according to the conditions defined in Table 1 we did the evaluation with 101×101 points in the intervals $0.1 \leq 2h/\lambda \leq 2$ and $10^{-4} \leq d/\lambda \leq 10$. The results are shown in the Barchart of Fig. 10.

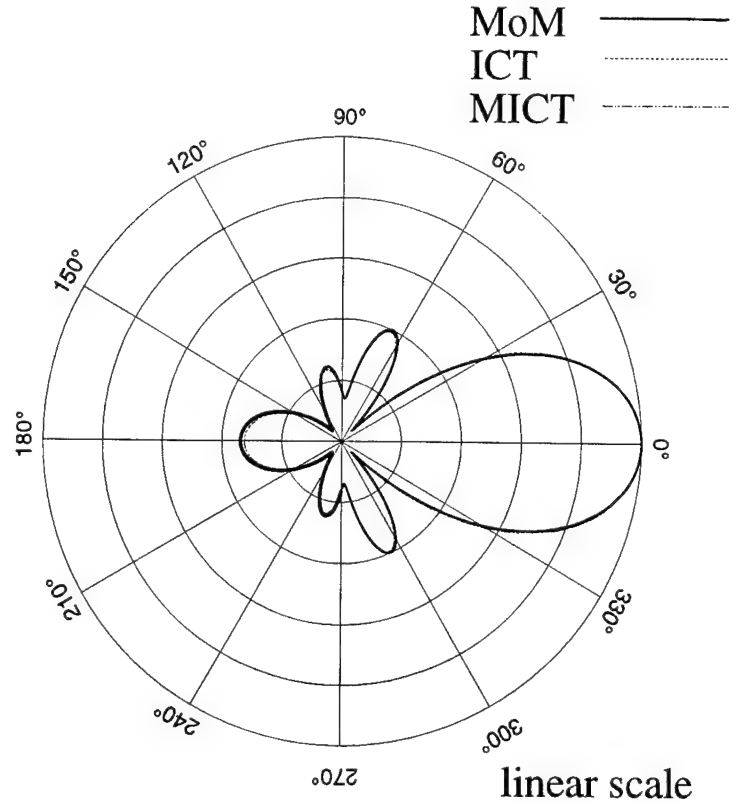


Figure 9: H-plane pattern of Six-element Yagi-Uda array for TV Channel 15 [14].

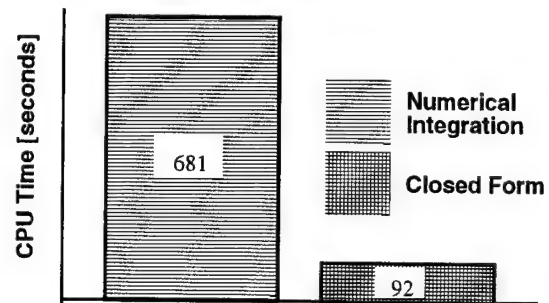


Figure 10: Closed form and numerical integration CPU times.

It is clear from the results that the closed-form formula is capable of reproducing Eq. (6) accurately and at one seventh the CPU time on the average. For configurations requiring a lesser number of terms, as shown in Fig. 3, the CPU time could be shorter.

Using the same personal computer as before the end-fire linear array described in Section IV.A has been analyzed using the two ICT and MoM algorithms. The results are shown in the Barchart in

Fig. 11. The advantage of the ICT and MICT methods in CPU time required to analyze wire antennas is clearly demonstrated here.

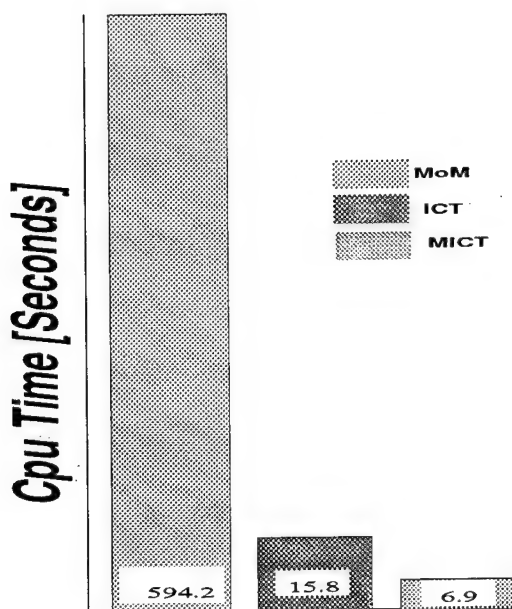


Figure 11: CPU time Statistics of 12 element linear Array analyzed with two ICT and MoM algorithms.

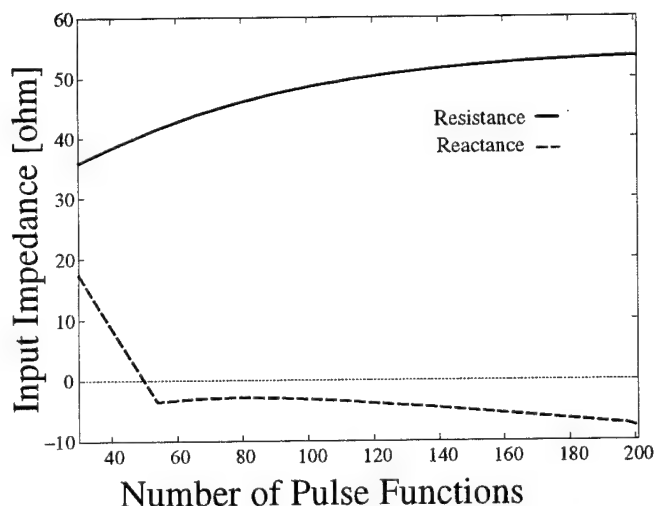


Figure 12: Curve showing convergence of input impedance as the number of pulse expansion functions with point matching is increased for six Element Yagi-Uda antenna.

2) *Computer Storage Limitation* : The moment method used for the Yagi-Uda Array is based on

[15] and required about 126 pulse functions to achieve accurate impedance results comparable to the other methods. This required considerable storage and we are therefore not surprised that the computation can not be easily carried out on both NEC PC-9801VX and NEC PC-9801DA personal computers without storage problems.

On Sun Workstation (Sparcstation 10), the rough¹ computational times were 36 seconds for the MoM scheme, 47 milliseconds for ICT and 20 milliseconds for MICT.

Of course the relatively large computational requirement and storage of the MoM can be explained in this case by the fact that though the array is actually a discontinuous structure in configuration, the evaluation has been carried out as if the array elements were connected together and formed a continuous structure. Piecewise pulse functions are then used to express closed-form the formula for the impedance matrix. But this requires us to use a large number of expansion functions to achieve reasonably accurate results. This leads to large matrix to be inverted. Figure 12 shows convergence curves for the input impedance for a six Element Yagi-Uda antenna. The largest matrix to be inverted by the ICT method is $2N \times 2N$ where N is the number of elements in the array.

In MICT all formulas are expressed in closed-form, making it very efficient in terms of CPU time. The usefulness of MICT as an efficient CAD/CAE tool as described in Section III is clearly demonstrated.

VI. Conclusion

We have for the first time in English text presented the Improved Circuit Theory generalized input impedance formulas which can be useful in the analysis of multielement dipole antennas with arbitrary configurations. By deriving a new and closed-form formula which is valid for practical range of most multielement antenna systems to avoid time intensive numerical integration, it has been possible to reduce more than half the CPU time required to analyze multielement antennas using the ICT method. It has also been demonstrated that the ICT method offers a much faster method of analyzing multielement antennas compared with the conventional method of moment. This faster ICT implementation scheme further enhances the method as a useful CAD/CAE tool.

¹Workstation was shared by other users during computation and so same conditions could not be guaranteed for each method unlike a PC which can ensure this.

However, the conventional ICT two current functions defined in Eq. 2 has been found to be inadequate for co-planar dipole element lengths greater than 1.85λ [16]. Even though this covers a large range of practical antennas, applications to much longer dipole antennas (e.g. large log-periodic dipole arrays required for wide bandwidth applications [17]) would necessitate the use of more appropriate trial function. A choice of better trial functions for expanded application of ICT is currently under study [16].

VII. Appendix

A. Generalized Impedance for Non-uniform Array Configurations

If the configurations of a multielement-element system are non-uniform, (the sizes, length and inter-element spacing vary), then the generalized impedance of the system is given as [8,18]

$$Z_{nm}^{11} = \frac{j}{4\pi} \sqrt{\frac{\mu_0}{\epsilon_0}} [-C^+ \sin \theta^+ - C^- \sin \theta^- + S^+ \cos \theta^+ + S^- \cos \theta^-] \quad (19)$$

$$Z_{nm}^{12} = Z_{mn}^{21} = \frac{j}{4\pi} \sqrt{\frac{\mu_0}{\epsilon_0}} [C^+ \cos \theta^+ - C^- \cos \theta^- + S^+ \sin \theta^+ - S^- \sin \theta^- - 2E_{kd}(\theta_m) \cos \theta_n + E_{kd}(\theta^+) - E_{kd}(\theta^-)] \quad (20)$$

$$Z_{nm}^{22} = \frac{j}{4\pi} \sqrt{\frac{\mu_0}{\epsilon_0}} [C^+ \sin \theta^+ - C^- \sin \theta^- - S^+ \cos \theta^+ + S^- \cos \theta^- - 2E_{kd}(\theta_n) \sin \theta_m - 2E_{kd}(\theta_m) \sin \theta_n + \theta^+ E_{kd}(\theta^+) - \theta^- E_{kd}(\theta^-) - j2 \exp \left\{ -j\sqrt{(kd)^2 + (\theta^+)^2} \right\} + j2 \exp \left\{ -j\sqrt{(kd)^2 + (\theta^-)^2} \right\}] \quad (21)$$

where

$$d = \begin{cases} a & n = m \\ d_{nm} & (n \neq m) \end{cases} \quad (22)$$

d_{nm} is the inter-spacing between elements n and m in the array

$$\theta^\pm = \theta_n \pm \theta_m, \quad \theta_n = kh_n, \quad \theta_m = kh_m \quad (23)$$

$$\begin{aligned} C^\pm &= C_{kd}(\theta_n) \pm C_{kd}(\theta_m) - C_{kd}(\theta^\pm) \\ S^\pm &= S_{kd}(\theta_n) + S_{kd}(\theta_m) - S_{kd}(\theta^\pm) \end{aligned} \quad (24)$$

$$\begin{aligned} C_y(x) &= E_i \left\{ -j \left(\sqrt{x^2 + y^2} + x \right) \right\} \\ &- E_i \left\{ -j \left(\sqrt{x^2 + y^2} - x \right) \right\} \end{aligned} \quad (25)$$

$$\begin{aligned} S_y(x) &= jE_i \left\{ -j \left(\sqrt{x^2 + y^2} + x \right) \right\} \\ &- jE_i \left\{ -j \left(\sqrt{x^2 + y^2} - x \right) \right\} \\ &- j2E_i(-jy) \end{aligned} \quad (26)$$

$$E_y(x) = 2 \int_0^x \frac{\exp(-j\sqrt{t^2 + y^2})}{\sqrt{t^2 + y^2}} dt \quad (27)$$

$$E_i(-jt) = - \int_t^\infty \frac{\exp(-js)}{s} ds \quad (28)$$

B. Details of $f(x, y)$

The function $f(x, y)$ is simplified from the Mathematica [13] integration as

$$\begin{aligned} f(x, y) &= b - j\frac{y}{6}b^3 - y \left[\frac{j + 3y}{120} \right] b^5 \\ &+ y \left[\frac{-j - 15y + j15y^2}{5040} \right] b^7 \\ &+ y \left[\frac{-j - 63y + 210jy^2 + 105y^3}{362880} \right] b^9 \\ &+ 10^5 \delta [-6 + j50 + 80y^2 + 23.7y^3] b^{11} \\ &+ 10^5 \delta y [j3 + 10.6y - 8.35y^2 - 1.67y^3] b^{13} \\ &+ 10^4 \delta y [j1.5 + 9.2y - j14.47y^2 - 7.234y^3 \\ &+ j1.0334y^4] b^{15} + 100\delta y [j5 + 58y - 163.4y^2 \\ &- 154.3y^3 + j53.2y^4 + 5.7y^5] b^{17} \\ &+ 10\delta y^2 [30 - j135y - 215y^2 + j135y^3 \\ &+ 34y^4 - j2.83y^5] b^{19} + \delta y^4 [-200 \\ &+ j200y + 100y^2 - j20y^3 - 1.3y^4] b^{21} \end{aligned} \quad (29)$$

where

$$b = \ln \frac{x + \sqrt{x^2 + y^2}}{y} \quad \text{and} \quad \delta = 10^{-11}y^2. \quad (30)$$

C. Details of $g(x, y)$

The function $g(x, y)$ is simplified from the Mathematica [13] integration as

$$\begin{aligned} g(x, y) = & -j10^{-2}y[20.710678 - j1.0723305y \\ & - 1.2944174]e^{-jv} \\ & - j10^{-2}[j6.25 - 50y^{-2} + 3.125]y^4u^{-2} \\ & - \left[E_i(v) - E_i\left(\frac{u}{2}\right) \right] \left(1 - \frac{y^2}{8} \right)^2. \quad (31) \end{aligned}$$

Here $v = -j1.207107y$, $u = -j(x + \sqrt{x^2 + y^2})$ and $E_i(z)$ is as defined in Eq. (28).

References

- [1] N. Inagaki, "An Improved Circuit Theory of Multielement Antenna", *IEEE Transactions On Antennas and Propagation*, Vol. Ap-17, No. 2, pp. 120-124, March 1969.
- [2] Editor: R. Mittra, "Topics in Applied Physics Volume 3 Numerical Techniques in Electromagnetics", Springer-Verlag Berlin Heidelberg New York 1975, pp. 17-18.
- [3] S. A. Schelkunoff, "Advanced Antenna Theory", New John Wiley & Sons Inc., 1952, pp. 136-138.
- [4] R. W. P. King, "The Theory of Linear Antennas", Cambridge, Mass.: Harvard University Press, 1956, p. 39.
- [5] N. Inagaki, T. Sekiguchi and K. Nagai, "Exact Design of an Array of Dipole Antennas Giving the Prescribed Radiation Patterns", *IEEE Transactions On Antennas and Propagation*, Vol. Ap-19, No. 1, pp. 128-129, January 1971.
- [6] A. Oyama, H. Ôyama, K. Katayama "Expression of Radiation Characteristics of Yagi-Uda Antenna with Vector Diagram", *The Transactions of the Institute of Electronics and Communication Engineers of Japan*, Vol. 56-B No. 5 pp. 205-206, May 1973.
- [7] A. Oyama, H. Ohyama, K. Katayama "Design of Multi-element Yagi-Uda Antennas with Required Gain", *The Transactions of the Institute of Electronics and Communication Engineers of Japan*, Vol. 57-B No. 6 pp. 337-344, June 1974.
- [8] Editors: S. Gentie, K. Haruo, "Antenna Theory and its Applications", Mimatsu Data Systems, Tokyo 1991, pp. 98-107.
- [9] W. Chujo, M. Fujise, S. Sogawa, N. Yamauchi, "Wire Antenna Design CAE System", *Technical Report of The Institute of Electronics, Information and Communication Engineers*, A-P92-122~134, Vol. 92, No. 414, pp. 81-88, January, 1993.
- [10] N. Inagaki, "A Method of Estimating the Frequency Dependence of an Antenna Radiation Impedance", *Trans. of Institute of Electronics and Communication Engineers* Vol. 50, No. 5, pp. 47-53, May 1967.
- [11] A. I. Imoro, N. Inagaki, N. Kikuma and S. Yano, "A Faster Improved Circuit Theory Algorithm" *Technical Report of The Institute of Electronics, Information and Communication Engineers*, A-P93-103 (1993-12), pp. 23-30, December 1993.
- [12] A. I. Imoro, N. Inagaki, N. Kikuma, "A Faster Improved Circuit Theory Algorithm" *IEEE Antenna and Propagation International Symposium*, Seattle, Washington, USA Vol. 3, pp. 780-782, June 1994.
- [13] S. Wolfram, "Mathematica A System for Doing Mathematics by Computer", Addison-Wesley Publishing Company, Inc., The Advanced Book Program, 2^{ed} Edition, 1991, pp. 672-679.
- [14] Warren L. Stutzman, Gary A. Thiele, "Antenna Theory and Design", John Willy & Sons, New York 1981, pp. 220-228, pp. 349-354, pp. 582-591.
- [15] R. F. Harrington, "Field Computation by Moment Methods", IEEE Press, New York 1993, pp. 62-68.
- [16] A. I. Imoro, Y. Kani, N. Inagaki, N. Kikuma, "Application of Tai's Trial Function in an Improved Circuit Theory Two-Term Representation", To be presented at ISAP, Chiba, Japan, 24-27 September 1996.
- [17] J. D. Kraus: et al.: "Antennas", McGraw-Hill, Inc, 1988 pp. 708-710.
- [18] Editor: Y. Mushiake, "Antenna Engineering Handbook" Ohmu-sha, Tokyo 1989, pp. 522-523.

An Algorithm for Solution of the Inverse Electromagnetic Liquid Metal Confinement Problem

G.J. BENDZSAK

Department of Metallurgy and Materials Science
University of Toronto, Toronto, Ontario

Abstract

The design of an electromagnetic levitation system for large amounts of liquid metal requires the solution of an inverse field problem. The objective is to calculate the electromagnetic pressure distribution which corresponds to a specified metallo-static head. This paper describes an algorithm for the design of coil systems which will produce the desired pressure distribution. The technique is illustrated by the design of a torroidal levitation system.

Keywords: electromagnetic confinement, liquid metals, pressure distribution, design methodology, algorithm.

1 Introduction

Defects found during the manufacture of equipment which require ultra-pure and/or highly reactive metals may be traced to contamination that occurred during their processing in the liquid state. Sources of the contaminants, in turn, can be often attributed to the vessels for the liquid materials. Thus, elimination of contact between the metal and its container would be highly advantageous and represents a goal that could be achieved by induction levitation.

In general, present-day electromagnetic levitation techniques of liquid metals are restricted to small amounts, typically in the order of few grams [1]. This can be attributed to the use of confinement systems which have inherent field singularities. That is, somewhere on the surface of the molten mass there is a

zero, or negligible, amount of electromagnetic pressure to counter balance the metallo-static head. Consequently, at some location, which often coincides with the requirement of highest pressure, only the weak forces of surface tension are available for the support of molten material. This places serious limitation on the weight which can be levitated in a stable manner. As a result the technique is more or less confined to metallurgical research laboratories, and practical industrial applications which require the suspension of significant amounts of metal have not received sustained attention to date.

It has been demonstrated, both theoretically and experimentally, that multiple frequency excitation system can confine large amounts of liquid metal [2]. The physical realization of such a system requires the solution of a difficult inverse electromagnetic problem which can be stated as:

For a given geometry, what are the exact locations and magnitudes of excitation current sources which will generate a prescribed pressure distribution?

To the best knowledge of the author, a unique solution to this problem is not guaranteed since a number of alternate excitation systems can produce identical final results. Design of a practical system is beset by a confusing array of alternatives which are difficult both to realize and evaluate in a systematic manner. Consequently, the main goal of this paper is the development of a design technique which determines the locations of the individual turns within a coil.

A solution to the magnetic problem is an integral part of

the algorithm, for which one of a number of alternate methods may be employed. One of these is the finite element method of Reference [3]. The purpose of this paper is to present a simple technique based on both easily identified physical parameters and clear cut design objectives. The approach takes into account limitations imposed by concerns such as the thermal cooling and physical protection of the coils. At the same time it specifies, a priori, a maximum value for the magnitude for the deviation for the confined shape from that specified. By relating the error to various spatial harmonics it is expressed in a physically meaningful manner. The present technique combines an analytical approximation for the high frequency magnetic field with a linear optimization method which drives the solution towards the appropriate displacements of the coil windings. The resulting solution for the shape of a freely levitated body is expected to be robust since the effect of surface tension is considered to be negligible. In this case, both bulk confinement and surface stability will be realized through electromagnetic forces. Any additional effect due to surface tension will further aid confinement.

2 Design criteria for shape compliant electromagnetic pressure fields

Principles for stable electromagnetic levitation of large amounts of molten metal have been investigated and successfully implemented [2]. Its basic features can be summarized as:

- a) the provision of a magnetic field which creates a metallo-static pressure distribution in conformity with the shape of the desired body,
- b) the assurance of bulk stability for the liquid mass, such that it is prevented from falling apart due to the appearance of disturbances,
- c) the automatic maintenance of surface stability which otherwise would lead to the eventual leakage of material and the destruction of confinement.

Implementation of these criteria lead to the design of multi-frequency confinement systems which both

eliminate the presence of singularities in the pressure field and ensure surface stability. The removal of singularities is achieved by the superposition of pressures created by independent electromagnetic fields. These are produced by currents having different frequencies in a number of excitation coils. Surface stability is ensured by the mutual orthogonality of the fields [4].

3 Design considerations

Electromagnetic body forces produced by an interaction between the magnetic field and the current in a conducting medium are given by:

$$\bar{F} = \frac{1}{2} \operatorname{Re} (\bar{J}^* \times \bar{B}) \quad (1)$$

where: F is the body force (N/m^3), J^* is the complex conjugate of the current density (A/m^2), and B is the flux density (Wb/m^2). When a conducting body is placed in an alternating magnetic field, confinement forces are produced by the tangential component of the flux density B_t , and the induced current \bar{J}_t . The normal component of the flux, B_n , and \bar{J}_t produces a tangential force along the free surface of the body.

The principle objective of a design procedure is to match the magnitude of electromagnetic pressure with the prevailing metallo-static head everywhere on the surface. The tangential forces cause the liquid to recirculate within the body. When these flows are turbulent, waves are produced on the surface to reduce the overall stability of the confinement system [5]. Consequently, it is highly desirable to eliminate, or at least minimize, the magnitudes of B_n . This can be achieved by using high excitation frequencies which confine the magnetic flux within thin boundary layers immediately below the free surface.

Liquid metal processing is associated with high magnitudes of heat flux, and it is necessary to protect water cooled excitation coils against thermal damage. While the actual thickness of the thermal insulation depends upon the characteristics of the metal, practices of the induction heating industry can be used as guidelines for design. The accommodation of insulation

introduces substantial gaps between the coils and the load which can seriously limit the magnitudes of magnetic flux. Hence, their thickness must be controlled to a bare minimum needed for coil integrity. With these considerations in mind, a general design approach for the shapes and locations of excitation coil is now investigated.

4 Solution of the inverse field problem

The required confinement field for a given geometry is determined by the variation of the metallo-static head. The final result of the analysis is known from the start, and the design task is reduced to determination of coil geometries and appropriate excitation current magnitudes. In this section, a solution to the inverse problem is described in the form of a series of design steps which are illustrated through the design of a levitation coil for an aluminium torus.

Step 1 Preliminaries

A confinement scheme for the desired shape and weight is first proposed. At this stage, it is necessary only to ensure qualitatively that all points on the free surface have tangential magnetic components. Should a single coil be inadequate to generate such a field, a multiple coil excitation system must be considered. The frequency of each coil current is different, hence the overall pressure distribution is the sum at the pressures contributed by each individual field.

Example: Consider the levitation of a toroidal aluminium ring of Figure 1, with the attributes specified in Table I.

PROPERTY	QUANTITY
Torus Diameter	200 mm
Ring Diameter	20 mm
Density	2700 kg/m ³
Torus Weight	0.533 kg

Table I Object geometry and weight

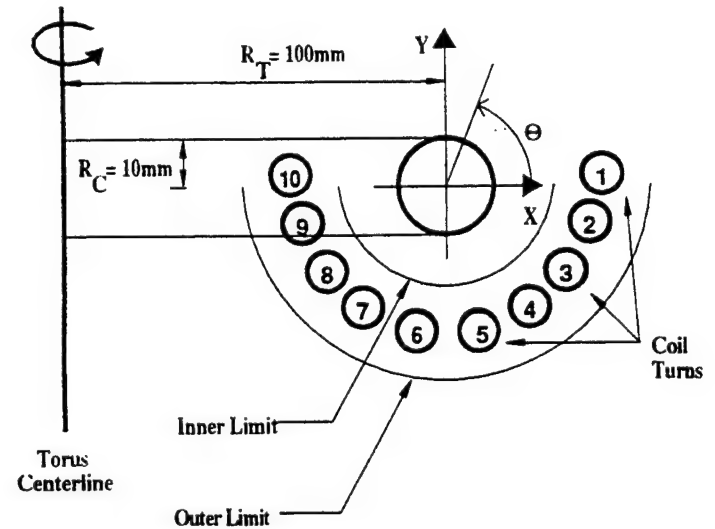


Figure 1 Relationships between load, coil geometry and limits

Since the torus has two planes of symmetry the design of the coil system is simplified, and the problem becomes two dimensional. When a high frequency current carrying single turn is wound parallel to the ring, a magnetic field is produced which has a tangential component everywhere on the surface. A coil, consisting of a set of turns placed at locations as yet to be defined, can be used to produce a pressure distribution that meets the requirements for levitation. Such a coil, shown in Figure 1, is initially assumed to have 20° spacing between its turns. It is now assumed that this estimate for coil design will result in a reasonable pressure field which can be improved upon by an iterative process. The purpose of this paper is to develop an algorithm that realizes the design objective for the generation of a compliant pressure field.

Step 2 Inner limit for coil locations

When the estimate for the numbers and shapes of the initial coils is completed, it is necessary to establish the minimum separation distances between these coils and the liquid metal. A first order analysis of the cooling requirement for the levitating coils will provide a guideline for minimum safe clearances. This establishes an inner limit for the location of the coils (See Figure 1).

Example: Since the temperature of a typical aluminium alloy melt is generally below 700 °C thermal insulation of the coils becomes an easy task. The magnitude of the heat flux at the coils can be estimated by the equality between the radiated heat flux from the ring and that conducted through the insulating refractory:

$$Q_r = \sigma \epsilon (T_s^4 - T_i^4) \quad (2)$$

$$Q_c = k \frac{T_i - T_o}{\Delta X} \quad (3)$$

where: Q_r =radiated heat flux (W/m^2), σ = Boltzman's constant, ϵ =emissivity of Al, T_s =Al temperature (K), T_i =insulator temperature facing the hot metal (K), T_o =coil temperature (K), k =thermal conductivity of the insulation (W/mK), ΔX = thickness of the insulation (m). For a 10 mm thick insulation, the substitution of typical values given in Table II, results in approximate values for the inside temperature $T_i=350$ °C and a heat flux $Q_c=6000$ W/m^2 . These values present no difficulty for water cooled coils.

PROPERTY	VALUE
Insulation thickness(ΔX)	10 mm
Thermal conductivity (k)	0.2 W/mK
Al temperature (T_s)	1000 K
Coil temperature (T_o)	300 K

Table II Approximate thermal parameters

A further allowance of 10 mm between the refractory and the ring is sufficient clearance for the disturbances caused by possible instabilities. Thus, the minimum inner limit is placed at 20 mm with respect to the surface of the ring.

Step 3 Outer limit for coil locations

The magnitude of magnetic flux decreases rapidly from a coil and in order to realize the required magnitude at the surface of the object, coil currents are in the order of several hundreds of amperes. This consideration leads to an outer limit for the location of the coils. In order not to exceed reasonable limits for power supply ratings, an outer limit for coil locations is in the vicinity of the

inner (see Figure 1). The coils are placed between these two limits at arbitrary locations with assumed values for respective currents. As the solution of the inverse problem proceeds, the distance between the limits decreases to the overall width of the coils and defines their final positions.

Example: The individual turns of the coil, at the end of the design, will not be at uniform distances from the ring. Thus, the outer limit must be set far enough to allow sufficient space for their movements as the algorithm seeks the minimum error in pressure distribution around the ring. The initial arbitrary location for the outer limit is set at a distance of 60 mm from the surface. The turns of the coil are initially distributed uniformly along a 50 mm radius arc, centred on the torroidal ring of Figure 1.

Step 4 Target pressure distribution

The shape of the levitated object determines the target pressure distribution. The required pressure is determined by the density of the load and the depth of the metallo-static head at every point on the surface. This is the target distribution which *must be satisfied* by the final summation of all pressure distributions created by the magnetic fields.

Example: The metallo-static pressure distribution for the torroidal ring geometry is given by the simple relationship:

$$P = \frac{1}{2} P_o (1 - \sin \theta) \quad (4)$$

where: $P_o=2\rho gR_C$ (N/m^2), R_C is the radius of the ring (m), θ (rad) is an angle measured counter clockwise and subtended from the centre of the ring. For the present case, $P_o=529$ N/m^2 .

Step 5 Magnetic field produced by a single turn

The magnetic field produced by each turn within each coil is calculated either analytically or numerically depending on the configuration. Since high excitation frequencies are used, the depths of field penetrations are small in comparison with load dimensions. Consequently, a perfect conductor is a reasonable

assumption for the load. This allows the solution of a

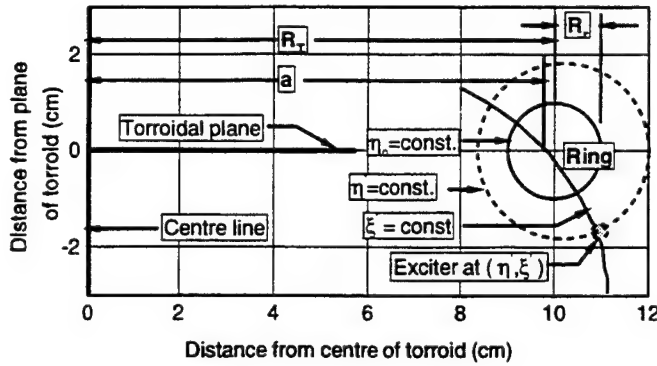


Figure 2 Definition of the toroidal coordinate system

DC magnetic field to represent the eddy current problem. The magnetic vector potential on the surface of the object becomes an arbitrary constant whose value set to zero. The normal component of the field does not penetrate, and only the tangential vector component exists on surface. The strength of the current sheet on the ring surface provides an estimate for the magnitude of the induced load current.

Example: The tangential component of the magnetic field due to a current carrying loop located parallel to the ring is given by [6]:

$$B_{\zeta ij} = \frac{\mu_o I_j \sinh \eta' (\cosh \eta_o - \cos \zeta)^{3/2}}{\pi a \sinh \eta_o (\cosh \eta' - \cos \zeta')^{1/2}} \cdot \sum_{n=0}^{\infty} \frac{P_{n-1/2}^1(\cosh \eta')}{(1 + \delta_{0n}) P_{n-1/2}^1(\cosh \eta_o)} \quad (5)$$

where: $B_{\zeta ij}$ is the magnetic flux density produced by the j -th turn of the i -th coil, I_j is the rms value of the current in the j -th turn, R_T is the radius of the torus, ζ' and η' are the toroidal coordinates of the loop, η_o and ζ are the toroidal coordinates for a point on the surface of the ring (see Figure 2), $P_{n-1/2}^1$ is the toroidal ring function [7]. Definition of the toroidal coordinates are shown in Figure 2, and the following relationships hold

amongst the geometrical variables [8]:

$$a = \sqrt{R_T^2 - R_r^2} \quad (6a)$$

$$\cosh \eta_o = R_T/R_r \quad (6b)$$

Step 6 The total magnetic pressure

The magnetic field due to one coil is the sum produced by its individual turns. Since the coil frequencies are different, the fields become completely independent of each other. Under these conditions, the total magnetic pressure P_{mag} is given by:

$$P_{mag} = \sum_{i=1}^{N_c} \frac{1}{2\mu_o} \left(\sum_{j=1}^{n_i} B_{\zeta ij} \right)^2 \quad (7)$$

where: N_c = number of coils, n_j = number of turns in the j -th coil.

Example: A ten turn coil has been selected for levitating the toroidal ring. For a given spatial distribution, between the inner and outer limits, their field contributions were determined by evaluating Eqn. 5 on the surface corresponding to the toroidal coordinate η_o (see figure 2). The total pressure distribution is determined by Eqn. 7.

Step 7 Error criterion

The Fourier series representations of the target and electromagnetic pressure distributions allows the formulation of a physically meaningful error criterion. This approach identifies clearly the total lifting force as the DC term of the series, while higher order terms can be related to the shape of the object. The differences between the two pressure series indicate the required adjustments in:

- the magnitudes of the excitation currents through the DC components,
- the locations of the of the current loops through the spatial harmonic terms.

The criterion for the equality of total electromagnetic lifting force and the weight of the liquid metal mass can be satisfied through adjustments in the current

magnitudes. The differences in spatial harmonics can be used as the driving term for the systematic re-positioning of the coil conductors for minimization of the harmonic rms error.

Example: The required pressure distribution for the torus, as given by Eqn. 4, is already in its Fourier form. The electromagnetic pressure given by Eqn. 7 is transformed into its Fourier components as:

$$P_{m DC} = \frac{1}{2\pi} \int_0^{2\pi} P_{mag} d\theta \quad (8)$$

$$P_{m 1s} = \frac{1}{2\pi} \int_0^{2\pi} P_{mag} \sin \theta d\theta \quad (9)$$

$$P_{m 1c} = \frac{1}{2\pi} \int_0^{2\pi} P_{mag} \cos \theta d\theta \quad (10)$$

$$P_{m n} = \frac{1}{2\pi} \int_0^{2\pi} P_{mag} e^{jn\theta} d\theta \quad (11)$$

where: $P_{m DC}$ is the average value of the magnetic pressure (N/m^2), $P_{m 1s}$ and $P_{m 1c}$ are its fundamental components (N/m^2), $P_{m n}$ is the magnitude of the n -th harmonic distortion term (N/m^2). Eqn. 8 and Eqn. 9 must be made identical to the two terms of Eqn. 6 respectively. Eqn. 10 is related to a shift in the location of the pressure centre in the X direction. Since this will result in a sideways displacement of the liquid metal, its magnitude must be reduced to the smallest possible minimum value. Eqn. 11 represents the deviation from the desired distribution. Its rms sum is a measure of the overall error in shape, and the purpose of the design method is to reduce this to as small a value as possible.

Step 8 Error minimization

Successive perturbation analyses in the location of each turn indicate the direction of its displacement needed for the minimization the pressure phase shift and overall spatial rms harmonic distortion. In this analysis, the location of any given turn is considered to be the centre of a small circle. The pressure field is recalculated for each displacement of a conductor along the circumference of the circle and the rms harmonic error for the total pressure is re-calculated with the positions of all other turns being unchanged. The magnitude of

the error with each position is stored in memory along with the associated geometrical data. After the completion of one perturbation cycle, the conductor is positioned at the location corresponding to the minimum error. When the calculated new position is outside the assumed inner or outer limit, the conductor is placed on it and is prevented from crossing it. The analysis proceeds from turn to turn, and upon completion of one cycle for all coils, the total geometrical error is less than that at the start. The continuous decrease of error with iteration is caused by allowing physical displacements only if it results in the reduction of the local error. Next, the distance between the inner and outer limits is reduced, where possible, to narrow the band of coil locations. Thus, with each iteration an increasingly better estimate is obtained for the coil geometries.

Example: Application of the above minimization technique for the design of a 10 turn confinement coil shown in Figure 1 results in a reduction of the harmonic error from an initial value in the order of 40% to less than 2.5% after the completion of 16 iterations. The final positions of the turns are shown in Figure 3.

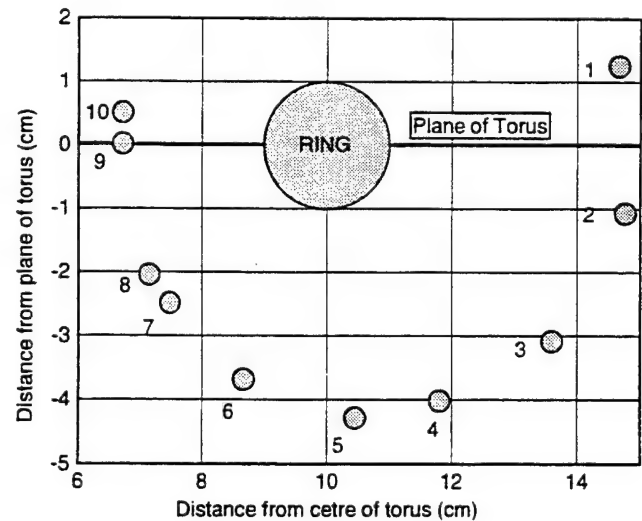


Figure 3 Final locations of turns 1 to 10 with respect to the toroidal plane and centre

The calculated value of the coil current is 335 A rms and an almost sinusoidal pressure distribution is obtained as seen in Figure 4. The results of a finite element analysis described in Section 5 below are also included

to confirm the results. The small distortion in the waveform is due to the second harmonic pressure term which will cause a slight vertical elongation of the liquid toroidal ring.

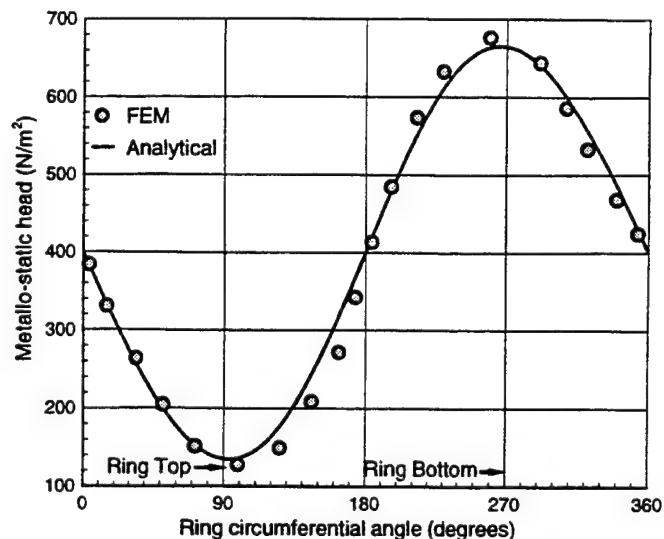


Figure 4 Electromagnetic pressure distribution

The variation of the vertical component of the force on the ring is calculated from the relationships given in Reference [7] and is shown in Figure 5. It is maximum at an angular position of 267° which almost coincides with the bottom of the ring. The magnetic field completely surrounds the ring to produce small negative

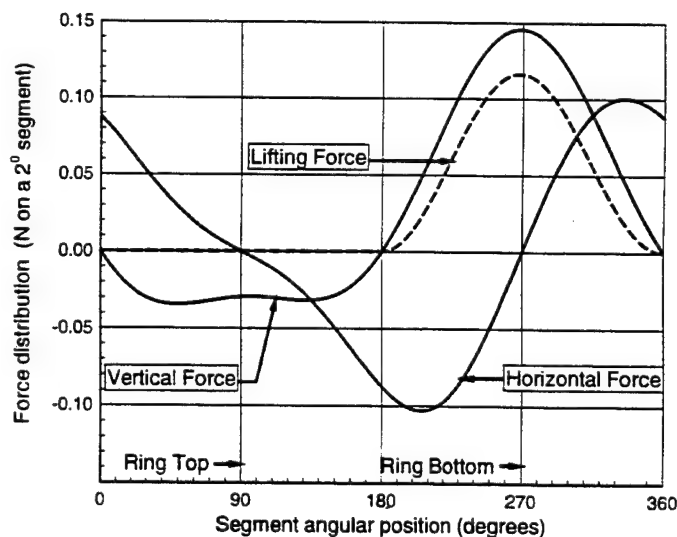


Figure 5 Force distributions on the ring

forces on the top surface. The net force differential between the lower and upper parts of the ring creates the almost perfect sinusoidal form for net effective lifting force of 5.22 N.

5 The design algorithm

The inverse method described above forms the basis of a design algorithm whose basic steps are described by the following pseudo-code:

Algorithm confine

{Function: solves for the pressure distribution required for the levitation of bulk amounts of liquid metal}

Start

```

Procedure basic_parameters
Procedure initial_geometry
Procedure initial_limits
do while spatial_error > target_error
do while coil_no ≤ total_coil_no
do while turn_no ≤ coil_turns
do while total_lift ≤ target_lift
Procedure field_single_turn
Procedure field_all_coils
Procedure pressure
Procedure Fourier
calculate total_lift
end while      ! end force calculation
calculate spatial_error
if spatial_error > target_error
Procedure turn_position_perturbation
end if
end while      ! end calculations for each turn
end while      ! end calculation for each coil
Procedure limits
end while      ! end calculation of error

```

Stop

The details of the procedures called for in the above algorithm change from problem to problem. These may be either solutions to analytical field problems or the results of numerical solutions. The choice regarding the method of solution does not, however, alter the overall algorithm.

6 Validation through finite element analysis

The shape of the magnetic field and the validity of the electromagnetic pressure profile can be confirmed by a number of methods. One of these is a coupled circuit approach which uses the self and mutual inductances for a large number of subdivisions of the load and the coils. This method produces good results and has been used successfully in a perturbation analysis of the shape of the liquid metal. Another is the calculation of the magnetic field using the finite element method. A commercial software package [9] (ANSOFT) was used for the solution for the high frequency eddy current problem. In order to minimize the impact of current penetration into the ring, the excitation frequency of the 335A coil was set to 500kHz. The shape of the magnetic field is shown in Figure 6. This result is consistent with the objectives of the design, and the calculated magnetic pressures are shown in Figure 4.

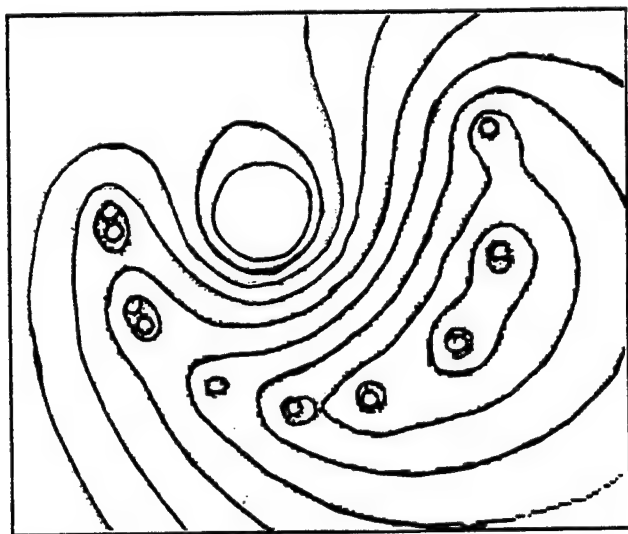


Figure 6 Spatial distribution of the electromagnetic field

7 Conclusions

The purpose of this paper was the development of an algorithm for the inverse electromagnetic field problem encountered in the design of levitation systems for large amounts of liquid metals. It is shown that an optimization procedure can be applied to determine the locations of lifting and confinement coils which define

a specified metallo-static pressure distribution. The main thrust of the procedure relates to the adjustment of inner and outer limits which bound the coil locations. The relocation of each turn of a high frequency coil system is guided by the successive minimization of an error term. This is obtained from the differences between the space harmonics of the Fourier series for the desired shape and the calculated magnetic pressure field. The steps of the design procedure are illustrated by the development of a confinement system for a toroidal ring of liquid aluminium. A finite element analysis of the final design step shows that the described methodology produces excellent results for the pressure field. The various stabilities of the system have not been investigated in this paper, and are the subjects of a paper in preparation.

8 References

- [1] E.C. Okress et al, "Electromagnetic Levitation of Solid and Molten Metals", J. Appl. Phys., Vol. 23, p. 83, 1952.
- [2] R.S. Sagardia, "Electromagnetic Levitation Melting of Large Conductive Loads", Ph. D. Thesis, University of Toronto, 1974.
- [3] T. Morisue, T.Yajima, K. Kume, S. Fujimori, "Analysis of Electromagnetic Force for Shaping the Free Surface of a Molten Metal in a Cold Crucible", IEEE Trans. on Magnetics, Vol. 29, No. 2, pp 1562-1565, March 1993.
- [4] S. Chandrasekhar, "Hydrodynamic and Hydromagnetic Stability", Dover Publications, Chapter IX and Chapter X, pp 382-480, 1981.
- [5] M. Garnier, R. Moreau, "Effect of Finite Conductivity on the Inviscid Stability of an Interface Submitted to High Frequency Magnetic Field", J. Fluid Mech. Vol. 127, pp. 365-377, 1983.
- [6] A.P. Vutsens, "Freely Levitating Torus in the Electromagnetic Field of a Current Carrying Loop and a Current Carrying Axial Conductor", Magnetohydrodynamics, No.4, pp. 478-485, 1976.
- [7] M. Abramowitz, I. Stegun, "Handbook of Mathematical Functions", National Bureau of Standards, p. 336, 1965.
- [8] E. Weber, "Electromagnetic Theory", Dover Publications, New York, pp. 513-516, 1965.
- [9] ANSOFT Corp, "User's Reference: MAXWELL 3D Field Simulator", 1993

Comparison of Magnetically Induced ELF Fields in Humans Computed by FDTD and Scalar Potential FD Codes

Trevor W. Dawson, Jan De Moerloose and Maria A. Stuchly

Department of Electrical and Computer Engineering

University of Victoria

P.O. Box 3055, Victoria, British Columbia, Canada, V8W 3P6

Abstract

This paper presents a detailed numerical comparison, of the magnetically-induced extremely low-frequency electric field and current density within an anatomically realistic model of the full human body, as computed using two different numerical techniques.

The first technique is a recently-described full-wave quasi-static finite-difference time-domain (FDTD) method. The use of a time-ramped excitation involving pairs of oppositely-directed plane waves allows for the calculation of decoupled magnetic and electric induction in complex heterogeneous bodies, in relatively short (5 ns) simulation times.

The second method is an implementation of Stevenson's method applied for isolated conducting bodies. With the lowest-order external magnetic field represented by a vector potential, the lowest-order internal electric field can be represented by a scalar conduction potential, and the magnetically-induced contribution can be calculated in isolation.

Both methods have an underlying similarity in their finite-difference approach, but are nevertheless very distinct. Each code was used to calculate the fields, induced by three orthogonal uniform magnetic fields, in a 7.2 mm-resolution human full-body model. Three-dimensional correlation coefficients of better than 99.9998% were observed between current densities computed by the two methods. Individual edge electric fields typically agree to 3 significant digits.

1 Introduction

Accurate numerical modelling is an important component of the assessment of any potentially detrimental health effects of power-frequency electromagnetic fields on humans, if such effects are related to the induced

electric fields and currents in tissue. Two commonly-used [1] numerical techniques are the finite-difference time-domain (FDTD) [2] method, and the impedance method (IM) [3, 4, 5]. In this paper, numerical computations using a modified FDTD method [6] will be compared to those computed using a less well-known scalar potential finite difference (hereafter frequently abbreviated as SPFD) technique, for magnetic excitation in an anatomically realistic heterogeneous human full-body model.

Although standard finite-difference time-domain codes are powerful and general, their direct application to extremely low-frequency modelling can result in excessively long simulation times on account of the stability criterion. For linear structures, however, it has recently been demonstrated [6] that the use of a time-ramped excitation involving pairs of oppositely-directed plane waves, can lead to an FDTD method that yields ELF fields in complex heterogeneous conducting bodies, in relatively short (5 ns) simulation times. By choosing the incident polarization appropriately, it is possible to treat the electric and magnetic source cases in a decoupled manner, as is desirable in a quasi-static framework. When applied to a human full-body model, the numerical FDTD implementation was shown [6] to give results that were both self-consistent, and in good agreement with previously-published data, for both electric and magnetic excitation. Nevertheless, as with any numerical model, independent verification of the numerical results is of utmost importance.

Interior calculations for magnetic sources have commonly been carried out using the Impedance Method, in which physical electric currents are represented by fictitious loop currents driven by the electromotive forces associated with the time-varying magnetic flux. The method has some attractive features. It can handle complex heterogeneous conductors, and gives rise to a sparse, naturally-preconditioned matrix system with only 13 non-zero diagonals. For the case of a

magnetic source, the forcing terms are available directly from the source fields. Solutions can be obtained using iterative methods. There are some drawbacks, however. Although the IM can be modified to incorporate injected currents, the result is not a comfortable match — fictitious external faces must be added around each surface node to support the partial loop currents that comprise the true injected current, and there is indeterminacy in the representation of a single scalar injection current in terms of multiple loop currents. Moreover, the underlying system of equations can be shown to be highly over-determined and is therefore singular. Nevertheless, iterative solution methods such as successive over-relaxation can in practice converge [3, 4, 5] to one of many possible solutions, and the indeterminacy is removed in the differencing of fictitious loop currents to yield physical edge currents. Also, in the case of multiply-connected domains, the method must be modified [7] to allow for generalized loop currents around the boundaries of insulating inclusions, or else physically incorrect solutions can be obtained. This modification becomes particularly onerous in three-dimensional modelling, but is nevertheless of major importance in human body modelling — insulating cavities occur in the airways, cranial sinuses and nasopharyngeal cavities, and pockets of gas may occur in the digestive tract.

At extremely low frequencies (ELF), electromagnetic induction in compact isolated conducting bodies can be handled by a simpler and more attractive scalar potential method. The indeterminacy in the underlying equations is removed, and the result is a matrix system which is approximately a factor of six smaller than in the impedance method formulation of the same problem. In Stevenson's Method [8], the electromagnetic fields external and internal to the conductor can each be expanded locally in a power series in frequency. The lowest-order internal electric field is proportional to frequency, and is driven by the static incident components of the (external) electric and magnetic fields. This results in a capacitive component associated with the surface charge density induced by the applied electric field, plus a system of eddy currents driven by the applied magnetic field. If a vector potential for the applied magnetic field is available, it is possible to express the internal electric field solely in terms of a static scalar electric conduction potential. This potential has two forcing terms, one associated with the external surface charges, and the other, which is distributed throughout the interior of the conductor, with the magnetically induced electromotive force. Again, as with the modified FDTD, it is possible to treat electric and magnetic sources in a decoupled manner. Since the

method appears to be less well-known, a self-contained description is provided in Section 2.3. The correctness of Stevenson's Method can be illustrated by examining the low-frequency limit of canonical problems, such as Mie scattering of a plane wave [8] from a uniformly conducting sphere.

Section 3 presents comparisons, from calculations using the FDTD and SPFD methods, of the electric fields and current densities induced by three orthogonal uniform magnetic fields, in a human full-body model at 7.2 mm resolution. Full three-dimensional correlation coefficients of better than 0.999998 were observed between the current density distributions computed by the two methods. Individual edge electric fields typically agree to 3 significant digits. In a companion paper [9], further validation of the SPFD method results is provided by a comparison with an analytical solution for low-frequency magnetic induction in a equatorially-stratified sphere.

2 Description of the Methods

2.1 General Description

A three-dimensional domain is described in terms of Cartesian coordinates (x, y, z) with associated unit vectors $\{\hat{x}, \hat{y}, \hat{z}\}$, so that a typical position vector is $\mathbf{r} = x\hat{x} + y\hat{y} + z\hat{z}$. A compact body, having a maximum diameter L and electrical conductivity and permittivity distributions $\sigma(\mathbf{r})$ and $\epsilon(\mathbf{r})$ respectively, is located in this domain, and subjected to incident time-harmonic electric and magnetic fields $\mathbf{E}^e(\mathbf{r})e^{+i\omega t}$ and $\mathbf{B}^e(\mathbf{r})e^{+i\omega t}$ of angular frequency ω .

It is assumed that the inducing frequency is sufficiently low (quasi-static) that the body is much smaller than both the free-space wavelength, $L \ll \lambda \equiv 2\pi/k_0 = 2\pi c/\omega$ and the skin depth, $L \ll \delta \equiv [\omega\mu_0\sigma(\mathbf{r})/2]^{-1/2}$, and that conduction currents completely dominate displacement currents, $\sigma(\mathbf{r}) \gg \omega\epsilon(\mathbf{r})$. The permittivity distribution plays no further role in the present analysis. Since the body is non-magnetic, the magnetic permeability has its vacuum value $\mu_0 = 4\pi \times 10^{-7} \text{ Hm}^{-1}$ everywhere. Under these quasi-static assumptions, it is known that the internal electric field is in quadrature with the applied fields [8].

The task is to compute the fields induced in the conductor by the applied fields. The solution will be considered using both the FDTD and SPFD methods. In both methods, the three-dimensional computational domain is discretized into a uniform set of elementary

parallelepipeds or voxels. Within each voxel the electrical properties are assumed constant. The electric fields are defined as a set of discrete vectors on a staggered array defined by the voxel edges [10], with field values defined at the edge centers. Representative vectors are depicted in Figure 1. Magnetic fields are defined on a

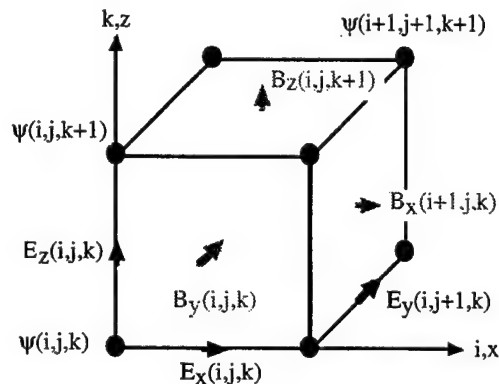


Figure 1: Representative discrete electric and magnetic field vectors, defined on conjugate staggered grids associated with the voxel edges and faces. The figure also illustrates representative discrete samples of the conduction potential, at the nodes defined by the voxel vertices.

conjugate mesh defined by the voxel face-normals.

In the full-wave FDTD method, the vector electric and magnetic fields are solved for directly, both interior and exterior to the conductor, by time-stepping. Absorbing boundaries are used to truncate the numerical mesh.

In contrast, the potential method is naturally confined only to the conductor (see Section 2.3), with potentials defined at the vertices of the voxels, as illustrated in Figure 1. It will be seen below that each discrete potential value is related to at most 6 others, so that the underlying matrix system has only 7 non-zero diagonals. Electric fields along the voxel edges are computed *a posteriori*, using finite differences of the potential field.

By way of comparison, it may be noted that the impedance method (which is also quasi-static) works with loop currents around the voxel faces, and so also is an intrinsically vector method. The final reduction of loop currents to physical edge currents yields the current density components along the voxel edges, as with the FDTD and SPFD methods. Each loop current is related to up to 12 others, leading to a matrix with 13 non-zero diagonals. Moreover, as it is a vector method, the number of unknowns is slightly more than 3 times as great.

The primary output of both the FDTD and SPFD codes is the set of discrete electric vector components. To allow for physical interpretation of the results, electric field vectors are defined at the voxel centers by averaging the three sets of four parallel edge components, and the current density is then computed by multiplication by the voxel conductivity.

For purposes of illustration, the methods will be applied to an anatomically realistic human full-body model, which is described in detail elsewhere [6]. It is a composite model, incorporating a Yale Medical School [11] head and torso model, augmented with legs and arms generated in our laboratory by the application of segmentation algorithms to CT and MRI data of the same man, obtained from the Visible Human Project at the U.S. National Library of Medicine. The tissue conductivities correspond to published [12], or where applicable, recently-measured [13], values. Particular care has been taken to ensure the correctness of the final model, verifying for example such items as continuity of major blood vessels and bone marrow, integrity of the skin, and encapsulation of bone marrow within bone, by visualization using IBM's Data Explorer program. The model provides a suitable complex heterogeneous domain for the rigorous comparison of numerical results. The original 3.6 mm resolution was decreased to 7.2 mm for this work. The end-result is described by a set of 213,782 cubic voxels with 7.2-mm edges. The model is oriented facing the \hat{y} direction with the long axis of the body along the \hat{z} direction. The source fields are taken to be uniform magnetic, at the 60-Hz power frequency.

2.2 FDTD Method

The finite-difference time-domain code is fully described and illustrated elsewhere [6]. This is a full-wave vector code, modified to take advantage of the fact that the phase of the external and internal fields is known in the quasi-static case. Indeed, fields exterior to the conductors all have the same phase as the incident field. Interior fields, however, are first-order fields in the quasi-static approximation and are proportional to the time derivative of the incident field. If a ramp function is used for the incident field, all fields will eventually have a linear (exterior) or constant (interior) behavior. The amplitude of the fields can then be read directly from their rate of change (exterior) or their actual values (interior). To obtain a solution, it is therefore sufficient to register all field values on two subsequent time steps after the transient response has decayed. The excitation function

used in this analysis is a ramp function with a smooth start to avoid high-frequency contamination. Absorbing boundary conditions [14] are used to truncate the numerical domain. On account of the retarded nature of any reflections and the short simulation times, these absorbing boundaries work well for low-frequency evanescent waves, even when placed close to the conductor. Another feature is that uniform electric and magnetic sources can be considered in isolation, by using oppositely-traveling plane waves with phases and polarizations adjusted to produce either uniform electric or magnetic source fields in the region of the conducting body.

2.3 SPFD Method

Under the present quasi-static assumptions, Stevenson's method [8] can also be applied. Each of the incident, scattered and interior electromagnetic fields can be expanded near the conductor in a power series involving the parameter $(-ik_0)$, where $k_0 = \omega/c$ denotes the vacuum wavenumber of the fields, and $c = (\epsilon_0\mu_0)^{-1/2} \approx 2.998 \times 10^8 \text{ ms}^{-1}$ is the vacuum speed of light. As explained by Van Bladel [8], the zeroth-order interior electric field in the series expansion is zero, and the interior magnetic field is equal to the zeroth-order applied magnetic field.

The first-order interior electric field has two sources. The first is the surface charge distribution $\rho_{s0}(\mathbf{r})$ induced by the zeroth-order applied electric field $\mathbf{E}_0^i(\mathbf{r})$. The second source is the applied zeroth-order external magnetic field $\mathbf{B}_0^e(\mathbf{r})$, which gives rise to the eddy currents that form the main focus of this work.

Mathematically, the first-order internal fields $\mathbf{E}_1^i(\mathbf{r})$ and $\mathbf{B}_1^i(\mathbf{r})$ satisfy the differential equations

$$\begin{aligned}\nabla \times \mathbf{E}_1^i(\mathbf{r}) &= -i\omega \mathbf{B}_0^e(\mathbf{r}) \\ \nabla \times \mathbf{B}_1^i(\mathbf{r}) &= \mu_0 \sigma(\mathbf{r}) \mathbf{E}_1^i(\mathbf{r})\end{aligned}\quad (2.1)$$

throughout the interior of the body. At its surface, where the outwardly-directed unit normal vector is $\hat{\mathbf{n}}(\mathbf{r})$, the appropriate boundary condition is

$$\sigma(\mathbf{r}) \hat{\mathbf{n}}(\mathbf{r}) \cdot \mathbf{E}_1^i(\mathbf{r}) = i\omega \rho_{s0}(\mathbf{r}). \quad (2.2)$$

Because of linearity, the contributions arising from the applied magnetic and surface charge forcing can be computed independently, by alternatively setting either the external magnetic field, or the surface charge density terms above to zero. The 'electric' contribution will be ignored for the remainder of this work, and the main focus will be on the internal electric field,

and associated current density, generated by the magnetic source. The internal first-order magnetic field is strictly dependent on the internal electric field, and can be computed afterwards, if desired.

The problem, therefore, is to solve the differential equations

$$\begin{aligned}\nabla \times \mathbf{E}_1^i(\mathbf{r}) &= -i\omega \mathbf{B}_0^e(\mathbf{r}) \\ \nabla \cdot [\sigma(\mathbf{r}) \mathbf{E}_1^i(\mathbf{r})] &= 0\end{aligned}\quad (2.3)$$

(which are just the first member of equation (2.1) combined with the divergence of the second) within the body, subject to the boundary condition

$$\hat{\mathbf{n}}(\mathbf{r}) \cdot \mathbf{E}_1^i(\mathbf{r}) = 0 \quad (2.4)$$

at its surface. It is supposed that the static limit of the applied magnetic field can be described by a vector potential,

$$\mathbf{B}_0^e(\mathbf{r}) = \nabla \times \mathbf{A}_0(\mathbf{r}). \quad (2.5)$$

It then follows from equation (2.3) that

$$\nabla \times \{ \mathbf{E}_1^i(\mathbf{r}) + i\omega \mathbf{A}_0(\mathbf{r}) \} = 0.$$

Consequently, the term in braces can be expressed as the negative gradient of a scalar potential $\psi(\mathbf{r})$, and the electric field has the representation

$$\mathbf{E}_1^i(\mathbf{r}) = -\nabla \psi(\mathbf{r}) - i\omega \mathbf{A}_0(\mathbf{r}). \quad (2.6)$$

This scalar potential must then satisfy the differential equation

$$\nabla \cdot [\sigma(\mathbf{r}) \nabla \psi(\mathbf{r})] = \nabla \cdot [-i\omega \sigma(\mathbf{r}) \mathbf{A}_0(\mathbf{r})], \quad (2.7)$$

subject to the boundary condition

$$\hat{\mathbf{n}}(\mathbf{r}) \cdot \nabla \psi(\mathbf{r}) = -i\omega \hat{\mathbf{n}}(\mathbf{r}) \cdot \mathbf{A}_0(\mathbf{r}). \quad (2.8)$$

In a numerical implementation, the potential is taken to be defined at the voxel vertices. A finite-difference approximation for equation (2.7) at a given node can then be constructed by an application of the divergence theorem to an imaginary voxel with that node at its centre. It is convenient to adopt a local indexing scheme, where the target node is labeled 0 and both the nodes and edges connected to it on the $+x$, $-x$, $+y$, $-y$, $+z$ and $-z$ sides are indexed from 1 to 6 respectively, as shown in Figure 2. Quantities associated with nodes or edges are then labeled with the local index of the associated object. With this shorthand, a simple finite difference equation

$$\left(\sum_{r=1}^6 s_r \right) \psi_0 - \sum_{r=1}^6 s_r \psi_r = i\omega \sum_{r=1}^6 (-1)^{r+1} s_r \ell_r A_{0r} \quad (2.9)$$

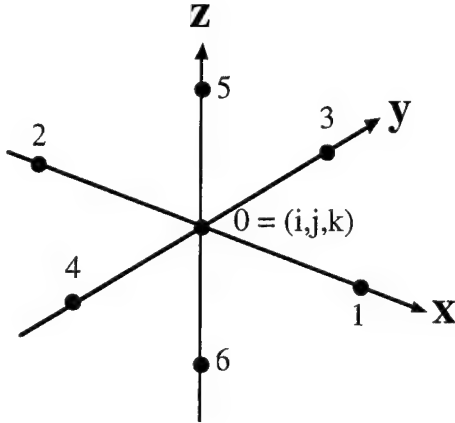


Figure 2: Local indexing scheme at a node.

results. In this equation, ℓ_r denote the various edge lengths in the local indexing scheme, and A_{0r} denotes the component of the external magnetic vector potential tangent to the r^{th} edge, evaluated at the edge centre. The coefficients are the edge conductances $s_r \equiv \bar{\sigma}_r a_r / \ell_r$, where $\bar{\sigma}_r$ denotes the average conductivity of the four voxels contacting edge r , a_r is the area of the voxel face normal to edge r . The above equations are to be modified in an obvious manner if the central point is connected to less than 6 neighbouring nodes in the conductor.

When this equation is written for each vertex of every conducting voxel in the distribution, the result is a heptadiagonal system of equations of the form $(N - E)y = f$. This set of equations is diagonally dominant, symmetric, positive semi-definite. It is also singular, since the potential is indeterminate to within an additive constant. It can be symmetrically preconditioned to the form $(I - A)x = b$, where $A = N^{-1/2} E N^{-1/2}$, $y = N^{-1/2} x$ and $b = N^{-1/2} f$. The singularity can be removed by augmenting the system with an equation requiring that the potential have zero mean. The net result of augmentation and preconditioning is a system, based on a symmetric sparse matrix with two borders, that is amenable to solution using the conjugate gradient iterative scheme.

3 Results

Results computed by the FDTD code for incident uniform magnetic field directed along the three Cartesian axes are described in detail elsewhere [6], and shown to be both self-consistent and in reasonable agreement with results computed by other methods. In these

computations, the bounding box containing the body model was surrounded by a single-voxel air layer, and the whole surrounded on all sides by a 15-voxel thick absorbing boundary. Thus the calculations were performed over a $107 \times 77 \times 280$ array, for an overall domain composed of 2,306,920 voxels. Each run employed 4200 time steps of 1.2 ps, for a total simulation time of 4.92 ns. All calculations were carried out on a Hewlett-Packard 9000/735 Unix workstation with 336 megabytes of physical memory. Typical computation times were of the order of 18 hours.

Results were also computed by the SPFD code, for the same body configuration and excitation fields. The resulting augmented and preconditioned potential matrix system consisted of 240,883 unknowns, and was found to be reliably solvable using the Conjugate Gradient Method (CGM) [15] from the PIM [16] package, running in sequential mode on the above-mentioned workstation. Typical run times were of the order of 1 hour.

As noted earlier, electric fields and current densities were defined at voxel centers using edge-averaged electric fields. This leads to fields defined for every voxel in the $75 \times 45 \times 248$ -voxel bounding box containing the body model, and the calculations can be compared voxel-by-voxel throughout the conducting voxels.

To illustrate the comparisons obtained, Figure 3 depicts the results in a horizontal (left-to-right, back-to-front) cross-section through the chest area (at a height $z = 1.357$ m above the lowest conducting voxel face) of the model, under induction by an x -directed (left-to-right) $1 \mu\text{T}$ uniform magnetic field. The upper left panel of the figure shows the magnitude of the electric field computed by the SPFD code, while the lower left panel shows the magnitude of the corresponding current density. The upper right panel shows the magnitude of the voxel-wise vector difference of the FDTD and SPFD electric fields, while the lower right panel displays the analogous difference of the current density. Particular attention is drawn to the approximately three orders of magnitude difference in scale between the electric field and the electric difference, and nearly four orders of magnitude for the corresponding current density plots.

Figure 4 shows a current density comparison along a vertical (back-to-front, groin-to-head) cross-section (at a distance $x = 26.28$ cm from the leftmost conducting voxel face), under forcing by a vertical magnetic field configuration.

To further quantify the agreement between results computed by the two methods, a set of scalar descriptors is provided in Table I. All measures are taken solely

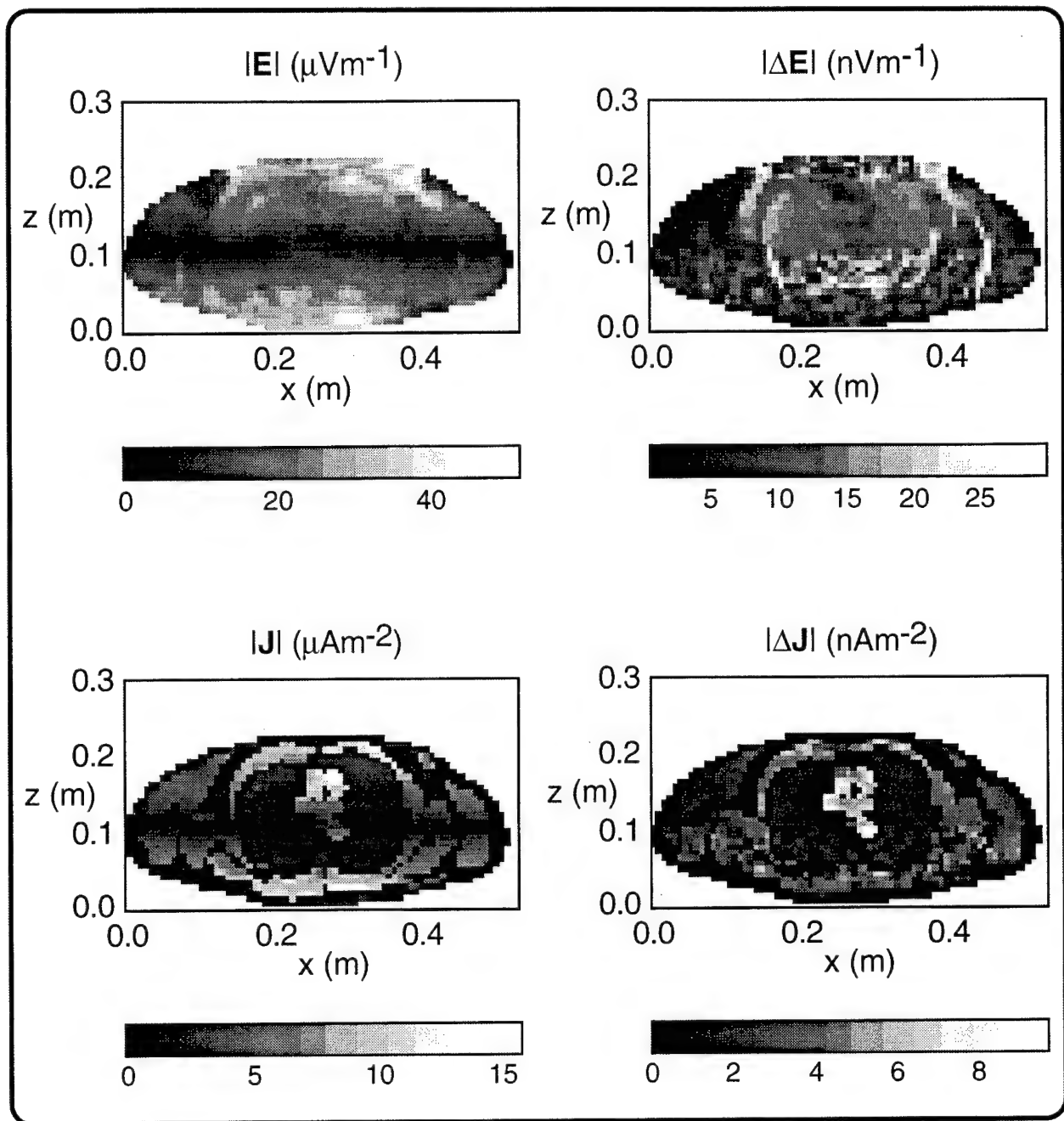


Figure 3: Comparison of the SPFD calculations (left-hand column) and voxel-wise differences between the FDTD and SPFD results (right-hand column) in a horizontal cross section through the chest. The 60-Hz, 1- μT magnetic source field is directed from left to right. The upper left panel depicts the magnitude of the electric field, while the upper right panel illustrated the magnitude of the vector difference. The lower row portrays analogous data for the current density. Note the factor of 1000 difference in units between the left- and right-hand units.

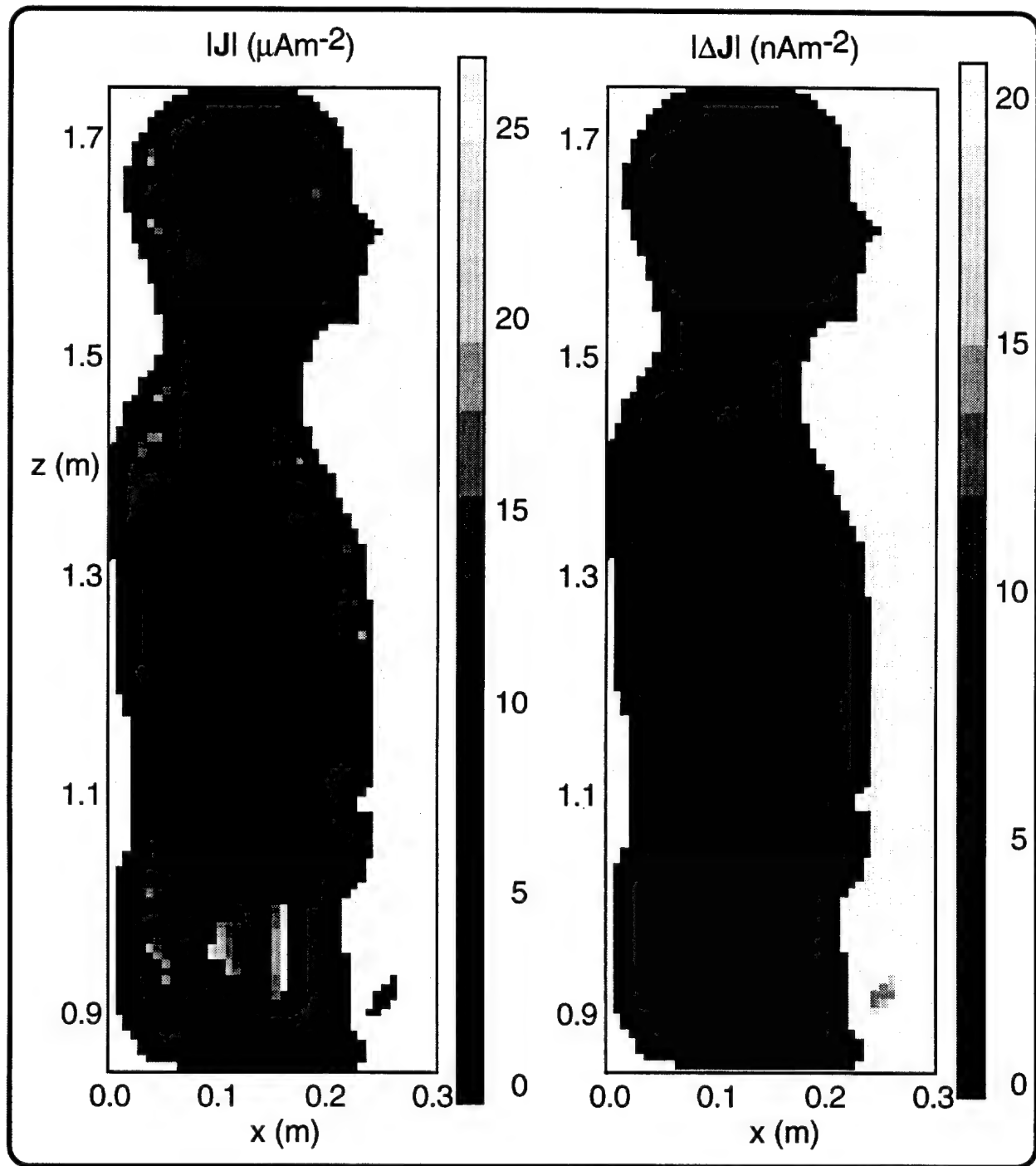


Figure 4: Comparison of the magnitudes of the current density (left) and difference (right) fields in a central vertical cross-section, for a vertical 60-Hz, $1\text{-}\mu\text{T}$ magnetic source field.

Field :		$ E (\mu V m^{-1})$			$ J (\mu A m^{-2})$		
Source :		B_x	B_y	B_z	B_x	B_y	B_z
Cor. (%)		99.05054	99.79887	99.63219	99.99997	99.99984	99.99998
FDTD	Maximum	123.0281	756.7335	104.7555	70.7892	75.6733	31.5956
	Average	15.0586	20.4341	13.3078	2.8565	3.9026	2.4186
	Std. Dev.	27.8941	39.1021	24.4372	5.7031	7.8438	4.7016
SPFD	Maximum	81.9336	758.5416	104.7452	70.7973	75.8542	31.5978
	Average	14.9101	20.3426	13.2235	2.8568	3.9021	2.4187
	Std. Dev.	27.6243	38.9712	24.3103	5.7037	7.8431	4.7018
Δ	Maximum	123.0281	83.9447	67.7967	0.0424	0.1736	0.0477
	Average	0.1484	0.0916	0.0842	-0.0003	0.0005	-0.0001
	Std. Dev.	2.5218	1.6959	1.3614	0.0033	0.0102	0.0019

Table I: Electric field and current density modulus comparisons for three orthogonal (left-to-right, back-to-front and foot-to-head) 1 μT uniform magnetic sources. The correlation coefficient for each field type relates the FDTD and SPFD calculations. The remaining rows show various scalar comparisons between the two calculated fields, plus measures of the voxel-wise difference between the fields computed by the two codes. All measures are taken solely over voxels belonging to the body model.

over voxels belonging to the body model, i.e. specifically excluding air cells external to the body. Scalar descriptors include the voxel-wise correlation between the FDTD and SPFD fields. In addition, for each method, the global maximum and average values are tabulated, as well as the standard deviation. The latter is included purely as an indicator of the variation in a given field, *not* as a statistical measure. These indicators are tabulated for the FDTD results and for the SPFD computations, as well as to the difference (FDTD-SPFD) fields. These comparisons were performed for the magnitude of the electric field and current density distributions, under excitation by x -, y - and z -directed 60-Hz, 1- μT uniform magnetic source fields.

The electric field measured indicate a reasonable agreement between the methods, with the global measures (average and standard deviation) differing only in the third decimal place. The smallest electric field correlation coefficient is 99.05%, for the x -directed magnetic field. The peak field values for this excitation are also in poor agreement. On closer examination however, it turns out that these differences are entirely associated with the occurrence of non-conducting air and gas pockets within the body. The electric fields are not computed and are automatically set to zero within such non-conducting volumes in the numerical implementation of the SPFD method. In the FDTD method, however, fields are computed at all voxels in the computational domain. The physical interpretation of the fields within interior non-conducting regions in the quasi-static FDTD code has not yet been clari-

fied.

As might then be expected and is verified by the figures, the additional order imposed by the incorporation of the conductivity distribution and its associated removal of any contributions from non-conducting cavities, dramatically improves the current density correlation coefficients (the smallest of which is now 99.9998%), as well as the overall agreement indicated by the various scalar measures. The peak values now differ in the third decimal place at worst, while the global measures differ in the fifth.

4 Conclusions

Two distinct numerical methods, namely a finite-difference time-domain code, and a static scalar potential finite-difference code, have been used to compute the magnetically-induced electric fields and current densities in an anatomically realistic heterogeneous human full-body model. With three orthogonal source orientations, the model provides a rigorous test of the methods and of the correctness of the computer coding.

In all cases, the minimum full-body three-dimensional voxel-wise correlation coefficient for the electric field magnitude was found to be 0.9905. The corresponding minimum for the current densities was 0.999998. A variety of other scalar measures verifies the high degree of agreement that was obtained using the two methods. Any significant electric field differences which do occur

are attributable to the presence of non-conducting cavities within the body, where the SPFD code does not presently compute electric fields. The agreement between the current density fields computed by the two codes is excellent.

While the resolution is still rather coarse for detailed organ dosimetry, and there is the possibility of appreciable staircasing errors introduced by the volumetric discretization, the agreement between the methods provides a degree of comfort in using results computed by either code.

Acknowledgment :

The authors thank Kris Caputa for his contribution to the development of the human body model, and the three anonymous reviewers for their suggested improvements to the paper. The financial support of this research by NSERC, B.C. Hydro, TransAlta Utilities and Ontario Hydro is gratefully acknowledged.

References

- [1] Om P. Gandhi. Some numerical methods for dosimetry: Extremely low frequencies to microwave frequencies. *Radio Science*, **30**(1):161-177, January-February 1995.
- [2] Om P. Gandhi and Jin-Yuang Chen. Numerical dosimetry at power-line frequencies using anatomically based models. *Bioelectromagnetics Supplement*, 1:43-60, 1992.
- [3] Om. P. Gandhi, John F. DeFord, and Hiroshi Kanai. Impedance method for calculation of power deposition patterns in magnetically induced hyperthermia. *IEEE. Trans. Biomedical Engineering*, **BME-31**(10):644-651, October 1984.
- [4] Niel Orcutt and Om P. Gandhi. A 3-D impedance method to calculate power deposition in biological bodies subjected to time varying magnetic fields. *IEEE. Trans. Biomedical Engineering*, **35**(8):577-583, August 1988.
- [5] Weiguo Xi, Maria A. Stuchly, and Om P. Gandhi. Induced electric currents in models of man and rodents from 60 Hz magnetic fields. *IEEE Trans. Biomed. Eng.*, **BME-41**(11):1018-1023, 1994.
- [6] Jan De Moerloose, Trevor W. Dawson, and Maria A. Stuchly. Application of FDTD to quasi-static field analysis. *Radio Science*, 1996. manuscript submitted for publication.
- [7] Francis X. Hart, Kimberly Evely, and Carla D. Finch. Use of a spreadsheet program to calculate the electric field/current density distributions in irregularly shaped, inhomogeneous biological structures by low-frequency magnetic fields. *Bioelectromagnetics*, **14**:161-172, 1993.
- [8] J. Van Bladel. *Electromagnetic Fields*. Hemisphere Publishing Corporation, Washington D.C., revised printing edition, 1985.
- [9] Trevor W. Dawson and Maria A. Stuchly. Analytic validation of a three-dimensional scalar-potential finite-difference code for low-frequency magnetic induction. *Applied Computational Electromagnetics Society Journal*, 1996. manuscript accepted for publication.
- [10] K.S. Yee. Numerical solutions to initial boundary value problem involving maxwell's equations in isotropic media. *IEEE Trans. Antennas Propag.*, **14**:302-307, 1966.
- [11] I. G. Zubal, C. R. Harrell, E. O. Smith, Z. Rattner, G. R. Gindi, and P. H. Hoffer. Computerized three dimensional segmented human anatomy. *Med. Phys. Biol.*, **21**:299-302, 1994.
- [12] K. R. Foster and H. P. Schwan. Dielectric properties of tissues and biological materials: a critical review. *CRC Critical Reviews in Biomedical Engineering*, **17**:25-104, 1989.
- [13] Dr. C. Gabriel. Personal communication, 1996.
- [14] J. P. Berenger. A perfectly matched layer for the absorption of electromagnetic waves. *J. Comp. Phys.*, **114**:185-200, 1994.
- [15] John L. Volakis. EM programmer's notebook. *IEEE Antennas and Propagation Magazine*, **37**(6):94-96, 1995.
- [16] R.D. da Cunha and T.R. Hopkins. PIM 2.0 : Parallel Iterative Methods package for systems of linear equations; (FORTRAN 77 version), 1993. ©1993 R.D. da Cunha, T.R. Hopkins and Computing Laboratory, University of Kent at Canterbury, Canterbury, U.K. and Centro de Processamento de Dados, Universidade Federal do Rio Grande do Sul, Porto Alegre, Brasil.

Analytic Validation of a Three-Dimensional Scalar-Potential Finite-Difference Code for Low-Frequency Magnetic Induction

Trevor W. Dawson and Maria A. Stuchly
Department of Electrical and Computer Engineering
University of Victoria
Victoria, British Columbia, Canada

Abstract

This paper presents a detailed comparison of numerical and analytical calculations of the low-frequency electric and current density fields, induced by an applied uniform axial magnetic field, in an equatorially stratified sphere having the conductivity distribution $\sigma(\varphi) = \sigma_0 e^{-\lambda \cos(p\varphi)}$ with $p \in \{1, 2\}$ and $\lambda > 0$. As shown by the analytic solution, the resulting induced fields are fully three-dimensional, and the model therefore serves as a rigorous test of numerical codes.

The numerical method is a scalar-potential finite-difference scheme based on Stevenson's method for isolated conducting bodies. This computer code was recently shown to provide excellent agreement with results computed independently by a modified Finite-Difference Time-Domain method. Nevertheless, both codes share some underlying similarities, such as their common use of parallelepiped material voxels to represent the conductivity distribution, and of an edge-based staggered grid to model the electric fields. Therefore, it is of value to compare the numerical results with analytic ones.

The analytic model has a freely adjustable contrast parameter, and supports both π - and 2π -periodic conductivity distributions. Numerical and analytical results are compared for several configurations. Full three-dimensional volumetric correlation coefficients are typically of the order of 99% or better. As might be expected, the main differences occur at the surface of the sphere, where the true circumferential fields are most poorly approximated by the staircasing approximation inherent in the numerical approximation.

1 Introduction

Accurate numerical modelling of electromagnetic fields is important in many areas, perhaps particularly in the

assessment of any potentially detrimental health effects of power-frequency electromagnetic fields on humans, if such effects are related to the induced electric fields and currents in tissue.

Among the numerical methods commonly used [1] to model extremely low-frequency (ELF) electromagnetic fields are the finite-difference time-domain (FDTD) [2] method, and the impedance method (IM) [3, 4, 5]. Although standard FDTD codes are powerful and general, their direct application to extremely low-frequency modelling can result in excessively long simulation times on account of the stability criterion. With appropriate modifications, however, FDTD can compute accurate decoupled electric and magnetic ELF fields in complex heterogeneous conducting bodies in relatively short (5 ns) simulation times [6]. The IM is particularly useful for induction by magnetic sources, but has several drawbacks [7], including a vastly over-determined matrix system, and difficulties in handling multiply-connected domains in three-dimensional modelling. Both the FDTD and IM are inherently vector codes, which can limit the size of the problems that they can handle.

It was recently shown [7] that ELF modelling in compact isolated conducting bodies can be handled by a simpler and more attractive scalar potential scheme based on Stevenson's Method [8]. At low frequencies, the electric field internal to the conductor can be represented in terms of a vector potential of the static limit of the applied magnetic field, plus a scalar conduction potential. The excitation for the conduction potential consists of surface injection currents driven by any applied electric field, together with a term related to the induced electromotive force, distributed throughout the conductor volume, driven by any applied magnetic field. The method has several advantages. The indeterminacy in the underlying equations is removed, and the result is a matrix system which is approximately a factor of six smaller than in the impedance method formulation of the same problem. By choosing the source term appropriately, it is possible

to treat electric and magnetic sources in a decoupled manner. Results computed by a numerical implementation of the Scalar-Potential Finite-Difference (SPFD) method [7] in a human full-body model at 7.2 mm resolution resulted in a 3-significant digit agreement with modified FDTD [6] calculations in the same model.

Although the modified FDTD and SPFD codes use drastically different formulations (full-wave vs. static potential descriptions), they nevertheless share some underlying similarities in their numerical approximations. Both codes use parallelepiped material voxels to represent the conductivity distribution, and therefore use a staircased approximation of the actual conductor shape. Both use a voxel-edge-based staggered grid approximation to the electric field. Therefore, it is of considerable value to compare the numerical results with analytic ones.

The uniformly conducting spherical model commonly used to verify ELF magnetic modelling codes is in fact not a rigorous test. The induced electric field is essentially the applied magnetic vector potential in this case. The calculation of the loop currents in an IM formulation is therefore essentially devoted to calculating the (known) vector potential.

Recently, it was shown [9] that the problem of induction by a uniform axial applied magnetic field in an equatorially stratified sphere having the conductivity distribution $\sigma(\varphi) = \sigma_0 e^{-\lambda \cos(p\varphi)}$ with $p \in \{1, 2\}$ and $\lambda > 0$ can be solved analytically. This model has p conductivity maxima and minima, and a freely adjustable contrast parameter. In the case $p = 1$ and as viewed in the plane $z = 0$, the conductivity has a single minimum on the positive x axis and a single maximum on the negative x axis. For the case $p = 2$, there are two minima, located on the positive and negative x -axes, and two maxima, located on the positive and negative y -axes. This behaviour is depicted in Figure 1. The associated conduction potential is entirely related to the conductivity gradient, and provides the deviation in the fields from those in the uniformly conducting case, which are driven only by the applied vector potential. The observed current distribution for moderate and greater conductivity contrasts typically has a vortex, associated with each conductivity maximum, which intercepts the sphere surface at high latitudes. The fields are fully three-dimensional, and the model therefore serves as a rigorous test for numerical codes.

In this paper, results computed by the SPFD method are compared to analytical ones for several values of the parameters. It will be seen in Section 3 that the numerical and analytical results are generally in excellent agreement. For example, full three-dimensional volumetric correlation coefficients between fields are mostly of the order of 99% or better. As might be expected, the main

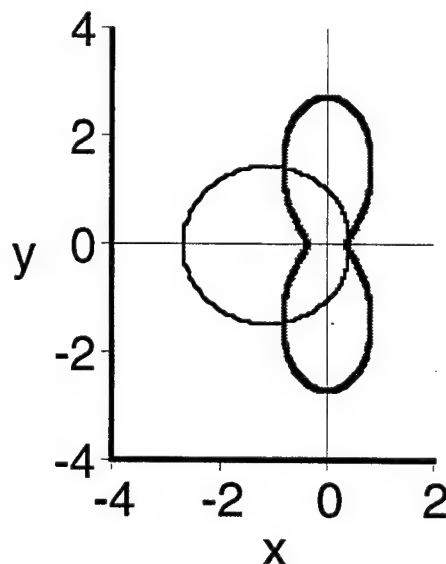


Figure 1: Polar diagrams of representative conductivity distributions in the $z = 0$ plane for $\sigma_0 = 1 \text{ Sm}^{-1}$ and $\lambda = 1$. The thin black curve and thick gray curve pertain to $p = 1$ and $p = 2$ respectively. The units indicated on the axes are Sm^{-1} .

differences occur at the surface of the sphere, where the true circumferential fields are most poorly approximated by the staircasing approximation inherent in the numerical approximation.

2 Summary of the SPFD Method and the Analytical Solution

2.1 Stevenson's Method

A three-dimensional domain is described in terms of Cartesian coordinates (x, y, z) with associated unit vectors $\{\hat{x}, \hat{y}, \hat{z}\}$, so that a typical position vector is $\mathbf{r} = x\hat{x} + y\hat{y} + z\hat{z}$. A compact body, having a maximum diameter L and electrical conductivity and permittivity distributions $\sigma(\mathbf{r})$ and $\epsilon(\mathbf{r})$ respectively, is located in this domain, and subjected to incident time-harmonic electric and magnetic fields $\mathbf{E}^e(\mathbf{r})e^{+i\omega t}$ and $\mathbf{B}^e(\mathbf{r})e^{+i\omega t}$ of angular frequency ω . It is assumed that the inducing frequency is sufficiently low (quasi-static) that the body is much smaller than both the free-space wavelength, $L \ll \lambda \equiv 2\pi/k_0 = 2\pi c/\omega$ and the skin depth, $L \ll \delta \equiv [\omega\mu_0\sigma(\mathbf{r})/2]^{-1/2}$, and that conduction currents completely

dominate displacement currents, $\sigma(\mathbf{r}) \gg \omega\epsilon(\mathbf{r})$. The permittivity distribution plays no further role in the present analysis. Since the body is non-magnetic, the magnetic permeability has its vacuum value $\mu_0 = 4\pi \times 10^{-7} \text{ Hm}^{-1}$ everywhere.

Under these quasi-static assumptions, Stevenson's method [8] can be applied. Each of the incident, scattered and interior electromagnetic fields can be expanded near the conductor in a power series involving the parameter $(-ik_0)$, where $k_0 = \omega/c$ denotes the vacuum wavenumber of the fields, and $c = (\epsilon_0\mu_0)^{-1/2} \approx 2.998 \times 10^8 \text{ ms}^{-1}$ is the vacuum speed of light. As explained by Van Bladel [8], the zeroth-order interior electric field in the series expansion is zero due to the induced surface charge distribution, and the interior magnetic field is equal to the zeroth-order applied magnetic field.

If the external zeroth-order electric field is ignored (electric and magnetic fields are commonly viewed as decoupled in the low frequency limit; moreover, by choosing the source to consist of two plane waves propagating in opposite directions with appropriate phasing, the electric fields can be made to cancel in the vicinity of the sphere [6]), then the surface charge density on the sphere is zero, and the complex amplitude of the first-order internal electric field may be shown [7, 8] to have the representation

$$\mathbf{E}_1^i(\mathbf{r}) = -\nabla\psi(\mathbf{r}) - i\omega\mathbf{A}_0(\mathbf{r}), \quad (2.1)$$

where $\mathbf{A}_0(\mathbf{r})$ is a vector potential for the zeroth-order applied magnetic field amplitude,

$$\mathbf{B}_0^e(\mathbf{r}) = \nabla \times \mathbf{A}_0(\mathbf{r}). \quad (2.2)$$

The conduction potential has to satisfy the differential equation

$$\nabla \cdot [\sigma(\mathbf{r}) \nabla\psi(\mathbf{r})] = \nabla \cdot [-i\omega\sigma(\mathbf{r}) \mathbf{A}_0(\mathbf{r})] \quad (2.3)$$

(which arises from the condition $\nabla \cdot \mathbf{J} = 0$), subject to the boundary condition $E_n = 0$, i.e.,

$$\hat{n}(\mathbf{r}) \cdot \nabla\psi(\mathbf{r}) = -i\omega\hat{n}(\mathbf{r}) \cdot \mathbf{A}_0(\mathbf{r}) \quad (2.4)$$

at the surface of the body. Additional constraints arise from the conditions of regularity and continuity of the electric field[8].

2.2 The SPFD Method

In the numerical implementation of the SPFD to solve equations (2.3) and (2.4), the three-dimensional computational domain is discretized into a uniform set of elementary parallelepipeds or voxels. Within each voxel the

electrical properties are assumed constant. The potential method is naturally confined only to the conductor, with potentials defined at the vertices of the voxels. The electric fields are defined as a set of discrete vectors on the staggered array defined by the voxel edges, with field values defined at the edge centers. These are computed *a posteriori*, using finite differences of the potential field. To allow for physical interpretation of the results, electric field vectors are defined at the voxel centers by averaging the three sets of four parallel edge components. The magnetic vector potential contribution indicated in eq.(2.1) must also be included. The current density is then computed by multiplication by the voxel conductivity.

A finite-difference approximation for equation (2.3) at a given node can be constructed by an application of the divergence theorem to an imaginary shifted voxel with that node at its centroid. It is convenient to adopt a local indexing scheme, where the target node is labeled 0 and both the nodes and edges connected to it on the $+x$, $-x$, $+y$, $-y$, $+z$ and $-z$ sides are indexed from 1 to 6 respectively, as shown in Figure 2. Quantities associated

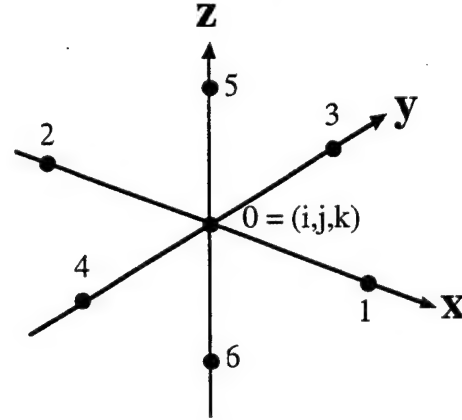


Figure 2: Local indexing scheme at a node.

with nodes or edges are then labeled with the local index of the associated object. With this shorthand, a simple finite difference equation results :

$$\left(\sum_{r=1}^6 s_r \right) \psi_0 - \sum_{r=1}^6 s_r \psi_r = i\omega \sum_{r=1}^6 (-1)^{r+1} s_r \ell_r A_{0r} \quad (2.5)$$

In this equation, ℓ_r denotes the various edge lengths in the local indexing scheme, and A_{0r} denotes the component of the external magnetic vector potential tangent to the r^{th} edge, evaluated at the edge centre. The coefficients are the edge conductances $s_r \equiv \bar{\sigma}_r a_r / \ell_r$, where $\bar{\sigma}_r$ denotes the average conductivity of the four voxels contacting edge r and a_r is the area of the voxel face normal to edge r . The above equations need to be modified in

an obvious manner if the central point is connected to less than 6 neighbouring nodes in the conductor. It may be noted here that the above equations may be viewed as modelling a Cartesian lattice of resistors associated with the voxel edges, and in this sense, the induced currents may be considered to be confined to these edges. This point of view has consequences for the surface discrepancies, observed in Section 3, between numerical and analytic calculations.

When equations of the above form are written for each vertex of every conducting voxel in the distribution, the result is a heptadiagonal system of equations which may be written as $(N - E)y = f$. This set of equations is diagonally dominant, symmetric, positive semi-definite. It is also singular, since the potential is indeterminate to within an additive constant. This system may be left-preconditioned to the form $(I - N^{-1}E)y = N^{-1}f$, or symmetrically preconditioned to the form $(I - A)x = b$, where $A = N^{-1/2}EN^{-1/2}$, $y = N^{-1/2}x$ and $b = N^{-1/2}f$. The singularity can be removed by augmenting the system with an equation requiring that the potential have zero mean. Either form is well-suited for solution on a computer, particularly using an iterative solvers [10]. The restarted Generalized Minimum Residual method converges well for the augmented and left-preconditioned system. However, the Conjugate Gradient Method applied to the symmetrically-preconditioned and augmented system proved to be the most efficient.

2.3 The Analytic Solution

It is assumed that the zeroth-order applied field is uniform and directed along the z -axis,

$$B_0^z(r) \equiv B_0 \hat{z}, \quad (2.6)$$

so that a suitable vector potential is

$$A_0(r) = \frac{1}{2} B_0 r \sin \theta \hat{\phi}. \quad (2.7)$$

The conducting body is specialized to a sphere of radius a , centred at the origin, and having the particular positive, periodic, and equatorially stratified conductivity distribution

$$\sigma(\varphi) = \sigma_0 e^{-\lambda \cos(p\varphi)}, \quad (2.8)$$

with $p \in \{1, 2\}$ and $\lambda > 0$. This model has p conductivity maxima and minima for $-\pi < \varphi \leq \pi$, and a maximum conductivity contrast of $e^{2\lambda}$. The logarithmic derivative of the conductivity is

$$s'(\varphi) \equiv \sigma'(\varphi) / \sigma(\varphi) = \lambda p \sin(p\varphi). \quad (2.9)$$

Under these restrictions, the conduction potential satisfies the differential equation

$$\nabla \cdot [\sigma(\varphi) \nabla \psi(r)] = -C\sigma'(\varphi), \quad (2.10)$$

where

$$C \equiv i\omega B_0/2. \quad (2.11)$$

The external boundary (2.4) condition reduces to

$$\partial\psi(r)/\partial r = 0 \quad (r = a) \quad (2.12)$$

in this case, since the magnetic potential is everywhere tangent to the sphere surface.

The solution to this problem is considered in detail elsewhere [9]. A suitable Green's function can be constructed by separation of variables, and a closed form expression for the conduction potential can then be derived. The solution has the form of the expansion

$$\psi(r') = C \sum_{\varphi \in \{e, o\}} \sum_{m, n=0}^{\infty} W_{mn}^{\varphi} \hat{F}_m^{\varphi}(\varphi') \hat{Q}_{mn}^{\varphi}(\theta') \tilde{R}_{\nu_{mn}}(r'), \quad (2.13)$$

where the prime indicates that the $m = n = 0$ term is to be omitted from the sum. Here the terms $\hat{F}_m^{\varphi}(\varphi')$ denote the even and odd eigenfunctions of the equatorial differential equation

$$[\sigma(\varphi) F'_m(\varphi)]' = -\mu^2 \sigma(\varphi) F_m(\varphi), \quad (2.14)$$

under the boundary conditions of periodicity

$$F_m(\varphi + 2\pi) = F_m(\varphi), \quad (2.15)$$

and regularity, normalized with respect to the inner product

$$\langle f | g \rangle_{\varphi} \equiv \int_{-\pi}^{+\pi} \sigma(\varphi) f(\varphi) g(\varphi) d\varphi. \quad (2.16)$$

In the case $p = 2$, this equation has both π -periodic and 2π -periodic even and odd eigenfunctions, but only 2π periodic ones in the case $p = 1$. The azimuthal functions $\hat{Q}_{mn}^{\varphi}(\theta')$ have the expression

$$\hat{Q}_{mn}^{\varphi}(\theta) = \sin^{\mu} \theta C_n^{(\mu+1/2)}(\cos \theta) / N_{m,n}^{\varphi}, \quad (n = 0, 1, \dots) \quad (2.17)$$

in terms of ultraspherical polynomials, and μ denotes any one of the equatorial eigenvalues. The denominator scale factors are chosen to make the functions orthonormal with respect to the inner product

$$\langle f | g \rangle_{\theta} \equiv \int_0^{\pi} f(\theta) g(\theta) \sin \theta d\theta. \quad (2.18)$$

The radial functions appearing in the potential are

$$\begin{aligned} \tilde{R}_{\nu}(r') &= \frac{r'^2}{10} \left(1 - 2 \ln \frac{r'}{a} \right), \quad (\nu = 2), \\ &= \left(\frac{a^2}{(\nu+3)(\nu-2)} \right) \left\{ \left(\frac{r'}{a} \right)^2 - \frac{2}{\nu} \left(\frac{r'}{a} \right)^{\nu} \right\}, \quad (\nu \neq 2), \end{aligned} \quad (2.19)$$

and have zero derivative at $r' = a$, as required. The expansion coefficients in the potential involve integrals of the equatorial and azimuthal eigenfunctions,

$$W_{mn}^{\omega} = \left\langle s' \left| \hat{F}_m^{\omega} \right\rangle_{\varphi} \left\langle 1 \left| \hat{Q}_{mn}^{\omega} \right\rangle_{\theta}. \quad (2.20)$$

The potential can be differentiated term-by-term in spherical coordinates to get the spherical components of the electric field. These can then be converted to Cartesian components for comparison with the SPFD results.

3 Results

Comparisons were made for five test cases, using the parameters shown in Table I. The cases cover a range of conductivity contrasts for the case of a π -periodic ($p = 2$) conductivity distribution, and a single run with a 2π -periodic ($p = 1$) conductivity distribution. The actual values of the conductivity scale σ_0 and sphere radius a are relatively unimportant — they essentially reduce to an overall scale factor for the calculated fields. The table indicates the minimum and maximum conductivity values, as well as the contrast parameter (which is the ratio of maximum conductivity value to the minimum, and is given by $e^{2\lambda}$). Runs A through D of the SPFD code used $N = 100$ voxels to span the sphere diameter, while Run E was done at higher resolution, using 150 voxels. The code embeds the conductor in a parallelepiped-shaped bounding box, with an extra layer of air added on all sides for bookkeeping purposes. The row labeled “Nodes (total)” indicates the number of nodes (located at voxel vertices) in the bounding box, which is 103^3 for Runs A through D, and 153^3 for Run E. Equations are written only of those nodes contacting at least one conducting voxel. The resulting number of equations is indicated in the row labeled “Nodes (active)”. In all cases, the inducing field was a 60-Hz, 1-T uniform magnetic field directed along the z -axis.

All SPFD calculations were carried out on a Hewlett-Packard 9000/735 Unix workstation with 336 megabytes of physical memory. As indicated in the Introduction, the SPFD conduction potential matrix system was found to be reliably solvable using either the restarted Generalized Minimal-Residual Method (GMRES) or the Conjugate Gradient Method [11] from the PIM package [10], running in sequential mode on the above-mentioned workstation. The latter was found to have the better performance. The primary output of the code is the values of the conduction potential at the conducting voxel vertices. Finite differences lead to electric field contributions defined at the voxel edges. These are then shifted to the voxel centroids using averages of the four edge fields parallel to

each Cartesian axis. Full electric fields are then calculated by inclusion of the applied magnetic vector potential, as indicated in eq.(2.1). Current densities are simply obtained by multiplication of the resulting voxel electric field by the voxel conductivity. The corresponding analytical fields can be computed at the same locations, and the two calculations compared pointwise.

Figures 3, 4 and 5 present a graphical comparison of the fields for Run E, in the three principal Cartesian planes. The upper left panel of each figure shows the modulus of the electric field as computed using the analytic solution, while the lower left panel shows the associated current density. The right-hand panels depict the voxel-wise difference of the absolute values of the analytically and numerically calculated results. It is evident that although the individual errors can be fairly large (for example, of the order of 25% in the $z = 0$ plane of Figure 3, and 10% in the $y = 0$ and $x = 0$ planes of Figures 4 and 5 respectively), they are almost entirely confined to the surface of the sphere. In the analytic solution, the surface fields are tangential to the sphere, whereas in the staircased numerical approximation, they are essentially confined to the voxel edges. It may be noted that the conducting edge-based path length between nodes at opposite vertices of a given face (voxel) is a factor of $\sqrt{2} = 1.414$ ($\sqrt{3} = 1.732$) times greater than the corresponding hypotenuse. This effectively changes the various resistances in the numerical model relative to the analytic one. The larger surface errors are therefore perhaps not too surprising. Noticeable differences also occur near the z -axis, where the discrete conductivity values inherent in the numerical model most poorly approximate the true distribution.

Analogous illustrations of the fields for the 2π -periodic conductivity distribution of Run B are presented in Figures 6 through 8. The error pattern is similar to those observed in Run E, again being largely confined to the surface of the conductor.

To further quantify the agreement between results computed by the two methods, a set of scalar comparison descriptors is provided for the five runs in Tables II through VI. All measures are taken solely over conducting voxels. The scalar descriptors include the voxel-wise correlation (“cor.”) between the analytical and numerical fields. In addition, for each method, the global minimum (“min.”), maximum (“max.”) and average (“avg.”) values are tabulated, as well as the standard deviation (“var.”). The latter is included purely as an indicator of the variation in a given field, *not* as a statistical measure. These four indicators are tabulated for the analytical (“A”) results and for the numerical (“N”) computations, as well as to the voxel-wise difference (analytical minus numerical, labelled “Δ”) fields. Finally, these com-

Run	A	B	C	D	E
p	2	1	2	2	2
λ	3.00	1.50	2.00	0.35	1.61
σ_0 (Sm ⁻¹)	0.20	0.22	0.14	0.71	0.20
σ_{\min} (Sm ⁻¹)	0.01	0.05	0.02	0.50	0.04
σ_{\max} (Sm ⁻¹)	4.02	1.00	1.00	1.00	1.00
Contrast	403.43	20.09	54.60	2.00	25.00
a	0.50	0.50	0.25	0.50	0.50
N	100	100	100	100	150
Nodes(total)	1092727	1092727	1092727	1092727	3581577
Nodes(active)	547865	547865	547865	547865	1822023

Table I: Parameters used for the five comparison runs.

parisons were performed for each Cartesian component and magnitude of the electric field and current density distributions. Electric field and current density values are in Vm⁻¹ and Am⁻² respectively. In all cases, excitation is by a vertical 1-T, 60-Hz uniform magnetic field.

Table II details the comparisons between the numerical and analytical calculations for the high-contrast π -periodic conductivity distribution of Run A. The comparisons appear to be worse in the pointwise comparators (maximum and minimum). For example, the worst agreement is in the x component of the electric field. However, the agreement is somewhat better (about 11%) for the dominant peak values of the y -component (which is required to drive the circumferential current flow through the conductivity minima at $\varphi = 0, \pm\pi$), and the error in the peak field amplitude is about 13%. This is not surprising — the numerical electric fields are derived in part from the conduction potential, which is generated iteratively as the solution of a global set of linear equations. The solution minimizes the residual over all nodes, and the larger numerical values may be expected to affect smaller ones. There are also large discrepancies evident in the difference comparators. Similar remarks apply to the current density, although the agreement is slightly better. For example, the error in the maximum current density amplitude is about 8.6%. Note that the peak current densities appear in the x -component and are associated with the conductivity maxima.

The agreement is markedly better in the global field comparators. For example, the average and standard deviation differ in only the third significant digit for both the electric and current density fields. The three-dimensional correlation coefficients for the electric field and current density amplitudes between the two methods are 99.977% and 99.948% respectively. The poorest per-component

electric correlation coefficient of 98.911% is obtained for the vertical electric field (which is entirely absent in the uniformly conducting sphere model).

Similar comments generally apply to the remaining four runs. There are perhaps only two features worthy of further explicit comment. The first concerns the poor correlations ($\approx 85\%$) for the vertical electric field and current density components in Run D as indicated in Table V. This run has a very low (2 : 1) conductivity contrast, and the vertical components are small (about 4%) compared to the peak magnitudes. Evidently, the vertical numerical fields are somewhat affected by the larger horizontal values in the iterative solution. Nevertheless, the global field comparators still indicate excellent agreement between the two methods. The second point concerns the effect of higher resolution on the numerical solution in Run E and Table VI. The addition of 50% more voxels along each axis leads to over 3 times as many unknowns in the linear system. The global comparators are perhaps only slightly better than for the other four runs. The peak values are not generally better-matched, and the effects of the staircasing approximation to the sphere surface still dominate the peak errors. Further improvement in the agreement would require the use of conformal meshing [12], for example, at the cost of additional coding complexity.

4 Closing Remarks

This paper has presented a rigorous comparison between fully three-dimensional extremely low-frequency electromagnetic fields calculated by a scalar potential finite-difference numerical code and an analytical solution. The model, consisting of an equatorially stratified sphere im-

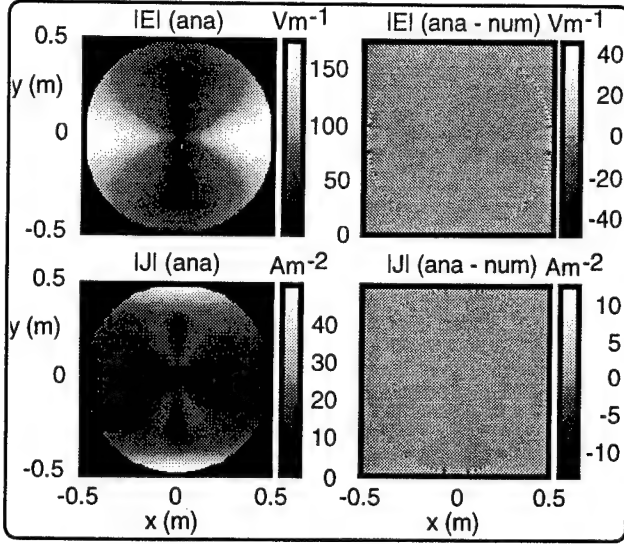


Figure 3: Field cross sections in the plane $z = 0$ for Run E (where $p = 2$).

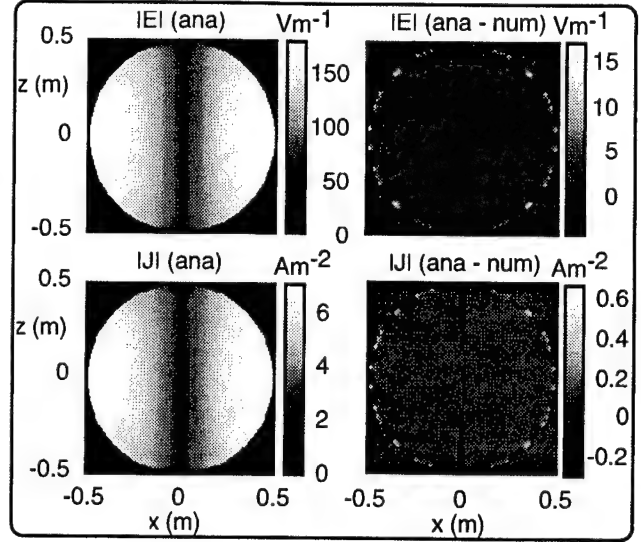


Figure 4: Field cross sections in the plane $y = 0$ for Run E.

Field :		E_x	E_y	E_z	$ E $
Cor. (%)		99.752	99.972	98.911	99.977
A	Min.	-51.27	-250.67	-27.34	0.00
	Max.	51.27	250.67	27.34	250.68
	Avg.	0.00	0.00	0.00	35.78
	Var.	14.28	65.65	5.10	57.09
N	Min.	-94.27	-278.01	-35.76	0.00
	Max.	94.27	277.86	35.76	283.32
	Avg.	0.00	-0.02	0.00	35.71
	Var.	14.28	65.54	5.12	57.01
Δ	Min.	-64.67	-73.66	-29.02	-61.05
	Max.	64.67	73.75	29.02	57.93
	Avg.	0.00	0.02	0.00	0.06
	Var.	1.01	1.55	0.75	1.44

Field :		J_x	J_y	J_z	$ J $
Cor. (%)		99.889	99.924	99.043	99.948
A	Min.	-152.12	-53.58	-24.72	0.00
	Max.	152.12	53.58	24.72	152.13
	Avg.	0.00	0.00	0.00	10.42
	Var.	16.73	14.54	3.06	19.80
N	Min.	-160.95	-61.12	-26.28	0.00
	Max.	160.94	61.11	26.27	164.85
	Avg.	0.00	0.00	0.00	10.40
	Var.	16.65	14.54	3.05	19.74
Δ	Min.	-46.60	-42.60	-18.38	-37.58
	Max.	46.62	42.61	18.37	35.82
	Avg.	0.00	0.00	0.00	0.02
	Var.	0.79	0.57	0.42	0.72

Table II: Electric field (top) and current density (bottom) comparisons for Run A. See the text for further information.

Field :		E_x	E_y	E_z	$ E $
Cor. (%)		99.930	99.964	98.726	99.973
A	Min.	-91.29	-141.05	-15.83	0.00
	Max.	91.29	66.25	15.83	141.06
	Avg.	0.00	-17.92	0.00	31.89
	Var.	26.79	39.15	3.60	39.59
N	Min.	-114.65	-174.31	-21.58	0.00
	Max.	114.66	81.34	21.58	177.72
	Avg.	0.00	-17.89	0.00	31.84
	Var.	26.74	39.08	3.62	39.53
Δ	Min.	-39.88	-45.83	-18.89	-38.24
	Max.	39.88	36.43	18.89	36.44
	Avg.	0.00	-0.03	0.00	0.05
	Var.	1.00	1.15	0.58	1.19

Field :		J_x	J_y	J_z	$ J $
Cor. (%)		99.927	99.926	98.589	99.957
A	Min.	-31.88	-30.05	-6.14	0.00
	Max.	31.88	65.85	6.14	65.97
	Avg.	0.00	0.00	0.00	7.54
	Var.	8.27	10.39	1.13	10.98
N	Min.	-40.07	-30.03	-8.95	0.00
	Max.	40.07	79.92	8.95	81.55
	Avg.	0.00	0.00	0.00	7.53
	Var.	8.26	10.36	1.14	10.96
Δ	Min.	-19.12	-17.06	-8.79	-17.91
	Max.	19.12	21.67	8.78	16.91
	Avg.	0.00	0.00	0.00	0.01
	Var.	0.32	0.40	0.19	0.39

Table III: As Table II, but for Run B.

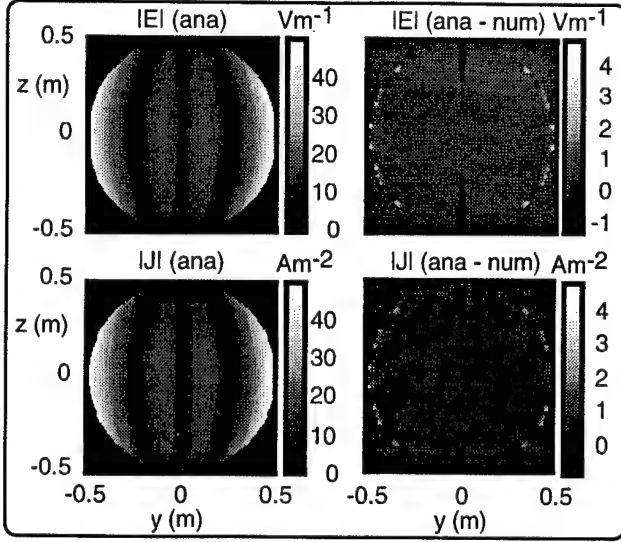


Figure 5: Field cross sections in the plane $x = 0$ for Run E.

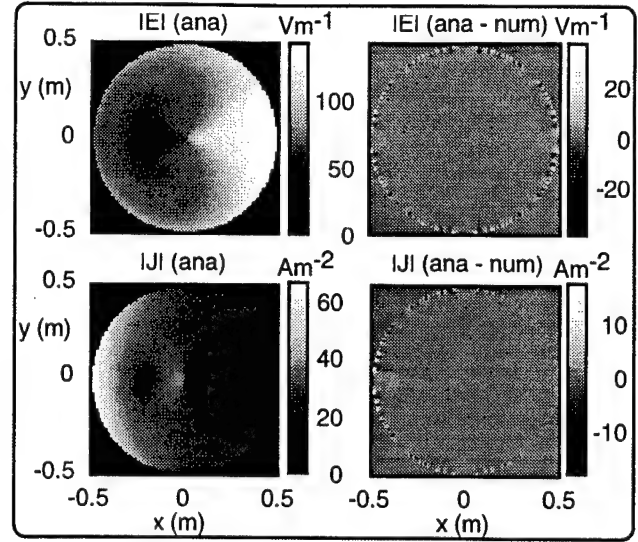


Figure 6: Field cross sections in the plane $z = 0$ for Run B (where $p = 1$).

Field :		E_x	E_y	E_z	$ \mathbf{E} $
Cor. (%)		99.755	99.969	98.624	99.974
A	Min.	-26.76	-98.59	-10.27	0.00
	Max.	26.76	98.59	10.27	98.60
	Avg.	0.00	0.00	0.00	16.39
	Var.	6.68	28.49	2.00	24.32
N	Min.	-38.84	-115.43	-14.43	0.00
	Max.	38.84	115.42	14.43	117.65
	Avg.	0.00	0.00	0.00	16.36
	Var.	6.68	28.44	2.02	24.28
Δ	Min.	-26.63	-30.49	-12.15	-25.31
	Max.	26.63	30.50	12.15	23.97
	Avg.	0.00	0.00	0.00	0.03
	Var.	0.47	0.71	0.33	0.66
Field :		J_x	J_y	J_z	$ \mathbf{J} $
Cor. (%)		99.891	99.927	98.902	99.948
A	Min.	-22.49	-7.18	-3.11	0.00
	Max.	22.49	7.18	3.11	22.50
	Avg.	0.00	0.00	0.00	2.12
	Var.	2.91	2.48	0.46	3.22
N	Min.	-25.21	-9.23	-3.46	0.00
	Max.	25.21	9.23	3.46	25.78
	Avg.	0.00	0.00	0.00	2.11
	Var.	2.90	2.48	0.46	3.21
Δ	Min.	-7.12	-6.41	-2.83	-5.79
	Max.	7.12	6.41	2.83	5.50
	Avg.	0.00	0.00	0.00	0.00
	Var.	0.14	0.09	0.07	0.12

Table IV: As Table II, but for Run C.

Field :		E_x	E_y	E_z	$ \mathbf{E} $
Cor. (%)		99.926	99.953	84.908	99.966
A	Min.	-80.04	-109.42	-4.09	0.00
	Max.	80.04	109.42	4.09	109.43
	Avg.	0.00	0.00	0.00	27.62
	Var.	24.75	34.90	0.84	32.69
N	Min.	-99.07	-134.93	-15.33	0.00
	Max.	99.08	134.93	15.33	137.58
	Avg.	0.00	0.00	0.00	27.57
	Var.	24.70	34.83	0.99	32.62
Δ	Min.	-31.19	-35.74	-14.63	-29.75
	Max.	31.20	35.75	14.63	28.36
	Avg.	0.00	0.00	0.00	0.05
	Var.	0.95	1.07	0.52	1.12
Field :		J_x	J_y	J_z	$ \mathbf{J} $
Cor. (%)		99.935	99.947	85.148	99.964
A	Min.	-79.54	-54.89	-3.01	0.00
	Max.	79.54	54.89	3.01	79.78
	Avg.	0.00	0.00	0.00	19.17
	Var.	20.85	20.81	0.60	22.38
N	Min.	-97.48	-68.56	-10.08	0.00
	Max.	97.49	68.57	10.08	99.45
	Avg.	0.00	0.00	0.00	19.14
	Var.	20.81	20.77	0.70	22.34
Δ	Min.	-26.16	-22.95	-10.69	-21.69
	Max.	26.15	22.95	10.69	20.63
	Avg.	0.00	0.00	0.00	0.03
	Var.	0.75	0.68	0.37	0.79

Table V: As Table II, but for Run D.

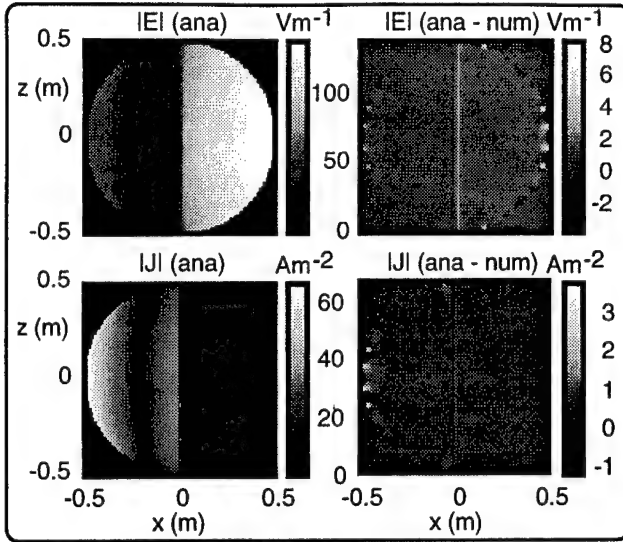


Figure 7: Field cross sections in the plane $y = 0$ for Run B.

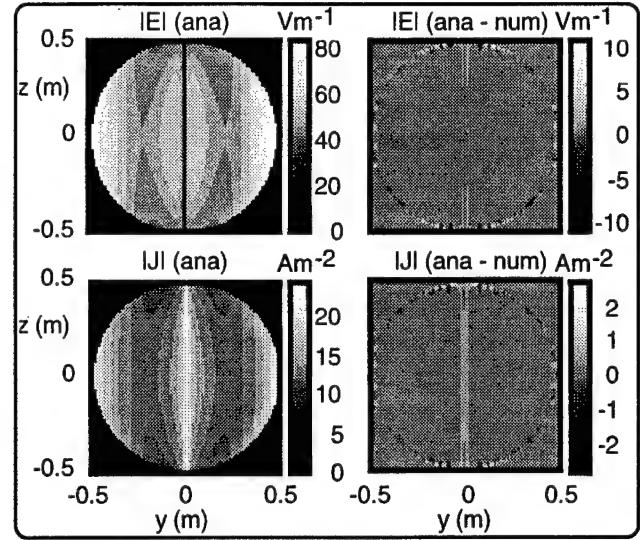


Figure 8: Field cross sections in the plane $x = 0$ for Run B.

Field :	E_x	E_y	E_z	$ E $
Cor. (%)	99.863	99.978	98.853	99.981
Min.	-55.12	-176.58	-17.37	0.00
Max.	55.12	176.58	17.37	176.59
Avg.	0.00	0.00	0.00	32.00
Var.	14.31	53.19	3.45	44.97
Min.	-72.51	-214.41	-26.73	0.00
Max.	72.51	214.39	26.73	218.18
Avg.	0.00	0.00	0.00	31.97
Var.	14.29	53.14	3.47	44.93
Min.	-50.21	-54.69	-24.24	-47.80
Max.	50.21	54.70	24.24	45.31
Avg.	0.00	0.00	0.00	0.03
Var.	0.75	1.12	0.52	1.07
Field :	J_x	J_y	J_z	$ J $
Cor. (%)	99.930	99.957	99.124	99.966
Min.	-49.91	-15.45	-6.12	0.00
Max.	49.91	15.45	6.12	49.91
Avg.	0.00	0.00	0.00	5.69
Var.	7.16	6.31	0.98	7.72
Min.	-59.22	-20.13	-7.79	0.00
Max.	59.22	20.13	7.79	60.34
Avg.	0.00	0.00	0.00	5.68
Var.	7.14	6.31	0.98	7.71
Min.	-15.43	-14.60	-6.96	-13.54
Max.	15.43	14.60	6.97	12.69
Avg.	0.00	0.00	0.00	0.01
Var.	0.27	0.19	0.13	0.25

Table VI: As Table II, but for Run E.

mersed in an axial quasi-uniform magnetic field, has a complex field pattern with a curved vortex system associated with each conductivity maximum. In particular, significant vertical fields can occur, in contrast to the uniformly conducting case. It has been shown that the numerical solution generally provides excellent global agreement, apart from significant discrepancies at the sphere boundary. Here the staircasing approximation inherent in the Cartesian-coordinate-based numerical code provides a poor representation to the true tangential current paths, and so leads to the observed errors.

Acknowledgment :

The authors thank the anonymous reviewers for their suggested improvements to this paper. The financial support of this research by NSERC, B.C. Hydro, TransAlta Utilities and Ontario Hydro is gratefully acknowledged.

References

- [1] Om P. Gandhi. Some numerical methods for dosimetry: Extremely low frequencies to microwave frequencies. *Radio Science*, 30(1):161-177, January-February 1995.
- [2] Om P. Gandhi and Jin-Yuang Chen. Numerical dosimetry at power-line frequencies using anatomically based models. *Bioelectromagnetics Supplement*, 1:43-60, 1992.

- [3] Om P. Gandhi, John F. DeFord, and Hiroshi Kanai. Impedance method for calculation of power deposition patterns in magnetically induced hyperthermia. *IEEE. Trans. Biomedical Engineering*, **BME-31**(10):644-651, October 1984.
- [4] Niel Orcutt and Om P. Gandhi. A 3-D impedance method to calculate power deposition in biological bodies subjected to time varying magnetic fields. *IEEE. Trans. Biomedical Engineering*, **35**(8):577-583, August 1988.
- [5] Weiguo Xi, Maria A. Stuchly, and Om P. Gandhi. Induced electric currents in models of man and rodents from 60 Hz magnetic fields. *IEEE Trans. Biomed. Eng.*, **BME-41**(11):1018-1023, 1994.
- [6] Jan De Moerloose, Trevor W. Dawson, and Maria A. Stuchly. Application of FDTD to quasi-static field analysis. *Radio Science*, 1996. (manuscript submitted for publication).
- [7] Trevor W. Dawson, Jan De Moerloose, and Maria A. Stuchly. Comparison of magnetically induced ELF fields in humans computed by FDTD and scalar potential FD codes. *Applied Computational Electromagnetics Society Journal*, 1996. (manuscript accepted for publication).
- [8] J. Van Bladel. *Electromagnetic Fields*. Hemisphere Publishing Corporation, Washington D.C., revised printing edition, 1985.
- [9] Trevor W. Dawson and Maria A. Stuchly. An analytic solution for verification of computer models for low-frequency magnetic induction. *Radio Science*, 1996. (manuscript submitted for publication).
- [10] R.D. da Cunha and T.R. Hopkins. PIM 2.0 : Parallel Iterative Methods package for systems of linear equations; (FORTRAN 77 version), 1993. ©1993 R.D. da Cunha, T.R. Hopkins and Computing Laboratory, University of Kent at Canterbury, Canterbury, U.K. and Centro de Processamento de Dados, Universidade Federal do Rio Grande do Sul, Porto Alegre, Brasil.
- [11] John L. Volakis. EM programmer's notebook. *IEEE Antennas and Propagation Magazine*, **37**(6):94-96, 1995.
- [12] Richard Holland. Pitfalls of staircase meshing. *IEEE Trans. Electromagn. Compat.*, **35**(4):434-439, 1993.

The Gradient Associated Conjugate Direction Method

Min Zhang

Deutsches Elektronen-Synchrotron (DESY) -MPY-
Notkestrasse 85, 22603 Hamburg, Germany

Abstract

A new conjugate direction (CD) based method, GaCD by name, is addressed with its full derivations. Comparison with some commonly used CD methods is made, concluding that the GaCD method is among the best of them, in terms of an assessment number. A practical example is presented in which a waveguide-microstrip transition section is optimized with respect to its transmission parameter S_{21} . The measurement of the transition agrees very well with the numerical results.

1 Introduction

A numerical optimization procedure can be divided into two distinctive parts: local extrema search and global area search, which is really necessary for most practical optimization problems. In its analytical counterpart, however, there will be no such clear classification. There, the determination of the global optimum is done relatively explicitly.

Here we will only concentrate on the local extrema search phase. As known, in a certain close vicinity of a local extremum, the goal function in question can be well approximated by an appropriate quadratic function, say, the 2nd order approximation of its Taylor's expansion series at that point.

For quadratic functions, there is a unique property that if there exist n conjugate directions, at most n 1d (one-dimensional) extrema searches along these directions are needed before the function's extremum is reached. This property is usually referred to as *quadratic convergence* or *quadratic cut-off*.

Based on this property, there developed a class of optimization methods, which are usually designated by the name of "Conjugate Direction" (CD) methods, e.g. DFP, Fletcher-Reeves, Powell, Daniel, Sorenson-Wolfe, etc [1].

In all the CD-derived methods, the key point is how to generate successively linearly independent search directions, which are conjugate to one another. In the GaCD method here, the gradient "G" of the goal function is used for providing an offset from current optimization point, which will never degenerate to zero unless a stagnation point has been reached. The offset serves as an indispensable ingredient for generating a next conjugate direction in this method. The above statements hold exactly true at least when the method is applied to the quadratic functions.

2 The GaCD Method

2.1 Preliminaries

Any n dimensional quadratic functions can be written in the following form:

$$\mathcal{G}(\mathbf{X}) = \frac{1}{2}\mathbf{X}^T\mathbf{H}\mathbf{X} + \mathbf{b}^T\mathbf{X} + c \quad (\mathbf{X} \in \mathbb{R}^n). \quad (1)$$

\mathbf{H} is an $n \times n$ positive-definite symmetric matrix. Therefore the function has one minimum point which is denoted by \mathbf{X}^* . \mathbf{X} and \mathbf{b} are n -dimensional vectors; c is a constant; T denotes transposition.

Conjugate: If there exist two n -dimensional vectors \mathbf{P}_i and \mathbf{P}_j , and they fulfill:

$$\mathbf{P}_i^T\mathbf{H}\mathbf{P}_j = 0, \quad \mathbf{P}_i^T\mathbf{H}\mathbf{P}_i \neq 0, \quad \text{and} \quad \mathbf{P}_j^T\mathbf{H}\mathbf{P}_j \neq 0, \quad (2)$$

then the two vectors \mathbf{P}_i and \mathbf{P}_j are called *conjugate* to each other with respect to \mathbf{H} , or simply, *\mathbf{H} -conjugate*.

Definitions below will be used throughout the derivation:

$$\mathbf{Q}_i \equiv \nabla \mathcal{G}(\mathbf{X}_i) = \mathbf{H}\mathbf{X}_i + \mathbf{b}, \quad (3)$$

$$\mathbf{R}_i \equiv \mathbf{Q}_{i+1} - \mathbf{Q}_i, \quad (4)$$

$$\nabla^2 \mathcal{G}(\mathbf{X}_i) \equiv \nabla \cdot \nabla \mathcal{G}(\mathbf{X}_i) = \mathbf{H}. \quad (5)$$

Let us assume that \mathbf{P}_i ($i = 1, 2, \dots, n$) are n \mathbf{H} -conjugate vectors. Since \mathbf{H} -conjugate vectors are linearly independent of one another, \mathbf{X}^* can be expressed with the n \mathbf{H} -conjugate vectors in the following form:

$$\mathbf{X}^* = \sum_{i=1}^n \lambda_i^* \mathbf{P}_i, \quad (6)$$

with λ_i^* ($i = 1, 2, \dots, n$) being coefficients to be determined. Since \mathbf{X}^* is an extremum point, it satisfies

$$\nabla \mathcal{G}(\mathbf{X}^*) = \mathbf{0}, \quad \text{i.e.} \quad (7)$$

$$\mathbf{H}\mathbf{X}^* + \mathbf{b} = \mathbf{0}. \quad (8)$$

Substituting \mathbf{X}^* in Eq. 8 with Eq. 6 yields

$$\mathbf{H} \left(\sum_{i=1}^n \lambda_i^* \mathbf{P}_i \right) + \mathbf{b} = \mathbf{0}. \quad (9)$$

Using the conjugate property (Eq. 2), we obtain

$$\lambda_i^* = -\frac{\mathbf{P}_i^T \mathbf{b}}{\mathbf{P}_i^T \mathbf{H} \mathbf{P}_i}. \quad (10)$$

Now the key point is how to find out \mathbf{H} and \mathbf{b} . For large dimensional problems, finding them is almost impossible or too time-consuming. Thus such a direct solution is not practically usable. We have to figure out other ways. One of them is an iteration procedure using the so-called *accurate 1d search*. To illustrate this method in a clearer manner, we split it into two steps. In the first, the concept of *accurate 1d search* is introduced, and then derivation of the iteration procedure is presented.

2.2 Accurate 1d Search

Below is a 1d search problem

$$\mathcal{G}(\mathbf{X}_{k+1}) \equiv \mathcal{G}(\mathbf{X}_k + \lambda_k \mathbf{P}_k) \equiv \min_{\forall \lambda \in \mathbb{R}} \{\mathcal{G}(\mathbf{X}_k + \lambda \mathbf{P}_k)\}, \quad (11)$$

with \mathbf{X}_k being current point and \mathbf{P}_k current search direction.

To solve this 1d problem, the following commonly used method can be employed:

$$\frac{d\mathcal{G}}{d\lambda} \big|_{\lambda=\lambda_k} = [\nabla \mathcal{G}(\mathbf{X}_k + \lambda \mathbf{P}_k)]^T \big|_{\lambda=\lambda_k} \mathbf{P}_k = 0. \quad (12)$$

Due to

$$\nabla \mathcal{G}(\mathbf{X}_{k+1}) = \mathbf{H}\mathbf{X}_{k+1} + \mathbf{b}, \quad (13)$$

inserting Eq. 13 into Eq. 12 yields

$$\begin{aligned} (\mathbf{H}\mathbf{X}_{k+1} + \mathbf{b})^T \mathbf{P}_k &= [\mathbf{H}(\mathbf{X}_k + \lambda_k \mathbf{P}_k) + \mathbf{b}]^T \mathbf{P}_k \\ &= [(\mathbf{H}\mathbf{X}_k + \mathbf{b}) + \lambda_k \mathbf{H}\mathbf{P}_k]^T \mathbf{P}_k \\ &= \nabla^T \mathcal{G}(\mathbf{X}_k) \mathbf{P}_k + \lambda_k \mathbf{P}_k^T \mathbf{H} \mathbf{P}_k \\ &= 0 \end{aligned} \quad (14)$$

(Note: The property $\mathbf{H}^T = \mathbf{H}$ is utilized above.). Then we obtain

$$\lambda_k = -\frac{\mathbf{P}_k^T \nabla \mathcal{G}(\mathbf{X}_k)}{\mathbf{P}_k^T \mathbf{H} \mathbf{P}_k} = -\frac{\mathbf{P}_k^T \mathbf{Q}_k}{\mathbf{P}_k^T \mathbf{H} \mathbf{P}_k}. \quad (15)$$

The above procedure is called *accurate 1d search*.

2.3 The Derivation

Assume we have n \mathbf{H} -conjugate vectors \mathbf{P}_i ($i = 1, 2, \dots, n$) and an initial point \mathbf{X}_1 , performing accurate 1d search once along \mathbf{P}_1 leads to \mathbf{X}_2 :

$$\mathbf{X}_2 = \mathbf{X}_1 + \lambda_1 \mathbf{P}_1, \quad (16)$$

(Note: λ_1 satisfies Eq. 15.). After n such searches which are performed along \mathbf{P}_i ($i = 1, 2, \dots, n$) respectively, a point denoted by \mathbf{X}_{n+1} is reached:

$$\mathbf{X}_{n+1} = \mathbf{X}_1 + \sum_{i=1}^n \lambda_i \mathbf{P}_i, \quad (17)$$

with λ_i ($i = 1, 2, \dots, n$) all fulfilling Eq. 15.

We will prove that \mathbf{X}_{n+1} must be the minimum point \mathbf{X}^* , i.e.

$$\mathbf{Q}_{n+1} = \nabla \mathcal{G}(\mathbf{X}_{n+1}) = \mathbf{0}. \quad (18)$$

From Eqs. 3 and Eq. 17, we have

$$\begin{aligned}
\mathbf{Q}_{n+1} &= \nabla \mathcal{G}(\mathbf{X}_{n+1}) \\
&= \mathbf{H} \left(\sum_{i=1}^n \lambda_i \mathbf{P}_i + \mathbf{X}_1 \right) + \mathbf{b} \\
&= \sum_{i=1}^n \lambda_i \mathbf{H} \mathbf{P}_i + (\mathbf{H} \mathbf{X}_1 + \mathbf{b}) \\
&= \sum_{i=1}^n \lambda_i \mathbf{H} \mathbf{P}_i + \mathbf{Q}_1.
\end{aligned} \tag{19}$$

Multiplying both sides with \mathbf{P}_1^T :

$$\begin{aligned}
\mathbf{P}_1^T \mathbf{Q}_{n+1} &= \mathbf{P}_1^T \left(\sum_{i=1}^n \lambda_i \mathbf{H} \mathbf{P}_i + \mathbf{Q}_1 \right) \\
&\stackrel{\text{Eq. 2}}{=} \lambda_1 \mathbf{P}_1^T \mathbf{H} \mathbf{P}_1 + \mathbf{P}_1^T \mathbf{Q}_1 \\
&\stackrel{\text{Eq. 15}}{=} -\frac{\mathbf{P}_1^T \mathbf{Q}_1}{\mathbf{P}_1^T \mathbf{H} \mathbf{P}_1} \mathbf{P}_1^T \mathbf{H} \mathbf{P}_1 + \mathbf{P}_1^T \mathbf{Q}_1 \\
&= 0;
\end{aligned} \tag{20}$$

And multiplying with \mathbf{P}_2^T :

$$\begin{aligned}
\mathbf{P}_2^T \mathbf{Q}_{n+1} &= \mathbf{P}_2^T \left(\sum_{i=1}^n \lambda_i \mathbf{H} \mathbf{P}_i + \mathbf{Q}_1 \right) \\
&= \mathbf{P}_2^T \left(\sum_{i=2}^n \lambda_i \mathbf{H} \mathbf{P}_i + \lambda_1 \mathbf{H} \mathbf{P}_1 + (\mathbf{H} \mathbf{X}_1 + \mathbf{b}) \right) \\
&= \mathbf{P}_2^T \left(\sum_{i=2}^n \lambda_i \mathbf{H} \mathbf{P}_i + \mathbf{H}(\lambda_1 \mathbf{P}_1 + \mathbf{X}_1) + \mathbf{b} \right) \\
&\stackrel{\text{Eq. 16}}{=} \mathbf{P}_2^T \left(\sum_{i=2}^n \lambda_i \mathbf{H} \mathbf{P}_i + \mathbf{H} \mathbf{X}_2 + \mathbf{b} \right) \\
&= \mathbf{P}_2^T \left(\sum_{i=2}^n \lambda_i \mathbf{H} \mathbf{P}_i + \mathbf{Q}_2 \right) \\
&\stackrel{\text{Eq. 15}}{=} 0.
\end{aligned} \tag{21}$$

Repeating the above for all other \mathbf{P}_i ($i = 3, \dots, n$), we have

$$\mathbf{P}_i^T \mathbf{Q}_{n+1} = 0 \quad (\forall i = 1, 2, \dots, n). \tag{22}$$

As known, \mathbf{H} -conjugate vectors are linearly independent of one another. It means that the n \mathbf{H} -conjugate vectors ($\mathbf{P}_i, i = 1, 2, \dots, n$) span a complete basis over \mathbb{R}^n . A vector in \mathbb{R}^n which is orthogonal to all the base vectors is nothing but a zero vector. That is,

$$\mathbf{Q}_{n+1} = \mathbf{0}. \tag{23}$$

Then Eq. 18 gets proved. From the above, following conclusions can be drawn:

For any function which can be expressed by Eq. 1, if there exist n \mathbf{H} -conjugate n -dimensional vectors \mathbf{P}_i ($i = 1, 2, \dots, n$), then its extremum point \mathbf{X}^* can be obtained by doing at most n accurate 1d searches in the directions of \mathbf{P}_i ($i = 1, 2, \dots, n$), respectively.

This relieves us from the difficulty in using the explicit form for λ 's (Eq. 15), since normally the matrix \mathbf{H} is unknown. In the following, whenever we say "do accurate 1d search", it implies an evaluation of Eq. 15.

Next we will discuss how to generate \mathbf{H} -conjugate vectors. First, let us derive three important properties, from which the method is deduced.

$$\begin{aligned}\mathbf{P}_i^T \mathbf{H} \mathbf{P}_j &= \frac{1}{\lambda_j} \mathbf{P}_i^T \mathbf{H} \lambda_j \mathbf{P}_j = \frac{1}{\lambda_j} \mathbf{P}_i^T \mathbf{H} (\mathbf{X}_{j+1} - \mathbf{X}_j) \\ &= \frac{1}{\lambda_j} \mathbf{P}_i^T [(\mathbf{H} \mathbf{X}_{j+1} + \mathbf{b}) - (\mathbf{H} \mathbf{X}_j + \mathbf{b})] = \frac{1}{\lambda_j} \mathbf{P}_i^T (\mathbf{Q}_{j+1} - \mathbf{Q}_j) \\ &= \frac{1}{\lambda_j} \mathbf{P}_i^T \mathbf{R}_j \begin{cases} = 0 & (i \neq j) \\ \neq 0 & (i = j) \end{cases} \quad (i, j = 1, 2, \dots, n)\end{aligned}\quad (24)$$

Eq. 24 can also be written in the following form:

$$\mathbf{P}_i^T \mathbf{Q}_i = \mathbf{P}_i^T \mathbf{Q}_{i-1} = \mathbf{P}_i^T \mathbf{Q}_{i-2} = \dots = \mathbf{P}_i^T \mathbf{Q}_1 \quad (i = 1, 2, \dots, n). \quad (25)$$

Below is given the derivation of another conclusion which reads as

$$\mathbf{P}_i^T \mathbf{Q}_j = 0 \quad (i < j). \quad (26)$$

Let $j = i + 1$,

$$\begin{aligned}\mathbf{P}_i^T \mathbf{Q}_{i+1} &= \mathbf{P}_i^T (\mathbf{H} \mathbf{X}_{i+1} + \mathbf{b}) = \mathbf{P}_i^T [\mathbf{H} (\mathbf{X}_i + \lambda_i \mathbf{P}_i) + \mathbf{b}] \\ &= \mathbf{P}_i^T [(\mathbf{H} \mathbf{X}_i + \mathbf{b}) + \lambda_i \mathbf{H} \mathbf{P}_i] = \mathbf{P}_i^T \mathbf{Q}_i + \lambda_i \mathbf{P}_i^T \mathbf{H} \mathbf{P}_i \\ &\stackrel{\text{Eq. 15}}{=} \mathbf{P}_i^T \mathbf{Q}_i - \frac{\mathbf{P}_i^T \mathbf{Q}_i}{\mathbf{P}_i^T \mathbf{H} \mathbf{P}_i} \mathbf{P}_i^T \mathbf{H} \mathbf{P}_i = 0.\end{aligned}\quad (27)$$

Likewise, let $j > i + 1$,

$$\begin{aligned}\mathbf{P}_i^T \mathbf{Q}_j &= \mathbf{P}_i^T (\mathbf{H} \mathbf{X}_j + \mathbf{b}) = \mathbf{P}_i^T [\mathbf{H} (\mathbf{X}_{j-1} + \lambda_{j-1} \mathbf{P}_{j-1}) + \mathbf{b}] \\ &= \mathbf{P}_i^T [(\mathbf{H} \mathbf{X}_{j-1} + \mathbf{b}) + \lambda_{j-1} \mathbf{H} \mathbf{P}_{j-1}] = \mathbf{P}_i^T \mathbf{Q}_{j-1} + \lambda_{j-1} \mathbf{P}_i^T \mathbf{H} \mathbf{P}_{j-1} \\ &= \mathbf{P}_i^T \mathbf{Q}_{j-1} = \dots \\ &= \mathbf{P}_i^T \mathbf{Q}_{i+1} = 0.\end{aligned}\quad (28)$$

Equation 26 gets proved.

This equation indicates that

The gradient \mathbf{Q}_{k+1} after k accurate 1d searches is orthogonal to all former search directions $(\mathbf{P}_i, i = 1, 2, \dots, k)$.

Besides this, it also delivers us another deep connotation: after n accurate 1d searches, the last gradient \mathbf{Q}_{n+1} satisfies $\mathbf{P}_i^T \mathbf{Q}_{n+1} = 0$, ($\forall i = 1, 2, \dots, n$). Since, as known, there are at most n linearly independent vectors in an n -dimensional linear space, the only solution to this equation is $\mathbf{Q}_{n+1} = \mathbf{0}$, which means that \mathbf{X}_{n+1} is nothing but the extremum point \mathbf{X}^* .

A next search direction may be formed using \mathbf{Q}_{k+1} . It is this that the so-called *conjugate gradient method* is based on. Here we will use it for another purpose, namely, for finding an offset which does not lie in the subspace which is spanned by all previous search directions. The actual usefulness of the offset will be investigated right after.

To derive the GaCD method, one more conclusion is needed.

Known that \mathbf{P}_i ($i = 1, 2, \dots, k$) are \mathbf{H} -conjugate. k successive accurate 1d searches in these directions from two different initial points, say \mathbf{X}'_1 and \mathbf{X}''_1 have been performed, yielding other two points \mathbf{X}'_{k+1} and \mathbf{X}''_{k+1} . Then the difference vector $(\mathbf{X}'_{k+1} - \mathbf{X}''_{k+1})$ is \mathbf{H} -conjugate to \mathbf{P}_i ($i = 1, 2, \dots, k$), that is,

$$(\mathbf{X}'_{k+1} - \mathbf{X}''_{k+1})^T \mathbf{H} \mathbf{P}_i = 0 \quad (\forall i = 1, 2, \dots, k). \quad (29)$$

Since

$$\mathbf{X}'_{k+1} = \mathbf{X}'_1 + \sum_{i=1}^k \lambda'_i \mathbf{P}_i, \quad (30)$$

$$\mathbf{X}''_{k+1} = \mathbf{X}''_1 + \sum_{i=1}^k \lambda''_i \mathbf{P}_i, \quad (31)$$

we have

$$\mathbf{X}'_{k+1} - \mathbf{X}''_{k+1} = \mathbf{X}'_1 - \mathbf{X}''_1 + \sum_{i=1}^k (\lambda'_i - \lambda''_i) \mathbf{P}_i. \quad (32)$$

For any \mathbf{P}_j ($j = 1, 2, \dots, k$),

$$\begin{aligned} (\mathbf{X}'_{k+1} - \mathbf{X}''_{k+1})^T \mathbf{H} \mathbf{P}_j &= (\mathbf{X}'_1 - \mathbf{X}''_1)^T \mathbf{H} \mathbf{P}_j + \sum_{i=1}^k (\lambda'_i - \lambda''_i) \mathbf{P}_i^T \mathbf{H} \mathbf{P}_j \\ &= (\mathbf{X}'_1 - \mathbf{X}''_1)^T \mathbf{H} \mathbf{P}_j + (\lambda'_j - \lambda''_j) \mathbf{P}_j^T \mathbf{H} \mathbf{P}_j \\ &= (\mathbf{X}'_1 - \mathbf{X}''_1)^T \mathbf{H} \mathbf{P}_j + \mathbf{P}_j^T \mathbf{Q}''_j - \mathbf{P}_j^T \mathbf{Q}'_j \\ &= [\mathbf{H}(\mathbf{X}'_1 - \mathbf{X}''_1)]^T \mathbf{P}_j + \mathbf{P}_j^T \mathbf{Q}''_j - \mathbf{P}_j^T \mathbf{Q}'_j \\ &= [(\mathbf{H} \mathbf{X}'_1 + \mathbf{b}) - (\mathbf{H} \mathbf{X}''_1 + \mathbf{b})]^T \mathbf{P}_j + \mathbf{P}_j^T \mathbf{Q}''_j - \mathbf{P}_j^T \mathbf{Q}'_j \\ &= (\mathbf{Q}'_1 - \mathbf{Q}''_1)^T \mathbf{P}_j + \mathbf{P}_j^T \mathbf{Q}''_j - \mathbf{P}_j^T \mathbf{Q}'_j \\ &= \mathbf{P}_j^T \mathbf{Q}'_1 - \mathbf{P}_j^T \mathbf{Q}''_1 + \mathbf{P}_j^T \mathbf{Q}''_j - \mathbf{P}_j^T \mathbf{Q}'_j \\ &\stackrel{\text{Eq. 25}}{=} 0. \end{aligned} \quad (33)$$

Because the above assumption is made for an arbitrary j , Eq. 29 gets proved.

Equation 29 provides us an effective way to acquire search directions which are \mathbf{H} -conjugate while Eq. 26 may be utilized to get an offset point which is needed by Eq. 29. No care needs to be taken whether the offset will degenerate to zero or not, since, if true, it means that current point is already the extremum one, i.e. the \mathbf{X}^* , therefore, no more search is needed.

2.4 The Algorithm

Based upon all the arguments above, the GaCD method can be formed as follows. $a \Leftarrow b$ stands for *assign b to a*. ϵ is a given stop-criterion. \mathbf{X}_1 is an initial point.

1. $j \Leftarrow 0$;
2. $j \Leftarrow j + 1$; $\mathbf{X}_j^0 \Leftarrow \mathbf{X}_j$;
3. Find $\mathbf{Q}_j^0 = \nabla \mathcal{G}(\mathbf{X}_j^0)$ and do *accurate 1d search* in the \mathbf{Q}_j^0 , i.e.

$$\mathbf{X}_j^0 \Leftarrow \mathbf{X}_j^0 + \lambda_j^0 \mathbf{Q}_j^0;$$

4. If $j > 1$, then for $i = 1, 2, \dots, j - 1$, do *accurate 1d searches*:

$$\mathbf{X}_j^i \Leftarrow \mathbf{X}_j^{i-1} + \lambda_j^i \mathbf{P}_i;$$

5. $\mathbf{X}_{j+1} \Leftarrow \mathbf{X}_j^{j-1}$; $\mathbf{P}_j \Leftarrow \mathbf{X}_{j+1} - \mathbf{X}_j$;

6. If $j > 1$, then do one more *accurate 1d search* in \mathbf{P}_j :

$$\mathbf{X}_{j+1} \Leftarrow \mathbf{X}_{j+1} + \lambda_j^j \mathbf{P}_j;$$

7. If $j < n$, then go back to 2; Else,
if $|\mathbf{X}_{n+1} - \mathbf{X}_n| < \epsilon$, then stop; Else

$$\mathbf{X}_1 \Leftarrow \mathbf{X}_{n+1},$$

and go back to 1.

2.5 A 2d Verification

Assume we have a 2d quadratic function as follows:

$$\mathcal{G}(x_1, x_2) = x_1^2 + 2x_2^2 - 4x_1 - 2x_1x_2. \quad (34)$$

It is found that

$$\mathbf{H} = \begin{pmatrix} 2 & -2 \\ -2 & 4 \end{pmatrix}, \quad \mathbf{b} = \begin{pmatrix} -4 \\ 0 \end{pmatrix}, \quad c = 0.$$

It reaches its minimum at point $\mathbf{X}^* = (x_1^*, x_2^*)^T = (4, 2)^T$.

By selecting an initial point

$$\mathbf{X}_1 = \begin{pmatrix} 1 \\ 1 \end{pmatrix},$$

and following the algorithm above step by step, we obtain the final result $\mathbf{X}^\wedge = (4, 2)^T = \mathbf{X}^*$ after two search loops, which verifies the *quadratic cut-off* property of the method. Note that the

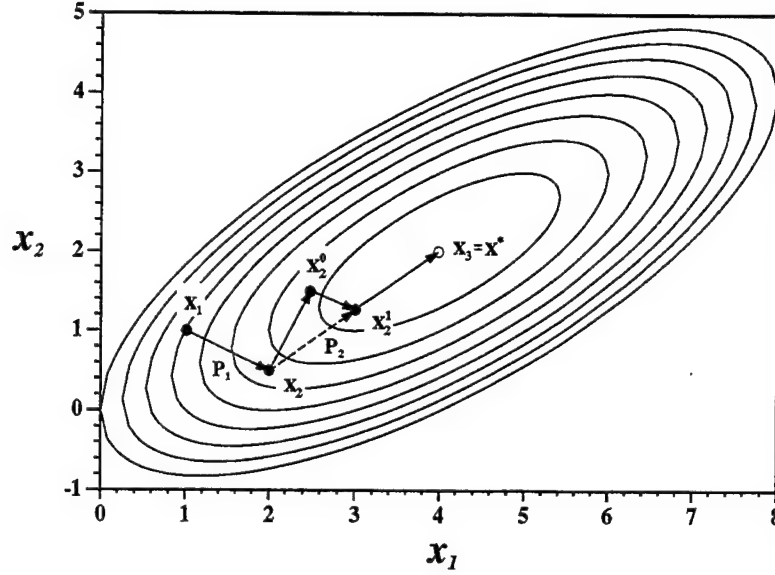


Figure 1: Search Path in Minimizing $\mathcal{G}(x_1, x_2)$

above verification holds true both analytically and numerically. The search path for the numerical verification is shown in Fig. 1.

Starting from \mathbf{X}_1 , evaluating the gradient at that point, using the gradient as a search direction \mathbf{P}_1 , it reaches \mathbf{X}_2 after the first loop. Then a search in the current gradient is performed, yielding \mathbf{X}_2^0 , which serves as the offset point. Searching in \mathbf{P}_1 , we get a new point \mathbf{X}_2^1 , which is a counterpart to \mathbf{X}_2 , for they are both the extremum points in the same search direction (\mathbf{P}_1) but from two different initial points, \mathbf{X}_2^0 and \mathbf{X}_1 respectively. From Eq. 29, it is known that the difference vector $\mathbf{P}_2 = (\mathbf{X}_2^1 - \mathbf{X}_2)$ must be \mathbf{H} -conjugate to \mathbf{P}_1 . Now down to this direction \mathbf{P}_2 , the algorithm finally converges to $\mathbf{X}_3 = \mathbf{X}^*$.

3 Comparison with Other CD Methods

The comparison is made by optimizing nine "standard" test functions [2], which are listed in Appendix A. The methods to be checked are GaCD, DFP, Fletcher-Reeves, M-Powell (modified Powell), of which DFP and Fletcher-Reeves' are among the best and most popularly used CD ones. In addition, the Evolution Strategy (ES) [3] is also tested and presented here for the readers who may be interested in such stochastic methods.

In order that a uniform assessment of optimization performance of the methods can be achieved, a parameter η is introduced, which is defined as

$$\eta \equiv \frac{|\log(\mathcal{G}^\wedge / \mathcal{G}^0)|}{N_{\mathcal{G}}} \times 100,$$

where \mathcal{G}^0 and \mathcal{G}^\wedge are the initial and final goal values, respectively; $N_{\mathcal{G}}$ is the number of function evaluations. The greater the number, the more effective the method is supposed to be. In the definition, we took the number of evaluations of goal function as a factor which reflects the computation time, not directly the time itself. It is because for numerical optimization procedures,

the evaluation of a goal function means a complete solution of an electromagnetic problem, which takes, normally, the most significant part of the whole computing time including the optimization strategy and other auxiliary operations.

The test runs are performed on a SUN SPARC-1 workstation. Each run takes normally less than one second. Table 1 shows the statistic summary and rankings of the methods, which are derived from the raw calculation results in Appendix B. It is seen that the GaCD method is the most robust (σ_η) while its effectiveness (η) comes to the second after the DFP method.

Comparison of Various Optimization Methods via Common Test Functions (Statistics&Rankings)							
		GaCD	BFGS	DFP	Fletcher	M-Powell	ES
Rankings	$\langle\eta_0\rangle$	0.86 (1)	0.84 (2)	0.77 (3)	0.65 (4)	0.35 (5)	0.17 (6)
	σ_{η_0}	0.17 (2)	0.24 (5)	0.19 (3)	0.22 (4)	0.28 (6)	0.10 (1)
BEALE		1.0	0.6284	0.7339	0.8970	0.0527	0.1085
CRAGG		0.9053	0.2524	1.0	0.3437	0.2660	0.1003
ENGVALL-2d		0.9170	1.0	0.8207	0.6696	0.7281	0.1540
ENGVALL-3d		0.8453	1.0	0.4120	0.3170	0.0	0.2465
POWELL		0.4286	1.0	0.7788	0.4342	0.2757	0.0896
WHITE		0.7663	1.0	0.5217	0.6521	0.3339	0.2352
WOOD		1.0	0.7594	0.7213	0.8710	0.5734	0.3802
ZANGWILL-2d		0.9070	0.9785	1.0	0.8722	0.0873	0.1795
ZANGWILL-3d		1.0	0.9357	0.8963	0.8220	0.8046	0.0534

Table 1: Rankings of the Optimization Methods Tested. The η 's associated with respective test functions are normalized with the highest η value of the different methods. For instance, η 's for the BEALE function are normalized with that of the M-Powell's, i.e. 1.923, which is the largest in that row (Appendix B). $\eta = 0$ means that the corresponding methods failed for the related functions, e.g. the Fletcher-Reeves method failed in handling the WHITE function. In principle, the larger the number η , the more effective the method is considered to be; while the smaller the number σ_η (deviation of η), the more versatile or stabler the method is regarded.

4 Optimization of a Waveguide-Microstrip Transition

The object to be optimized is a *pair* of transitions between a rectangular waveguide and a microstrip line. Scattering parameter S_{21} is used to assess the performance of the component. It is maximized at the center frequency 10GHz with a ± 400 MHz bandwidth.

4.1 The Structure

A basic structure of such Waveguide-Microstrip Transition Pairs (WMTP) is shown in Fig. 2. Such layout with two identical back-to-back transitions will accommodate a more accurate mea-

surement.

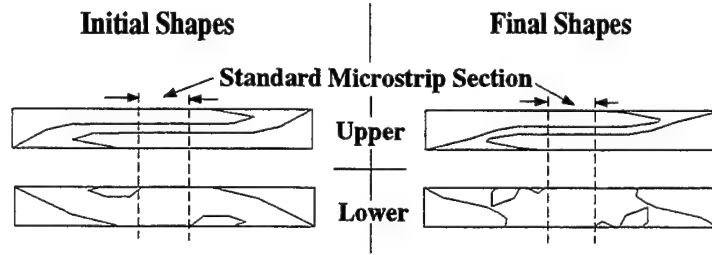
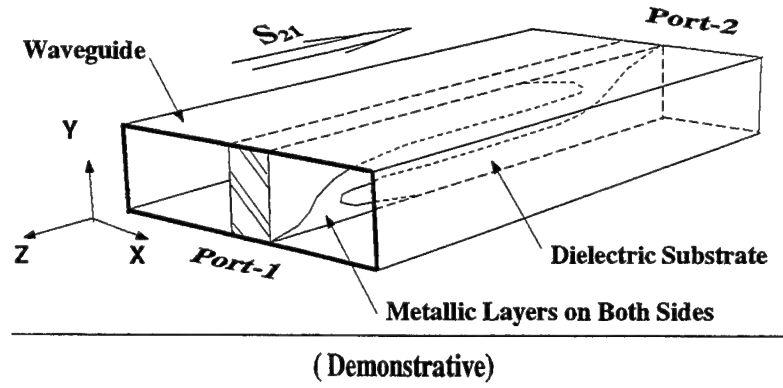


Figure 2: Basic Structure of a WMTTP. The standard X-band rectangular waveguide is used, i.e. $a \times b = 22.8\text{mm} \times 10.0\text{mm}$. The dielectric is RT/duroid 5880 from Rogers with a thickness of $1.57 \pm 0.05\text{mm}$, $\epsilon_r = 2.20$.

4.2 Definition of the Problem

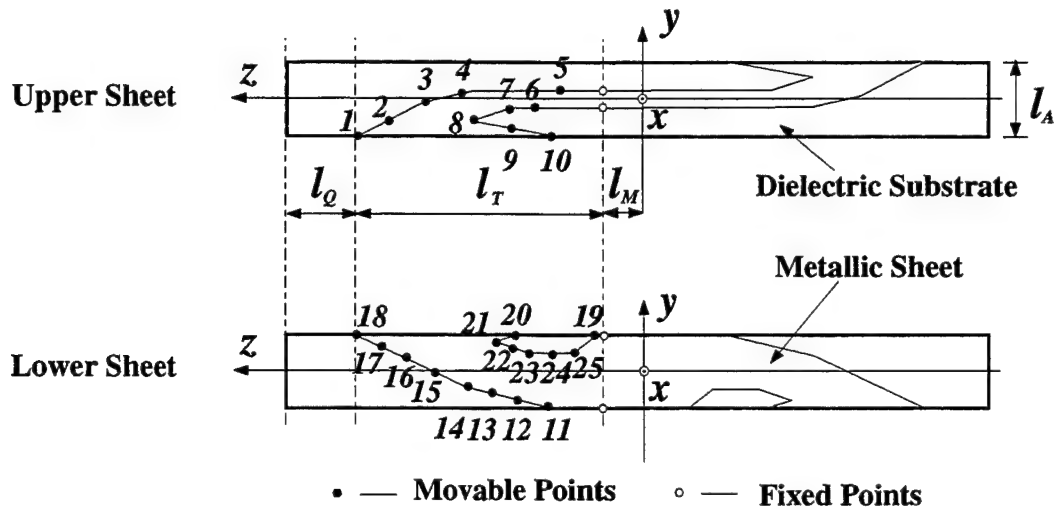


Figure 3: Optimization Vector for WMTTP

Total 25 points along the profiles of the upper and the lower metallic sheets are used as the optimization vector \mathbf{X} (Fig. 3). Among them, points #21 to #25 are changeable in both y and z

directions while the rest only in z . It is therefore a problem of 30 degrees of freedom. The definition range is: $l_M \leq z \leq (l_M + l_T)$ for points #1 to #20 and $l_M \leq z \leq (l_M + l_T)$, $-l_A/2 \leq y \leq l_A/2$ for points #21 to #25. The whole set of the definition ranges for \mathbf{X} is denoted by $\mathcal{X} \subset \mathbb{R}^{30}$. A standard microstrip section in the middle of the structure is maintained by imposing the constraint that points #5, #6, #11, and #19 are not allowed to pass the limit of $z < l_M$.

The goal function is defined as

$$\mathcal{G}(\mathbf{X}) \equiv \overline{S_{21}}(\mathbf{X}), \quad (35)$$

with $\overline{S_{21}}$ being an average of $|S_{21}|$ over the desired bandwidth, that is,

$$\overline{S_{21}} \equiv \frac{1}{n-m} \sum_{i=m}^n |S_{21}(f_i)|. \quad (36)$$

f_m to f_n covers the desired bandwidth, i.e. 9.6GHz - 10.4GHz.

The optimization problem can then be expressed as

$$\mathcal{G}^* \equiv \max \{\mathcal{G}(\mathbf{X})\} \quad (\forall \mathbf{X} \in \mathcal{X}). \quad (37)$$

Note: The mode in question is the fundamental one, i.e. H_{10} .

4.3 The Optimization

The optimization is performed by using the optimization driver which is implemented in the general purpose electromagnetic software package – MAFIA [4], which is a finite difference solver. With this driver, the whole optimization procedure is carried out fully automatically, from data initialization to printout of final results.

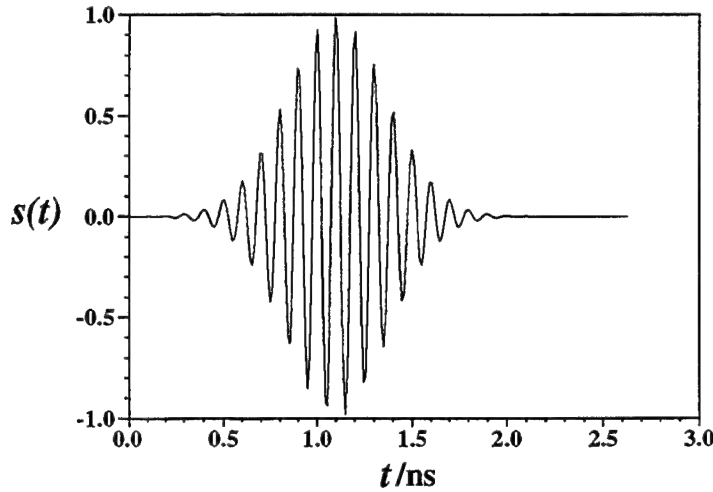


Figure 4: The excitation Signal

The optimization method used is the GaCD presented here. In addition to this local search method, a global search scheme is employed that uses the so-called Evolution Strategy. It should be pointed out that no satisfactory result could have been achieved if this global search phase had not been implemented.

The evaluation of the goal function is achieved by exciting the structure at the port-1 with a Gaussian modulated carrier signal (Fig. 4) and picking up the response at the port-2 of the same mode (i.e. mode H_{10}). After an FFT of the two signals, the goal function can be evaluated. The simulation is the common FDTD procedure.

The simulation is carried out in three dimensions. In the whole process of the optimization, the mesh is fixed to avoid discretization noises, which may cause wrong actions in the optimization strategy. Figure 5 describes the mesh in the area of the microstrip in the y - z plane. In x , an equi-distance mesh is employed. Total number of mesh points is $n_x \times n_y \times n_z = 12 \times 11 \times 59 = 7788$. The resolution for the optimization points is about 1 mm. With this being known, the stop criteria for this optimization should be accordingly set (see "Error Analysis" later).

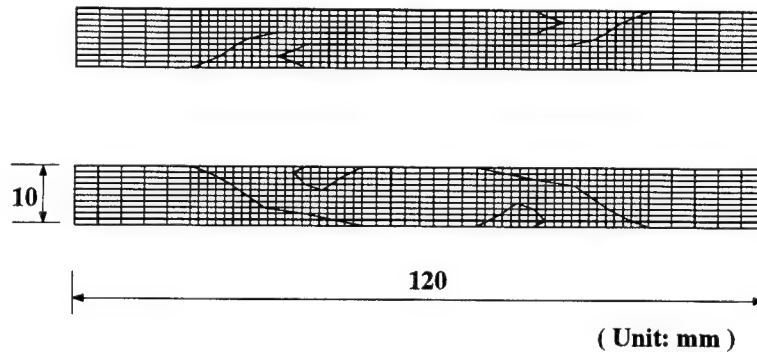


Figure 5: Mesh in the yz Plane

4.4 Results Acquired

After total 338 field calculations (i.e. goal function evaluations), which took about 103 hours on an IBM550 workstation, the final goal value of $\overline{S_{21}} = 0.996$ over the desired bandwidth was achieved, with the initial $\overline{S_{21}}$ being 0.501! The initial and final patterns are shown in Fig. 6.

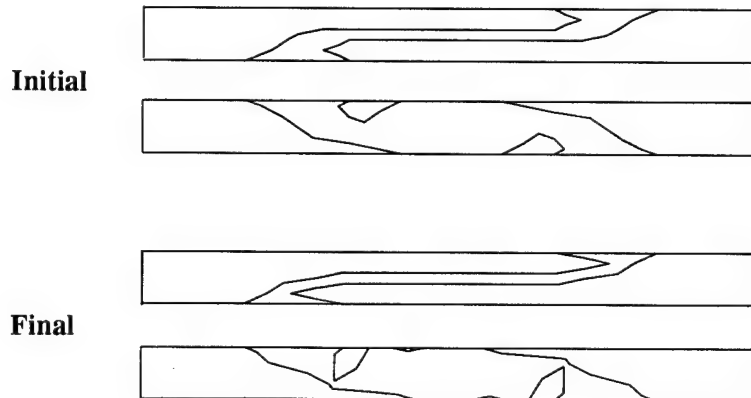


Figure 6: Initial and Final Patterns of the Transition Pair

4.5 The Measurement

Both the initial and the final transition pairs were fabricated and measured (Fig. 7). The grooves in the left block of the mounting waveguide were used for inserting the transition strips.

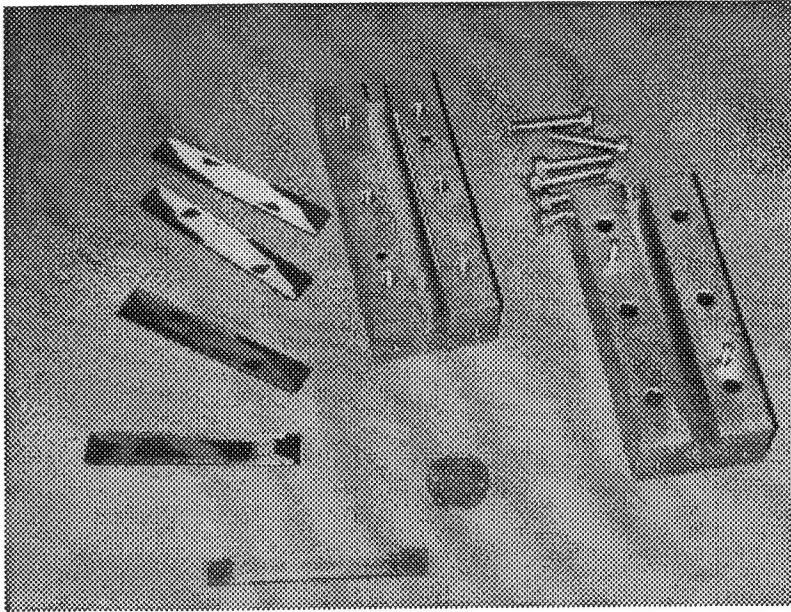


Figure 7: Transition Microstrips and Mounting Waveguide Blocks

The measurement showed a good agreement with the calculated results. The measured S_{21} together with the calculated one can be found in Fig. 8. It is found that the measured S_{21} is generally poorer than the calculated one. It is, most probably, because ohmic losses and the mounting grooves of the structure were not taken into account in the simulation.

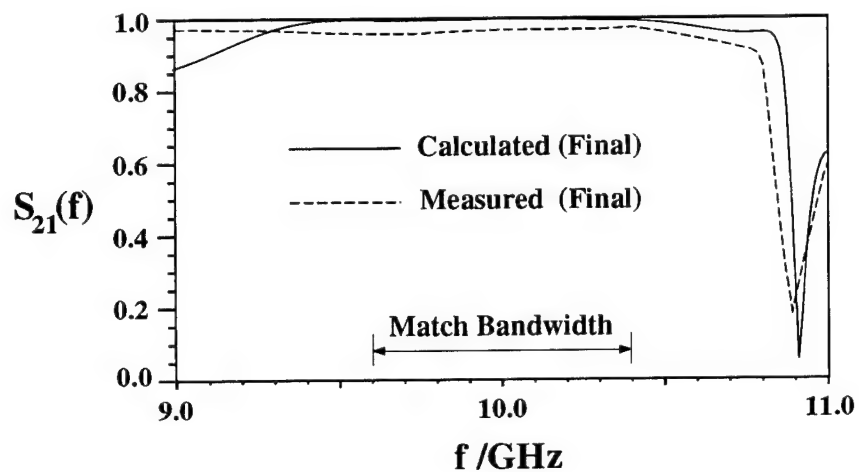


Figure 8: Measured and Calculated S_{21} for the Final Structure

5 Error Analysis

There are mainly three types of error sources. The first is coming from the evaluation of the goal function, or in other words, errors from the numerical solvers of the electromagnetic problems. This part of error has a strong relation with mesh sizes; Computer digital length is another error source, which limits the sensitivity of the optimization algorithms to the fine changes in goal functions. If the changes are too small to be digitized with the available effective length, the algorithm will do nothing and treat the values as unchanged. This can be influenced also by the definition of the goal function, which is the third source of errors. An inappropriate definition of the same problem will surely lead to either a premature stop of the algorithm or a wrong action by it.

5.1 More on Mesh-related Errors

For mesh-supported solvers, like the orthogonal mesh used here, attention should be paid to the selection of mesh. If the mesh is to be fixed throughout whole optimization processes, the stop criteria for the algorithm should be chosen accordingly. Figure 9 describes two different choices of mesh: one is fixed, the other adaptive.

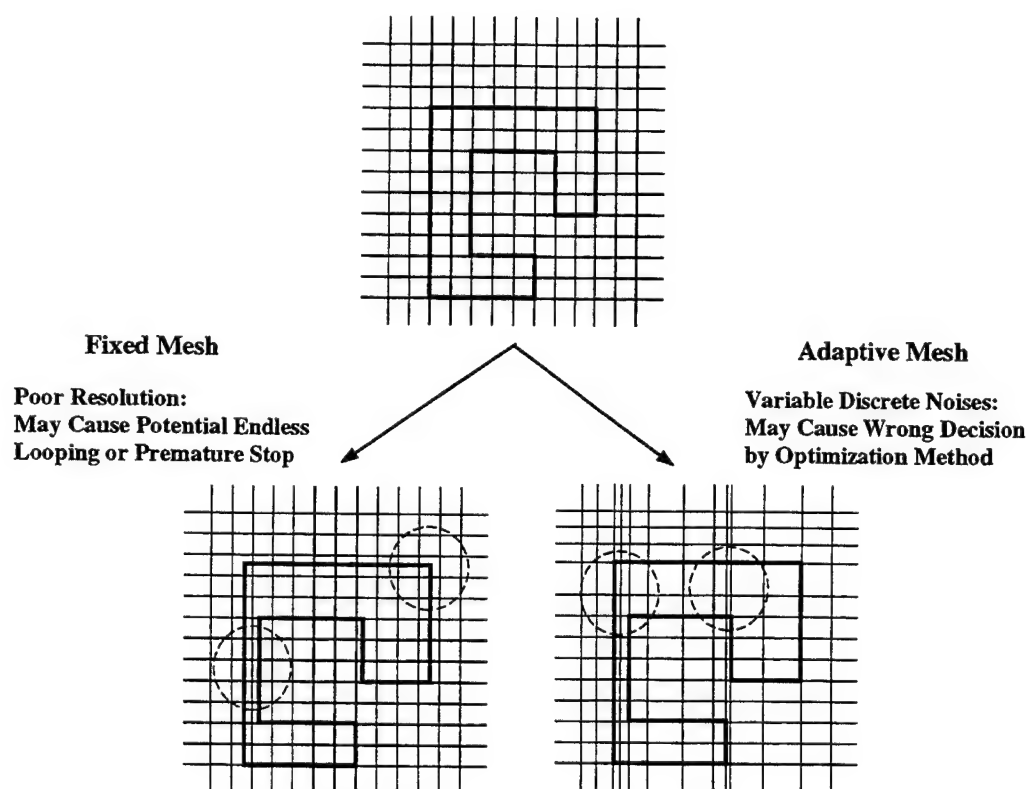


Figure 9: Two Types of Error Source Related to Mesh

For the fixed mesh case, an endless optimization looping is most likely to occur, if the stop criteria are set too fine or bear no account of the repeated failures due to that any fine tuning of the geometry will be impossible if the tune step is smaller than half of the local mesh size. This is

really very hard for practical design problems, since one should have some preknowledge about the relationship between the stop criteria and the mesh sizes. The best solution for this would be to impose a stop criterion which checks such non-improvement failures.

For the adaptive case, there comes another problem where due to computer discretization noises, the algorithms may make wrong decisions if the noises are comparable to the actual changes in the goal function. Such kind of noises is normally solver-type dependent. It becomes severer only when a very accurate result is to be achieved. For FDTD, it is relatively loose compared to eigenvalue cases, where the solution has a relatively high sensitivity to the local mesh size ratios.

6 Conclusions

A full derivation of the GaCD method was presented. In terms of the newly introduced assessment number η , the effectiveness of the method was compared with other commonly used conjugate direction methods against the test functions. It has been shown that the GaCD method is among the best of the methods tested. Further more, a practical optimization was successfully carried out using this new method. A hardware was built based on the numerical results, which delivered a very good performance as numerically predicted.

As a final remark, we would like to point out that for multipeak goal functions, a global search phase is absolutely necessary, since otherwise, starting from different initial points will, most probably, lead to different final results.

References

- [1] Donald A. Pierre, "Optimization Theory with Applications", Dover Publications Inc. (New York) 1986, pp314-322
- [2] F. A. Lootsma (Ed.), "Numerical Methods for Non-linear Optimization", Academic Press Inc. (London), 1972, pp69-97
- [3] M. Zhang, "Numerical Optimization of Electromagnetic Components", PhD Thesis, Technische Hochschule Darmstadt, 1995, Darmstadt, Germany
- [4] The MAFIA Collaboration, User's Guide MAFIA Version 3.x, CST GmbH, Lauteschlägerstraße 38, 64289 Darmstadt, Germany

Appendix A

The test functions used are defined below.

1. BEALE

$$\mathcal{G}(\mathbf{X}) = [1.5 - x_1(1 - x_2)]^2 + [2.25 - x_1(1 - x_2^2)]^2 + [2.625 - x_1(1 - x_2^3)]^2$$

2. CRAGG

$$\mathcal{G}(\mathbf{X}) = [\exp(x_1) - x_2]^4 + 100(x_2 - x_3)^6 + \tan^4(x_3 - x_4) + x_1^8 + (x_4 - 1)^2$$

3. ENGVALL-2d

$$\mathcal{G}(\mathbf{X}) = x_1^4 + x_2^4 + 2x_1^2x_2^2 - 4x_1 + 3$$

4. ENGVALL-3d

$$\mathcal{G}(\mathbf{X}) = \sum_{i=1}^5 g_i^2(\mathbf{X})$$

$$\begin{aligned} g_1(\mathbf{X}) &= x_1^2 + x_2^2 + x_3^2 - 1 \\ g_2(\mathbf{X}) &= x_1^2 + x_2^2 + (x_3^2 - 2)^2 - 1 \\ g_3(\mathbf{X}) &= x_1 + x_2 + x_3 - 1 \\ g_4(\mathbf{X}) &= x_1 + x_2 - x_3 + 1 \\ g_5(\mathbf{X}) &= x_1^3 + 3x_2^2 + (5x_3 - x_1 + 1)^2 - 36 \end{aligned}$$

5. POWELL

$$\mathcal{G}(\mathbf{X}) = (x_1 + 10x_2)^2 + 5(x_3 - x_4)^2 + (x_2 - 2x_3)^4 + 10(x_1 - x_4)^4$$

6. WHITE

$$\mathcal{G}(\mathbf{X}) = 100(x_2 - x_1^3)^2 + (1 - x_1)^2$$

7. WOOD

$$\begin{aligned} \mathcal{G}(\mathbf{X}) &= 100(x_2 - x_1^2)^2 + 90(x_4 - x_3^2)^2 + (1 - x_1)^2 + (1 - x_3)^2 + \\ &10.1[(1 - x_2)^2 + (1 - x_4)^2] + 19.8(1 - x_2)(1 - x_4) \end{aligned}$$

8. ZANGWILL-2d

$$\mathcal{G}(\mathbf{X}) = \frac{1}{15}(16x_1^2 + 16x_2^2 - 8x_1x_2 - 56x_1 - 256x_2 + 991)$$

9. ZANGWILL-3d

$$\mathcal{G}(\mathbf{X}) = (-x_1 + x_2 + x_3)^2 + (x_1 - x_2 + x_3)^2 + (x_1 + x_2 - x_3)^2$$

Appendix B

X^0 and G^0 are the initial point and the initial function value; X^* , G^* the analytical ones; X^\wedge , G^\wedge the ones found by the optimization methods; N_G the number of function evaluations.

Raw Results for Test Optimization Runs

Comparison of Various Optimization Methods via Common Test Functions (Test Runs Summary)								
	Init/Final	Item	GaCD	BFGS	DFP	Fletcher	M-Powell	ES
BEALE	$X^0: (10, -10)$	X^\wedge	(6.3668, 0.8117)	(6.3442, 0.8142)	(2.9883, 0.4959)	(6.3426, 0.8155)	(-12.5481, 1.0742)	(2.9861, 0.4963)
	$G^0: 1.0114e8$	G^\wedge	2.1017e-1	2.0256e-1	5.4101e-5	2.0166e-1	5.7019e-1	3.2355e-5
	$X^*: (3, 0.5)$	N_G	350	558	674	391	6308	4641
	$G^*: 0$	η, η_0	5.7119, 1.0	3.5894, 0.6284	4.1924, 0.7339	5.1236, 0.8970	0.3011, 0.0527	0.6199, 0.1085
CRAGG	$X^0: (5, 5, 5, 5)$	X^\wedge	(-0.0102, 0.9445, 0.9861, 0.9992)	(0.2806, 1.2365, 1.1070, 1.0068)	(0.1747, 1.1523, 1.0520, 0.9976)	(0.1692, 1.1400, 1.0608, 0.9954)	(0.1313, 1.1028, 1.0404, 1.0008)	(0.1326, 1.1128, 1.0583, 0.9997)
	$G^0: 4.2340e8$	G^\wedge	5.3529e-6	7.1738e-4	1.1994e-4	6.9229e-5	1.1058e-5	1.5332e-5
	$X^*: (0, 1, 1, 1)$	N_G	761	2312	622	1844	2531	6641
	$G^*: 0$	η, η_0	4.2052, 0.9053	1.1723, 0.2524	4.6451, 1.0	1.5966, 0.3437	1.2357, 0.2660	0.4661, 0.1003
ENG-VALL (2d)	$X^0: (10, 10)$	X^\wedge	(0.9949, 0.0007)	(0.9951, -0.0024)	(1.0009, -0.0058)	(0.9964, 0.0049)	(0.9950, -1.91e-6)	(0.9986, -0.0021)
	$G^0: 39963.0$	G^\wedge	1.5187e-4	1.5593e-4	7.2479e-5	1.2493e-4	1.4830e-4	2.0504e-5
	$X^*: (1, 0)$	N_G	475	435	551	657	599	3121
	$G^*: 0$	η, η_0	4.0817, 0.9170	4.4510, 1.0	3.6530, 0.8207	2.9807, 0.6696	3.2407, 0.7281	0.6854, 0.1540
ENG-VALL (3d)	$X^0: (5, -5, -5)$	X^\wedge	(-0.5195, -0.3588, 0.8870)	(1.5646, -2.8408, 0.0365)	(0.0972, -0.1124, 1.0180)	(0.3715, -0.9582, 1.0313)	Failed	(0.5986, -0.6582, -1.2334)
	$G^0: 1025177.0$	G^\wedge	2.0974	335.6351	7.1720e-3	3.0082		118.2426
	$X^*: (0, 0, 1)$	N_G	506	262	1488	1312		1201
	$G^*: 0$	η, η_0	2.5889, 0.8453	3.0627, 1.0	1.2619, 0.4120	0.9710, 0.3170	0.0, 0.0	0.7550, 0.2465
POWELL	$X^0: (5, -5, -5)$	X^\wedge	(0.0601, -0.0101, -0.0489, -0.0420)	(-0.0466, 0.1047, -0.6756, 0.1404)	(-0.1104, 0.0116, -0.1024, -0.1044)	(0.0296, -0.0014, -0.1072, -0.1256)	(-0.8386, 0.0628, -0.3853, -0.4822)	(-0.1806, 0.0217, -0.1053, -0.1027)
	$G^0: 153150.0$	G^\wedge	3.0639e-3	8.8360	2.2369e-3	9.8247e-3	7.3507e-1	4.6038
	$X^*: (0, 0, 0, 0)$	N_G	1339	316	750	1235	1438	3761
	$G^*: 0$	η, η_0	1.3239, 0.4286	3.0887, 1.0	2.4056, 0.7788	1.3411, 0.4342	0.8517, 0.2757	0.2768, 0.0896
WHITE	$X^0: (-5, -5)$	X^\wedge	(-1.7196, -5.0435)	(-1.7088, -4.9851)	(-1.5010, -3.3602)	(-1.7192, -5.0762)	(-1.7146, -5.0458)	(-1.6492, -4.4786)
	$G^0: 1440036.0$	G^\wedge	7.5649	7.3401	6.3007	7.3969	7.3716	7.0226
	$X^*: (1, 1)$	N_G	220	169	328	259	506	721
	$G^*: 0$	η, η_0	5.5258, 0.7663	7.2111, 1.0	3.7620, 0.5217	4.7024, 0.6521	2.4076, 0.3339	1.6964, 0.2352
WOOD	$X^0: (-3, -1, -3, -1)$	X^\wedge	(1.0180, 1.0407, 0.9709, 0.9406)	(0.7458, 0.5275, -0.7379, 0.5027)	(1.3441, 1.8087, 0.0541, 0.0246)	(1.0740, 1.1627, 0.8236, 0.6697)	(0.8279, 0.7390, 0.7766, 0.6563)	(-1.0139, 1.0307, -0.7823, 0.6445)
	$G^0: 19192.0$	G^\wedge	7.9214e-3	12.7312	1.6522	3.5732e-1	4.2780	8.3979
	$X^*: (1, 1, 1, 1)$	N_G	810	531	715	689	808	1121
	$G^*: 0$	η, η_0	1.8149, 1.0	1.3782, 0.7594	1.3091, 0.7213	1.5808, 0.8710	1.0407, 0.5734	0.6899, 0.3802
ZANG-WILL (2d)	$X^0: (0, 0)$	X^\wedge	(3.9936, 8.9948)	(4.0049, 9.0002)	(4.0049, 8.9999)	(3.9950, 8.9979)	(3.9379, 8.9928)	(4.0337, 9.0108)
	$G^0: 66.0667$	G^\wedge	-18.2000	-18.2000	-18.2000	-18.2000	-18.1961	-18.1989
	$X^*: (4, 9)$	N_G	301	279	273	313	3128	1521
	$G^*: -18.2$	η, η_0	*, 0.9070	*, 0.9785	*, 1.0	*, 0.8722	*, 0.0873	*, 0.1795
ZANG-WILL (3d)	$X^0: (100, -1, 2.5)$	X^\wedge	(-0.0246, -0.0045, -0.0067)	(-0.0282, -0.0104, -0.0161)	(-0.0208, -0.0245, -0.0248)	(0.0246, 0.0169, 0.0172)	(-0.0305, 0.0005, -0.0171)	(-0.0004, -0.0009, 0.0010)
	$G^0: 29726.75$	G^\wedge	1.3991e-3	1.6628e-3	1.6782e-3	1.3041e-3	2.6743e-3	8.4492e-6
	$X^*: (0, 0, 0)$	N_G	830	878	916	1014	992	20241
	$G^*: 0$	η, η_0	2.0327, 1.0	1.9019, 0.9357	1.8220, 0.8963	1.6708, 0.8220	1.6355, 0.8046	0.1086, 0.0534

1996 INSTITUTIONAL MEMBERS

THE AEROSPACE CORPORATION
PO Box 92957
Los Angeles, CA 90009-2957

ANDREW CORPORATION
10500 W. 153rd Street
Orland Park, IL 60462

ATOMIC WEAPONS ESTAB. UK
Bldg. E3, Awe Aldermaston
Reading, BERKS, UK RG7 4PR

BRITISH AEROSPACE
Wharton Aerodrome, Nr. Wharton
Preston, LANCS. UK PR4 1AX

BRITISH AEROSPACE
FPC 267 PO Box 5
Filton, BRISTOL, UK BS12 7QW

BRITISH BROADCASTING CO.
Kingswood Warren
Tadworth, SURREY, UK KT20 6NP

CAMBRIDGE CONSULTANTS LTD
Milton Road, Science Park
Cambridge, CAMBS, UK CB5 4DW

CHALMERS UNIV OF TECHNOLOGY
Dept. of Microwave Technology
Gothenburg, SWEDEN S 412 96

CSC PROFESSIONAL SERVICES GP.
10101 Senate Drive
Lanham, MD 20706-4368

CSELT
Via Guglielmo Reiss Romoli 274
Turin, ITALY 10148

CSIRO, CENTER FOR ADV. TECH.
PO Box 883
Kenmore, QLD, AUSTRALIA 4069

CUBIC COMMUNICATIONS INC.
PO Box 85587
San Diego, CA 92186-5587

CULHAM LAB
UK Atomic Energy Authority
Abingdon, OXFORD, UK OX14 3D8

D.L.R. OBERPFAFFENHOFEN
Zentralbibliothek
Wessling, OBB, GERMANY 8031

DEFENCE TECH & PROCUREMENT
Nemp Lab - AC Zentrum
Spiez, SWITZERLAND CH 3700

DEFENSE RESEARCH ESTAB. LIB.
3701 Carling Avenue
Ottawa, ON, CANADA K1A 0Z4

DERA INFORMATION CENTRE
A-4 Bldg. Ively Road
Farnborough, HAMPSH. UK GU14 0LX

DSTO LIBRARY
Box 1500
Salisbury, SA AUSTRALIA 5108

ELECTRICAL COMM. LAB/LIBRARY
1 2356 Take Yokosuka Shi
Kanagawa, KEN, MZ, JAPAN 238

ESCUELA TRANSMISIONES
EJERCITO DEL AIRE
Ctr. Extremadura, Km 10, 200
Madrid, SPAIN 28024

FANFIELD LTD.
Braxted Park
Witham, ESSEX, UK CM8 3XB

FELDBERG LIBRARY
Dartmouth College
Hanover, NH 03755

FGAN/FHP
Neuenahr Strasse 20
Wachtberg-Werthoven, GERMANY
53343

GEC MARCONI RESEARCH CTR, LIB.
W. Hanningfield Road
Gt. Baddow, CHLMSFRD, UK CM2 8HN

HKUST LIBRARY
Clear Water Bay Road
Kowloon, HONG KONG

HOKKAIDO DAIGAKU
Nishi 8, Kita 13
Sapporo, JAPAN 060

HUGHES RESEARCH LIBRARY
3011 Malibu Canyon Road
Malibu, CA 90265-4737

HUNTING ENGINEERING LTD
Reddings Wood, Ampthill
Bedford, UK MK45 2HD

IABG
Einsteinstrasse 20
Ottobrunn, GERMANY D-85521

IIT RESEARCH INSTITUTE
185 Admiral Cochrane Drive
Annapolis, MD 21401-7396

IMAGINEERING LIMITED
95 Barber Greene Road, Suite. 112
Toronto, ON, CANADA M3C 3E9

IPS RADIO & SPACE SVC., LIBRARY
PO Box 5606
W. Chatswood, NSW, AUSTRALIA 2057

KATHREIN-WERKE KG
Postbox 100 444
Rosenheim, GERMANY D-83004

KERSHNER, WRIGHT & HAGAMAN
5730 Gen. Washington Drive
Alexandria, VA 22312

LIBRARY, IREQ
1800 Montee Ste.- Julie
Varenes, QC, CANADA J3X 1S1

LICOSA LIBRERIA COMM SANSONI
Via Duca Di Calabria 1/1
Florence, ITALY 50125

LINDA HALL LIBRARY
5109 Cherry Street
Kansas City, MO 64110-2498

MATRA DEFENSE
37 Av. Louis Breguet BP 1
Velizy, Cedex, FRANCE 78590

METAWAVE COMMUNICATIONS
8700 148th Avenue, N.E.
Redmond, WA 98052

MISSISSIPPI STATE UNIV LIBRARY
PO Box 9570
Mississippi State, MS 39762

MITRE CORPORATION LIBRARY
202 Burlington Road
Bedford, MA 01730-1407

MONASH UNIVERSITY
900 Dandenong Road, Caulfield East
Melbourne, VIC, AUSTRALIA 3145

MOTOROLA CSGR
600 N. US Hwy 45
Libertyville, IL 60048

MPB TECHNOLOGIES INC.
151 Hymus Blvd.
Pointe-Claire, QC, CANADA H9R 1E9

NATIONAL AEROSPACE LAB, LIB.
Anthony Fokkerweg 2, PO Box 153
Emmeloord, THE NETHERLANDS
CM 1059

NATIONAL RADIOLOGICAL PROT. BD.
Chilton
Didcot, OXON, UK OX11 0RQ

NAVITALIA
5301 Wisconsin Avenue, N.W.
Washington, DC 20015

NIKSAR
35/45 Gilbey Road
Mt. Waverley, VIC, AUSTRALIA 3149

NORTEL TECHNOLOGY
London Road
Harlow, ESSEX, UK CM17 9NA

OXFORD INSTRUMENTS PLC
Osney Mead
Oxford, OXON, UK OX2 0DX

PENN STATE UNIVERSITY
Pattee Library
University Park, PA 16802

QUEEN MARY & WESTFIELD COLL.
Mile End Road
London, UK E14NS

RADIO FREQUENCY SYSTEMS, PL.
36 Garden Street
Kilsyth, VIC, AUSTRALIA 3137

RADIO FREQUENCY SYSTEMS, PL.
12 Waddikee Road
Lonsdale, SA, AUSTRALIA 5600

INSTITUTIONAL MEMBERS (CONT)

RES. INST. OF IND. SCIENCE LIB.
17 Haengdang-Dong
Sungdong-Ku, SEOUL,
S. KOREA 133-791

ROYAL MILIT COLL OF SCIENCE
Cranfield University
Swindon, WILTS, UK SN6 8LA

SAAB-SCANIA AB
Saab Military Aircraft
Linkoping, SWEDEN S-58188

SERCO SERVICES
Cheeseman's Lane
Hambrook, W. SUSSEX, UK PO18 8U

TASC-LIBRARY
55 Walkers Brook Drive
Reading, MA 01867-3297

TECHNISCHE UNIVERSITEIT DELFT
Mekelweg 4
Delft, HOLLAND
THE NETHERLANDS 2628 CD

TELEBRAS - CPQD LIBRARY
CP 1579
Campinas, SP, BRAZIL 13088-061

TELSTRA, LIBRARY
Private Bag 37, 770 Blackburn Road
Clayton, VIC, AUSTRALIA 3168

UNIV OF CENTRAL FLORIDA LIB.
PO Box 162440
Orlando, FL 32816-2440

UNIVERSITY OF COLORADO LIB.
Campus Box 184
Boulder, CO 80309-0184

UNIV OF MISSOURI-ROLLA LIB.
Periodicals
Rolla, MO 65401

UNIVERSITY OF SURREY
Center for Satellite Research
Guildford, SURREY, UK GU2 5XH

UNIV. DER BUNDESWEHR MUNCHEN
Werner Heisenberg Weg 39
Neubiberg, GERMANY D-85577

US COAST GUARD ACADEMY
15 Mohegan Avenue
New London, CT 06320-4195

VECTOR FIELDS LTD.
24 Bankside Kidlington
Oxford, UK OX5 1JE

VIT, TECH RESEARCH CENTER
PO Box 1202
Espoo, FINLAND FIN-02044

WATKINS-JOHNSON CO. LIB.
700 Quince Orchard Road
Gaithersburg, MD 20878-1794

YORK ELECTRONICS CENTRE
University of York
Heslington, YORK, UK YO1 5DD

ACES COPYRIGHT FORM

This form is intended for original, previously unpublished manuscripts submitted to ACES periodicals and conference publications. The signed form, appropriately completed, MUST ACCOMPANY any paper in order to be published by ACES. PLEASE READ REVERSE SIDE OF THIS FORM FOR FURTHER DETAILS.

TITLE OF PAPER:

AUTHORS(S)

PUBLICATION TITLE/DATE:

RETURN FORM TO:

Dr. Richard W. Adler
Naval Postgraduate School
Code EC/AB
833 Dyer Road, Room 437
Monterey, CA 93943-5121 USA

PART A - COPYRIGHT TRANSFER FORM

(NOTE: Company or other forms may not be substituted for this form. U.S. Government employees whose work is not subject to copyright may so certify by signing Part B below. Authors whose work is subject to Crown Copyright may sign Part C overleaf).

The undersigned, desiring to publish the above paper in a publication of ACES, hereby transfer their copyrights in the above paper to The Applied Computational Electromagnetics Society (ACES). The undersigned hereby represents and warrants that the paper is original and that he/she is the author of the paper or otherwise has the power and authority to make and execute this assignment.

Returned Rights: In return for these rights, ACES hereby grants to the above authors, and the employers for whom the work was performed, royalty-free permission to:

1. Retain all proprietary rights other than copyright, such as patent rights.
2. Reuse all or portions of the above paper in other works.
3. Reproduce, or have reproduced, the above paper for the author's personal use or for internal company use provided that (a) the source and ACES copyright are indicated, (b) the copies are not used in a way that implies ACES endorsement of a product or service of an employer, and (c) the copies per se are not offered for sale.
4. Make limited distribution of all or portions of the above paper prior to publication.
5. In the case of work performed under U.S. Government contract, ACES grants the U.S. Government royalty-free permission to reproduce all or portions of the above paper, and to authorize others to do so, for U.S. Government purposes only.

ACES Obligations: In exercising its rights under copyright, ACES will make all reasonable efforts to act in the interests of the authors and employers as well as in its own interest. In particular, ACES REQUIRES that:

1. The consent of the first-named author be sought as a condition in granting re-publication permission to others.
2. The consent of the undersigned employer be obtained as a condition in granting permission to others to reuse all or portions of the paper for promotion or marketing purposes.

In the event the above paper is not accepted and published by ACES or is withdrawn by the author(s) before acceptance by ACES, this agreement becomes null and void.

AUTHORIZED SIGNATURE

TITLE (IF NOT AUTHOR)

EMPLOYER FOR WHOM WORK WAS PERFORMED

DATE FORM SIGNED

PART B - U.S. GOVERNMENT EMPLOYEE CERTIFICATION

(NOTE: If your work was performed under Government contract but you are not a Government employee, sign transfer form above and see item 5 under Returned Rights).

This certifies that all authors of the above paper are employees of the U.S. Government and performed this work as part of their employment and that the paper is therefore not subject to U.S. copyright protection.

AUTHORIZED SIGNATURE

TITLE (IF NOT AUTHOR)

NAME OF GOVERNMENT ORGANIZATION

DATE FORM SIGNED

PART C - CROWN COPYRIGHT

(Note: ACES recognizes and will honor Crown Copyright as it does U.S. Copyright. It is understood that, in asserting Crown Copyright, ACES in no way diminishes its rights as publisher. Sign only if ALL authors are subject to Crown Copyright.

This certifies that all authors of the above Paper are subject to Crown Copyright. (Appropriate documentation and instructions regarding form of Crown Copyright notice may be attached).

AUTHORIZED SIGNATURE

TITLE OF SIGNED

NAME OF GOVERNMENT BRANCH

DATE FORM SIGNED

Information to Authors

ACES POLICY

ACES distributes its technical publications throughout the world, and it may be necessary to translate and abstract its publications, and articles contained therein, for inclusion in various compendiums and similar publications, etc. When an article is submitted for publication by ACES, acceptance of the article implies that ACES has the rights to do all of the things it normally does with such an article.

In connection with its publishing activities, it is the policy of ACES to own the copyrights in its technical publications, and to the contributions contained therein, in order to protect the interests of ACES, its authors and their employers, and at the same time to facilitate the appropriate re-use of this material by others.

The new United States copyright law requires that the transfer of copyrights in each contribution from the author to ACES be confirmed in writing. It is therefore necessary that you execute either Part A-Copyright Transfer Form or Part B-U.S. Government Employee Certification or Part C-Crown Copyright on this sheet and return it to the Managing Editor (or person who supplied this sheet) as promptly as possible.

CLEARANCE OF PAPERS

ACES must of necessity assume that materials presented at its meetings or submitted to its publications is properly available for general dissemination to the audiences these activities are organized to serve. It is the responsibility of the authors, not ACES, to determine whether disclosure of their material requires the prior consent of other parties and if so, to obtain it. Furthermore, ACES must assume that, if an author uses within his/her article previously published and/or copyrighted material that permission has been obtained for such use and that any required credit lines, copyright notices, etc. are duly noted.

AUTHOR/COMPANY RIGHTS

If you are employed and you prepared your paper as a part of your job, the rights to your paper initially rest with your employer. In that case, when you sign the copyright form, we assume you are authorized to do so by your employer and that your employer has consented to all of the terms and conditions of this form. If not, it should be signed by someone so authorized.

NOTE RE RETURNED RIGHTS: Just as ACES now requires a signed copyright transfer form in order to do "business as usual", it is the intent of this form to return rights to the author and employer so that they too may do "business as usual". If further clarification is required, please contact: The Managing Editor, R.W. Adler, Naval Postgraduate School, Code EC/AB, Monterey, CA, 93943, USA (408)656-2352.

Please note that, although authors are permitted to re-use all or portions of their ACES copyrighted material in other works, this does not include granting third party requests for reprinting, republishing, or other types of re-use.

JOINT AUTHORSHIP

For jointly authored papers, only one signature is required, but we assume all authors have been advised and have consented to the terms of this form.

U.S. GOVERNMENT EMPLOYEES

Authors who are U.S. Government employees are not required to sign the Copyright Transfer Form (Part A), but any co-authors outside the Government are.

Part B of the form is to be used instead of Part A only if all authors are U.S. Government employees and prepared the paper as part of their job.

NOTE RE GOVERNMENT CONTRACT WORK: Authors whose work was performed under a U.S. Government contract but who are not Government employees are required to sign Part A-Copyright Transfer Form. However, item 5 of the form returns reproduction rights to the U.S. Government when required, even though ACES copyright policy is in effect with respect to the reuse of material by the general public.

ACES MEMBERSHIP - NEWSLETTER & JOURNAL SUBSCRIPTION FORM

please print

LAST NAME _____ FIRST NAME _____ MIDDLE INITIAL _____

COMPANY/ORGANIZATION/UNIVERSITY _____ DEPARTMENT/MAIL STATION _____

PLEASE LIST THE ADDRESS YOU WANT USED FOR PUBLICATIONS

MAILING ADDRESS _____

CITY _____ PROVINCE/STATE _____ COUNTRY _____ ZIP/POSTAL CODE _____

TELEPHONE _____ FAX _____ AMATEUR RADIO CALL SIGN _____

E-MAIL ADDRESS _____ E-MAIL ADDRESS CAN BE INCLUDED IN ACES DATABASE ☐ YES ☐ NO

PERMISSION IS GRANTED TO HAVE MY NAME PLACED ON MAILING LISTS WHICH MAY BE SOLD ☐ YES ☐ NO

CURRENT SUBSCRIPTION PRICES

AREA	INDIVIDUAL SURFACE MAIL	INDIVIDUAL AIRMAIL	ORGANIZATIONAL (AIRMAIL ONLY)
U.S. & CANADA	() \$ 65	() \$ 65	() \$115
MEXICO, CENTRAL & SOUTH AMERICA	() \$ 68	() \$ 70	() \$115
EUROPE, FORMER USSR TURKEY, SCANDINAVIA	() \$ 68	() \$ 78	() \$115
ASIA, AFRICA, MIDDLE EAST & PACIFIC RIM	() \$ 68	() \$ 85	() \$115

FULL-TIME STUDENT/RETIRED/UNEMPLOYED RATE IS \$25 FOR ALL COUNTRIES

CREDIT CARD USERS

IF YOU ARE PAYING BY CREDIT CARD & CARD IS YOUR OWN, YOU MUST, (1) PRINT AND SIGN YOUR NAME BELOW; (2) MAKE SURE YOUR COMPLETE ADDRESS IS LISTED ABOVE. IF THE CARD YOU ARE USING IS NOT YOUR CARD, THE CARD HOLDER MUST, (3) PRINT AND SIGN HIS/HER NAME AND, (4) ENTER HIS/HER COMPLETE ADDRESS BELOW.

PRINT FIRST AND LAST NAME OF CARD HOLDER _____

SIGNATURE OF CARD HOLDER _____

MAILING ADDRESS _____

MAILING ADDRESS (cont) _____

METHOD OF PAYMENT	<input type="checkbox"/> A bank check for the total amount is enclosed. ⁽¹⁾ <input type="checkbox"/> Traveler's checks for the total amount are enclosed. ⁽²⁾ <input type="checkbox"/> International Money Order is enclosed. ⁽³⁾ <input type="checkbox"/> Charge to: <input type="checkbox"/> MasterCard <input type="checkbox"/> Visa. <input type="checkbox"/> Discover <input type="checkbox"/> Amex. ⁽⁴⁾
-------------------	--

Card No.

Card Exp. Date:
Mo. _____ Year _____

MAKE CHECKS PAYABLE TO "ACES" and send to: RICHARD W. ADLER, EXEC. OFFICER,
NAVAL POSTGRADUATE SCHOOL, ECE DEPT., CODE EC/AB, 833 DYER ROAD, ROOM 437, MONTEREY, CA 93943-5121

Non-USA participants may remit via (1) **Bank Checks**, if (a) drawn on a U.S. Bank, (b) have bank address, (c) contain series of (9) digit mandatory routing numbers; (2) **Traveler's Checks** (in U.S. \$\$); (3) **International Money Order** drawn in U.S. funds, payable in U.S.; (4) **Credit Cards**: Visa, Master Card, Discover Card, Amex.

Total Remittance (U.S. Dollars Only) \$ _____ 103

October 1996

ADVERTISING RATES		
	FEE	PRINTED SIZE
Full page	\$200.	7.5" x 10.0"
1/2 page	\$100.	7.5" x 4.7" or 3.5" x 10.0"
1/4 page	\$ 50	3.5" x 4.7"
<p>All ads must be camera ready copy.</p> <p>Ad deadlines are same as Newsletter copy deadlines.</p> <p>Place ads with Ray Perez, Newsletter Editor, Martin Marietta Astronautics, MS 58700, PO Box 179, Denver, CO 80201, USA. The editor reserves the right to reject ads.</p>		

ACES NEWSLETTER AND JOURNAL COPY INFORMATION	
<u>Issue</u>	<u>Copy Deadline</u>
March	January 13
July	May 25
November	September 25

APPLIED COMPUTATIONAL ELECTROMAGNETICS SOCIETY JOURNAL

INFORMATION FOR AUTHORS

PUBLICATION CRITERIA

Each paper is required to manifest some relation to applied computational electromagnetics. **Papers may address general issues in applied computational electromagnetics, or they may focus on specific applications, techniques, codes, or computational issues.** While the following list is not exhaustive, each paper will generally relate to at least one of these areas:

1. Code validation. This is done using internal checks or experimental, analytical or other computational data. Measured data of potential utility to code validation efforts will also be considered for publication.

2. Code performance analysis. This usually involves identification of numerical accuracy or other limitations, solution convergence, numerical and physical modeling error, and parameter tradeoffs. However, it is also permissible to address issues such as ease-of-use, set-up time, run time, special outputs, or other special features.

3. Computational studies of basic physics. This involves using a code, algorithm, or computational technique to simulate reality in such a way that better or new physical insight or understanding is achieved.

4. New computational techniques, or new applications for existing computational techniques or codes.

5. "Tricks of the trade" in selecting and applying codes and techniques.

6. New codes, algorithms, code enhancement, and code fixes. This category is self-explanatory but includes significant changes to existing codes, such as applicability extensions, algorithm optimization, problem correction, limitation removal, or other performance improvement. **Note: Code (or algorithm) capability descriptions are not acceptable, unless they contain sufficient technical material to justify consideration.**

7. Code input/output issues. This normally involves innovations in input (such as input geometry standardization, automatic mesh generation, or computer-aided design) or in output (whether it be tabular, graphical, statistical, Fourier-transformed, or otherwise signal-processed). Material dealing with input/output database management, output interpretation, or other input/output issues will also be considered for publication.

8. Computer hardware issues. This is the category for analysis of hardware capabilities and limitations in meeting

various types of electromagnetics computational requirements. Vector and parallel computational techniques and implementation are of particular interest.

Applications of interest include, but are not limited to, antennas (and their electromagnetic environments), networks, static fields, radar cross section, shielding, radiation hazards, biological effects, electromagnetic pulse (EMP), electromagnetic interference (EMI), electromagnetic compatibility (EMC), power transmission, charge transport, dielectric and magnetic materials, microwave components, MMIC technology, remote sensing and geophysics, communications systems, fiber optics, plasmas, particle accelerators, generators and motors, electromagnetic wave propagation, non-destructive evaluation, eddy currents, and inverse scattering.

Techniques of interest include frequency-domain and time-domain techniques, integral equation and differential equation techniques, diffraction theories, physical optics, moment methods, finite differences and finite element techniques, modal expansions, perturbation methods, and hybrid methods. This list is not exhaustive.

A unique feature of the Journal is the publication of unsuccessful efforts in applied computational electromagnetics. Publication of such material provides a means to discuss problem areas in electromagnetic modeling. Material representing an unsuccessful application or negative results in computational electromagnetics will be considered for publication only if a reasonable expectation of success (and a reasonable effort) are reflected. Moreover, such material must represent a problem area of potential interest to the ACES membership.

Where possible and appropriate, authors are required to provide statements of quantitative accuracy for measured and/or computed data. This issue is discussed in "Accuracy & Publication: Requiring quantitative accuracy statements to accompany data", by E.K. Miller, *ACES Newsletter*, Vol. 9, No. 3, pp. 23-29, 1994, ISBN 1056-9170.

EDITORIAL REVIEW

In order to ensure an appropriate level of quality control, papers are refereed. They are reviewed both for technical correctness and for adherence to the listed guidelines regarding information content. Authors should submit the initial manuscript in draft form so that any suggested changes can be made before the photo-ready copy is prepared for publication.

APPLIED COMPUTATIONAL ELECTROMAGNETICS SOCIETY JOURNAL

INFORMATION FOR AUTHORS

STYLE FOR CAMERA READY COPY

The ACES Journal is flexible, within reason, in regard to style. However, certain requirements are in effect:

1. The paper title should NOT be placed on a separate page. The title, author(s), abstract, and (space permitting) beginning of the paper itself should all be on the first page. The title, author(s), and author affiliations should be centered (center-justified) on the first page.
2. An abstract is REQUIRED. The abstract should state the computer codes, computational techniques, and applications discussed in the paper (as applicable) and should otherwise be usable by technical abstracting and indexing services.
3. Either British English or American English spellings may be used, provided that each word is spelled consistently throughout the paper.
4. Any commonly-accepted format for referencing is permitted, provided that internal consistency of format is maintained. As a guideline for authors who have no other preference, we recommend that references be given by author(s) name and year in the body of the paper (with alphabetical listing of all references at the end of the paper). Titles of Journals, monographs, and similar publications should be in boldface or italic font or should be underlined. Titles of papers or articles should be in quotation marks.
5. Internal consistency shall also be maintained for other elements of style, such as equation numbering. As a guideline for authors who have no other preference, we suggest that equation numbers be placed in parentheses at the right column margin.
6. The intent and meaning of all text must be clear. For authors who are NOT masters of the English language, the ACES Editorial Staff will provide assistance with grammar (subject to clarity of intent and meaning).
7. Unused space should be minimized. Sections and subsections should not normally begin on a new page.

MATERIAL, SUBMITTAL FORMAT AND PROCEDURE

The preferred format for submission and subsequent review, is 12 point font or 12 cpi, double line spacing and single column per page. Four copies of all submissions should be sent to the Editor-in-Chief. Each submission must be accompanied by a covering letter. The letter should include the name, address, and telephone and/or fax number and/or e-mail address of at least one of the authors.

Only camera-ready original copies are accepted for publication. The term **"camera-ready"** means that the material is neat, legible, and reproducible. The preferred font style is Times Roman 10 point (or equivalent) such as that used in this text. A double column format similar to that used here is preferred. **No author's work will be turned down once it has been accepted because of an inability to meet the requirements concerning fonts and format.** Full details are sent to the author(s) with the letter of acceptance.

There is NO requirement for India ink or for special paper; any plain white paper may be used. However, faded lines on figures and white streaks along fold lines should be avoided. Original figures - even paste-ups - are preferred over "nth-generation" photocopies. These original figures will be returned if you so request.

While ACES reserves the right to re-type any submitted material, this is not generally done.

PUBLICATION CHARGES

ACES members are allowed 12 pages per paper without charge; non-members are allowed 8 pages per paper without charge. Mandatory page charges of \$75 a page apply to all pages in excess of 12 for members or 8 for non-members. Voluntary page charges are requested for the free (12 or 8) pages, but are NOT mandatory or required for publication. A priority courtesy guideline, which favors members, applies to paper backlogs. Full details are available from the Editor-in-Chief.

COPYRIGHTS AND RELEASES

Each primary author must sign a copyright form and obtain a release from his/her organization vesting the copyright with ACES. Forms will be provided by ACES. Both the author and his/her organization are allowed to use the copyrighted material freely for their own private purposes.

Permission is granted to quote short passages and reproduce figures and tables from an ACES Journal issue provided the source is cited. Copies of ACES Journal articles may be made in accordance with usage permitted by Sections 107 or 108 of the U.S. Copyright Law. This consent does not extend to other kinds of copying, such as for general distribution, for advertising or promotional purposes, for creating new collective works, or for resale. The reproduction of multiple copies and the use of articles or extracts for commercial purposes require the consent of the author and specific permission from ACES. Institutional members are allowed to copy any ACES Journal issue for their internal distribution only.